

4 JSAP-Optica Joint Symposia 2024 | 一般セッション(ポスター講演): 4 JSAP-Optica Joint Symposia 2024 (ポスター)

## **[19a-P08-1~9] 4 JSAP-Optica Joint Symposia 2024 (ポスター)**

[19a-P08-1]

Laser-induced Photothermal- and Magneto-Responsive Polymer Composites for Soft-Bodied Devices

○Hoon Eui Jeong<sup>1</sup>, Moonkyu Kwak<sup>3</sup>, Hosup Jung<sup>2</sup> (1.UNIST, 2.Seoul National Univ., 3.Kyungpook Nat. Univ.)

[19a-P08-2]

Silicon Waveguide Output Coupler Based on Nanohole Array

Ya-Cin Chung<sup>1,2</sup>, Min-Hsiung Shih<sup>2</sup>, Shu-Wei Chang<sup>2</sup>, ○Wan-Shao Tsai<sup>1</sup> (1.National Chung Hsing Univ., 2.Academia Sinica)

[19a-P08-3]

Determining Elastic Modulus of Fiber Material by Cantilever Vibration Method

○(D)Saikat Mondal<sup>1</sup>, Partha Roy Chaudhuri<sup>1</sup> (1.IIT Kharagpur)

[19a-P08-4]

Large-Area Moiré Metamaterials with Adjustable Chiroptical Properties Using TiO<sub>2</sub> Nanoantenna Stickers

○Jiayang He<sup>1</sup>, Shunsuke Murai<sup>1</sup>, Tienyang Lo<sup>1</sup>, Katsuhisa Tanaka<sup>1</sup> (1.Kyoto Univ.)

[19a-P08-5]

Spectroscopic Investigation of Physico-Chemical Characteristics of Rice Varieties

○(M1C)MANIKANTH KARNATI<sup>1</sup>, Adline Rebello<sup>1</sup>, Nandana B<sup>1</sup>, Indira Govindaraju<sup>1</sup>, Bharath Prasad AS<sup>2</sup>, Nirmal Mazumder<sup>1</sup> (1.Department of Biophysics, Manipal School of Life Sciences, Manipal Academy of Higher 6 Education, Manipal, Karnataka, India -576104 7, 2.Department of Public Health Genomics, Manipal School of Life Sciences, Manipal 8 Academy of Higher Education, Manipal, Karnataka, India -576104)

[19a-P08-6]

Revisable Tuning of Tamm Plasmon Polaritons

○(D)MingJyun Ye<sup>1,3</sup>, Satoshi Ishii<sup>3</sup>, Kuo-Ping Chen<sup>2</sup> (1.College of Photonics, National Yang Ming Chiao Tung Univ., Taiwan, 2.Institute of Photonics Technologies, National Tsing Hua Univ. , Taiwan, 3.Research Center for Materials Nanoarchitectonics (MANA), NIMS, Japan)

[19a-P08-7]

Development of Four Channel based Stokes-Mueller Polarimetry Integrated with Machine Learning for Characterization and Classification of Ductal Carcinoma Tissue

Spandana K U<sup>1</sup>, Sindhoora Kaniyala Melanthota<sup>1</sup>, Raghavendra U<sup>1</sup>, Sharada Rai<sup>1</sup>, K K Mahato<sup>1</sup>, ○Nirmal Mazumder<sup>1</sup> (1.Manipal Academy of Higher Education)

[19a-P08-8]

Unidirectional plasmons propagation

○Subaru Yoshida<sup>1</sup>, Tongyao Li<sup>1</sup>, Takayuki Umakoshi<sup>1,2</sup>, Prabhat Verma<sup>1</sup> (1.Dept. of Applied Physics, Osaka Univ, 2.Inst. Adv. Co-Creation Studies, Osaka Univ)

[19a-P08-9]

## Enhancing SERS Sensor Reliability with Intensity-Based Self-Referencing Using 4-Amino Thiophenol

○(D)Arti Yadav<sup>1</sup>, Sachin Kumar Srivastava<sup>1,2</sup> (1.Dept. of Physics, IIT Roorkee, 2.CPQCT, IIT Roorkee)

---



## **Laser-induced Photothermal- and Magneto-Responsive Polymer Composites for Soft-Bodied Devices**

**UNIST<sup>1</sup>, Seoul National Univ.<sup>2</sup>, Kyungpook National Univ. <sup>○</sup>Hoon Eui Jeong<sup>1</sup>, Hosup Jung<sup>2</sup>, Moon Kyu Kwak<sup>3</sup>**

**E-mail: hoonejeong@unist.ac.kr**

Despite recent advancements, artificial composite muscles have not yet been able to strike the right balance between exceptional mechanical properties and dexterous actuation abilities that are found in biological systems. Here, we present an artificial composite muscle that exhibits multiple remarkable mechanical properties and demonstrates comprehensive actuating performance, surpassing those of biological muscles. This composite integrates a phase-change polymer and ferromagnetic particles, enabling active control over mechanical properties and complex actuating motions through remote photothermal laser heating and magnetic field manipulation. Consequently, the dual-responsive composite muscle can dynamically adjust its stiffness as needed, achieving a switching ratio exceeding  $2.7 \times 10^3$ . This remarkable adaptability facilitates substantial load-bearing capacity. Moreover, it demonstrates reversible extension, contraction, bending, and twisting. We leverage these distinctive attributes to showcase the versatility of this composite muscle as a soft-bodied devices. (This work was supported by the National Research Foundation (NRF) of Korea grant 2021R1A2C3006297).

# Silicon Waveguide Output Coupler Based on Nanohole Array

Ya-Cin Chung<sup>1,2</sup>, Min-Hsiung Shih<sup>2</sup>, Shu-Wei Chang<sup>2</sup>, and Wan-Shao Tsai<sup>1,3</sup>

<sup>1</sup> Graduate Institute of Optoelectronic Engineering, National Chung Hsing University, Taiwan, <sup>2</sup> Research Center of Applied Sciences, Academia Sinica, Taiwan, <sup>3</sup> Department of Electrical Engineering, National Chung Hsing University, Taiwan

E-mail: [wstsai@nchu.edu.tw](mailto:wstsai@nchu.edu.tw)

## 1. Introduction

Silicon waveguide output couplers based on nanohole array structures is presented around 1550 nm [1]. Compared with conventional grating couplers on silicon-on-insulator (SOI) platforms, the presented coupler shows less fabrication complexity since only one-step etching is required in both waveguide and coupler regions.

Our devices are designed using the finite-difference time-domain simulations and fabricated with electron-beam lithography (EBL) followed by dry-etching through ridged structures. A self-built measurement system is utilized to characterize the devices.

The proposed device provides an alternative method for vertical light coupling on the SOI platform [2].

## 2. Methods

### Design and Simulation

The devices are fabricated on SOI substrates with a 3  $\mu\text{m}$  buffer oxide and a 220 nm Si layer. The structure includes the grating, taper mode-size converter, 400 nm wide single-mode waveguide, and nanohole array.

Figure 1(a) and (b) show the top and side views of simulated field magnitude near the nanohole array, respectively. A far-field radiation angle of  $15.36^\circ$  is estimated from the Fourier transformed field as, as shown in Fig. 1(c). Based on simulations, the coupling efficiency of the nanohole coupler is 46.6% at periods  $P_x = P_y = 690$  nm and hole diameter  $D = 350$  nm. For comparison, a conventional grating coupler is also designed, and the optimized coupling efficiency for the etch-through structure is 12.7% at period  $p = 820$  nm and gap  $g = 295$  nm. The coupling efficiency of the taper is 90% at a length of 70  $\mu\text{m}$ .

### Fabrication

The structures of grating, taper, waveguide, and nanohole array are defined with EBL. A 30 nm thick Cr film is thermally deposited as the hard-mask for dry-etching. The inductively coupled plasma reactive ion etching process under 70 secs of  $\text{CHF}_3$  gas results in full etching of the 220 nm top Si layer. The Cr layer is then removed by wet-etching. A subsequent 250 nm  $\text{SiO}_2$  cladding layer is deposited by plasma-enhanced chemical-vapor deposition. Figure 2(a), 2(b), and 2(c) show the scanning electron microscope (SEM) images of the grating, taper, and nanohole array before oxide deposition, respectively.

### Characterization

Figure 3(a) shows the schematic of our measurement system. A tunable laser at C-band acts as the light source, and an InGaAs power detector is used for detection. From simulations, the coupling angles of grating and nanohole array are 10 and  $15^\circ$ , respectively. The device under an optical microscope (OM), which is aligned with a red laser, is shown in Fig. 3(b). Single-mode fibers are used in both the input and output. The detected output power at 1550 nm is about 100 nW at an input power of 5 mW. The overall cou-

pling efficiencies of fabricated devices are shown in Fig. 3(c) and compared with the designed one. It is around  $-46$  dB at 1550 nm, which is much lower than the designed value of  $-13.19$  dB. However, a similar wavelength dependent trend can be seen.

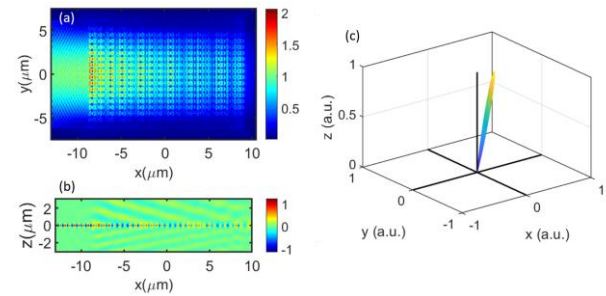


Fig. 1 (a) top and (b) side views of simulated field. (c) Far-field pattern.

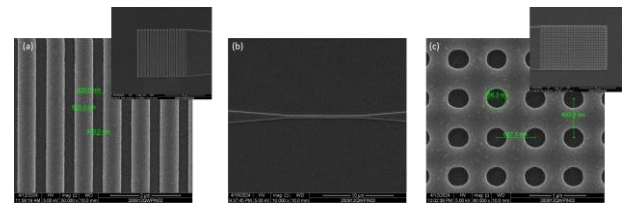


Fig. 2. SEM images of fabricated devices: (a) Grating coupler, scale bar: 2  $\mu\text{m}$  and inset 10  $\mu\text{m}$ , (b) taper, scale bar: 10  $\mu\text{m}$ , and (c) nanohole array, scale bar: 1  $\mu\text{m}$  and inset 10  $\mu\text{m}$ .

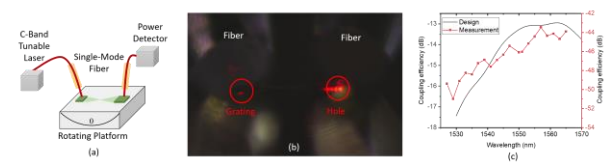


Fig. 3. (a) Measurement setup. (b) Measured device under OM view with alignment of red laser. (c) Coupling efficiency of the fabricated device.

## 3. Conclusions

We have designed, fabricated, and characterized output couplers based on nanohole arrays. The experimental overall coupling efficiency is  $-46$  dB and should be improved by optimizing the fabrication process and the characterization setup.

## Acknowledgements

This work was supported by the National Science and Technology Council (Taiwan) under Grant 113-2222-E-005-002.

## References

- [1] Xia Chen and Hon Ki Tsang, IEEE Photonics J. **1** (2009) 184.
- [2] Akio Mizutani, Yohei Eto, and Hisao Kikuta, Appl. Phys. Express **10** (2017) 122501.

# Determining Elastic Modulus of Fiber Material by Cantilever Vibration Method

Saikat Mondal<sup>1</sup>, Partha Roy Chaudhuri<sup>1\*</sup>

<sup>1</sup> Department of Physics, Indian Institute of Technology Kharagpur - 721302, India

\*E-mail : [roycp@phy.iitkgp.ac.in](mailto:roycp@phy.iitkgp.ac.in)

## 1. Introduction

This research demonstrates the determination of the elastic modulus of the material of optical fiber by experimentally calculating natural vibration frequency utilizing Euler-Bernoulli cantilever beam vibration theory[1]. An optical fiber cantilever of length  $L$ , material density  $\rho$  have natural oscillation frequency for fundamental mode [2]

$$f = \frac{1.875^2}{2\pi L^2} \sqrt{\frac{EI}{\rho A}} \quad (1)$$

where  $E$  is the elastic modulus of the fiber,  $\rho$  ( $\sim 2200 \text{ kg/m}^3$ ) is the density of the fiber material,  $A$  is the cross-section area of the fiber,  $I$  is the second moment of the cross-section, here it is  $\pi r^4/4$ ,  $r$  ( $\sim 62.5 \text{ }\mu\text{m}$ ) is the radius of the fiber. So, by experimentally calculating  $f$  we can evaluate the  $E$ . The adjustment on  $f$  due to damping in air is not considered, as it is negligible (usually 0.05%) [3].

## 2. Experimental Details and Results

We take bare optical fiber (Nufern 780-HP) clamped at one end with the other end free, as our cantilever. We have coated a selected length of the fiber tip with electro-strictive nanocomposite  $\text{BiFe}_{0.8}\text{Co}_{0.2}\text{O}_3$ , and placed between two parallel metal plate connected with a DC voltage supply. The light emitted from the free end passes via a converging lens with a large focal length, and the resulting spot is observed on a screen. The information about fiber tip vibration is obtained by capturing video of the light spot position on the

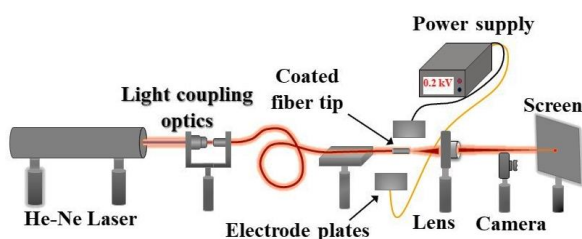


Fig. 1. The schematic of experimental setup.

screen using a digital camera. The schematic of experimental setup is shown in Fig. 1. By using MATLAB programming, we extract the displacement-time data of the fiber tip from the recorded video and this data is further utilized through fast Fourier transform (FFT) analysis to evaluate the natural frequency  $f$ .

Using this coated optical fiber cantilever system, we examined the natural frequency of the system by varying cantilever length  $L$ . One typical FFT analysis figure is shown in Fig. 2 for  $L = 9.0 \text{ cm}$  and we find that the  $f$  of the system is 12.26 Hz. The results are tabulated in Table I, for every

experiment we use applied electric field 0.25 kV/cm.

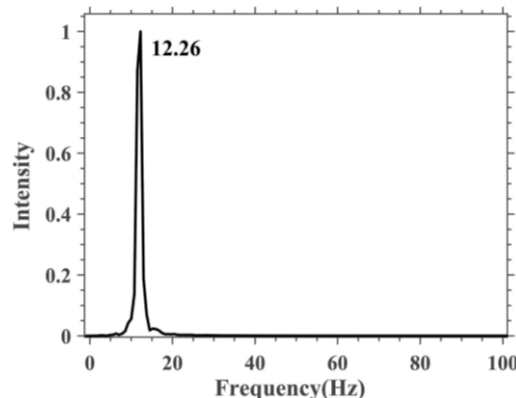


Fig. 2. The FFT analysis of the cantilever vibration data for cantilever length 9.0 cm ( $f = 12.26 \text{ Hz}$ ).

Table I Estimated Elastic Modulus

Cantilever length (cm)	$f$ (from experiment) (Hz)	Elastic modulus (GPa)
9.0	12.26	70.96
9.5	10.98	70.66

## 3. Conclusions

We have successfully established the method of determining the elastic modulus of an optical fiber using vibrating fiber cantilever beam by computing its natural frequency of vibration. The obtained results matches very well with previously reported findings [4]. This method is new and offers several potential benefits as it is simple, dynamic and repeatable yielding good accuracy. Being all-fiber system, the design can be implemented in any environment for studying cantilever vibration devices and related instrumentation.

## References

- [1] M. A. Mahmoud, "Validity and Accuracy of Resonance Shift Prediction Formulas for Microcantilevers: A Review and Comparative Study," *Critical Reviews in Solid State and Materials Sciences*, vol. 41, no. 5, pp. 386-429, 2016/09/02 2016.
- [2] R. M. Digilov, "Flexural vibration test of a cantilever beam with a force sensor: fast determination of Young's modulus," *European Journal of Physics*, vol. 29, no. 3, p. 589, 2008/04/25 2008.
- [3] G. Chen, M. M. Alam, and Y. Zhou, "Dependence of added mass on cylinder cross-sectional geometry and orientation," *Journal of Fluids and Structures*, vol. 99, p. 103142, 2020/11/01/ 2020.
- [4] P. Li *et al.*, "A Nondestructive Measurement Method of Optical Fiber Young's Modulus Based on OFDR," *Sensors*, vol. 22, no. 4, p. 1450, 2022.

# Large-Area Moiré Metamaterials with Adjustable Chiroptical Properties Using TiO<sub>2</sub> Nanoantenna Stickers

Jiayang He<sup>1</sup>, Shunsuke Murai<sup>1</sup>, Tienyang Lo<sup>1</sup>, Katsuhisa Tanaka<sup>1</sup>

<sup>1</sup> Kyoto University, Japan

E-mail: [murai@dipole7.kuic.kyoto-u.ac.jp](mailto:murai@dipole7.kuic.kyoto-u.ac.jp)

## 1. Introduction

Chiral metamaterials, known for their chiroptical effects, exhibit asymmetric responses to left- and right-circularly polarized light, resulting in higher circular dichroism (CD) compared to natural materials<sup>1,2</sup>. Currently, some chiral metamaterials, exemplified by helices<sup>3</sup>, offers inherent handedness, but their 3D nanostructure fabrication can be complex<sup>2</sup>.

In this study, we present a novel chiral metamaterial composed of two identical achiral TiO<sub>2</sub> nanoparticles array. The top layer consists of TiO<sub>2</sub> nanoantenna sticker, while the bottom layer features an array of TiO<sub>2</sub> nanoparticles on a quartz substrate. Its chiroptical response is tunable by varying the in-plane rotation angle or twist angle between the two layers, yielding CD spectra varied with the twist angle. Additionally, we investigated the dependence of the CD spectra on the interlayer spacing by applying PMMA thin films of different concentrations to the surface of the lower substrate.

## 3. Results and Discussion

The TiO<sub>2</sub> nanoparticles array was embedded into a transparent, flexible PDMS substrate to create stickers that were reusable and handled with ease (Fig. 1a). We then adhered this TiO<sub>2</sub> sticker to the TiO<sub>2</sub> nanoparticles array with a twist angle, spaced by a PMMA interlayer about 35 nm thick. The circular dichroism (CD) spectra, defined as  $\Delta CD = (T_R - T_L) / (T_R + T_L)$ , were measured and plotted (Fig. 1b). The flip of the sign of the CD signal is notable between the twist angles in opposite directions at normal incidence. Furthermore, by keeping the twist angle constant and increasing the interlayer thickness, the CD spectra exhibited a gradual weakening of the signal (Fig. 1c).

## 3. Conclusions

The TiO<sub>2</sub> nanoantenna stickers embedded in PDMS were successfully fabricated through a series of treatments such as heat treatment and transfer technology and can be utilized as chiral metamaterial. The CD results for the stacked identical nanoparticles array exhibit dependence on incident angles, revealing symmetry in CD response intensity for equal clockwise (CW) and anticlockwise (ACW) rotations. As the interlayer distance increases, there is an observed decrease in the CD value.

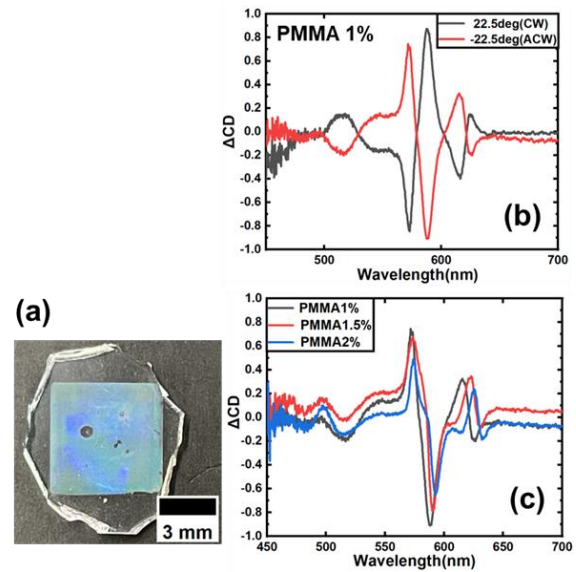


Fig. 1. (a) Photograph of TiO<sub>2</sub> nanoantenna sticker. (b) CD spectra of the twisted metamaterial with twist angles of  $\pm 22.5^\circ$  at normal incidence, along with the interlayer thickness of about 35nm and (c) the dependence of the CD signal on the interlayer spacing for a twist angle of  $-22.5^\circ$ .

## Acknowledgements

We would like to thanks the financial support from Kakenhi (22K18884) and the Futaba foundation.

## References

- [1] Wu, Zilong, and Yuebing Zheng. Adv. Opt. Mater 5, (2017)1700034.
- [2] Hentschel, M et al. Sci. Adv 3, (2017) e1602735.
- [3] Justyna K. Gansel et al. Appl. Phys. Lett 100, (2012)101109.

## Appendix

Kyoto university, Tanaka Katsuhisa Lab

E-mail: [murai@dipole7.kuic.kyoto-u.ac.jp](mailto:murai@dipole7.kuic.kyoto-u.ac.jp)

# Spectroscopic Investigation of Physico-Chemical Characteristics of Rice Varieties

Manikanth Karnati<sup>1</sup>, Adline S. Rebello<sup>1</sup>, Nandana B<sup>1</sup>, Indira Govindaraju<sup>1</sup>, Bharath Prasad AS<sup>2</sup>, Nirmal Mazumder<sup>1\*</sup>

<sup>1</sup>Department of Biophysics, Manipal School of Life Sciences, Manipal Academy of Higher 6 Education, Manipal, Karnataka, India -576104 7  
<sup>2</sup>Department of Public Health Genomics, Manipal School of Life Sciences, Manipal 8 Academy of Higher Education, Manipal, Karnataka, India -576104  
\*Corresponding author: nirmal.mazumder@manipal.edu

**Introduction:** Rice (*Oryza sativa* L.), a versatile grain, is a dietary staple enjoyed worldwide, cherished for its culinary adaptability and nutritional richness. Its widespread consumption underscores its integral role in diverse cuisines and as a vital source of sustenance for countless cultures. As a significant source of carbohydrates, rice production has been rising, reaching 510.6 million tonnes in 2017 (FAO, 2018) Starch, a prevalent carbohydrate in rice, comprises two primary constituents: amylose and 85 amylopectin. Long linear chains with limited branching characterize amylose, whereas amylopectin consists of shorter chains with numerous branches, resulting in a complex three-dimensional structure. This structural complexity confers a semi-crystalline nature upon starch granules, attributed to the formation of double-helices by short amylopectin chains

**Materials and methods:** Amylose and resistant starch levels were examined in various rice cultivars. Morphological structures were examined under an optical microscope (Olympus BX51), and chemical groups were identified using FTIR spectroscopy (Bruker Alpha). Thermal characteristics were measured using differential scanning calorimetry (Shimadzu DSC60). The glycemic index was determined in vivo with Sprague Dawley rats by measuring blood glucose levels after ingestion and computing the Incremental Area Under the Curve (IAUC) using the trapezoidal rule. The rice variety with the most resistant starch was chosen for in vivo research to monitor changes in the gut flora.

**Results:** DSC (Shimadzu’s DSC60, Japan) was employed to analyze the gelatinization parameters of the different rice flours. 4-5mg of rice flour was coated on an aluminum pan and was crimped with a sample-encapsulating press (Shimadzu’s DSC, Japan). It was then heated to temperatures ranging from 30-110 °C in 10 °C increments. The resulting curves were examined for the peak, onset, and endset temperature using TA-60WS software (Shimadzu, Japan).

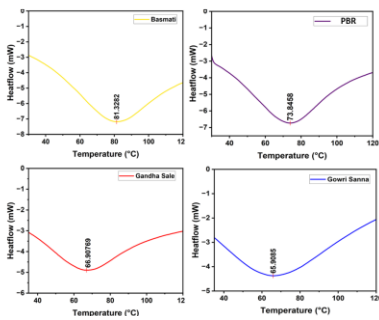


Fig.1. DSC thermograms of different rice flour, illustrating peak gelatinization temperature.

Rice varieties	Onset temperature To(°C)	Peak Gelatinization temperature Tp(°C)	Gelatinization Enthalpy (ΔH)/(J/g)
Basmati	26.43	81.32	-157.61
PBR	31.24	73.84	-150.39
Gandha Sale	31.57	66.90	-81.46
Gowri Sanna	21.32	65.90	-131.01

Table.1. Gelatinization temperatures of rice flour

**Conclusion:** The rice flour samples had structural uniformity and polygonal forms, and FTIR analysis revealed amylose and amylopectin functional groups. Parboiled brown rice, which has the greatest resistant starch levels, was chosen for further in vivo gut microbiota investigation in SD rats. The study's findings may influence dietary choices and agricultural practices by emphasizing the nutritional and gut health benefits of Karnataka rice varieties. This information could help evolve these rice variants into functional foods with broader health benefits.

**Acknowledgment:** We thank Manipal School of Life Sciences, Manipal, Karnataka, India for providing infrastructure and facilities.

**References:**[1] Govindaraju, I., Zhuo, G.-Y., Chakraborty, I., Melanthota, S. K., Mal, S. S., Sarmah, B., Baruah, V. J., Mahato, K. K., & Mazumder, N. (2022). Investigation of structural and physico-chemical properties of rice starch with varied amylose content: A combined microscopy, spectroscopy, and thermal study. *Food Hydrocolloids*, 122, 1-12.  
[2] Han, F., Wang, Y., Han, Y., Zhao, J., Han, F., Song, G., Jiang, P., & Miao, H. (2018). Effects of Whole-Grain Rice and Wheat on Composition of Gut Microbiota and Short-Chain Fatty Acids in Rats. *Journal of Agricultural and Food Chemistry*, 66(25), 6326–6335.



# Revisable Tuning of Tamm Plasmon Polaritons

Ming-Jyun Ye<sup>1,3</sup>, Satoshi Ishii<sup>3</sup> and Kuo-Ping Chen<sup>2\*</sup>

<sup>1</sup> College of Photonics, National Yang Ming Chiao Tung University, Tainan, Taiwan

<sup>2</sup> Institute of Photonics Technologies, National Tsing Hua University, Hsinchu, Taiwan

<sup>3</sup> Research Center for Materials Nanoarchitectonics (MANA), National Institute for Materials Science (NIMS), 1-1 Namiki, Japan

\*kpchen@ee.nthu.edu.tw

**Abstract:** Phase-change materials (PCMs) provide a specific combination of properties. The binary semiconducting chalcogenide  $\text{Sb}_2\text{S}_3$  is consider one of the promising candidates, especially its intrinsic high refractive index, low loss and wide bandgap properties, in near infrared (NIR). Here, the  $\text{Sb}_2\text{S}_3$  transformation from amorphous to crystal state embedded between the distribute Bragg reflector (DBR) and metal layer. At the interface between DBR and metal layer in specific parameter, Phase-change Tamm plasmon-polariton (PC-TPP) resonance could be produce. The PC-TPP resonance has a 70 nm modulation wavelength. Also, the resonance achieves around 100 nm-shifted in NIR at the proper incident angle.

**Key Words--**  $\text{Sb}_2\text{S}_3$ , distribute Bragg reflector (DBR), Phase-change materials (PCMs), Tamm Plasmon Polaritons metasurface (TPP), High Refractive Index (HRI)

## 1. Introduction

Phase-change materials (PCMs) has been widely applied in switchable electronic and photonics [1-5]. The crystal phase of vanadium dioxide ( $\text{VO}_2$ ) was changed from monoclinic state near 340 K. Also, the working system of germanium-antimony-tellurium (GST) was above 380 K at communication wavelength. However, these two PCMs have a high extinction coefficient around 0.5 and 2.0 in visible, respectively [6]. Here, the binary semiconducting chalcogenide  $\text{Sb}_2\text{S}_3$  has bandgap 1.8 to 2.1 eV to move the absorption band-edge in visible. Meanwhile, the high refractive index of  $\text{Sb}_2\text{S}_3$  could be tuned from 3 to 4 at around 650 nm. And, its extinction coefficient was below 0.5 after 600 nm in both states.

One of the plasmon resonance was theoretically demonstrated at the surface photonic crystal and metals, called Tamm state. Between distributed Bragg reflector and metal layer, it has the strong confinement at the interface, known as Tamm plasmon polariton (TPP) [7, 8].

In this research,  $\text{Sb}_2\text{S}_3$  was used as function layer in the TPP structure. After annealing process, the modulable wavelength was demonstrate around 70 nm. The analysis of angle-dependence resonance also was proved close to 100 nm in proper incidence light. In the future, the optical signal would be encoded to electrical signal, called photocurrent. It was shown that our design would be added in LiDAR [9], sensor [10].

## 2. Results and discussion

The finite-difference time-domain (FDTD) method has been used to calculate the Phase change Tamm plasmon-polariton (PC-TPP) resonance with normal light incidence in NIR. In this modeling setup, the DBR unit cell consist of two layers 145 nm silica and 95 nm  $\text{TiO}_2$  with several pairs, as shown in Figure 1 (a). With the specific  $\text{Sb}_2\text{S}_3$  and gold thickness, the PC-TPP resonance could be achieved 70 nm modulation after  $\text{Sb}_2\text{S}_3$  annealing from amorphous to crystal state, as shown in Figure 1 (b). The optical constants of  $\text{Sb}_2\text{S}_3$  were taken in the visible spectra range from, as shown in Figure 1 (c). It was shown phase change material  $\text{Sb}_2\text{S}_3$  has the HRI and low extinction coefficient property, compared to commercial material, silicon, in NIR.

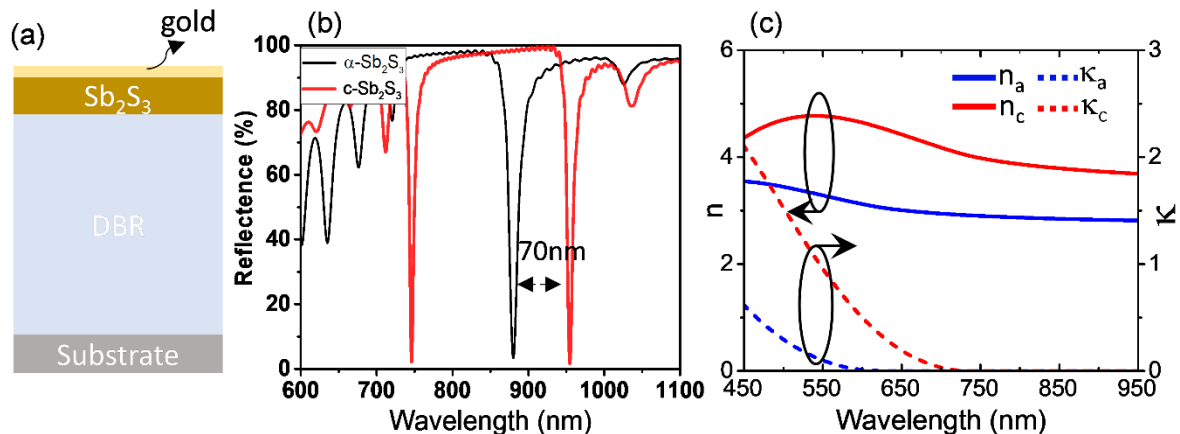


**Figure 1** (a) The structure of  $\text{Sb}_2\text{S}_3$  TPP device. (b) The TPP resonance shifted from 870 nm to 960 after transformation state. (c) The real optical constant of the  $\alpha$ - and  $c$ -  $\text{Sb}_2\text{S}_3$  after annealing.

# Development of Four Channel based Stokes-Mueller Polarimetry Integrated with Machine Learning for Characterization and Classification of Ductal Carcinoma Tissue

Spandana K U<sup>1</sup>, Sindhoora Kaniyala Melanthota<sup>1</sup>, Raghavendra U<sup>2</sup>, Sharada Rai<sup>3</sup>, K K Mahato<sup>1</sup>, Nirmal Mazumder<sup>1,\*</sup>

<sup>1</sup>Department of Biophysics, Manipal School of Life Sciences, Manipal Academy of Higher Education, Manipal, India

<sup>2</sup>Department of Instrumentation and Control Engineering, Manipal Institute of Technology, Manipal Academy of Higher Education, Manipal, Karnataka, India

<sup>3</sup>Department of Pathology, Kasturba Medical College, Manipal Academy of Higher Education, Mangalore, Karnataka, India

\* E-mail: nirmal.mazumder@manipal.edu

## 1. Introduction

This study presents a Stokes-Mueller polarimetry based imaging system for tissue characterization, specifically for distinguishing normal from cancer regions in ductal carcinoma samples. The fibrous structures present in the tissue enhances the contrast through the measurement of polarization signal, making it easier to analyze images in detail and higher classification accuracy [1].

## 2. Materials and methods

Four channel based Stokes Mueller polarization imaging system has been built in linear optics and used for tissue characterization. It consists of LES as light source, a polarization state generator (PSG), polarization state analyzer (PSA) and detection system. The details can be found in ref. [1]. Figure 1 shows the schematic of four channel based Stokes Mueller polarization system.

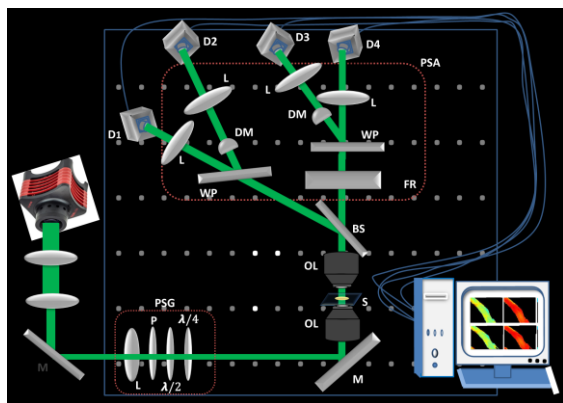


**Figure 1:** Schematic diagram of the Four channel Stokes Mueller Polarisation system. L – Lens; M – Mirror; P – Polarizer;  $\lambda/4$  – Quarter Wave Plate;  $\lambda/2$  – Half Wave Plate; B – Beam Splitter; OL – Objective Lens; S – Sample; FR – Fresnel's Rhomb; WP – Wollaston Prism; D1, D2, D3, D4 - Detectors

## 3. Results

The Stokes images represent the dependence of polarization signal on the tissue architecture mainly due to the collagen fibre orientation. For  $0^\circ$  polarization, the  $S_2/S_0$  images for the normal region exhibit greater values than that of tumour regions. From Figure 2, it is evident that the  $S_3/S_0$  parameter for both normal and tumour breast tissue is nearly equivalent to zero when the sample is incident with  $0^\circ$  linearly polarized light. In addition, the reduced  $S_3/S_0$  value for the tumour region compared to normal regions indicates the lower birefringence property of the sample. Additionally, the 2D images of four polarization parameters,

namely DOP, DOLP, DOCP, and anisotropy ( $r$ ) are reconstructed from Stokes parameters.

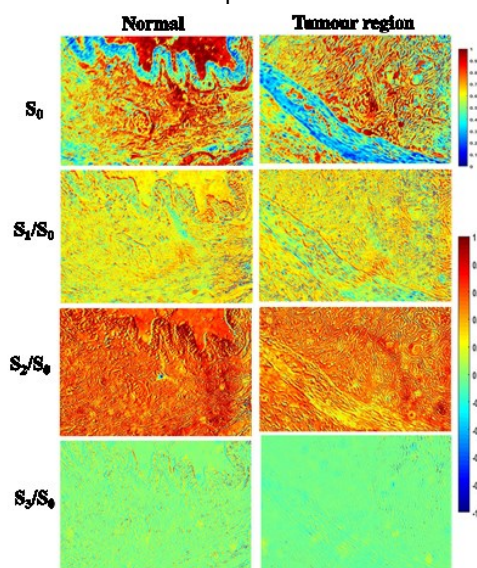


**Figure 2.** Reconstructed Stokes vector 2D images from normal regions (left), and (b) tumour regions of DC samples (right) with the input polarization of  $0^\circ$ . The color bar has a value ranging from 0 to 1 for  $S_0$  and -1 to 1 for the remaining parameters. Reproduced from ref [1].

## 3. Conclusions

A dataset is created using various polarization parameters, and validation accuracy of 95.78% and testing accuracy of 94.81% is achieved using machine learning (ML) based support vector machine image classification model. In this study, the average depolarization value of 0.644 in normal regions of tissue, while a slightly higher value of 0.826 is observed. The tumor regions showed a reduction in retardance value from 2.373 to 0.748 as compare to normal. The results demonstrate the potential of ML integrated to Stokes-Mueller polarimetry in investigating detail micro-structural characterization of tissue.

## Acknowledgements

We would like to express sincere thanks to Department of Science and Technology (DST) -Science and Engineering Science and Engineering Research Board (SERB), Government of India, India (Project Number—ECR/2016/00194), for financial support.

## References

[1] Spandana KU, Lasers in Med. Sci.. **39** (2024) 123.

## Unidirectional plasmons propagation

Subaru Yoshida<sup>1</sup>, Tongyao Li<sup>1</sup>, Takayuki Umakoshi<sup>1,2</sup>, Prabhat Verma<sup>1</sup>

<sup>1</sup>Dept. of Applied Physics, Osaka Univ.,

<sup>2</sup>Inst. Adv. Co-Creation Studies, Osaka Univ.,

E-mail: yoshida@ap.eng.osaka-u.ac.jp

### 1. Introduction

To excite surface plasmons efficiently, the surface plasmons must receive energy from incident light, in which conservation of momentum must be satisfied between light propagating in free space and the surface plasmons. However, the momentum of light propagating through air never matches the momentum of surface plasmons. One solution is to use a grating as a plasmon coupler. This allows the momentum of the incident light to match the momentum of the surface plasmons for efficient surface plasmon excitation. However, in this method, the direction of propagation of surface plasmons cannot be controlled due to the diffraction.

In this study, metasurface was used to solve this issue. Metasurface is a collection of nanoscale structures called meta-atoms. Like a grating, metasurface can also excite surface plasmons efficiently by matching the momentum of the incident light. Additionally, metasurface can change the phase of the plasmon waves, which means that the shape of the wavefront changes, and as a result it changes the direction of propagation of plasmons. By selecting a suitable polarization of the incident light with the design of the metasurface, the direction of plasmon propagation can be changed efficiently. In previous research [1], rectangular meta-atoms inclined at 45° and circularly polarized light were used. In experimental results, it was confirmed that by changing the incident light from right circular to left circular polarization, the surface plasmons propagated in opposite directions.

### 2. Experimental results

In this research, we also used circularly polarized light as incident light to change the direction of propagation of surface plasmons and to confirm that plasmons propagate unidirectionally by changing the state of polarization from right to left. First, we prepared clean glass substrates using piranha solution. Then, a 45nm-thick silver layer was evaporated using an evaporation machine. The evaporation speed was around 1.5nm/s to keep the roughness of silver layer below 2nm because propagation losses can be sufficiently reduced with a surface roughness of 2 nm or less [2]. After that, we fabricated a diamond structure and a metasurface at the center of the diamond structure by using a focused ion beam. Lastly, we irradiated circularly polarized light on the metasurface to confirm that this metasurface made plasmons propagate unidirectionally. The size of the whole diamond structure was 12μm. An image of the

diamond structure and metasurface was taken by scanning ion microscope (SIM), which is shown in Fig.1(a). From this image, we confirmed that diamond structure and metasurface were fabricated properly. In experiments, the incident light had a wavelength of 642 nm and circular polarization. When left circularly polarized light was irradiated on the metasurface, we confirmed that near-field light was generated at the upper apex of this diamond structure, as shown in Fig.1(b). This means that plasmons were excited on the metasurface and then plasmons propagated only to upper direction. On the other hand, near-field light was generated at the lower apex when the incident light was right circularly polarization as shown in Fig.1(c).

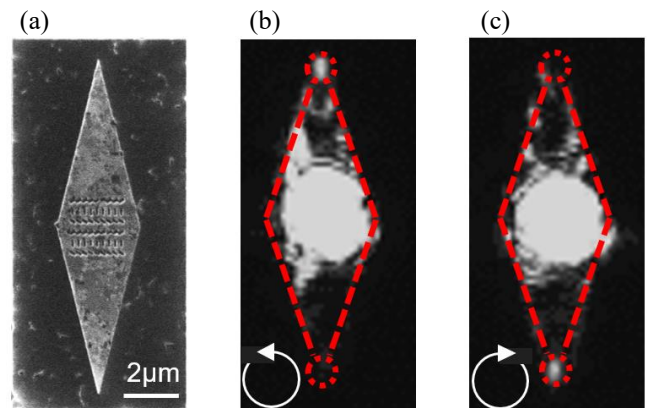


Figure1:(a) SIM image of a diamond structure and metasurface. (b) and (c) Optical images of silver coated glass diamond structure and metasurface under circularly polarized light.

### 3. Conclusion

We succeeded in confirming through optical images that metasurface design fabricated in this study makes plasmons propagate unidirectionally. Since a variety of metasurface designs can be used, it may be possible to achieve unidirectional plasmon propagation in different ways. It is believed that by making plasmons propagate unidirectionally, higher energy near-field light is produced. Therefore, as an application, this can be efficiently used for nanoimaging and nanospectroscopy.

### References

- [1] Lin, J. et al., Science **340**, 331–334 (2013)
- [2] T. Umakoshi. et al., Nanoscale **8**, 5634-5640(2016)



# Enhancing SERS Sensor Reliability with Intensity-Based Self-Referencing Using 4-Amino Thiophenol

Arti Yadav<sup>1</sup>, Sachin Kumar Srivastava<sup>1,2</sup>

<sup>1</sup> Department of Physics, Indian Institute of Technology Roorkee, Roorkee – 247667, INDIA

<sup>2</sup> Centre for Photonics and Quantum Communication Technology, Indian Institute of Technology Roorkee, Roorkee – 247667, INDIA

E-mail: [sachin.srivastava@ph.iitr.ac.in](mailto:sachin.srivastava@ph.iitr.ac.in)

## 1. Introduction

The performance parameters such as limit of detection, and dynamic range of a surface enhanced Raman spectroscopy (SERS)-based sensor are limited by laser power, integration time of the detector of the spectrometer (IntT), and ambient conditions [1]. The intensity-based self-referencing mechanism offers an innovative solution, providing independence of sensor performance on these factors. Integration of 4-Amino thiophenol (4-ATP) as a self-referenced layer with SERS sensor offers the advantage of independence of Raman signal on the laser power, integration time, or ambient conditions.

The SERS sensor chip consists of an Ag nano-sculptured thin film (Ag-nSTF) fabricated using glancing angle deposition method (GLAD). The Ag-nSTF sensor chips offer uniformity, reproducibility, reproducibility, stability, and large-area SERS substrates [2].

## 2. Result and discussions

We improve the reliability of the SERS sensor by integrating a self-referenced layer of 4-ATP in the sensor fabrication. The SERS sensor is composed of an Ag-nSTF over a monolayer of 4-ATP self-assembled onto Ag nanoparticles (AgNP) positioned over a Si substrate. Figure 1(a) displays a FESEM image of the top view of the sensor Ag-nSTF/4-ATP/AgNP/Si. Ag-nSTF consists of an array of nanorods (AgNR) of length  $339 \pm 30$  nm. The inset of the same figure presents the schematic of the cross-sectional profile. It can be seen that the 4ATP layer is sandwiched between the AgNP and Ag-nSTF, while the analyte molecule is placed on top of the Ag-nSTF. The SERS signal from the sandwiched 4ATP molecules serves as self-reference signal. Figure 1(b) shows the SERS spectra of 1 mM cysteamine dihydrochloride (Cys) over the sensor chip for various IntT values. With the increase in IntT, the intensity of the Raman bands increases. However, the relative SERS intensity of Raman bands of Cys (at  $501 \text{ cm}^{-1}$ ) and 4-ATP (at  $1078 \text{ cm}^{-1}$  taken as reference) is almost constant with the standard deviation of 0.009 as shown in Figure 1(c). This independence ensures consistent performance of the sensor under varying IntT. Intensity-based self-referencing mechanism proposes to resolve a

long-lasting issue of SERS-based quantitative detection with high reliability [3]. The sensor response is also independent of different spots across the sensor chip as presented in Figure 1(d). This confirms the uniformity of the sensor, hence the improved reliability.

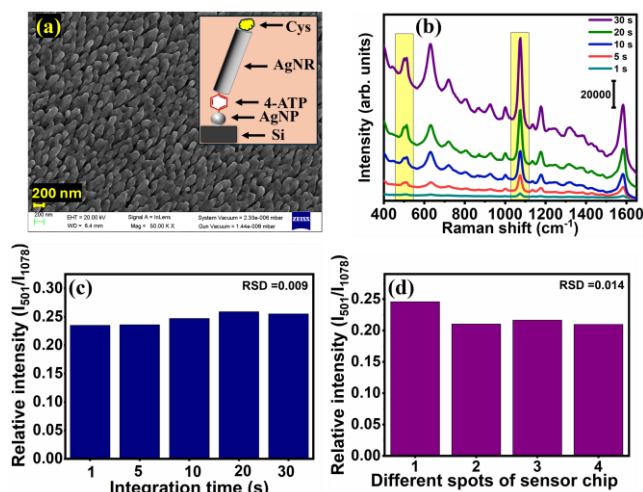


Figure. 1. (a) FESEM image of the SERS sensor chip, (b). SERS spectra of Cys over sensor chip for different integration times of the detector of the spectrometer (c). Variation of relative SERS intensity  $I_{501}/I_{1078}$  for integration time variations (d). Variation of relative SERS intensity for variations of the different spot of the sensor.

## 3. Conclusions

The intensity-based self-referenced mechanism significantly improves the SERS sensor's reliability by the independence of the sensor performance over the integration time variations.

## Acknowledgements

Financial support from MoE-STARS, DST-BDTD, DST-Indo Korea JNC grants are acknowledged. Arti thanks CSIR-India for senior research fellowship.

## References

- [1] Lingxiao et al., Appl. Surf. Sci. **603** (2022), 154419.
- [2] Kun Yao et al., Appl. Phys. Lett., **104** (2014), 073110.
- [3] Arti Yadav et al., Sens. Actuators B. **396** (2023) 134569.

4 JSAP-Optica Joint Symposia 2024 | 一般セッション(口頭講演) : 4.1 Plasmonics and Nanophotonics

## [16a-B4-1~9] 4.1 Plasmonics and Nanophotonics

[16a-B4-1]

[JSAP-Optica Joint Symposia Invited Talk] Electromagnetic Asymmetry, Quantum Conductivity and Optical Magnetism for Nonlinear Plasmonics

○Dangyuan Lei<sup>1</sup> (1.City Uni. of Hong Kong)

---

[16a-B4-2]

[JSAP-Optica Joint Symposia Invited Talk] Super-resolution microscopy using nonlinear behavior of fluorescent molecules

○Kenta Temma<sup>1,2</sup> (1.Osaka Univ. Eng., 2.Osaka Univ. Med.)

---

[16a-B4-3]

Anomalous Measurement of Imbert-Fedorov Shift at Surface Plasmon Resonance

○(P)CherrieMay Olaya<sup>1</sup>, Norihiko Hayazawa<sup>1</sup>, Maria Herminia Balgos<sup>1</sup>, Takuo Tanaka<sup>1</sup> (1.RIKEN)

---

[16a-B4-4]

Modelling Purcell effect mediated by metasurfaces with spectral parameters

○(P)JoshuaTinYau Tse<sup>1</sup>, Shunsuke Murai<sup>1</sup>, Katsuhisa Tanaka<sup>1</sup> (1.Kyoto Univ.)

---

[16a-B4-5]

Broadband Absorption Spectroscopy via Plasmon Nanofocusing

○(M2)Haruki Kidoguchi<sup>1</sup>, Prabhat Verma<sup>1</sup>, Takayuki Umakoshi<sup>1</sup> (1.Osaka Univ.)

---

[16a-B4-6]

Suppression of Modulated Electron Beam Diffraction Radiation from Finite Array of Circular Graphene Nanotubes due to the Lattice-Mode Effect

○(P)Dariia Herasymova<sup>1</sup> (1.Institute of Radio-Physics and Electronics NASU)

---

[16a-B4-7]

Floquet-Mie Scattering of Time-Varying Core-Shell Nanoparticles

○(D)YUCHEN SUN<sup>1</sup>, GUANGWEI HU<sup>1</sup> (1.School of Electrical and Electronic Engineering, Nanyang Technological University)

---

[16a-B4-8]

Plasmon nanofocusing vs plasmon resonance: Which generates the strongest near-field light?

○(D)Tongyao Li<sup>1</sup>, Andrea Schirato<sup>2,3</sup>, Remo Proietti Zaccaria<sup>4</sup>, Prabhat Verma<sup>1</sup>, Takayuki Umakoshi<sup>1</sup> (1.Osaka Univ., 2.Politecnico di Milano, 3.Rice Univ., 4.Instituto Italiano di Tecnologia)

---

[16a-B4-9]

Nanoantennas with In-plane Asymmetry for Sensing and Non-centric Emission

○Shunsuke Murai<sup>1</sup>, Taisuke Enomoto<sup>1</sup>, Katsuhisa Tanaka<sup>1</sup>, Minpeng Liang<sup>2</sup>, Jaime Gomes Rivas<sup>2</sup> (1.Kyoto University, 2.TU/e)

---

## Electromagnetic Asymmetry, Quantum Conductivity and Optical Magnetism for Nonlinear Plasmonics

Dangyuan Lei

Department of Materials Science and Engineering, City University of Hong Kong, Hong Kong

E-mail: [dangylei@cityu.edu.hk](mailto:dangylei@cityu.edu.hk)

In general, symmetric plasmonic nanocavities, such as a pair of two closely spaced metal nanospheres of the same size and constituting material, support only symmetry-allowed bright modes under light illumination. Breaking the cavity symmetry introduces mode hybridization between its bright and dark modes, leading to new plasmon modes like Fano resonance and bound states in the continuum.

In this talk, I will go on to discuss three “dark” aspects of symmetry-broken plasmonic nanocavities, including 1) light-induced electromagnetic asymmetry for enhancing the surface second-harmonic generation (SHG) of noble metals (*Nature Communications* **2021**, **12**, 4326), a mechanism well beyond conventional enhancement strategies, 2) photon-assisted tunnelling induced second-order nonlinear optics in conductive molecular nano-junctions (*Nano Letters* **2023**, **23**(12), 5851-5858), and 3) plasmon-induced optical magnetism in an asymmetric nanoparticle dimer-on-mirror cavity and its theoretical implication as a new second-order nonlinear source (*Laser & Photonics Reviews* **2020**, **14**(9), 200068).

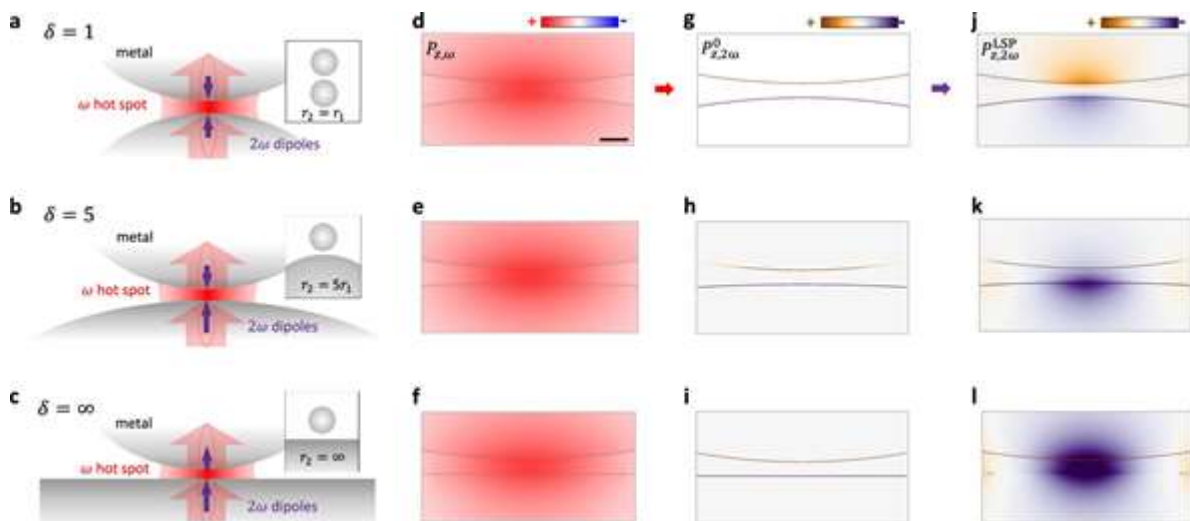


Figure 1: Suppressed and amplified surface second-harmonic generation in symmetric (upper panel) and asymmetric (middle and lower panels) plasmonic nanocavities



### Short Bio:

**Dangyuan LEI** received his PhD degree in Physics from Imperial College London, UK. He is Professor of Materials Science and Engineering at The City University of Hong Kong, China, and Provost's Visiting Professor of Physics at Imperial College London. His research interest centres on nanophotonics and low-dimensional quantum materials, with particular interest in the nanoscale cavity-matter interaction.

## Super-resolution microscopy using the nonlinear behavior of fluorescent molecules

Dept. of Applied Physics, Osaka Univ.<sup>1</sup>, Dept. of Neurosurgery, Osaka Univ.<sup>2</sup>,

Kenta Temma<sup>1,2</sup>

E-mail: [temma@ap.eng.osaka-u.ac.jp](mailto:temma@ap.eng.osaka-u.ac.jp)

Fluorescence microscopy is an indispensable tool for observing biological samples due to its less invasiveness, target specificity, and single-molecule sensitivity. The development of super-resolution techniques such as stimulated emission depletion (STED) [1], single-molecule localization [2], and structured illumination microscopy (SIM) [3] have overcome the limitation in spatial resolution, expanding the capability for imaging with higher spatial resolution beyond the classical diffraction limit. However, most of the super-resolution techniques fully exhibit their resolving capability only near the surface of samples, due to the requirement of complex illumination patterns or single molecule detection. These techniques are often hampered by background light from out-of-focus or optical aberrations, making the observation of internal structure difficult, especially in thick samples.

We developed several super-resolution techniques that leverage the nonlinear behavior of fluorescent molecules such as multiphoton [4], saturable [5], and step-wise absorption [6,7]. Nonlinear fluorescence signals derived from these behaviors are three-dimensionally localized within the excitation area, suppressing background light and improving the spatial resolution even within thick samples.

In this talk, I will introduce our development of super-resolution techniques using reversibly photo-switchable fluorescent proteins (RSFPs) whose capability of fluorescence emission (off and on state) can be modulated by light irradiation. We combined the nonlinear property of RSFPs and two-photon excitation to induce higher-order nonlinear response for further improvement of spatial resolution [6]. We also utilized RSFPs to integrate two illumination patterns: selective plane illumination and structured illumination [7]. Localizing fluorescent regions through selective plane activation of RSFPs enables the use of SIM in thick samples by suppressing background light. We succeeded in observing the internal structure of a single cell and large cell clusters with high spatial resolution, which was a difficult task for conventional super-resolution microscopy.

### References

- [1] S. W. Hell and J. Wichmann, *Opt. Lett.* **19**, 780-782 (1994)
- [2] E. Betzig et al., *Science*, **313**, 1642-1645 (2006)
- [3] M. G. L. Gustafsson, *J. Microsc.*, **198**, 82-87 (2000)
- [4] T. Kubo, K. Temma et al., *Opt. Lett.*, **46**, 37-40 (2021)
- [5] T. Kubo, K. Temma et al., *ACS Photonics*, **8**, 2666-2673 (2021)
- [6] K. Temma et al., *Opt. Express*, **30**, 13825-13838 (2022)
- [7] K. Temma and R. Oketani, et al, *Nat. Methods*, **21**, 889-896 (2024)

# Anomalous Measurement of Imbert-Fedorov Shift at Surface Plasmon Resonance

Cherrie May Olaya<sup>1</sup>, Norihiko Hayazawa<sup>1,2</sup>, Maria Herminia Balgos<sup>1</sup>, Takuo Tanaka<sup>1,3</sup>

<sup>1</sup> Innovative Photon Manipulation Research Team, RIKEN Center for Advanced Photonics, Japan,

<sup>2</sup> Surface and Interface Science Laboratory, RIKEN Cluster for Pioneering Research, Japan

<sup>3</sup> Metamaterials Laboratory, RIKEN Cluster for Pioneering Research, Japan

E-mail: cherriemay.olaya@riken.jp

## 1. Introduction

The interaction of a real optical beam and a planar interface results in an apparent shift of the reflected beam with respect to the prediction of geometric optics. The reflected beam could be displaced along the optical axis, called Goos-Hänchen (GH) shift, or transverse to the optical axis, called Imbert-Fedorov (IF) shift [1,2]. GH shift arises from the diffraction corrections in the reflection coefficients while IF shift originates from the spin-orbit (SOI) interaction of photons due to the conservation of total angular momentum. IF shifts are typically observed under circularly polarized source or under 45° linearly polarized source which correspond to the eigenmode of the shift [3]. As such, upon excitation of surface plasmon resonance under p-polarized illumination, GH shifts occurs whereas no IF shift is expected. In our previous works [4-6] and elucidated during the 2020 JSAP Autumn Meeting [7], we demonstrated significant enhancement of GH shifts at the SPR region that agree well with theoretical calculations. In this work, however, we show a large anomalous IF shift measured at the SPR angle.

## 2. Methodology

Modifications to the experimental system used in our previous works in [4-6] allowed for the simultaneous measurements of GH and IF shifts around the SPR region. Thin film of gold ( $t_{Au} = 47.5$  nm) with titanium ( $t_{Ti} = 2.5$  nm) adhesion layer was used as substrate. Excitation of surface plasmons were made using the standard Kretschmann configuration where a linearly polarized laser diode ( $\lambda = 633$  nm) impinges the substrate through a hemispherical prism ( $\phi = 25$  mm). The polarization state of the incident beam is switched between p and s states using an electro-optic (EO) modulator. Reflected beam centroid displacements were obtained using a quadrant detector (QD) positioned 4.5 cm from the incident beam waist.

## 3. Results and Discussion

Fig. 1 shows the GH and IF shifts measured around the SPR region. The gray line shows the location of the SPR angle which was obtained from reflectivity measurements performed simultaneously with beam shift measurements. The measured GH shift agrees well with analytical calculations where an angular GH shift-dominated is shown for a focused incident beam.

Analytically, no IF shift should be measured since IF shift does not have an eigenmode at p and s polarization state. Our measurements, however, show otherwise where a sharp

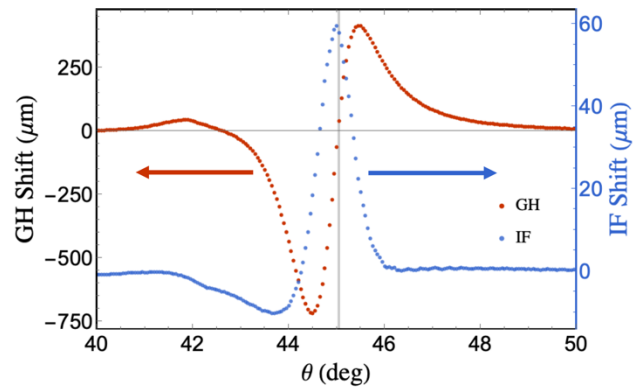


**Figure 1.** GH (red) and IF (blue) shift of the reflected beam. The gray line corresponds to the location of the SPR angle.

IF shift is measured at the SPR angle as shown in blue dots in Fig. 1. We surmise that the sharp IF shift arises from the polarization mixing from the focused incident beam and the finite extinction of the EO modulator, where for a focused incident beam, any slight deviation from the pure polarization state would result to large IF shifts. We deem our results essential to measurements requiring high precision especially for microscopy-based setups where high numerical aperture lenses are used.

## 3. Conclusions

We measured significantly large beam shifts along and perpendicular to the optical axis upon excitation of surface plasmon resonance. While the in-plane GH shift agrees well with analytical calculation, we measured significantly large anomalous IF shift at the SPR angle which we surmise to have originated from the polarization mixing of the focused incident beam.

## References

- [1] K. Y. Bliokh, A. Aiello, J. Opt. **15** (2013) 014001.
- [2] C. F. Li Phys. Rev. A. **76** (2007) 013811.
- [3] K. Y. Bliokh, F. J. Rodríguez-Fortuño, F. Nori, and A. V. Zayats, Nat. Photonics **9**, 796–808 (2015).
- [4] C. Olaya, N. Hayazawa, N. Hermosa, T. Tanaka, J. Phys. Chem. A, 2021, **1**, 451–458.
- [5] C. Olaya, N. Hayazawa, M. Balois-Oguchi, N. Hermosa, T. Tanaka, Sensors, 2021, **21**, 13, 4593.
- [6] C. Olaya, N. Hayazawa, M. Balgos, T. Tanaka, Appl. Opt., 2023, **62**, 8426–8433.
- [7] C. Olaya, N. Hayazawa, N. Hermosa, T. Tanaka, in JSAP-OSA Joint Symposia, 2020.

# Modelling Purcell effect mediated by metasurfaces with spectral parameters

Joshua Tin Yau Tse<sup>1</sup>, Shunsuke Murai<sup>1</sup>, Katsuhisa Tanaka<sup>1</sup>

<sup>1</sup> Department of Material Chemistry, Graduate School of Engineering, Kyoto University  
E-mail: tse@dipole7.kuic.kyoto-u.ac.jp

## 1. Introduction

Empirically measuring the Purcell factor, which represents the maximum enhancement to spontaneous emission in an optical cavity, is straightforward as the photoluminescence enhancement (PLE) can be determined directly by comparing the luminescence intensity with and without the cavity. However, predicting the Purcell factor have been proven to be tricky. In particular, the effective modal volume is difficult to analyze empirically, especially for non-Hermitian systems which includes open resonators and systems with dissipative materials [1].

Surface lattice resonances (SLR) is a hybrid plasmonic-photonic resonance supported on nanoparticle arrays that provides strong and directional PLE via Purcell effect and directional out-coupling. In this work, we analyzed the Purcell effect arising from SLR and proposed an analytical model that predicts the PLE only with parameters that can be obtained through spectral measurements. We also studied a wide variety of structures to ensure the predictive power of the model.

## 2. Analytical Model

In our recent work that explores the effectiveness of different materials used in PLE [2], we discovered that the nearfield enhancement of SLR in the embedded dye layer can be mapped to the absorptive decay rate contributed by dye  $\Gamma_{abs,dye}$ , which is a parameter that is obtained through spectral measurement and fitting. Through the Lorentz reciprocity theorem, we also learned that the nearfield enhancement is a predictor of PLE that is commonly used in numerical analysis [3]. By connecting these insights, we derived a new method in determining the Purcell factor of SLR that only uses parameters that can be obtained from spectral measurements. In particular, we find the spontaneous emission enhancement provided by the SLR to be described by:

$$PLE(\omega_0) = \frac{c\Gamma_{rad}}{\omega_0 t \Gamma_{tot}^2} \frac{\Gamma_{abs,dye}}{\kappa}$$

where  $\omega_0$  is the resonant frequency,  $\Gamma_{rad}$  is the radiative decay rate of the SLR,  $t$  is the dye layer thickness,  $\kappa$  is the extinction coefficient of the dye layer, and  $c$  is the speed of light in vacuum.  $\Gamma_{tot}$  is the total decay rate and  $\Gamma_{tot} = \Gamma_{rad} + \Gamma_{abs,dye} + \Gamma_{abs,NP}$ , where  $\Gamma_{abs,NP}$  is the absorptive decay rate contributed by the nanoparticles.

## 3. Results and Discussion

In order to verify our analytical model, we numerically simulated SLRs on nanoparticle arrays of different

materials and geometries with the finite-difference time-domain (FDTD) method. The numerically simulated PLE of each structure are plotted against the PLE predicted by our analytical model in Figure 1 for comparison. As illustrated in Figure 1, the data closely follows the diagonal line, which indicates that our model predicted the PLE in numerous simulated structures.

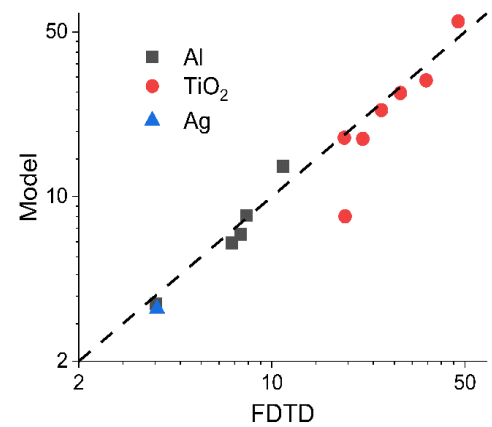


Figure 1. The PLE predicted by the analytical model was plotted against the FDTD simulated PLE.

We also experimentally analyzed PLE measurements with TiO<sub>2</sub> nanoparticle arrays. The experimental results verified the predictions from our analytical model. We also discovered that some parameters can be generalized over multiple structures with similar features. This insight allows us to further extend the predicting power of our analytical model with limited information.

## 4. Conclusions

In conclusion, we developed an analytical model that describes the Purcell effect using Lorentz reciprocity theorem. With our analytical model, we predicted the PLE mediated by SLRs on multiple structures made of a variety of materials in both numerical simulations and experiments. This study presents a useful analytical framework for optimizing PLE on a wide variety of plasmonics and nanophotonics resonators.

## References

- [1] C. Sauvan, J. P. Hugonin, I. S. Maksymov, and P. Lalanne, Phys. Rev. Lett. **110** (2013), 237401.
- [2] J. T. Y. Tse, S. Murai, and K. Tanaka, Adv. Photonics Res. (2024), 2400050.
- [3] M. Ramezani, G. Lozano, M. A. Verschuuren, and J. Gómez-Rivas, Phys. Rev. B **94** (2016), 125406



# Broadband Absorption Spectroscopy via Plasmon Nanofocusing

Haruki Kidoguchi<sup>1</sup>, Prabhat Verma<sup>1</sup>, Takayuki Umakoshi<sup>1,2</sup>

<sup>1</sup>Dept. of Applied Physics, Osaka University, <sup>2</sup>Inst. Adv. Co-creation Studies, Osaka University

E-mail: [umakoshi@ap.eng.osaka-u.ac.jp](mailto:umakoshi@ap.eng.osaka-u.ac.jp)

## 1. Introduction

Plasmon nanofocusing is a phenomenon that generates strong near-field light at an apex of a metallic tapered structure through plasmon propagation and focusing toward the apex. Among its various characteristics such as background-free from incident light, one of its distinctive advantages is the broadband property. Unlike localized plasmon resonance of a metallic nanostructure, which is excited only near the plasmon resonance wavelength, plasmon nanofocusing is excited over an extremely broad wavelength range as it is not based on resonance, but propagation of plasmons. As we have previously demonstrated the generation of white nanolight source through plasmon nanofocusing for optical nanoimaging [1], broadband plasmon nanofocusing holds a great potential for various nanophotonics techniques.

In this study, we applied plasmon nanofocusing for broadband absorption spectroscopy. Absorption spectroscopy has been a fundamental analytical technique for various samples. The previous study has further demonstrated the highly sensitive absorption sensing based on the localized surface plasmon resonance [2]. However, this resonance-based approach is limited in its detection wavelength range, which makes it difficult to precisely analyze absorption spectral shape or to simultaneously detect multiple different peaks. To overcome this issue, we employed broadband plasmon nanofocusing, and experimentally demonstrated broadband absorption spectroscopy.

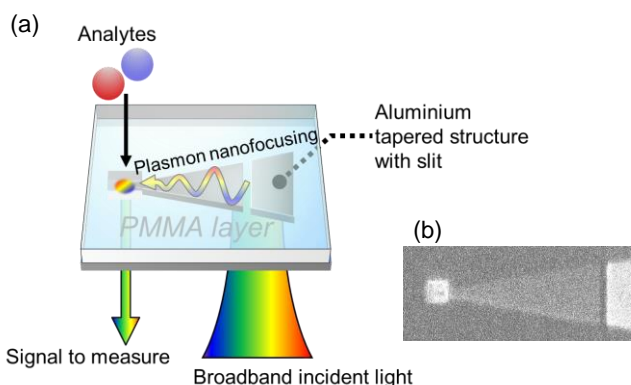


Fig. 1 (a) Schematic of our method. (b) SIM image of the tapered metallic structure (after deposition of the protection layer).

## 2. Results and Discussion

To demonstrate broadband absorption spectroscopy based on plasmon nanofocusing, we used the setup summarized in Fig. 1a. The aluminium tapered structure was fabricated by first depositing an aluminium thin film via vac-

uum evaporation and then patterning it using a focused ion beam (FIB). A slit structure was fabricated as a plasmon coupler. Subsequently, the entire tapered structure was covered with a PMMA thin film as a protection layer, and a detection hole was fabricated near the apex using FIB so that only the apex was exposed to detect absorption at the tip of the tapered structure (Fig.1b). The white supercontinuum laser was shined on the plasmon coupler to excite plasmons. Propagating plasmons generate a white nanolight source at the apex, which was used for the broadband absorption spectroscopy.

For absorption measurement, a water drop was first deposited on the substrate, and analytes solution was subsequently injected for measurements. Absorption spectra were calculated by comparing the scattering signals from the taper apex with analytes and without analytes. As shown in Fig. 2, we successfully acquired absorption spectra of three different analytes Cy3, Cy5 and Cy7.5 simultaneously, which have different absorption peaks from 500 to 800 nm over a broad wavelength range. The result was in a good agreement with the spectrum obtained with the conventional absorption spectrometer. Also, we confirmed that our method has a linearity despite the limited detection sensitivity due to the mechanical drift of optical components at this moment.

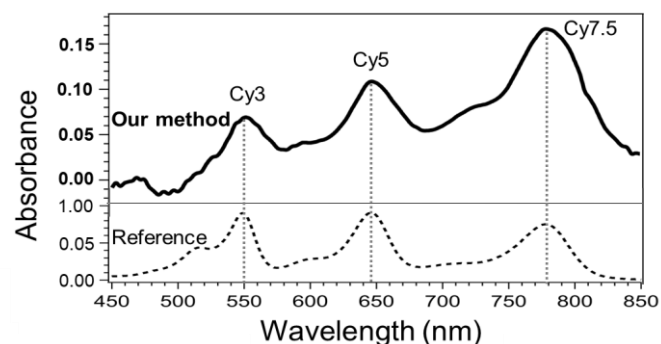


Fig. 2 Absorption spectrum acquired via plasmon nanofocusing (solid line) and reference spectrum by conventional spectrometer (dashed line).

## 3. Conclusion

We successfully demonstrated broadband absorption spectroscopy based on plasmon nanofocusing ranging from 500 nm to 850 nm.

## References

- [1] T. Umakoshi, et al. *Sci. Adv.* **6**, eaba4179 (2020).
- [2] Liu, G. et al. *Nat. Methods.* **4**, 1015–1017 (2007).

# Suppression of Modulated Electron Beam Diffraction Radiation from Finite Array of Circular Graphene Nanotubes due to the Lattice-Mode Effect

Dariia O. Herasymova

Laboratory of Micro and Nano Optics, Institute of Radio-Physics and Electronics NASU, Kharkiv 61085, Ukraine

E-mail: [dariia.heras@gmail.com](mailto:dariia.heras@gmail.com)

We analyze the effect of the suppression of the diffraction radiation (DR) caused by the electron beam flowing above a finite grating made of dielectric circular nanowires with graphene covers – see Fig.1. The work focuses on the combined effect of the plasmon-mode and the lattice-mode resonances on DR.

In our analysis, we assume that the zero-thickness electron beam density is time-harmonically modulated with the cyclic frequency  $\omega$  and its velocity is constant,  $v = \beta c$ , and consider its field in the free space as the incident field [1-4]. To characterize the graphene, we employ the quantum-theory Kubo formalism and the resistive sheet boundary conditions [5]. Then, the DR problem is a full-wave two-dimensional boundary-value problem for the Helmholtz equation with exact boundary conditions, plus the condition of local power finiteness and the radiation condition at infinity. To cast this problem to the form convenient for computations, we use the separation of variables in local coordinates and the addition theorem for cylindrical functions that yields a block type  $(M \times M)$  infinite-matrix equation of the Fredholm second kind. This enables precise control of numerical accuracy [4]. The DR power characteristics, such as the total scattering cross-section, are calculated.

Fig. 2 shows the color map of the DR total scattering cross-section (TSCS) for the electron beam excited grating of  $M = 500$  wires with the radius varying from 60 nm to 125 nm near the 300 THz frequency. The chemical potential of graphene is 1 eV, and the electron beam relative velocity is  $\beta = 0.5$ . The red “ridge” on the map, visible for the wires of all radii, corresponds to the resonance on the dipole plasmon mode  $P_1$  of the graphene cover of each nanowire. The Q-factor of that resonance is moderate, around 53 according to equation (26) from [4]. Our previous works [6] have revealed that such a grating with the number of wires that is counted in large dozens and hundreds possesses an ultrahigh-Q lattice-mode resonance [7,8] at the frequency where period is entirely divisible by wavelength/ $\beta$ . If the frequencies of the plasmon and lattice mode resonances are well separated, each of them yields a peak in the DR power spectrum. In the studied here case of the 2- $\mu\text{m}$  period, the mentioned two resonance frequencies coincide. As one can observe from Fig. 2, then the collective lattice-mode effect is not distinguished if the wire radius is smaller than around 90 nm. However, if it gets larger, then there happens a suppression of the plasmon-mode resonance peak – TSCS has a deep minimum. The larger the wire radius, the deeper the suppression. The potential application of the studied effects is discussed.

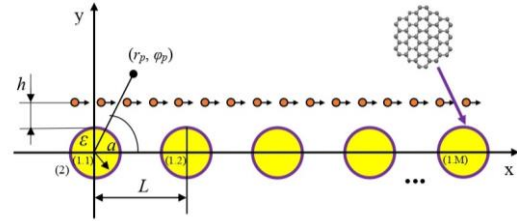


Fig. 1. Cross-sectional geometry of flat zero-thickness electron beam moving near  $M$  identical circular dielectric nanowires.

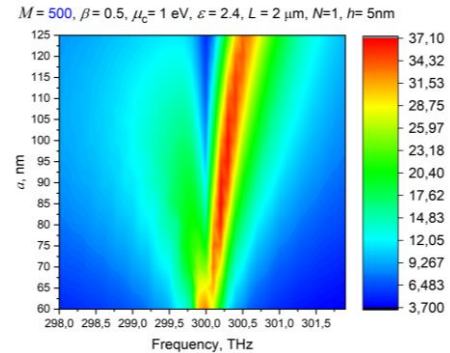


Fig. 2. Color map of the DR power versus the frequency and the wire radius for the  $M = 500$  graphene-wrapped nanowire grating.

## References:

- [1] A. I. Boltosov and V. G. Sologub, "Excitation of an open strip-type resonator by a modulated beam of charged particles," *Sov. J. Commun. Technol. Electron.*, vol. 33, no 6, pp. 133-140, 1988.
- [2] M. Castellano, et al., "Measurements of coherent diffraction radiation and its application for bunch length diagnostics in particle accelerators," *Phys. Rev. E*, vol. 63, art. no 056501, 2001.
- [3] D. Assante, et al., "Longitudinal coupling impedance of a particle traveling in PEC rings: A regularised analysis," *IET Microwaves, Antennas Propag.*, vol. 15, no 10, pp. 1318–1329, 2021.
- [4] D. O. Herasymova, S. V. Dukhopelnykov, and A. I. Nosich, "Infrared diffraction radiation from twin circular dielectric rods covered with graphene: plasmon resonances and beam position sensing," *J. Opt. Soc. Am. B*, vol. 38, no 9, pp. C183-C190, 2021.
- [5] G. W. Hanson, "Dyadic Green's functions and guided surface waves for a surface conductivity model of graphene," *J. Appl. Phys.*, vol. 103, art. no 064302, 2008.
- [6] D. O. Herasymova, "Diffraction radiation analysis of finite graphene-covered nanowire grating excited by electron beam," *Proc. European Microwave Conf. (EuMC-2023)*, Berlin, 2023, pp. 544-547.
- [7] V. O. Byelobrov, T. L. Zinenko, K. Kobayashi, et al., "Periodicity matters: grating or lattice resonances in the scattering by sparse arrays of sub-wavelength strips and wires," *IEEE Antennas Propag. Mag.*, vol. 57, no 6, pp. 34-45, 2015.
- [8] A. D. Utyushev, et al., "Collective lattice resonances: plasmonics and beyond," *Rev. Phys.*, vol. 6, art. no 100051, 2021.



# Floquet-Mie Scattering of Time-Varying Core-Shell Nanoparticles

Yuchen Sun<sup>1</sup>, Guangwei Hu<sup>1</sup>

<sup>1</sup> School of Electrical and Electronic Engineering, 50 Nanyang Avenue,  
Nanyang Technological University, Singapore, 639798, Singapore  
E-mail: [guangwei.hu@ntu.edu.sg](mailto:guangwei.hu@ntu.edu.sg)

## 1. Introduction

Extreme scattering phenomena, such as nonreciprocity, and parametric amplification, in periodically time-varying mediums have attracted numerous attentions in recent years. Periodically time-varying permittivity is used as an additional degree of freedom in metamaterials or metasurfaces. Here, we investigate the Floquet Mie scattering properties of a spherical nanoparticle coated with a time-varying dispersive shell. Our result can provide insight into the light-matter interaction in the time-varying system and can also guide the antenna design based on the core-shell structure.

## 2. General Instructions

We consider a circularly polarized light impinges on a temporal modulated spherical core-shell nanoparticle. The spherical particle consists of a dielectric core with radius  $a$  and a time-varying dispersive shell with radius  $b$ . The electric field inside the shell can be expanded as a series of vector spherical harmonics (VSFs)  $\mathbf{F}(\kappa\mathbf{r})$ ,

$$\mathbf{E}(\mathbf{r}, \omega) = \sum_{\kappa} A(\kappa) S_{\kappa}(\omega) \mathbf{F}(\kappa\mathbf{r}),$$

where  $\kappa$  is the wavenumber,  $S_{\kappa}(\omega)$  is the spectral part of the eigenmode.

### Dispersion relation inside the periodically time-varying dispersive material

We consider the plasmonic materials with periodically modulated electron density, which can be realized via “shaking” the metal with pulse etc. The electron motion can be described by the equation of motion [1,2],

$$\left[ \frac{\partial^2}{\partial t^2} + \gamma \frac{\partial}{\partial t} + \omega_e^2 \right] \mathbf{P}(\mathbf{r}, t) = \frac{q_e^2}{m_e} N(t) \mathbf{E}(\mathbf{r}, t)$$

where  $N(t) = N_0(1 + \Delta \cos \Omega t)$ . And the permittivity can be solved from this equation. After substituting the permittivity into the Maxwell's equations, the dispersion relation takes this form,

$$k(\omega)^2 (\varepsilon_{st}(\omega) S_{\kappa}(\omega) + \varepsilon_{dyn}(\omega) S_{\kappa}(\omega + \Omega) + \varepsilon_{dyn}(\omega) S_{\kappa}(\omega - \Omega)) = \kappa^2 S_{\kappa}(\omega)$$

$$\text{where } \varepsilon_{st} = 1 + \frac{\omega_p^2}{\omega_r^2 - \omega^2 - i\gamma\omega}, \varepsilon_{dyn} = \frac{\Delta}{2} \frac{\omega_p^2}{\omega_r^2 - \omega^2 - i\gamma\omega}$$

### The results

The electromagnetic field inside the time-varying shell can be written as,

$$\begin{aligned} \mathbf{E}_{shell}(\mathbf{r}, \omega) &= \sum_{\alpha, \mu\nu} \sum_{l=-\infty}^{\infty} \sum_{n=-\infty}^{\infty} \sum_{j=1,2} S_{\kappa_j}(\omega - n\Omega) A_{\alpha, \mu\nu, \kappa_j}^{(j), shell} \mathbf{F}_{\alpha, \mu\nu, \kappa_j}^{(j)}(\mathbf{r}) \\ \mathbf{H}_{shell}(\mathbf{r}, \omega) &= \sum_{\alpha, \mu\nu} \sum_{l=-N}^N \sum_{n=-N}^N \sum_{j=1,2} B_{\alpha, \mu\nu, \kappa_j}^{(j), shell} \mathbf{F}_{\alpha, \mu\nu, \kappa_j}^{(j)}(\mathbf{r}) \end{aligned}$$

Applying the boundary conditions, i. e., the continuity of the tangential component of electric and magnetic field, the scattered field can be solved.

We calculate its elastic scattering cross section using the scattered field. As is shown in Figure 1, the elastic scattering cross section is strongly suppressed at the resonance frequency.

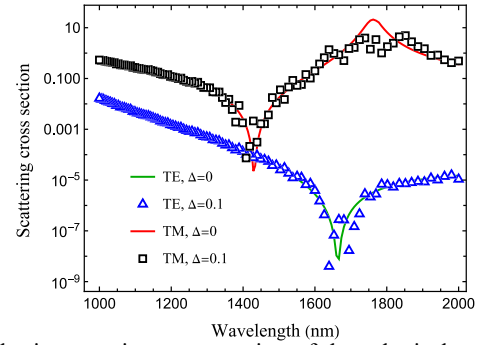


Figure 1. Elastic scattering cross section of the spherical particle with core-shell structure. [3] Their radius is set as  $a = 100 \text{ nm}$  and  $b = 150 \text{ nm}$ , the modulation strength  $\Delta = 0$  and  $1$ , and modulation frequency  $\Omega = 0.377 \text{ THz}$ .

## 3. Conclusions

We have proposed a rigorous method to describe the scattering properties of the spherical particle with a time-varying dispersive shell. We calculated the scattering cross section. The results may help us understand the energy transfer between the EM field and the time-varying medium.

## References

- [1] I. Stefanou, J. Opt. Soc. Am. B **38** (2021) 407.
- [2] G. Ptitcyn, Laser Photon. Rev. **17** (2022) 2100683.
- [3] F. Monticone, Phys. Rev. Lett. **110** (2013) 113901.

## Plasmon nanofocusing vs plasmon resonance: Which generates the strongest near-field light?

Tongyao Li<sup>1</sup>, Andrea Schirato<sup>2,3</sup>, Remo Proietti Zaccaria<sup>4</sup>, Prabhat Verma<sup>1</sup>, Takayuki Umakoshi<sup>1,5</sup>

<sup>1</sup>Dept. of Applied Physics, Osaka Univ., <sup>2</sup>Physics Dept., Politecnico di Milano, <sup>3</sup>Dept. of Physics and Astronomy, Rice University, <sup>4</sup>Instituto Italiano di Tecnologia, <sup>5</sup>Institute of Advanced Co-Creation Studies, Osaka Univ.,  
E-mail: umakoshi@ap.eng.osaka-u.ac.jp

### 1. Introduction

Strongly localized and enhanced near-field light generated near plasmonic nanostructures has been widely applied in various fields from material science to biology. The near-field light is often generated by localized plasmon resonance of metallic nanostructures such as a gold nanoparticle and nanorod. Recently, plasmon nanofocusing has also attracted much attention as another method to generate the near-field light due to its distinctive advantages such as background-free from incident light [1]. The near-field light is generated at an apex of a plasmonic tapered structure, such as a gold cone, through plasmons propagating toward the apex. Considering both methods of localized plasmon resonance and plasmon nanofocusing, one of pivotal questions is “Which generates more intense near-field light?”, as the near-field light intensity is a fundamental and important property for most of optical applications.

### 2. Results and discussion

In this study, we numerically investigated which of localized plasmon resonance and plasmon nanofocusing generates intense near-field light. To evaluate the maximum near-field light intensities for both methods, we considered not only light field intensity but also heat generation and temperature in plasmonic structures. The near-field light intensity can be simply increased by increasing the incident light intensity. However, it is limited by the fact that too strong incident light destroys plasmonic structures as temperature goes beyond the melting point. Therefore, we calculated both electric field and temperature around the plasmonic structures using finite element method.

Figure 1(a) shows the calculation models for the localized plasmon resonance and plasmon nanofocusing. We chose 785 nm as the incident light wavelength. We used a gold nanorod and cone for the localized plasmon resonance and plasmon nanofocusing, respectively, as typical structures. Their geometries were optimized for the wavelength of 785 nm. We used a grating as a plasmon coupler for plasmon nanofocusing, which was located 3.75  $\mu\text{m}$  far from the apex. Under incident light irradiation to the gold nanorod and the grating of the gold cone, we simulated the distributions of both the electric field and temperature, as shown in Figs. 1 (b, c). We confirmed that near-field light was generated for both cases. At the same time, we found that temperature of the structures increased due to heat generation. We further increased incident light intensity

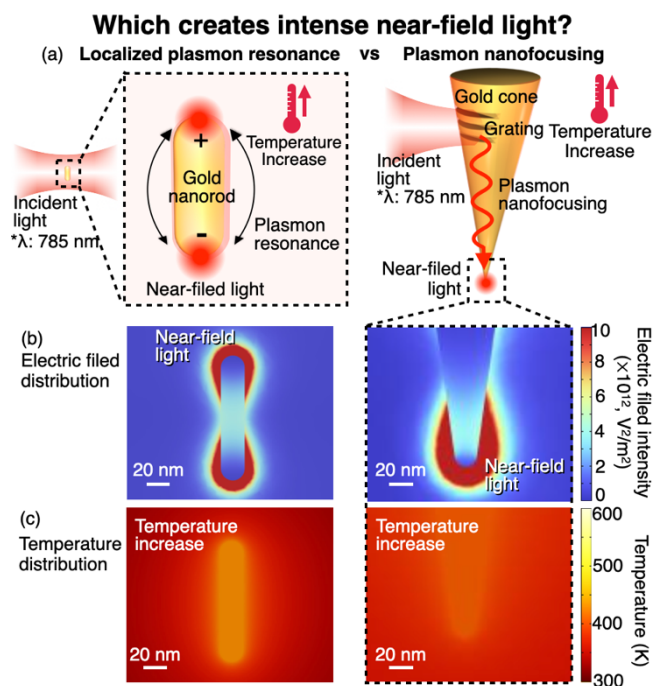


**Figure 1** Fig 1. (a) Schematics of calculation modes of (b) Electric field and (c) temperature distributions of the gold nanorod and cone.

until temperature reaches the melting point of gold (1337K). In this situation, we found that the maximum near-field light intensity by plasmon resonance was  $6.26 \times 10^{13} \text{ V}^2/\text{m}^2$ . As for plasmon nanofocusing with the gold cone, the maximum near-field light intensity was  $11.40 \times 10^{13} \text{ V}^2/\text{m}^2$ . Therefore, we concluded that plasmon nanofocusing is capable of creating approximately twice stronger near-field light compared with localized plasmon resonance.

### 3. Conclusions

In conclusion, we found that plasmon nanofocusing generates twice more intense near-field light compared with localized plasmon resonance. However, it was investigated only at a particular condition, which calls more extensive studies at various conditions in the future. In the presentation, we also discuss the case of more moderate temperature. Also, an interesting phenomenon of the near-field light intensity decrease with respect to the incident light intensity will be discussed.

### References

[1] T. Umakoshi, et al., *Sci. Adv.* **6**, eaba4197 (2020)

# Nanoantennas with In-plane Asymmetry for Sensing and Non-centric Emission

Shusuke Murai<sup>1</sup>, Taisuke Enomoto<sup>1</sup>, Katsuhisa Tanaka<sup>1</sup>, Minpeng Liang<sup>2</sup>, Jaime Gómez Rivas<sup>2</sup>

<sup>1</sup> The Japan Society of Applied Physics, Department of Material Chemistry, Graduate School of Engineering, Kyoto University  
<sup>2</sup> Department of Applied Physics and Science Education, Institute for Complex Molecular Systems, and Eindhoven

Hendrik Casimir Institute, Eindhoven University of Technology, The Netherlands

E-mail: murai.shunsuke.2m@kyoto-u.ac.jp

## 1. Introduction

When light is incident on a nanoantenna, i.e., a periodic array of nanoparticles, individual local resonances couple cooperatively and produce surface lattice resonance (SLR). Operating the in-plane symmetry of the nanoantenna would break the in-plane symmetry of the optical response of the SLRs, and also lead to the suppression of radiation of the SLRs to become bound-states in the continuum (BICs) [1]

In this study, we prepared two samples with in-plane asymmetry: the first sample is the square lattice comprising asymmetric-shaped TiO<sub>2</sub> nanoparticles. The second sample is non-Bravais lattice of Si nanoparticles array, supporting quasi-BIC states at normal incidence. Using these asymmetric nanoantennas, we investigated non-centric directional photoluminescence and sensitivity to the surrounding refractive index.

## 2. Asymmetric TiO<sub>2</sub> nanoantenna for non-centric emission

The asymmetric TiO<sub>2</sub> nanoparticle arrays were fabricated by a glancing angle deposition of titanium on the square lattice of TiO<sub>2</sub> nanoparticle array at an angle of 45° to the substrate, followed by rapid thermal annealing (RTA) to convert the deposited Ti to TiO<sub>2</sub>. The shape of the nanoparticle was observed by scanning electron microscopy (SEM) and atomic force microscopy. In the SEM image (Fig. 1(a)), a shadow can be seen on the right side of each nanoparticle, indicating that the titanium was deposited from the left side.

We measured the incident angle dependence of the extinction spectra of the poly(methyl methacrylate) (PMMA)-coated array on the substrate (Fig. 1(b)) and the emission angle dependence of the PL enhancement of the PMMA-coated array containing a fluorescent dye (Fig. 1(c)) along the x-axis. In the extinction spectra, two dispersive features are found along the ( $\pm 1, 0$ ) diffraction orders. Their intensities are very different because of the asymmetric shape of the nanoparticles. The PL enhancement map (in Fig. 1(c)) follows this asymmetric intensity. These results show that the simple glancing angle deposition makes the asymmetric nanoparticle arrays to shift the center of the luminescence intensity distribution.

## 3. Doubly-detuned Si nanoantenna for sensing

We broke the in-symmetry by detuning the size and position of silicon particles periodically arranged in an array, resulting in magnetic and electric quasi-BICs at gamma point. We investigated the sensing characteristics of them by measuring the spectral shift in response to changes in the refractive index of the surrounding medium[2]. In addition,

we revealed the sensing range of the different resonances through simulations involving a layer of deviating refractive index of increasing thickness. Interestingly, the resonances show very different responses, which we describe via the analysis of the near-field. This work contributes to the development of highly sensitive and selective BIC-based sensors that can be used for a wide range of applications.

## Acknowledgements

Financial support from JSPS bilateral Joint Research Project (JPJSBP120239921) was acknowledged.

## References

- [1] S. Murai et al., Laser Photon. Rev. 2100661 (2022)
- [2] T. van Loon et al. Optics Express 32, 14289-1429 (2024)

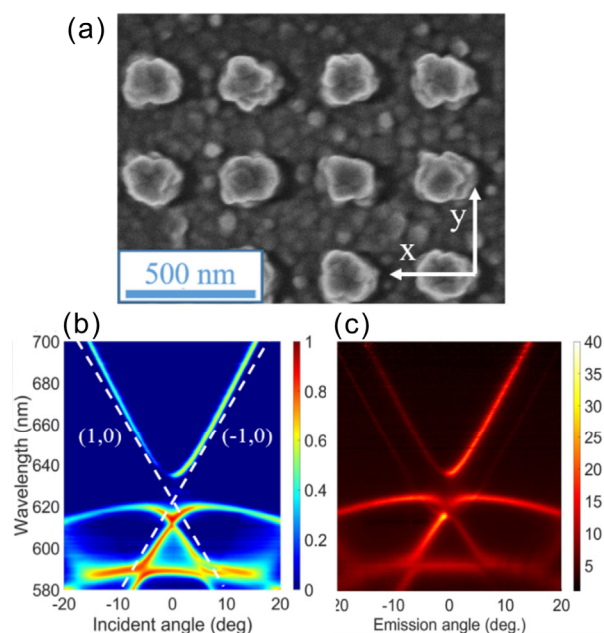


Fig.1(a) SEM image of asymmetric TiO<sub>2</sub> nanoparticle arrays prepared with glancing angle deposition. Angular dependent (b) extinction and (c) photoluminescence enhancement (PLE) spectra of the asymmetric TiO<sub>2</sub> nanoparticles arrays. The dotted lines in (b) denote ( $\pm 1, 0$ ) diffraction orders. PLE was defined as the PL intensity from the luminous layer on the array divided by that from the same layer but on a flat substrate.

4 JSAP-Optica Joint Symposia 2024 | 一般セッション(口頭講演) : 4.1 Plasmonics and Nanophotonics

**[16p-B4-1~13] 4.1 Plasmonics and Nanophotonics**

[16p-B4-1]

[JSAP-Optica Joint Symposia Invited Talk] Plasmonic nanowire based intracellular material delivery

○Tomoko Inose<sup>1,2,3</sup> (1.Kyoto Univ., 2.iCeMS, Kyoto Univ., 3.JST PRESTO)

[16p-B4-2]

[JSAP-Optica Joint Symposia Invited Talk] Controlling lyotropic liquid crystalline self-assembly for creating nano carriers for biomedical applications

○Nhiem Tran<sup>1</sup> (1.RMIT University)

[16p-B4-3]

Ultra-wide dynamic structural colors with width-modulated Cr-subwavelength grating on Ni/SiO<sub>2</sub> films○Yuusuke Takashima<sup>1,2</sup>, Kentaro Nagamatsu<sup>1,2</sup>, Yoshiki Naoi<sup>1,2</sup> (1.Tokushima Univ., 2.pLED, Tokushima Univ.)

[16p-B4-4]

Spectroscopic thermal emitters based on bimetallic compounds for high temperature plasmonic applications

○Andrea RuizPerona<sup>1,2</sup>, Toan Tran Phuoc<sup>1</sup>, Thien Duc Ngo<sup>1</sup>, Tadaaki Nagao<sup>1,2</sup> (1.NIMS, 2.Hokkaido Univ.)

[16p-B4-5]

Designing Reconfigurable Metamaterials Toward Structural Color Generation

M. Pourmand<sup>1</sup>, ○Pankaj Kumar Choudhury<sup>2</sup> (1.Umea University, 2.Zhejiang University)

[16p-B4-6]

Investigation of Plasmonic Effect in Slot Rectangular Waveguide by Applying a Gold as Metal Optimization

○(D)Km Priyanka<sup>1</sup>, Ritu Raj Singh<sup>1</sup> (1.NETAJI SUBHAS UNIVERSITY OF TECHNOLOGY, NEW DELHI)

[16p-B4-7]

Capillary-Interactions based Single-step and Scalable Fabrication of Gap-tuneable Plasmonic Nanostructures

○(DC)Renu Raman Sahu<sup>1</sup>, Alwar Samy Ramasamy<sup>1</sup>, Tapajyoti Das Gupta<sup>1</sup> (1.LANSPE, IAP, IISc)

[16p-B4-8]

Self-Assembled Silicon Metasurface for Mechanically Tunable Optical Properties

○(M1)Yongan Hu<sup>1</sup>, Patrick Probst<sup>1</sup>, Mojtaba Karimi Habil<sup>1</sup>, Hiroshi Sugimoto<sup>1</sup>, Minoru Fujii<sup>1</sup> (1.Kobe Univ.)

[16p-B4-9]

A Fano resonance enhanced surface plasmon sensing for IgG/anti-IgG immunosensor with high sensitivity

○(D)Yiming Lu<sup>1,3</sup>, Hidekazu Ishitobi<sup>1,2,3</sup>, Zouheir Sekkat<sup>4,5</sup>, Yasushi Inouye<sup>1,2,3</sup> (1.FBS, Osaka Univ., 2.Dept. of Appl. Phys. Osaka Univ., 3.PhotoBIO-OIL, AIST-Osaka Univ., 4.MAScIR, 5.Univ.

Mohammed VI Polytechnic)

---

[16p-B4-10]

Tunable abrupt autofocusing meta-devices

○(DC)Rong Lin<sup>1</sup>, Mu Ku Chen<sup>1</sup>, Din Ping Tsai<sup>1</sup> (1.CityU)

---

[16p-B4-11]

Wavelength-multiplexed full color 3D metasurface hologram made of silicon nitride

○Tetsuhito Omori<sup>1</sup>, Junpei Beppu<sup>1</sup>, Masakazu Yamaguchi<sup>1</sup>, Tamaki Onozawa<sup>1</sup>, Kentaro Iwami<sup>1</sup> (1.TUAT)

---

[16p-B4-12]

A Cost-Effective, Flexible 1D Metasurface Absorber in The Infrared Region

○(DC)Jhuma Pan<sup>1</sup>, Sachin Kumar Srivastava<sup>1</sup> (1.IIT Roorkee)

---

[16p-B4-13]

Polyaniline coated U-bent Fiber Optic Aptasensor for Arsenite Detection in Environmental Matrices

○(DC)Ashish Shukla<sup>1</sup>, Tathagata Pal<sup>1</sup>, Soumyo Mukherji<sup>1</sup> (1.IIT Bombay, Mumbai)

---

**プラズモニックナノワイヤーを用いた細胞内物質導入技術の開発****Plasmonic nanowire based intracellular material delivery**京大白眉センター<sup>1</sup>, 京大 iCeMS<sup>2</sup>, JST さきがけ<sup>3</sup> ○猪瀬 朋子<sup>1,2,3</sup>Kyoto Univ.<sup>1</sup>, JST PRESTO<sup>2</sup>, °Tomoko Inose<sup>1,2</sup>

E-mail: inose.tomoko.1v@kyoto-u.ac.jp

The technology for introducing biomolecules such as proteins and DNA into cells is widely used as a method to artificially control cell functions, ranging from basic biology to the pharmaceutical field. Methods employing liposomes, viral vectors, and the electroporation have been currently widely used, although these methods show low introduction efficiency or cell toxicity to some cell types. Another method for introducing biomolecules into cells is microinjection.<sup>1)</sup> This method physically introduces micro/nano needles directly into the cells, ensuring that biomolecules are reliably delivered within a cell.

Although several micro/nano needle methods have been reported, traditional micro/nano needles have limitations in the substances they can carry, posing challenges to their versatility. In this study, we developed a new method for introducing biomolecules into cells by applying the plasmonic nanowire single-cell endoscopy technique.<sup>2)</sup> By utilizing the plasmonic effects occurring on nanowires, we have recently succeeded in controlling the spatiotemporal introduction of biomolecules into a single live cell.

- 1) Advanced tools and methods for single-cell surgery. A. Shakoor, W. Gao, L. Zhao, Z. Jiang, D. Sun , *Microsystems & Nanoengineering*, **2022**, 8, 47.
- 2) Live-Cell SERS Endoscopy Using Plasmonic Nanowire Waveguides. G. Lu, H. De Keersmaecker, L. Su, B. Kenens, S. Rocha, E. Fron, C. Chen, P. Van Dorpe, H. Mizuno, J. Hofkens, J. A. Hutchison, H. Uji-i, *Adv. Mater.*, **2014**, 26, 5124



## Controlling lyotropic liquid crystalline self-assembly for creating nano carriers for biomedical applications

Nhiem Tran

School of Science, RMIT University, Melbourne, Victoria, Australia

[nhiem.tran@rmit.edu.au](mailto:nhiem.tran@rmit.edu.au)

### Abstract

Lipid nanoparticles (LNP) have been widely used as carriers for drugs and genes, including in mRNA-vaccines for COVID-19. A special class of LNP, lyotropic liquid crystalline LNP, comprise mainly of amphiphilic lipids self-assembling into two- and three-dimensional, inverse hexagonal, and cubic nanostructures (Fig. 1). Mesophase structures of self-assembled lyotropic liquid crystalline nanoparticles are important factors that directly influence their ability to encapsulate and release drugs and their biological activities.<sup>1,2</sup> For example, the release rate of hydrophilic compounds was found to be much faster in the cubic phase than in the hexagonal phase, micellar cubic phase, and microemulsion.<sup>3</sup> Additionally, it has been shown that the internal nanostructures also affect cellular response such as cell uptake of nanoparticles, hemolysis, and cytotoxicity.<sup>4</sup> Importantly, the *in vivo* behavior of nanoparticles such as biodistribution appears to be regulated by their nanostructures.<sup>5</sup> However, it is difficult to predict and precisely control the mesophase behavior of these self-assembled nanomaterials, especially in complex systems with several components.

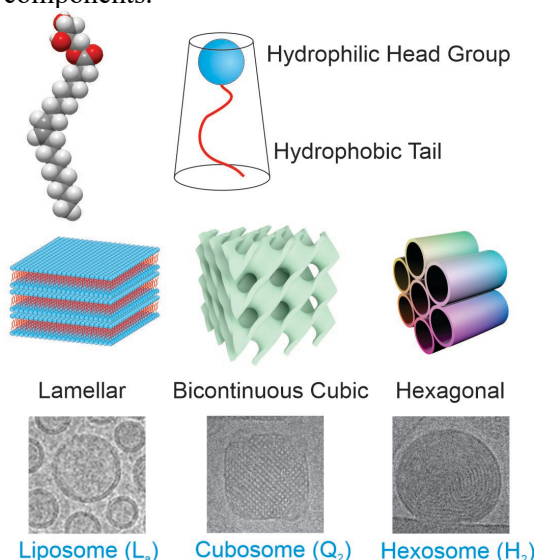


Figure 1. Molecular structure of monoolein, an amphiphile that can self-assemble into various mesophase structures, which can be dispersed and form nanoparticles including liposomes, cubosomes, and hexosomes.

In this presentation, a structural study of self-assembled lipid mesophase using synchrotron small angle X-ray scattering will be reported. Using the understanding of the lipid self-assembled structures, lipid nanoparticles with different internal nanostructures will be created to study their *in vitro* interaction with cells and *in vivo* biodistribution. Furthermore, formulation of “smart” LNP, which switch between structures in response to pH will be reported (Fig. 2). Since low pH conditions are observed in tumours and infected sites, an elevated release rate allows for better targeted therapies. Herein, pH responsive LNP containing novel ionisable lipids and their applications as carriers for anticancer and antimicrobial agents are reported.

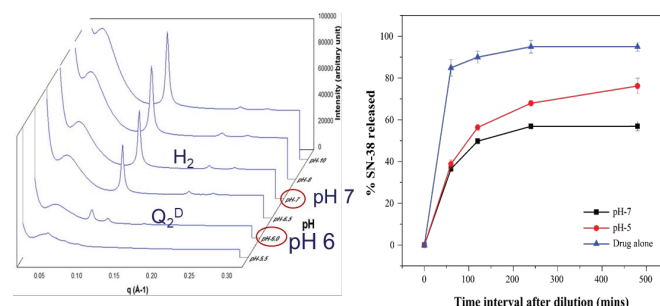


Figure 2: pH responsive LNP showing a hexagonal structure at pH 7 and a cubic structure at pH 6. When used to encapsulate anti-cancer drug SN-38, the structural difference at pH 5 and pH 7 resulted in varied drug release kinetics.<sup>6</sup>

### References

1. Clogston, J. & Caffrey, M. J. Controlled Release 107, 97-111 (2005).
2. Zhai, J. et al. ACS nano 13, 6178-6206 (2019).
3. Phan, S. et al., I. J. Pharm. 421, 176-182 (2011).
4. Tan, A., et al. Adv. Sci. (2018).
5. Tran, N. et al. Mater. Sci. Eng.: C 71, 584-593 (2016).
6. Rajesh, S. et al. Pharmaceutics 2022, 14(10), 2175

# Ultra-wide dynamic structural colors with width-modulated Cr-subwavelength grating on Ni/SiO<sub>2</sub> films

Yuusuke Takashima<sup>1,2</sup>, Kentaro Nagamatsu<sup>1,2</sup>, Yoshiki Naoi<sup>1,2</sup>

<sup>1</sup> Faculty of Science and Technology, Tokushima University, Tokushima, Japan,

<sup>2</sup> Institute of Post-LED Photonics, Tokushima University, Tokushima, Japan

E-mail: takashima@tokushima-u.ac.jp.

## 1. Introduction

The structural color resulting from the interaction between light and artificially designed nanostructures is attractive for many fields including display, imaging, and security [1]. Dynamic control of the interaction significantly promotes the flexibility of design and is very important for the applications mentioned above. Many researchers tried to produce the dynamic structural color using mechanical displacement [2], polarization [3], and phase-change materials [4]. However, the color gamut from one design unit still be restricted. In this work, we demonstrated ultra-wide dynamic structural colors utilizing highly lossy metal/insulator/metal (MIM) structures with width-modulated subwavelength grating (SWG).

## 2. Results and discussions

Figure 1 shows a sketch of our proposed structure. A 100 nm-Ni and 65 nm-SiO<sub>2</sub> films were electron-beam (EB) evaporated onto the glass substrate. The 30 nm-thickness Cr-subwavelength grating (SWG) is formed by the EB lithography technique. The grating period is 400 nm. The designed structure supports spectrally broadened gap-plasmon resonance due to the strong damping of Cr and Ni. The spectrally broadened resonance also gives a large phase-retardation between orthogonal polarizations. When the polarized incident light with 45° to the grating bars is irradiated, the polarization of the reflected light is changed by the phase-retardation. Moreover, we employed two-type grating widths (210 nm/100 nm) to expand of the resonant bandwidth and induce the phase-retardation in further wide spectral region. Thus, ultra-wide tunability of the reflection color is expected by simply rotating the analyzing polarizer.

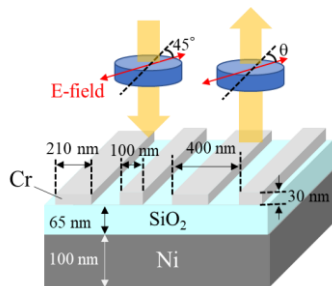


Figure 1 Schematic sketch of Ni/SiO<sub>2</sub>/width-modulated Cr-SWG structure.

The normal reflection spectra from the fabricated sam-

ple at a certain analyzer angle  $\theta$  are shown in Fig. 2 (a). For  $\theta = 0^\circ$  (E-field is parallel to the grating bars, namely s-polarization), the reflection dip associated with destructive interference Air/SiO<sub>2</sub> and Ni/SiO<sub>2</sub> is obtained at 550 nm. In contrast, the reflectivity at  $\theta = 90^\circ$  (namely, p-polarization) is decreased at the broad wavelength region around 600 to 700 nm because of excitation of gap plasmon mode. The excited gap plasmon mode also provides significant phase-retardation, and this modifies the polarization state of reflected light. Hence, the different colors from p- and s-polarization appear at  $\theta = 45^\circ$  and  $135^\circ$ . Figure 2 (b) shows the gamut of the fabricated sample in CIE1931 color space (the conversion used standard illuminant D65 and 2° observer color-matching function). When rotating the analyzer, the gamut shows an ultra-wide oval covering the whole visible region. The tunable range covers 37% of the sRGB area by only one design unit, and we demonstrated a wider dynamic range than previous reports [3,4].

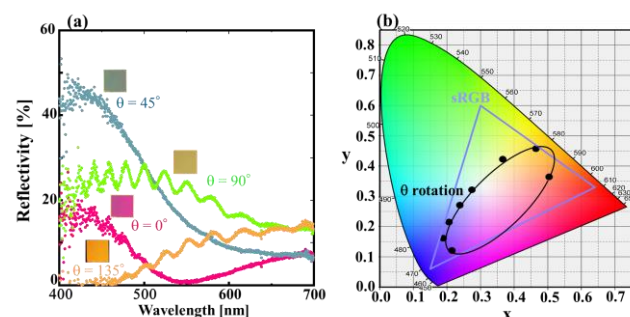


Figure 2 (a) Normal reflection spectra from the fabricated Ni/SiO<sub>2</sub>/width-modulated Cr-SWG at various analyzing polarizer angle  $\theta$  (b) Color gamut of our structure in CIE1931 color space.

## 3. Conclusions

Ultra-wide polarization-tunable structural color was demonstrated using spectrally broadened resonance in Ni/SiO<sub>2</sub>/width-modulated Cr-SWG. This wide-tunability is very attractive for the design of many applications.

## Acknowledgements

This work is supported in part by JSPS KAKENHI JP24K1731100.

## References

- [1] D. Wang *et al.*, *Nanophotonics* **12** (2023) 1019.
- [2] A. L. Holsteen *et al.*, *Science* **365** (2019) 257.
- [3] X. Shang *et al.*, *Photonics* **10** (2023) 448.
- [4] F. Shu *et al.*, *Adv. Opt. Mater.* **6** (2018) 1700939.



## Spectroscopic thermal emitters based on bimetallic compounds for high temperature plasmonic applications

NIMS<sup>1</sup>, Hokkaido Univ.<sup>2</sup>, °Andrea Ruiz-Perona<sup>1,2</sup>, Toan Tran Phouc<sup>1,2</sup>, Thien Duc Ngo<sup>1</sup>, Tadaaki Nagao<sup>1,2\*</sup>

Email: NAGAO.Tadaaki@nims.go.jp

Metallic refractory materials, such as single-element metals, bimetallic alloys, metal borides, and metal silicides, are attracting increasing interest and usage in industrial furnaces, aerospace technology, and energy harvesting, due to their outstanding chemical and structural stability at high temperatures. Nevertheless, their optical properties are much inferior in comparison to representative plasmonic metals like Au, Cu, or Al, which, in contrast, exhibit lower melting points and are susceptible to oxidation, thereby hindering the development of thermophotonics applications in high-temperature environments.

Spectroscopic infrared thermal emitters selectively emit or absorb infrared radiation with very narrow spectral resolution, making them increasingly appealing for applications such as plasmon-enhanced vibrational spectroscopy, material-selective heating/drying systems, thermophotovoltaics, or spectroscopic infrared light sources in gas sensors. Consequently, there is an increasing need to find materials with a strong plasmonic response and high-temperature stability suitable for use in high-temperature photo-energy applications, such as thermal emitters or thermal detectors. We propose binary metallic compounds such as nickel-based superalloys as promising candidates for photothermal applications due to their high oxidation resistance in air and good optical performance.

In this study, nickel aluminum (NiAl) thin films are fabricated via direct current (DC) sputtering deposition under different growth conditions. These layers grow in unique uniaxial fashion, which yields high crystallinity and results in strong plasmonic polarizability within the IR spectral region. Simulations of plasmonic thermal emitters based on our material's optical properties have reached absorptivity/emissivity values close to 1 for targeted wavelengths. Plasmonic emitter devices following the simulation parameters are fabricated to demonstrate the optical performance of the materials. The experimental results demonstrate the applicability of nickel-based alloys similar to the case of metal borides for high-temperature plasmonic applications in vacuum as well as in atmosphere.

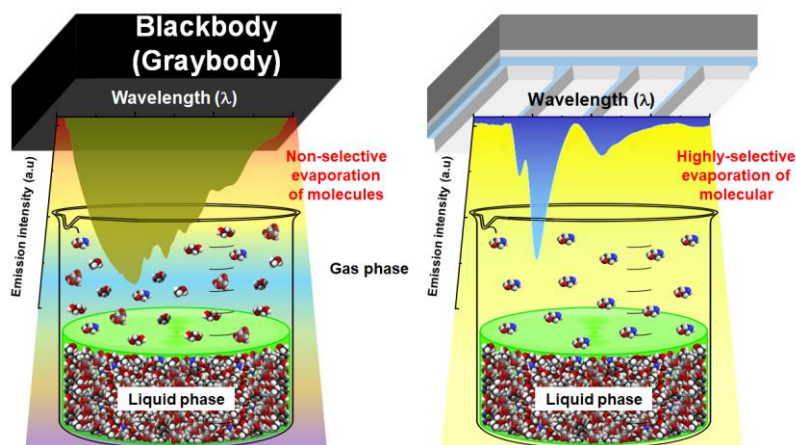


Fig. 1. Example of use of wavelength-selective thermal emitters.

[1] T.P. Tran, T.D. Ngo, H.D. Ngo, T. Nagao, Appl. Phys. Express **14**, 087001 (2021).

[2] P.T. Tran, D.T. Ngo, H.D. Ngo, O.S. Handegård and T. Nagao, Optics Express **30**, 38630 (2022).

# Designing Reconfigurable Metamaterials Toward Structural Color Generation

M. Pourmand<sup>1</sup> and Pankaj K. Choudhury<sup>2\*</sup>

<sup>1</sup>Department of Applied Physics and Electronics, Umeå University, SE-901 87 Umeå, Sweden

<sup>2</sup>International Research Center for Advanced Photonics, Zhejiang University, Haining 314400, China

\*E-mail: pkchoudhury@icape.org

## 1. Introduction

Dynamic color-generation structures provide higher resolution and scalability compared to the traditional pigmentation-based displays [1]. The main roadblock to the wide adoption of structural colors is the fixed optical response after the realization process. To address this issue, several kinds of tunability mechanisms have been introduced including the implementation of plasmonic nano-antennas enabled by liquid crystals [2] and plasmonic resonators exploiting stretchable materials [3]. The chalcogenide phase-change mediums- (PCMs) based plasmonic structures [4–6] offer advantages including flexibility, color durability, high resolution, cost-effectiveness, and CMOS compatibility [7]. Herein, we propose an optimized PCM-integrated structure to generate a wide spectrum of colors.

## 2. Structural Configuration

Figure 1 illustrates the structure comprising  $n$  bilayers of GeSe<sub>3</sub> (of thickness  $d_D^n$ ) and Al (of thickness  $d_m^n$ ). To thermally excite the structure, we use a 1 nm thick heating layer of tri-layer graphene. The SiO<sub>2</sub> layers on the top and bottom of the structure have their own merits. The capping SiO<sub>2</sub> layer protects the GeSe<sub>3</sub> medium from evaporation, and the SiO<sub>2</sub> buffer layer above the substrate isolates graphene sheets from the metallic layer above. Also, it provides sufficient adhesion between the graphene sheet and SiO<sub>2</sub> substrate during the fabrication process. Furthermore, the structure can be fabricated by using lithography-free techniques, such as the physical vapor deposition (PVD) method, namely thermal evaporation and/or RF sputtering [8].

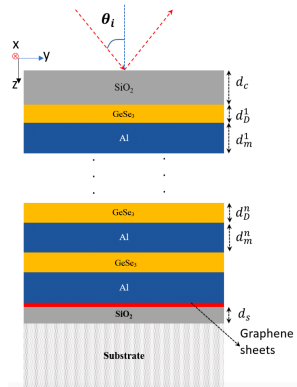


Fig. 1. Two-dimensional schematic of the proposed structure.

## 3. Results and Discussion

Figure 2 illustrates the reflection spectra of the optimized configuration, wherein we demonstrate the generation of primary colors (red, green, and blue) by the optimized structures corresponding to the amorphous and crystalline states of GeSe<sub>3</sub>. It is obvious that the peak reflectance has values

above 0.6 in all structural configurations. Moreover, the reflectivity undergoes a blue shift upon transition of the phase of GeSe<sub>3</sub> from amorphous to crystalline.

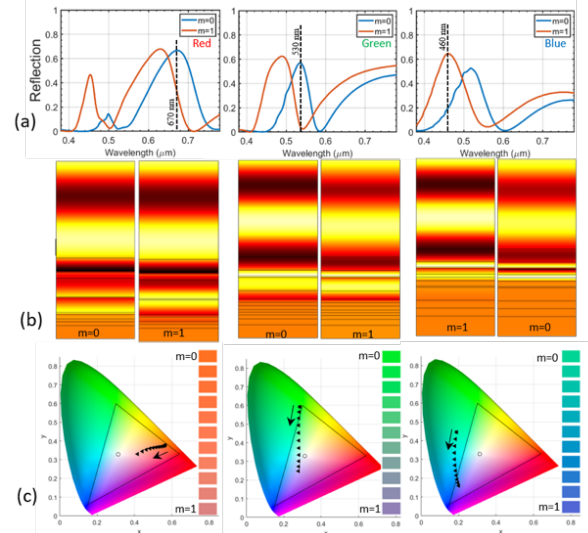


Fig. 2. Spectral features of the optimized structure for the fully amorphous ( $m = 0$ ) and fully crystalline ( $m = 1$ ) states of GeSe<sub>3</sub> medium in the configuration. (a) Reflection spectra for the red (left), green (center), and blue (right) pixels for the amorphous and crystalline states of GeSe<sub>3</sub>; dashed lines denote the target wavelengths of primary colors considered in the optimization process. (b) Distribution of magnetic field at the target wavelengths of primary colors. (c) The trajectory of reflected colors as a function of  $m$ .

## 4. Conclusion

A reconfigurable layered metamaterial configuration comprising GeSe<sub>3</sub>/Al bilayer stacks has been investigated. The implemented design optimization exhibits the generation of primary colors, i.e., the red, green, and blue pixels. The embedded graphene micro-heater facilitates control over the ambient temperature upon being excited due to external electrical pulses, which ultimately governs the pixel-sized tunability of the reflected color. The proposed layered configuration has potential in designing reflective display systems.

## Acknowledgement

PKC acknowledges the financial support by Zhejiang University (China) through the grant 11133000\*194232301/002.

## References

- [1] A. Kristensen et al., *Nature Rev. Mater.* **2** (2016) 16088.
- [2] D. Franklin et al., *Nature Commun.* **6** (2015) 7337.
- [3] B. H. Miller, H. Liu, and M. Kolle, *Nature Mater.* **21** (2022) 1014.
- [4] M. Pourmand and P. K. Choudhury, *J. Opt. Soc. Am. B* **39** (2022) 1222.
- [5] M. Pourmand and P. K. Choudhury, *IEEE Trans. Nanotechnol.* **21** (2022) 586.
- [6] M. Pourmand and P. K. Choudhury, *J. Opt. Soc. Am. B* **40** (2023), 1625.
- [7] M. Wuttig et al., *Nature Photon.* **11** (2017) 465.
- [8] S. S. Ghazi et al., *Nano Lett.* **19**, (2019) 7377.

# Investigation of Plasmonic Effect in Slot Rectangular Waveguide by Applying a Gold as Metal Optimization

Km Priyanka<sup>1,\*</sup>, Ritu Raj Singh<sup>1</sup>

<sup>1</sup>Department of Electronics and Communication Engineering, Netaji Subhas University of Technology, Delhi, India.

E-mail: [km.priyanka.phd22@nsut.ac.in](mailto:km.priyanka.phd22@nsut.ac.in)

## Introduction

Surface plasmon polaritons (SPPs) are the electromagnetic excitations that evaporate when confined in a direction perpendicular to the interface and propagate along the interface between two different media with opposite dielectric constants in a wave-like pattern [1]. It gives a strong light confinement power in integrated photonic circuit [2]. In this paper, by using SoI technology light confinement for the plasmonic slot rectangular waveguide is studied. The most promising dimension of the recommended design is represented by the values of  $d_3$  and  $d_4$ , which are 180 nm and 220 nm, respectively, for the waveguide's width and height [3]. The slot rectangular waveguide confinement power and mode effective area are studied by applying a Gold (Au) layer around the core at a distance  $M_g$ .

## Structure

The cross-sectional and three-dimensional (3-D) views of the slot rectangular silicon on insulator waveguide (SRSOIW) structural design are displayed in Fig. 1(a) and (b). The thickness of metal ( $\Delta t$ ) is taken 100 nm [4]. With coherent oscillations of free electrons between metal dielectric surface, surface plasmon waves are conceptualized. The waveguide design consists of  $\text{SiO}_2$  as substrate, Au as a plasmon and Si as core material. At operating wavelength taken as 1550 nm, the Refractive index (RI) of substrate and core are 1.44 and 3.47 respectively. Additionally, the Johnson and Christy model [5] is used to incorporate the RI of the Au layer.

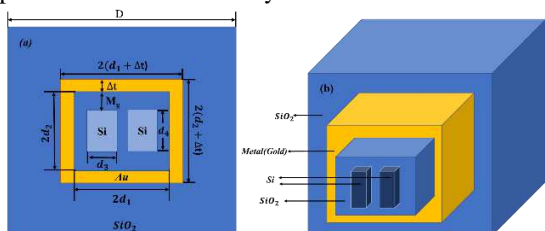


Fig. 1 (a) Cross sectional view and (b) 3-D view of plasmonic based slot rectangular waveguide.

## Result and discussion

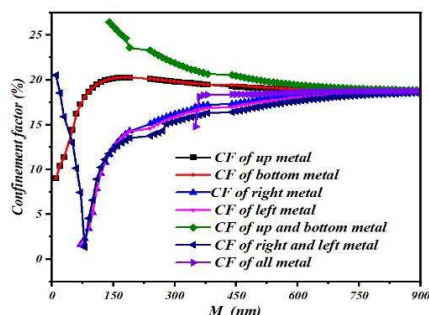


Fig. 2 Confinement factor for optimization of the  $M_g$ .

After investigating the plasmonic effect of Si material, Fig. 2 represents the variation of the metal gap ( $M_g$ ) with respect to the confinement factor (CF). It reveals that CF saturates at 900 nm, and at this point, there is strong light-confinement in the slot region which is required for the propagation of the light in the slot.

Considering CF,  $M_g = 900$  nm, comes out to be optimum value for placing the metal.

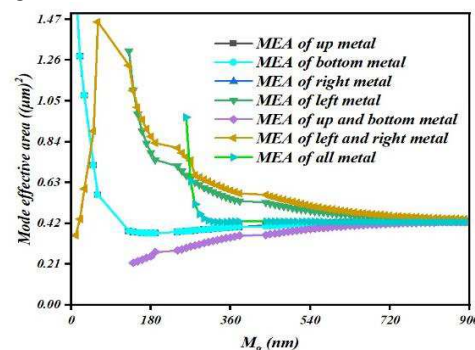


Fig. 3 Mode effective area for optimization of the  $M_g$ .

Similarly, in Fig. 3, the Mode Effective Area (MEA) is  $0.44 \mu\text{m}^2$  for all Au layers at  $M_g = 900$  nm. Considering MEA, the optimal value for  $M_g$  comes out to be  $\sim 900$  nm. The optimization of the structure is to maximize the CF and minimize MEA.

## Conclusion

Using the Finite Element Method (FEM), the plasmonic slot rectangular waveguide with Gold (Au) placed at all sides of the core at distance ( $M_g$ ) is examined. The CF and MEA obtained as  $\sim 18.75\%$  and  $\sim 0.44 \mu\text{m}^2$  at the distance ( $M_g$ ) of 900 nm. Hence, the optimal value to place a metal layer from the core is approx. 900 nm is achieved for this waveguide. The goal of using metal in a waveguide for strong light confinement with low loss is best achieved at this distance.

## Reference

- [1] S. Kumari, R. R. Singh, and S. M. Tripathi, "Parametric Optimization of Hybrid Plasmonic Waveguide-Based SOI Ring Resonator Refractive Index Sensor," *Plasmonics*, vol. 17, no. 6, pp. 2417–2430, Dec. 2022, doi: 10.1007/s11468-022-01724-6.
- [2] B. Banan, M. S. Hai, E. Lisicka-Skrzek, P. Berini, and O. Liboiron-Ladouceur, "Multichannel Transmission Through a Gold Strip Plasmonic Waveguide Embedded in Cytosol," *IEEE Photonics J.*, vol. 5, no. 3, pp. 2201811–2201811, Jun. 2013, doi: 10.1109/JPHOT.2013.2267537.
- [3] S. Vardhan and R. R. Singh, "Optimization and Comparative Analysis of Rectangular and Slot Waveguide based Symmetric Ring and Racetrack Resonators for SoI Photonic Integrated Filters," *Silicon*, vol. 16, no. 7, pp. 2913–2926, May 2024, doi: 10.1007/s12633-024-02879-z.
- [4] S. H. Badri and M. M. Gilarlue, "Coupling Between Silicon Waveguide and Metal-Dielectric-Metal Plasmonic Waveguide with Lens-Funnel Structure," *Plasmonics*, vol. 15, no. 3, pp. 821–827, Jun. 2020, doi: 10.1007/s11468-019-01085-7.
- [5] P. Joensen, J. C. Irwin, J. F. Cochran, and A. E. Curzon, "Transmission method for determining the optical constants of metals," *J. Opt. Soc. Am.*, vol. 63, no. 12, p. 1556, Dec. 1973, doi: 10.1364/JOSA.63.001556.



## Capillary-Interactions based Single-step and Scalable Fabrication of Gap-tuneable Plasmonic Nanostructures

(DC) Renu Raman Sahu<sup>1</sup>, Alwar Samy Ramasamy<sup>2</sup>, Tapajyoti Das Gupta<sup>3</sup>

Lab. of Adv Nanostructures for Photonics and Electronics<sup>1, 2, 3</sup>, Instrumentation and Applied Physics,

Indian Institute of Science, C. V. Raman Road, Bengaluru, India, 560012

E-mail: renuraman@iisc.ac.in

**Abstract:** A scalable and single-step method (Fig 1a) exploiting capillary interactions (Fig 1b) for creating sub-100nm (Fig 1c, 1d) non-coalescent metallic(Ga) nanodroplets on Polydimethylsiloxane (PDMS), a bio-compatible elastomeric substrate, is shown herein. The nanoscale gap between Gallium nanodroplets thus formed allows for spectrally dependent electric field enhancement (Fig 1e), owing to plasmon hybridization of neighboring Ga nanodroplets. The substrate, PDMS, allows not only for gap tuneability but also actively participates in determining the Ga nanosphere sizes. It thus enables numerous potential technologies involving mechanochromic sensing (Fig 1f, 1g) and display applications (Fig 1h).

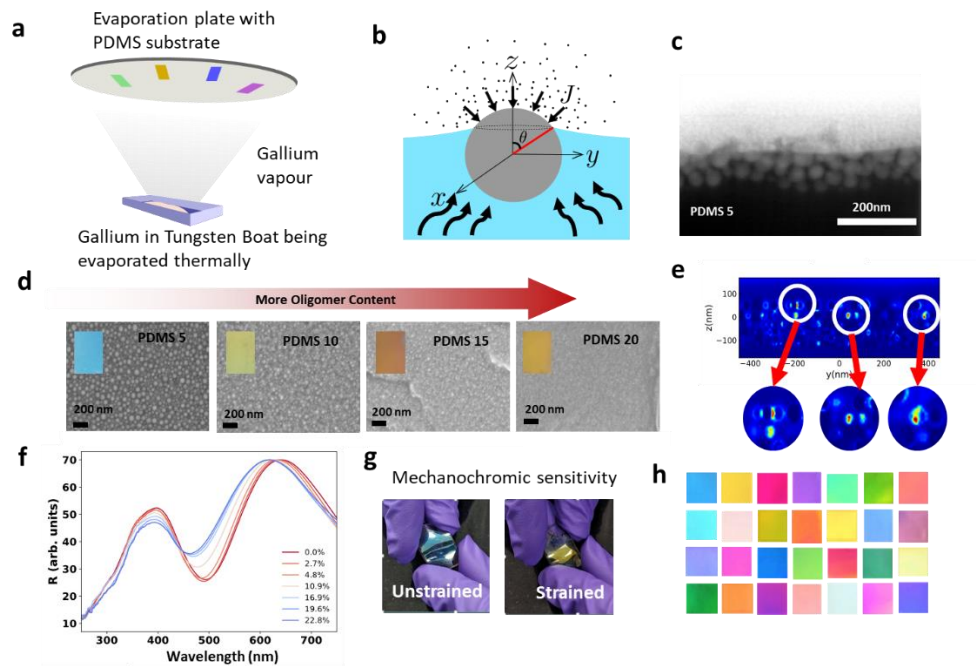


Figure 1: a. Thermal evaporation of Ga onto PDMS with different oligomer content. b. Capillary interaction of Ga and liquid oligomers results in the growth of nanodroplets and encapsulation by the liquid oligomers. c. The cross-section image of Ga nanodroplets on PDMS. d. Top-view image of Ga nanodroplets on PDMS, showing different size distributions as the oligomer content varies. (inset) Optical images of real samples. e. Gap plasmon resonances excited in the inter-droplet gaps. f. The reflectivity spectra of Ga-on-PDMS sample for different strain values. The blue shift in the visible region is a result of gap plasmon resonances, whereas UV spectral features are due to scattering by individual Ga nanodroplets, unchanging with strain. g. Sample changing its color from blue to yellow on mechanical deformation. h. Palette of samples with Ga-on-PDMS based structural colors, fabricated by the capillary interactions of liquid Ga and liquid-oligomers of PDMS.



# Self-Assembled Silicon Metasurface for Mechanically Tunable Optical Properties

Yongan Hu, Patrick T. Probst, Mojtaba Karimi Habil, Hiroshi Sugimoto, Minoru Fujii

Kobe University,  
E-mail: sugimoto@eedept.kobe-u.ac.jp

## 1. Introduction

The metasurface approach is an effective way to manipulate light at the nanoscale. Dielectric metasurfaces benefit from low losses as compared to their plasmonic counterpart, which comprises metal nanoparticles. Moreover, Mie-resonant dielectric metasurfaces support magnetic resonances in addition to electric ones. In a 2D array, the resonance from the individual nanoparticles interferes with the Rayleigh anomalies (RAs) of the periodic structure to produce a collective surface lattice resonance (SLR). In-situ control over this lattice resonance can be realized by employing external stimuli like mechanical deformation.<sup>[1]</sup> Due to its elastic, inert and nontoxic properties, PDMS is popular as stretchable substrate. Conventionally, 2D metasurface arrays are fabricated via electron beam lithography. Nevertheless, this method is time-consuming, requires expensive facilities and is challenging to combine with stretchable substrates.

In this work, we present a mechanically tunable 2D Si nanoparticle array produced via templated colloidal self-assembly on a PDMS substrate. We successfully excite the collective electric dipole resonance in the periodic array. Stretching the elastic substrate shifts the spectral position of the resonance by tuning the periodicity. When the collective resonance overlaps with the single-particle magnetic resonance, the lattice Kerker effect arises and the reflectivity is strongly reduced.

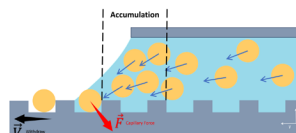
## 2. Results

The tunable 2D array is fabricated by assembling colloidal Si nanoparticles inside a PDMS nanohole array, via template-assisted self-assembly,<sup>[2,3]</sup> as shown in Figure 1a. Stretching the elastic substrate is accomplished with a customized device to tune the periodicity of the 2D array. Figure 1b shows a dark field image of the highly filled 2D array. The average diameter of Si nanoparticles and the periodicity of the unstrained sample are 116 nm and 550 nm, respectively.

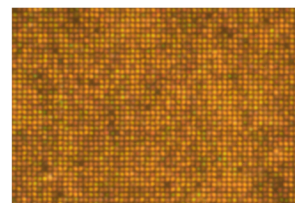
The optical properties of 2D array with smaller periodicity of 300 nm under different strains are studied using an optical microscope. Figure 1c and Figure 1d show the measured and simulated reflection spectra of the 2D Si nanoparticle array under various strains. Here, the specified strain indicates the change in periodicity relative to the original particle-to-particle distance of 300 nm. The spectra show good agreement with the simulations: the collective electric dipole lattice resonance (ED-LR) shifts from around 460 nm to 500 nm. At 50 nm strain, it overlaps with the magnetic dipole (MD) resonance, which results in the suppression of the reflection by the lattice Kerker effect. For

the strain beyond 50 nm, the collective electric dipole resonance further red-shifts and becomes broader with lower intensity.

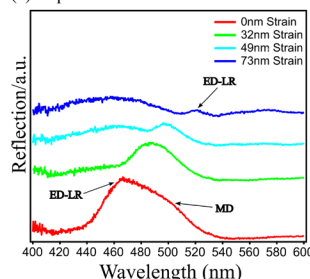
(a) Self-assembly



(b) Dark field image of the Si nanoparticles 2D array



(c) Experiment



(d) Simulation

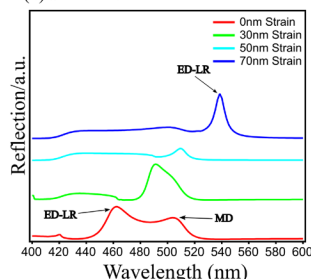


Figure 1. (a) Schematic illustration of template-assisted self-assembly. (b) Dark field image of the Si nanoparticle 2D array. (c) Experimental and (d) simulated reflection spectra of the Si nanoparticles 2D array under different strains, the arrows indicate the spots of the collective electric dipole resonance (ED-LR) and the magnetic dipole resonance (MD).

## 3. Conclusion

We have successfully fabricated a high-quality 2D array of Si nanoparticles on a PDMS substrate via colloidal self-assembly. By applying tensile strain to the substrate, we have succeeded in tuning the lattice constant and to adjust the electric dipole lattice resonance to match the magnetic one, which suppressed the reflection by the lattice Kerker effect.

## References

- [1] Yonghao Cui, et al., ACS Nano 2012 6 (3), 2385-2393
- [2] Gupta, V., Probst, P. T., et al., ACS Appl. Mater. 2019, 11, 28189–28196.
- [3] H. Negoro, et al., Adv. Opt. Mater. 10 (2022), 2102750.

# A Fano resonance enhanced surface plasmon sensing for IgG/anti-IgG immunosensor with high sensitivity

○(D)Lu Yiming<sup>1,3</sup>, Hidekazu Ishitobi<sup>1,2,3</sup>, Zouheir Sekkat<sup>4,5</sup>, Yasushi Inouye<sup>1,2,3</sup>

FBS, Osaka Univ.<sup>1</sup>, Dept. of Appl. Phys. Osaka Univ.<sup>2</sup>, PhotoBIO-OIL, AIST-Osaka Univ.<sup>3</sup>, MAScIR<sup>4</sup>,  
University Mohammed VI Polytechnic<sup>5</sup>  
E-mail: Lu\_Yiming@ap.eng.osaka-u.ac.jp

## 1. Introduction

Surface plasmon resonance (SPR) is widely used as a label-free method for monitoring molecular interactions such as antigen-antibody interactions by measuring the shift in the SPR angle due to changes in the refractive index of the sensing surface. Recently, SPR sensors based on Fano resonance have been proposed to improve the sensitivity of SPR sensors [1]. In our previous report, SF11/Ag/SiO<sub>2</sub>/TiO<sub>2</sub> multilayer system for Fano resonant SPR was developed and applied to the detection of glucose concentration, successfully improving the sensitivity by about one order of magnitude [2].

In this study, the SF11/Ag/SiO<sub>2</sub>/TiO<sub>2</sub> Fano multilayer system was investigated to be extended to the monitoring of molecular interactions such as antigen-antibody interactions. In particular, the interaction between immunoglobulin G (IgG) and anti-IgG was to be examined.

## 2. Methods and Results

At first, SF11/Ag/SiO<sub>2</sub>/TiO<sub>2</sub> multilayer Fano substrates were prepared by sequential deposition by sputtering method. Then, a surface modification process was investigated to immobilize IgG on the SF11/Ag/SiO<sub>2</sub>/TiO<sub>2</sub> Fano substrates (Fig. 1). ATR spectra of the modified Fano substrates were subsequently measured under conditions of pure water, IgG solution and anti-IgG solution, respectively, as shown in Fig. 2. In pure water, an asymmetric Fano dip was observed around 60.59° angle of incidence, whereas in the 50 µg/mL IgG solution, the Fano dip was shifted towards the 0.12° higher angle. As the solution was changed from 50 µg/mL IgG solution to 55 µg/mL anti-IgG solution, a further shift of ca. 0.12° to the higher angle side was seen. The refractive index and thickness of the IgG and anti-IgG layers were also determined using numerical analysis based on Fresnel formulae.

## 3. Conclusion

We have prepared SF11/Ag/SiO<sub>2</sub>/TiO<sub>2</sub> substrates for Fano resonance SPR measurements

and developed a surface modification method for monitoring intermolecular interactions. An experimental scheme for detecting IgG/anti-IgG interactions was thereby established. Evaluation of the detection limit of this method, improvement of sensitivity by reducing the extinction coefficient of the TiO<sub>2</sub> layer and improvement of the chemical stability of the substrate surface are to be investigated.

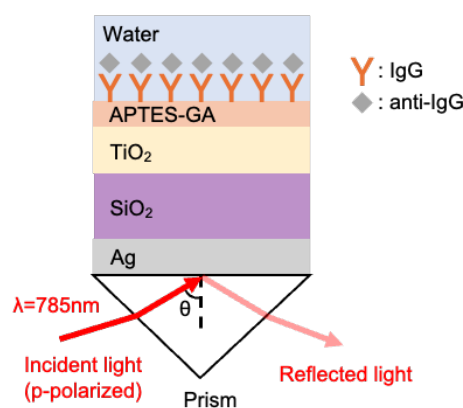


Figure1 Structure of modified SF11/Ag/SiO<sub>2</sub>/TiO<sub>2</sub> multilayer Fano substrate

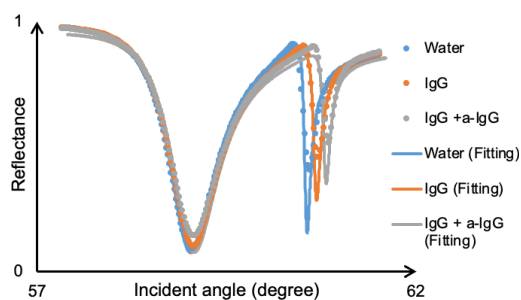


Figure2 ATR spectra and fitting curve of modified SF11/Ag/SiO<sub>2</sub>/TiO<sub>2</sub> substrate under the condition of water, 50 µg/mL IgG solution and 55 µg/mL anti-IgG solution

## References

- [1] S. Hayashi et al., Sci. Rep. **6** (2016) 33144.
- [2] T. Ishizu et al., 21a-A200-2, the 83rd JSAP Autumn Meeting (2022).

# Tunable abrupt autofocusing meta-devices

Rong Lin<sup>1</sup>, Mu Ku Chen<sup>1,2,3</sup>, Din Ping Tsai<sup>1,2,3</sup>

<sup>1</sup> Department of Electrical Engineering, City University of Hong Kong, Kowloon, Hong Kong SAR 999077, China

<sup>2</sup> Centre for Biosystems, Neuroscience, and Nanotechnology, City University of Hong Kong, Kowloon, Hong Kong SAR 999077, China

<sup>3</sup> The State Key Laboratory of Terahertz and Millimeter Waves, City University of Hong Kong, Kowloon, Hong Kong SAR 999077, China

E-mail: rong.lin@my.cityu.edu.hk

## 1. Introduction

Abrupt autofocusing (AAF) beams [1], integrating features of circular Airy and Bessel beams, offer extended focal depths, self-healing properties, high precision, and minimal energy loss. These qualities make them ideal for advanced optical imaging, particle trapping, and laser surgery. Traditionally, spatial light modulators (SLMs) have been used to generate AAF beams by encoding their Fourier transform. However, SLMs suffer from low resolution, energy inefficiency, and a limited operational wavelength range, which hinder precise nanoscale operations. Additionally, their bulky size is at odds with the trend towards device miniaturization and integration. Metasurfaces [2-4], capable of manipulating wavefronts at subwavelength scales, present a superior alternative to traditional optical devices by offering reduced weight, increased efficiency, smaller size, and lower energy consumption. Metasurfaces have found applications [5-7] in beam shaping, achromatic imaging, light-field sensing, holography, optical computing, quantum technologies, and biological imaging. Yet, challenges remain in biomedical applications, particularly in creating dynamic beams essential for improving image contrast, optical tweezing, and optimizing photodynamic therapy.

In this research, we introduce two types of tunable abrupt autofocusing meta-devices composed of dual metasurfaces. By adjusting the relative rotation between these metasurfaces, one device can dynamically steer the AAF beam, while the other adjusts its focal length. Importantly, these tuning methods are wavelength-independent and scalable. We anticipate that these tunable meta-devices will significantly advance the use of AAF beams in precise biomedical applications such as laser therapy, particle manipulation, and biological imaging.

## 2. Results

The capability to generate tunable abrupt autofocusing beams relies on the precise superposition of phase profiles. Take AAF beam with steered angles as an example, the Fourier transform of an AAF beam should be added on the first metasurface. To realize the dynamic steering function, a gradient phase distribution can be introduced and decomposed into two distinct phase profiles of off-axis Fresnel lenses. Fig. 1 shows the schematic diagram of tunable abrupt autofocusing meta-devices.

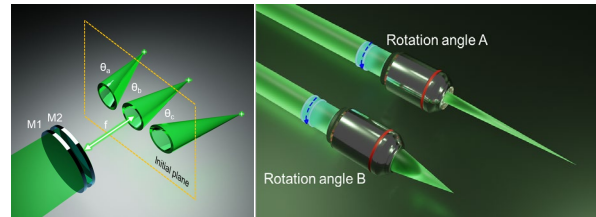


Fig. 1. Schematic diagrams of tunable abrupt autofocusing meta-devices. (Left) Steered AAF beam generation; (Right) Vari-focal AAF beam generation.

It should be emphasized that any discrepancies, such as gaps, mismatches, and fabrication defects, can significantly impair the performance of beam steering and autofocusing. Therefore, it is advisable to construct the metasurfaces with a larger scale and minimize the distance between them to reduce wavefront fluctuations as much as possible.

## 3. Conclusions

To summarize, we employed the superimposed phase method to design metasurfaces capable of generating an AAF beam and dynamically tuning the deflection angle or the focal length. We believe that this work clearly reveals one of the tunability methods within the field of metasurfaces and enhances the functionality of AAF beams, which benefits the possibility of application in bioimaging, biomedical applications, and laser surgery.

## Acknowledgements

This work is supported by the University Grants Committee / Research Grants Council of the Hong Kong Special Administrative Region, China [Project No. AoE/P-502/20, CRF Project: C1015-21E; C5031-22G, GRF Project: CityU15303521; CityU11305223; and Germany/Hong Kong Joint Research Scheme: G-CityU 101/22], City University of Hong Kong [Project No. 9380131, 9610628, and 7005867], and National Natural Science Foundation of China [Grant No. 62375232].

## References

- [1] Nikolaos K. Efremidis, *Optica* 6 (2019) 686.
- [2] Shuming Wang, *Nat. Nanotech.* 13 (2018) 227.
- [3] Jin Yao, *Adv. Photonics* 5 (2023) 024001.
- [4] Yuan Luo, *Small Methods* 6 (2022) 2101228.
- [5] Rong Lin, *J. Phys. D Appl. Phys.* 54 (2021) 145108
- [6] Rong Lin, *Opt. Express* 29 (2021) 30357
- [7] Rong Lin, *J. Phys. Chem. C* 128 (2024) 7661

# Wavelength-multiplexed full color 3D metasurface hologram made of silicon nitride

Tetsuhito Omori, Junpei Beppu, Masakazu Yamaguchi, Tamaki Onozawa, and Kentaro Iwami

Tokyo University of Agriculture and Technology

E-mail: omori@st.go.tuat.ac.jp

## 1. Introduction

Metasurface holograms, which enable a wide viewing angle and high resolution by using subwavelength-sized nanostructures, are expected to be applied to 3D displays<sup>[1]</sup>. In our previous studies, full-color 2D holograms<sup>[2]</sup> and large-area monochromatic 3D holograms<sup>[3]</sup> have been achieved. In this research, we have proposed a method to reproduce a full-color 3D image without misalignment by integrating the phase distribution of each RGB into a single hologram as a matrix of phase vectors  $\phi_{All} = (\phi_B, \phi_G, \phi_R)$  as shown in Fig. 1.

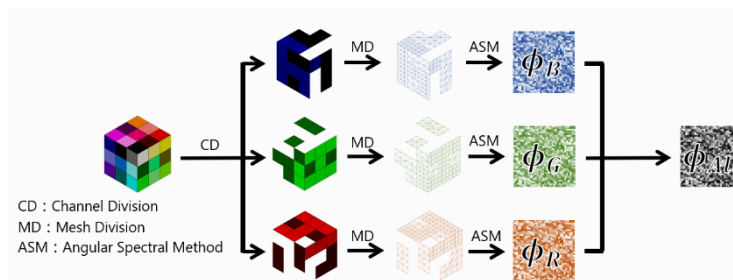


Fig. 1 Method for making holograms

## 2. Design and simulation

Silicon nitride (SiN) pillars with various cross-sectional shapes were adopted as meta-atoms. As shown in Fig. 1, first, the surfaces of an artificial 3D object was decomposed into each RGB color channels, and the intensity of each channel was converted to mesh density. Then, the phase distributions for each channel was calculated using the angular spectrum method. The propagation distance and the deflection angle were set to 10 mm and 20°, respectively, to prevent overlap with the conjugate image. Finally, meta-atoms that could reproduce the phase vector  $\phi_{All} = (\phi_B, \phi_G, \phi_R)$  were selected from the library with approximately 20,000 species using the least square errors method.

We then simulated the reproduction of a target image shown in Fig. 2. Simulation based on our meta-atom library with the phase coverage of Fig. 3(a) shows the limited color reproduction with a peak signal-to-noise ratio (PSNR) of 27.9 dB, as shown in Fig. 3(b). In order to obtain a high reproducibility with PSNR higher than 30 dB, we found that the uniformly-distributed phase vectors with at least  $12^3$  lattice points as shown in Fig. 4(a), which can reproduce the image as shown in Fig. 4(b) which was calculated by iterative Fourier transform. One possible method to achieve this is to introduce hole-shaped meta-atoms or meta-atoms using polarized light.

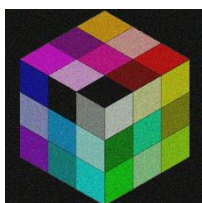


Fig. 2 Target image

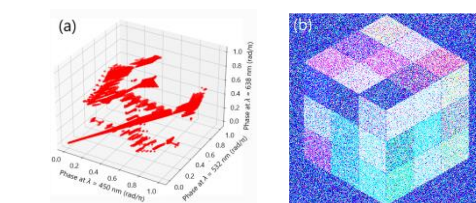


Fig. 3 (a) Phase coverage of our library, and (b) the reproduced image (PSNR = 27.9 dB) (brightness adjusted)

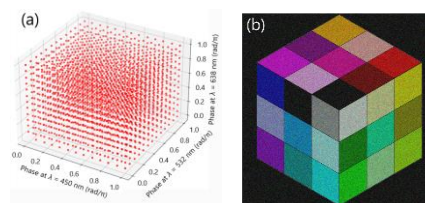


Fig. 4 (a) Uniformly-distributed library, and (b) the simulated image (PSNR = 30.2 dB)

## 3. Conclusion

In this study, full-color 3D metasurface holograms were designed and simulated. We will proceed with fabrication and evaluation, and aim to improve the reproducibility of the target by incorporating a new shape of meta-atoms to increase the coverage of the phase distribution.

## Acknowledgements

We would like to thank Prof. K. Matsushima, the developer of the "WaveField Library" used to calculate the phase distributions.

## References

- [1] L. Huang, S. Zhang, T. Zentgraf, "Metasurface holography: from fundamentals to applications", *Nanophotonics*, vol. 7, no. 6, pp. 1169-1190, 2018
- [2] M. Yamaguchi, H. Saito, S. Ikezawa, K. Iwami, "Highly-efficient full-color holographic movie based on silicon nitride metasurface", *Nanophotonics*, vol. 13, no. 8, pp. 1425-1433, 2024
- [3] T. Onozawa, J. Beppu, M. Yamaguchi, K. Iwami, "3D metasurface holograms of SiN for multicolor projection", *The 13<sup>th</sup> Advanced Lasers and Photon Sources*, 30-03, 2024



# A Cost-Effective, Flexible 1D Metasurface Absorber in the Infrared Region

Jhuma Pan<sup>1</sup>, Sachin Kumar Srivastava<sup>1, 2</sup>

<sup>1</sup> Department of Physics, Indian Institute of Technology Roorkee, Uttarakhand, India

<sup>2</sup> Centre for Photonics and Quantum Communication Technology, Indian Institute of Technology Roorkee, India  
E-mail: sachin.srivastava@ph.iitr.ac.in

## 1. Introduction

Metasurfaces are widely studied to enhance the light absorption in the infrared (IR) spectral regions for their significant importance in space, military and industry applications. Metasurfaces are composed of metal-dielectric structures with subwavelength geometrical parameters and possess the unique capability to manipulate electromagnetic waves in a desired manner. Plasmonic metasurface supports surface plasmon (SP) modes at metal-dielectric interface for the incoming radiation on the structure [1]. The reported IR absorbers utilized complex lithography techniques which increase the overall cost of the absorber. The fabrication of a low-cost, thin and flexible perfect IR absorber using techniques like e-beam lithography (EBL) is still challenging. This study reports an IR absorber based on the excitation of SP mode using an 1D metasurface structure, fabricated by nanoimprint lithography and physical vapor deposition (PVD).

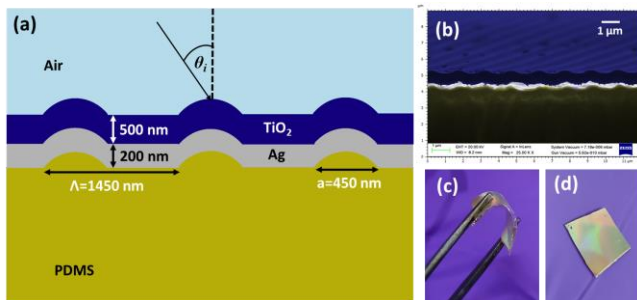


Fig. 1. (a) Schematic of the structure of IR metasurface absorber (b) FE-SEM image of the cross section of the metasurface absorber on a PDMS substrate (Scale bar= 1  $\mu$ m). Picture of (c) flexible metasurface absorber being held by a tweezer, (d) uniform and large-area fabricated absorber.

## 2. Results and Discussions

The metasurface structure consists of an 1D patterned polydimethylsiloxane (PDMS) substrate with a periodic bump of periodicity  $\Lambda=1450$  nm. The structure was obtained by templating the polymer over a compact disk (CD). The patterned PDMS substrate was further coated with a thin film of silver (Ag) of about 200 nm thickness, and a titanium dioxide ( $\text{TiO}_2$ ) film of 500 nm thickness using PVD technique. The use of PDMS substrate makes the absorber flexible. Fig.1a shows the schematic of the absorber which is illuminated by an incident light through air at an angle of incidence of  $\theta_i$ . A field emission scanning electron microscope (FE-SEM) image of the cross-sectional view of the metasurface absorber has been shown in Fig.1b. Ag and  $\text{TiO}_2$  layers are clearly visible. The reported thick-

nesses were cited from FE-SEM measurements only. A picture of the fabricated flexible absorber sample is shown in Fig.1c and fig.1d depicts its large area fabrication. The colors in the diffracted light confirm the formation of the nanopatterned structure on the metasurface.

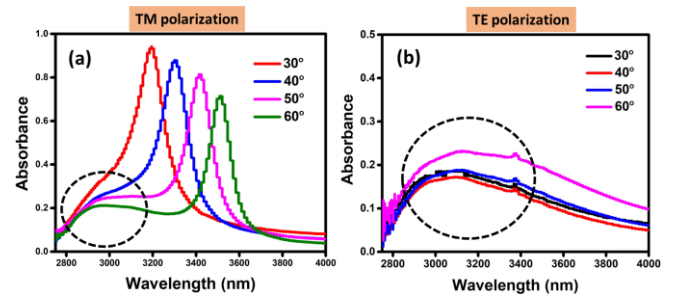


Fig. 2. Experimental absorbance spectra of the metasurface absorber for (a) TM polarized light and (b) TE polarized light at various angle of incidence.

The optical characterization was performed using a Fourier transform infra-red (FTIR) spectrometer equipped with a variable angle specular reflectance accessory and an IR polarizer. Fig.2a shows the measured absorbance spectra for transverse magnetically (TM) polarized light at varying  $\theta_i$ . Absorbance peak with 94% absorbance is obtained at  $\theta_i = 30^\circ$  and a red shift can be observed as the value of  $\theta_i$  increases from  $30^\circ$  to  $60^\circ$ . Fig.2b shows the absorbance spectra for transverse electrically (TE) polarized light at various  $\theta_i$ . A circle has been made around a small peak in both Fig.2a and 2b. This small absorbance peak is observed in case of both TM and TE polarized light but the large absorption peak is only present in Fig. 2a for the incidence of TM polarized light. Hence, it can be claimed that the high absorbance is attributed to the excitation of SP mode.

## 3. Conclusions

A plasmonic metasurface IR absorber with near unity absorbance at large angle of incidence has been demonstrated experimentally. It can be useful in many applications such as refractive index sensor, photodetector, optical filters etc.

## Acknowledgements

Funding from MoE-STARs and SERB-SRG grants and IIT Roorkee are thankfully acknowledged.

## References

- [1] D. Ray, TV Raziman, C. Santschi, D. Etezadi, H. Altug, O. J. Martin, Nano Letters 20 (2020), 8752-8759.

## Polyaniline coated U-bent Fiber Optic Aptasensor for Arsenite Detection in Environmental Matrices

Ashish Shukla<sup>#1</sup>, Tathagata Pal<sup>#1</sup>, Soumyo Mukherji<sup>1\*</sup>

<sup>1</sup> Department of Bioscience and Bioengineering, Indian Institute of Technology Bombay

<sup>#</sup> Authors contributed equally

\*Corresponding author e-mail: mukherji@iitb.ac.in

Arsenic has been a serious contaminant for decades now. Being the 20<sup>th</sup> most abundant element on the earth's crust[1], it is found in various organic and inorganic forms. The inorganic form arsenite is known to be the most hazardous to almost all DNA-based life forms[2]. Currently, multiple countries are affected by the elevated concentrations of arsenic contamination [3], [4].

Aptamer as a bio-receptor is a very selective, cost-efficient means for detecting small target analyte [5] such as arsenite oxyanion. Aptamers need certain conditions for their optimum operation. Optical-fiber-based sensors have various advantages such as high sensitivity, small size, lightweight, integration capability, immunity to electrical interference, etc. For absorbance-based fiber-optic sensing, the evanescent wave interaction at the core-cladding interface is a key parameter to achieve high sensitivity in the sensing probe. The cladding can be removed and replaced with the choice of target analyte. The evanescent wave interaction can be improved by bending the optical fiber core in a U shape. To further enhance the sensitivity, the bent fiber core can be coated with conductive polymer e.g., polyaniline. It has been claimed that polyaniline has interesting optical properties. When coated on optical fiber it positively influences evanescent wave-based absorbance in the slightest change of affinity-based interactions. Furthermore, Polyaniline has an immense number of amine groups for crosslinking bioreceptors. These properties lead to the increase of the sensitivity of the fiber-sensing probe significantly.

In the current work, we have developed an aptamer immobilized on a polyaniline-coated U-bent fiber-optic sensor (illustrated in Figure 1) for the detection of arsenite oxyanion in various environmental matrices. The synergistic combination of specificity from aptamer and sensitive combination of polyaniline coating and U-bent fiber gives the sensing probe its ability to detect arsenite in complex water matrices. For this study, the aptamer sequence H<sub>2</sub>N-(CH<sub>2</sub>)<sub>3</sub>-5'-(GT)<sub>21</sub>-3' was utilized as an arsenic-specific bio-receptor. Under the provided conditions, the arsenic-specific aptamer undergoes formation of tertiary structure that specifically binds to arsenite oxyanion. The optimization of aptamer folding conditions resulted in the sensitive binding of arsenite oxyanion. The aptamer was bound on the polyaniline-coated fiber probe by utilizing a homobifunctional group, glutaraldehyde. The exposed sites on the fiber core were also blocked away by utilizing hexylamine to avoid cross-sensitivity. The optimization of poly-

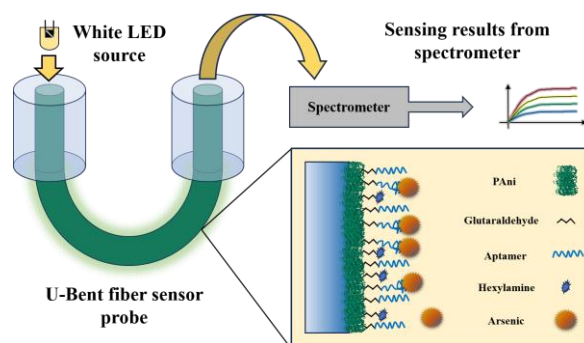


**Figure 1:** Schematics for the fiber-optic Aptamer based sensing scheme

aniline coating, glutaraldehyde binding and aptamer folding conditions was crucial to achieve the desired sensing results. We were able to get an experimental detection limit of arsenite to as low as 1 ppb in complex environment matrices such as lake water, tap water, etc. The sensing probe gave  $R^2 > 0.99$  and a linear range of operation in the range from 1 ppb to 1000 ppb (in log scale). The developed optical fiber aptasensor demonstrates great promise for widescale field deployable arsenic biosensing at low cost.

### References

- [1] W. R. Cullen and K. J. Reimer, "Arsenic Speciation in the Environment," *Chemical Reviews*, vol. 89, no. 4, pp. 713–764, 1989, doi: 10.1021/cr00094a002.
- [2] K. P. Raven, A. Jain, and R. H. Loeppert, "Arsenite and arsenate adsorption on ferrihydrite: Kinetics, equilibrium, and adsorption envelopes," *Environmental Science and Technology*, vol. 32, no. 3, pp. 344–349, 1998, doi: 10.1021/es970421p.
- [3] Natasha *et al.*, "Arsenic Environmental Contamination Status in South Asia," *Arsenic in Drinking Water and Food*. Springer Singapore, pp. 13–39, 2020, doi: 10.1007/978-981-13-8587-2\_2.
- [4] Y. H. T. Kohda *et al.*, "Arsenic uptake by *Pteris vittata* in a subarctic arsenic-contaminated agricultural field in Japan: An 8-year study," *Science of the Total Environment*, vol. 831, p. 154830, 2022, doi: 10.1016/j.scitotenv.2022.154830.
- [5] M. Kuwahara and N. Sugimoto, "Efficacy of Base-Modi fication on Target Binding of Small Molecule," *Journal of the American Chemical Society*, vol. 135, pp. 9412–9419, 2013.

**[17a-A34-1~9] 4.1 Plasmonics and Nanophotonics**

[17a-A34-1]

[JSAP-Optica Joint Symposia Invited Talk] Selective Accumulation of SERS Signal

○Yuika Saito<sup>1</sup>, Takahiro Kondo<sup>1</sup>, Kota Uchiyama<sup>1</sup> (1.Gakushuin Univ.)

[17a-A34-2]

[JSAP-Optica Joint Symposia Invited Talk] Contribution of sub-radiant plasmon resonance to surface-enhanced spectroscopy

○Tamitake Itoh<sup>1</sup>, Yuko S. Yamamoto<sup>2</sup> (1.AIST, 2.JAIST)

[17a-A34-3]

Optical chirality enhancement at the nanoscale using inversely-designed 3D nanogap antennas

○Atsushi Taguchi<sup>1</sup>, Keiji Sasaki<sup>1</sup> (1.Hokkaido Univ.)

[17a-A34-4]

Surface-enhanced Fluorescence by Mie Resonant Silicon Nanosphere Monolayer

○(M2)VU THI OANH<sup>1</sup>, HIROSHI SUGIMOTO<sup>1</sup>, MINORU FUJII<sup>1</sup> (1.Kobe Univ.)

[17a-A34-5]

SERS Detection of Chemical Reactions Induced by Optical Heat

○(D)Balaji Sanap<sup>1</sup>, Takuo Tanaka<sup>1,2</sup>, Taka-aki Yano<sup>1,2</sup> (1.Tokushima University, 2.RIKEN)

[17a-A34-6]

Bessel Beam-Instigated Two-Fold SERS Enhancement in AuNP Structures Compare to Drop Casting

○(D)Riya Choudhary<sup>1</sup>, Kaushal Vairagi<sup>2</sup>, Samir K. Mondal<sup>2</sup>, Sachin K. Srivastava<sup>1,3</sup> (1.Dept. of Physics, IIT Roorkee, 2.micro-NOC, CSIR-CSIO, 3.CPQCT, IIT Roorkee)

[17a-A34-7]

High-Sensitivity Plasmonic Sensors Probe for Uric Acid Detection using Surface Funtionalized Gold-Graphene Quantum Dotes stacked Nanocomposites

○AHMAD SHUKRI MUHAMMAD NOOR<sup>1,2</sup>, Olabisi Abdullahi Onifade<sup>1,2</sup>, Muhammad Hafiz Abu Bakar<sup>1,2</sup>, Mohd Adzir Mahdi<sup>1,2</sup> (1.Department of Computer and Communication Systems Engineering, Faculty of Engineering, Universiti Putra Malaysia, 2.Wireless and Photonics Research Centre of Excellence, Faculty of Engineering, Universiti Putra Malaysia)

[17a-A34-8]

Enhanced Red Emission in Europium-Doped Niobate Phosphors for High-Efficiency Warm White LEDs

○(DC)Kanishk Poria<sup>1</sup>, Nisha Deopa<sup>2</sup>, Jangvir Singh Shahi<sup>1</sup> (1.Panjab Univ., 2.Ch. Ranbir Singh Univ.)

[17a-A34-9]

Probing Forbidden Low-Frequency Raman Modes in MoS<sub>2</sub> via Plasmonic Nanoparticle○(D)Zhen Zong<sup>1</sup>, Ryosuke Morisaki<sup>1</sup>, Kanami Sugiyama<sup>2</sup>, Masahiro Higashi<sup>3</sup>, Takayuki Umakoshi<sup>1</sup>, Prabhat Verma<sup>1</sup> (1.Osaka Univ., 2.Kyoto Univ., 3.Nagoya Univ.)

## 表面増強ラマン散乱の選択的信号積算

### Selective Accumulation of SERS Signal

学習院大理<sup>1</sup> ○齊藤 結花<sup>1</sup>, 近藤 崇博<sup>1</sup>, 内山 高汰<sup>1</sup>

Gakushuin Univ.<sup>1</sup>, °Yuika Saito<sup>1</sup>, Takahiro Kondo<sup>1</sup>, Kota Uchiyama<sup>1</sup>

E-mail: yuika.saito@gakushuin.ac.jp

We developed a new method for obtaining surface-enhanced Raman scattering (SERS) spectra with extremely high sensitivity and spectral resolution[1]. In this method, thousands of SERS spectra are acquired, followed by a data selection procedure based on density-based spatial clustering of applications with noise (DBSCAN)[2]. Each spectrum is recorded by exposure with a single nanosecond laser pulse to avoid the effect of time averaging. The reconstructed spectrum consists of the data which belong to the clusters. The method was applied to a crystal violet (CV) aqueous solution  $10^{-7}$  mol/L.

#### Methods

The data selection using DBSCAN is firstly, thousands of SERS spectra were acquired, with each spectrum measured by a single-shot nanosecond laser pulse to avoid time averaging. Secondly, an intensity–wavelength plot (I–W plot) was constructed by extracting the data sets of the highest intensity and its pixel number from each SERS spectrum. Thirdly, we applied DBSCAN to the I–W plot to automatically

separate the signal (cluster) from the noise (non cluster).

DBSCAN process classify the high density of data points as a cluster, and the other part as a noise.

#### Results

Figure 1 shows the Raman spectra of CV, reconstructed by single-pulsed SERS with DBSCAN. The red line indicates the reconstructed spectrum obtained by DBSCAN, while the black line indicates the average of 10,000 single-pulsed spectra. For comparison, a spectrum of high-concentration CV solution ( $10^{-4}$  mol/L) is shown by the blue line. According to Figure 1, it can be observed that the reconstructed spectrum improved signal-to-noise ratio in comparison with the averaged spectrum. The peaks 751, 944, 977, 991  $\text{cm}^{-1}$  are clearly recognized in the red spectra, while in the black spectra, these peaks are difficult to see. Similarly, the peak at 1540 and 1562  $\text{cm}^{-1}$  is more easily observed in the red spectrum than in the black spectra. These results suggest that we successfully recovered all the Raman peaks found in the spectrum under high concentration.

#### References

- [1] Kondo T., Saito Y., *J. Phys. Chem. A* (2022); **126**, 1755-1760.
- [2] Ester, M.; Kriegel, H.-P.; J. Sander; X. Xu., *KDD-96 proceedings* (1996) 226–231.

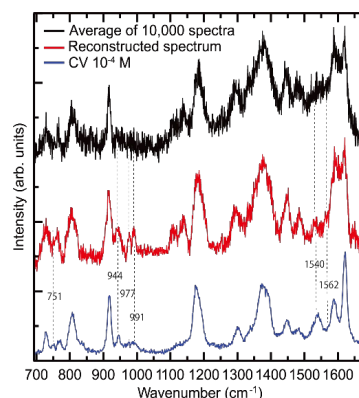


**Figure 1.** Reconstructed single-pulsed SERS spectra of  $10^{-7}$  mol/L CV (532 nm excitation). Red line: DBSCAN reconstruction, Black line: Average of all (10,000) spectra, Blue line: thick solution.

## 表面増強分光における準放射プラズモン共鳴の寄与

Contribution of sub-radiant plasmon resonance to surface-enhanced spectroscopy

産総研健医工<sup>1</sup>, 北陸先端大<sup>2</sup>, <sup>○</sup>伊藤 民武<sup>1</sup>, 山本 裕子<sup>2</sup>AIST<sup>1</sup>, JAIST<sup>2</sup>, <sup>○</sup>Tamitake Itoh<sup>1</sup>, Yuko S. Yamamoto<sup>2</sup>

E-mail: tamitake-itou@aist.go.jp

The electromagnetic (EM) mechanisms of surface-enhanced spectroscopy e.g. surface-enhanced Raman scattering (SERS) and surface-enhanced fluorescence (SEF) have been examined using superradiant plasmon resonance, such as the dipole or dipole–dipole (DD) coupled plasmon resonance localized at the gaps between small and symmetric metallic nanoparticle (NP) dimers [1]. The large EM enhancement of DD-coupled resonance at the gaps, namely hotspots (HSs), has received considerable attention because HSs exhibit exotic phenomena such as cw laser excited nonlinear emissions, ultrafast SEF, vibrational pumping, and the field gradient effect [2]. Furthermore, the EM coupling energy between DD-coupled plasmons and a molecular excitons at the HSs exceeds several hundred millielectronvolts, resulting in new physics and chemistry e.g. strong coupling, molecular optomechanics, and polariton chemistry [2,3].

However, higher-order plasmon resonance, such as the dipole–quadrupole (DQ) coupled plasmon resonance, which is subradiant, mainly determines the EM enhancement for large or asymmetric NP systems. Thus, clarifying the contribution of the subradiant resonance to EM enhancement is important for evaluating various plasmonic systems for SERS related spectroscopies and phenomena [4-7].

First, the contribution of DQ coupled plasmon resonance to EM enhancement is explained using the spectral uncorrelation between the experimentally obtained SERS with ultrafast SEF and the Rayleigh scattering spectra of silver NP dimers [4]. Second, the radiation properties of the SERS light generated by the DQ coupled resonance were determined through EM calculations [5]. Third, the importance of absorption spectroscopy in the evaluation of DQ coupled resonance is clarified based on quantum optics [6]. Finally, we introduce a method to directly evaluate the EM enhancement factors induced by DQ coupled resonance using ultrafast SEF [7].

**References**

- [1] T. Itoh, Y. S. Yamamoto, and Y. Ozaki, *Chem. Soc. Rev.* 2017, **46**, 3904-3921.
- [2] T. Itoh, M. Prochazka, Z.-C. Dong, W. Ji, Y. S. Yamamoto, Y. Zhang, and Y. Ozaki, *Chem. Rev.* 2023, **123**, 1552-1634.
- [3] T. Itoh, and Y. S. Yamamoto, *Nanoscale* 2021, **13**, 1566-1580.
- [4] T. Itoh, and Y. S. Yamamoto, *J. Phys. Chem. C* 2023, **127**, 5886–5897.
- [5] T. Itoh, and Y. S. Yamamoto, *J. Phys. Chem. B* 2023, **127**, 4666-4675.
- [6] T. Itoh, and Y. S. Yamamoto, *J. Chem. Phys.* 2023, **159**, 2 034709.
- [7] T. Itoh, and Y. S. Yamamoto, *J. Chem. Phys.* 2024, **160**, 024703.



# Optical chirality enhancement at the nanoscale using inversely-designed 3D nanogap antennas

Hokkaido Univ.<sup>1</sup>, <sup>○</sup>Atsushi Taguchi<sup>1</sup>, Keiji Sasaki<sup>1</sup>

E-mail: taguchi@es.hokudai.ac.jp

We present a 3D nanogap antenna with a high chiral dissymmetry—the field intensity at the nanogap is high for a particular handedness of circularly polarized incident light while not for the other[1]. The antenna structure was found using a computational inverse design technique called topology optimization. With circularly polarized incident light implemented into the algorithm, a spiral structure was created that is too complex to attain by human intuition or imagination. We calculated the near-field intensity at the nanogap of the structure, and the resultant dissymmetry factor was as high as 1.40. We also found a 50-fold enhancement of the optical chirality within the nanogap compared to that of the circularly polarized plane wave propagating in the free space. The chirality enhancement was elucidated with a fluid model of the chirality flux within the 3D nanoantenna, which is then correlated to light's spin angular momentum (SAM). This finding can be a novel design strategy to enhance optical chirality density at the nanoscale using nanophotonic structures, potentially revolutionizing the field of nanophotonics and plasmonics.

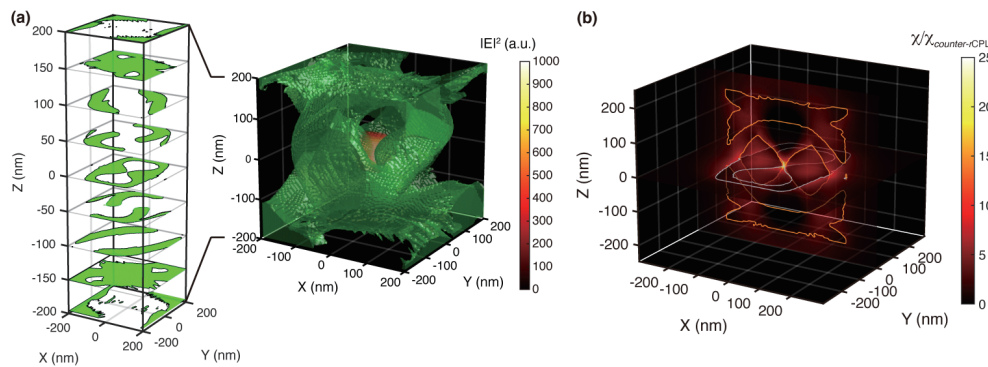


Figure 1: (a) A 3D-rendered model of the topology-designed structure (right) and Z-sliced sections at a 50-nm interval (left). The structures were optimized for a counter-propagating circularly polarized light traveling along the Z axis. The electric field intensity distribution is overlaid in the right panel. The material is  $\text{TiO}_2$ . (b) Optical chirality density,  $\chi$ , normalized to that without the structure, displayed at planes  $Z = 0$  nm and  $Y = 0$  nm.

## References

- [1] A. Taguchi, *et al.*, arXiv:2402.10742 [physics.optics].

# Surface-enhanced Fluorescence by Mie Resonant Silicon Nanosphere Monolayer

Kobe Univ<sup>1</sup>, <sup>°</sup>(M2) Vu Thi Oanh<sup>1</sup>, Hiroshi Sugimoto<sup>1</sup>, Minoru Fujii<sup>1</sup>

E-mail: sugimoto@eedept.kobe-u.ac.jp

Surface-enhanced fluorescence (SEF) biosensors are vital for biomedical applications due to their exceptional sensitivity, enabling rapid and precise analyses. Compared to plasmonic resonators suffering from high Ohmic losses, dielectric Mie resonators exhibit lower losses and higher Q resonances. As a dielectric Mie resonator, silicon (Si) nanosphere (NS) with diameters of 100–250 nm is an almost ideal candidate for SEF biosensors due to their strong Mie resonances in the range of visible to near-infrared wavelengths. So far, Si nanostructure arrays have been fabricated with high precision by using electron-beam lithography on a solid substrate. However, it is challenging to create arrays larger than a millimeter scale for naked-eye readable biosensors.

In this work, the monolayers of Si NS with diameters of 100 to 250 nm [1] developed in our group are studied for a surface-enhanced fluorescence biosensor platform. Figure 1a shows the photographs of the monolayers fabricated by drop-casting colloidal Si NSs with different average diameters onto amino-modified SiO<sub>2</sub> substrates (1 cm × 1 cm). The filling factor is fixed to ~60% for all the samples. Figure 1b shows the corresponding reflectance spectra, demonstrating the size-tunable Mie resonance peaks at 430 to 800 nm. The fabricated Si NS monolayer substrates were functionalized with fluorophores (Lucifer Yellow) and the fluorescence properties were studied under an optical microscope (Fig. 2a). The averaged fluorescence spectrum obtained from 100 different spots of the monolayer with the average Si NS diameter of 128.7 nm (Fig. 2) shows about 14-fold enhancement with respect to that of the reference. In the presentation, from the comparison with the calculation results, we will discuss the size dependence of the fluorescence enhancement factor in detail.

[1] Tanaka, H et al. *ACS Appl Nano Mater* 7, 2605–2613 (2024).

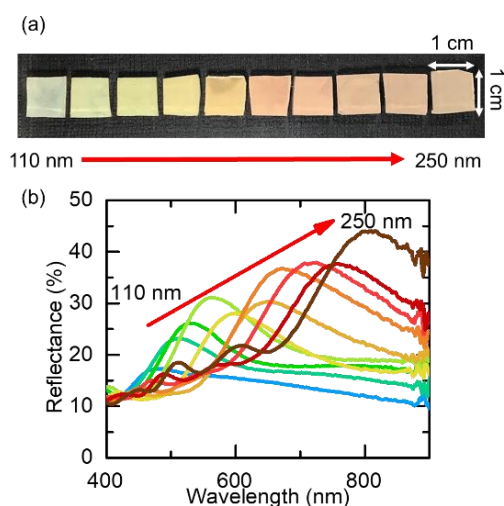


**Fig. 1** (a) Photographs and (b) reflectance spectra of Si NS monolayer with different average diameters.

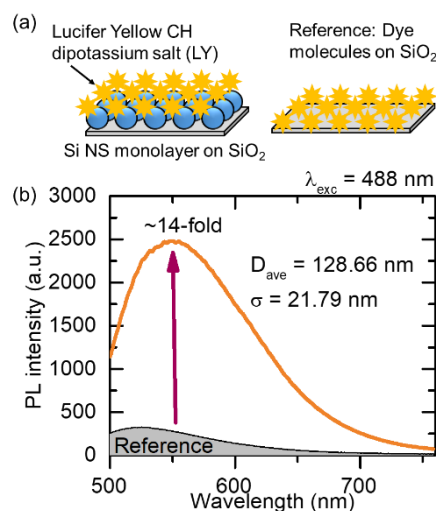


**Fig. 2** (a) Illustration of dye molecules attached on the top of a Si NS monolayer and a SiO<sub>2</sub> substrate. (b) Photoluminescence spectra of dye molecules on a Si NS monolayer and a SiO<sub>2</sub>.

## SERS Detection of Chemical Reactions Induced by Optical Heat

Tokushima Univ.<sup>1</sup>, RIKEN<sup>2</sup>, °Balaji Sanap<sup>1</sup>, Takuo Tanaka<sup>1,2</sup>, Taka-aki Yano<sup>1,2</sup>

E-mail: yano.takaaki@tokushima-u.ac.jp

Surface Enhanced Raman Scattering (SERS) is a powerful technique that enables molecular fingerprint-based ultra-sensitive detection through an enhanced electromagnetic field generated by plasmonic metal nanoparticles. This technique has found extensive use in various fields, including chemical sensing, biological imaging, and photochemical reactions, due to its ability to enhance reaction rates and decrease energy barriers at the nanoscale.

In this study, we demonstrated SERS detection of a chemical reaction induced by optical heat generated in the vicinity of plasmonic nanoparticles and substrates. As schematically shown in Fig. 1(a), the generated heat facilitates an interaction between the amine group ( $-\text{NH}_2$ ) of 4-aminothiophenol adsorbed on the smooth Ag metallic surface and the carboxylic acid ( $-\text{COOH}$ ) of 4-mercaptobenzoic acid adsorbed on the Au nanoparticle. This interaction leads to the formation of an amide bond through dehydration, identified by the new appearance of specific vibrational peaks. Notably, a newly appeared vibrational mode at  $521\text{ cm}^{-1}$ , indicated by the arrow in the SERS spectrum (Fig. 1(b)), was observed. According to quantum chemical simulation based on density functional theory, this peak is attributed to the bending between the nitrogen and hydrogen of the amide group. The simulations also indicate that the vibration of the  $\text{C}=\text{O}$  bond shifted to a lower wavenumber region due to the formation of the amide bond.

These findings highlight the potential of using SERS to monitor chemical reactions at the molecular level, providing insights into reaction mechanisms facilitated by plasmonic nanostructures. Further research may explore the applications of this technique in other types of chemical reactions and its integration with other analytical methods.

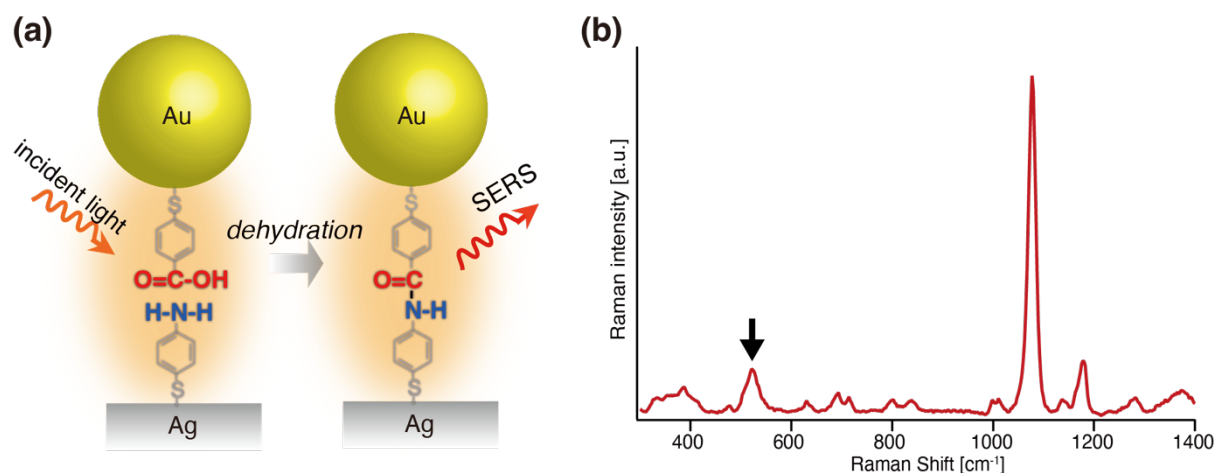


Figure 1: (a) Schematic of chemical reaction (amide bond formation) through optical heat generated between a plasmonic nanoparticle and substrate, (b) the corresponding SERS spectrum.

# Bessel Beam-Instigated Two-Fold SERS Enhancement in AuNP Structures Compare to Drop Casting

Riya Choudhary<sup>1</sup>, Kaushal Vairagi<sup>2</sup>, Samir K. Mondal<sup>2</sup>, Sachin K. Srivastava<sup>1,3</sup>

<sup>1</sup> Department of Physics, Indian Institute of Technology Roorkee, Roorkee- 247667, India

<sup>2</sup>  $\mu$ -NOC, CSIR-CSIO, Chandigarh-160030, India

<sup>3</sup> CPQCT, Indian Institute of Technology Roorkee, India

E-mail: sachin.srivastava@ph.iitr.ac.in

## 1. Introduction

Since the discovery of SERS, due to its high sensitivity, it has been widely used in various fields such as biosensing, chemical sensing, and food safety etc., [1]. In SERS, when a probe molecule is placed near a metallic nanostructure it feels a localized field generated due to localized surface plasmons (LSPs) which effectively amplifies its Raman signal. The LSPs are the collective oscillation of free electrons in metallic nanostructures [2]. For the fabrication of the SERS active substrates various methods have been introduced to arrange the metallic nanoparticles (NPs) in specific morphologies and arrangements [3]. Optical forces of a laser beam can be employed to arrange metallic NPs efficiently on a substrate [4].

## 2. Results and discussions

In Fig.1(a-d), scanning electron microscope (SEM) image of the axicon tip, microscopic image of Bessel beam, SEM images of gold (Au) NPs dried with Bessel beam and without illumination of light are shown respectively. AuNPs dried with Bessel beam illumination are arranged in the Bessel beam rings, while AuNPs were drop cast and dried without illumination of light are agglomerated as can be seen from SEM images in Fig.1 (d). The Raman spectra has been recorded with a fiber optic Raman probe coupled to laser of excitation wavelength 785 nm. The recorded Raman spectra of R6G on coverslip is shown in Fig.2 (a) in a absence of AuNPs, in presence of AuNPs with Bessel beam

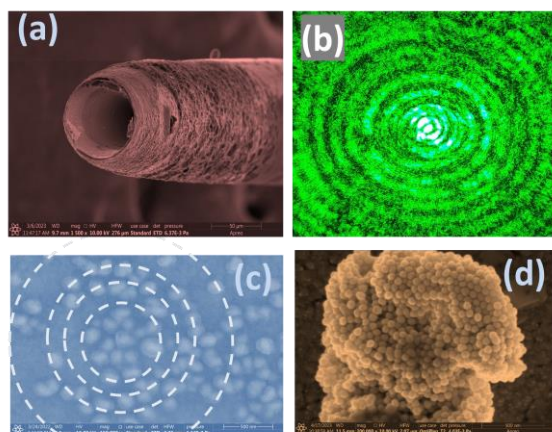


Fig.1. (a) SEM image of axicon tip, (b) microscopic image of Bessel beam, SEM image of AuNPs dried (c) with Bessel beam illumination, and (d) without illumination of light.

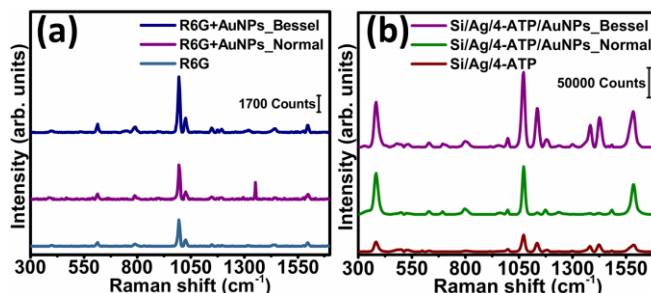


Fig.2. SERS spectra of (a) R6G in transmission mode (b) 4-ATP in reflection mode.

illumination and without illumination of light. It can be seen clearly from the figure that in presence of AuNPs, Raman signal enhances even if there is no illumination of light but the enhancement in Raman signal increases when we illuminate with Bessel beam. In Fig.2 (b), the Raman spectra recorded for 4-ATP molecule on reflecting substrate (Si/Ag substrate) is shown for Bessel beam illumination, without illumination of light and without AuNPs. It can be seen from the figure that there is more enhancement in Raman signal of 4-ATP molecule in case of Bessel beam illumination on reflecting substrate similar to transmitting substrate.

## 3. Conclusions

We have shown 2-fold enhancement in SERS signal of R6G and 4-ATP molecules on transmitting and reflecting substrates respectively with Bessel beam illumination as compared to without illumination of light (drop casting method).

## Acknowledgements

We would like to express sincere thanks to MoE-STARs, DST-BDTD, and IIT Roorkee. Riya Choudhary thanks to Council of Scientific & Industrial Research (CSIR) -India for fellowship.

## References

- [1] J. Langer et al., ACS Nano **14** (2020) 28.
- [2] M. Pelton, and G. Bryant, Hoboken, NJ, John Wiley & Sons, 2013.
- [3] J. Dong et al., Opt. Express **31** (2023) 21225.
- [4] R. Choudhary et al., J. Appl. Phys. **135** (2024) 073104.

## High-Sensitivity Plasmonic Sensors Probe for Uric Acid Detection using Surface Funtionalized Gold-Graphene Quantum Dots stacked Nanocomposites

Department of Computer and Communication Systems Engineering, Faculty of Engineering,  
Universiti Putra Malaysia, Wireless and Photonics Network Research Centre of Excellence,  
Faculty of Engineering, Universiti Putra Malaysia<sup>2</sup>

°Ahmad Shukri Muhammad Noor<sup>1,2</sup>, Olabisi Abdullahi Onifade<sup>1,2</sup>, Muhammad Hafiz Abu Bakar<sup>1,2</sup>,  
Mohd Adzir Mahdi<sup>1,2</sup>  
E-mail: ashukri@upm.edu.my

This study introduces a surface-functionalized sensor probe incorporating 3-aminopropyltriethoxysilane (APTES) self-assembled monolayers (SAM) on a Kretschmann-configured plasmonic sensor. The probe employs stacked nanocomposites of gold deposited through sputtering and graphene quantum dots (GQD) deposited via spinning, enabling highly sensitive and accurate uric acid (UA) detection within the physiologically relevant concentration range. Comprehensive characterization of the sensor probe was conducted and validated through field emission scanning electron microscopy (FESEM), energy-dispersive X-ray spectroscopy (EDX), and Fourier transform infrared spectroscopy (FTIR) techniques. Surface functionalization yielded a 60.64% increase in sensitivity for the sensor probe, resulting in values of  $0.0221^{\circ}/(\text{mg/dL})$  for gold-GQD probe and  $0.0355^{\circ}/(\text{mg/dL})$  for gold-APTES-GQD probe, accompanied by linear correlation coefficients of 0.8249 and 0.8509, respectively. The highest sensitivity achieved was  $0.0706^{\circ}/(\text{mg/dL})$ , exhibiting a linear correlation coefficient of 0.993 and a low limit of detection (LOD) of 0.2 mg/dL. Furthermore, surface functionalization significantly enhanced binding affinity, as evidenced by Langmuir constants of  $14.29 \mu\text{M}^{-1}$  for the gold-GQD probe and  $0.0001 \mu\text{M}^{-1}$  for the gold-APTES-GQD, probe representing a remarkable 142,900-fold increase. The functionalized sensor probe demonstrated notable reproducibility and repeatability, with relative standard deviations of 0.166% and 0.013%, respectively, along with exceptional temporal stability of 99.66%. These findings represent a transformative leap in plasmonic UA sensors, delivering a marked enhancement in precision, reliability and substantial increase in sensitivity.

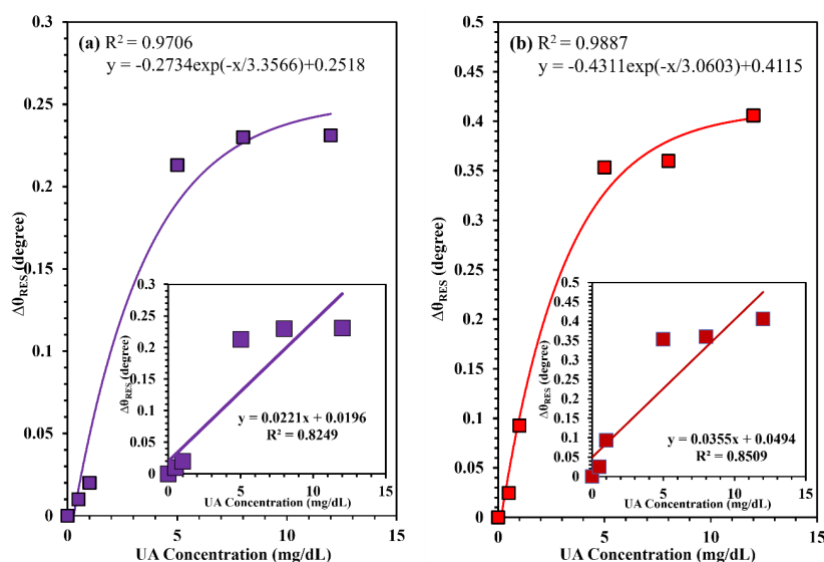


Figure 1: Fitting curves and linearity plots for (a) gold-GQD sensor probe at 60 nm configuration exhibits a sensitivity of  $0.0221^{\circ}/(\text{mg/dL})$  and (b) gold-APTES-GQD sensor probe at 60 nm configuration boasts a higher sensitivity of  $0.0355^{\circ}/(\text{mg/dL})$

### References

1. O.A. Onifade, Z.-H.M. Zin, M.H.B.A. Bakar, M.T. Alresheedi, M.A. Bin Mahdi, A.S.M. Noor, Salivary Uric Acid Detection With Graphene-Gold Bilayers Surface Plasmon Resonance, IEEE Sens J. (2023) 1–1. <https://doi.org/10.1109/JSEN.2023.3319702>.
2. D. Dey, T. Goswami, Optical biosensors: A revolution towards quantum nanoscale electronics device fabrication, J Biomed Biotechnol. 2011 (2011). <https://doi.org/10.1155/2011/348218>.



# Enhanced Red Emission in Europium-Doped Niobate Phosphors for High-Efficiency Warm White LEDs

Kanishk Poria<sup>1</sup>, Nisha Deopa<sup>2</sup>, Jangvir Singh Shahi<sup>1</sup>

<sup>1</sup>Department of Physics, Panjab University, Chandigarh-160014, India

<sup>2</sup>Department of Physics, Chaudhary Ranbir University, Jind-126102, India

E-mail: kanishk.chaudhary15@gmail.com

## 1. Introduction

Rare-earth doped crystalline materials are of significant interest for photonic and optoelectronic applications, particularly in phosphor-converted white-light-emitting diodes (pc-WLEDs), which offer high brightness, energy efficiency, compact size, durability, and environmental friendliness. However, pc-WLEDs lack a red color component. To address this, europium-doped niobate-based phosphors were synthesized using a high-temperature solid-state reaction technique at 1300°C[1].

## 2 Results and Discussions

The XRD patterns of both undoped and Eu-doped phosphors showed excellent crystallinity and phase purity, with diffraction peaks matching the standard JCPDS data, indicating that  $\text{Eu}^{3+}$  ions did not alter the tetragonal tungsten bronze (TTB) structure. Photoluminescence excitation (PLE) spectra for  $\text{Eu}^{3+}$ -doped niobate phosphors across various concentrations (1.0-10.0 mol%) revealed efficient excitation at 392 nm (near-UV) and 466 nm (blue). Photoluminescence (PL) spectra under 392 nm excitation displayed five main emission peaks (550-700 nm), with the optimal  $\text{Eu}^{3+}$  concentration at 9.0 mol% to avoid quenching. The internal quantum yield (IQE) measures the efficiency of converting electrical power into optical power for a phosphor, with IQE representing the ratio of emitted to absorbed photons and external quantum efficiency (EQE) representing the ratio of emitted to incident photons. For optimal  $\text{Eu}^{3+}$ -doped phosphor, IQE, absorption efficiency, and EQE under 392 nm excitation are more than 90%, 60%, and 55%, respectively. These high values, along with color coordinates close to standard red phosphors, indicate their potential for use in warm white LEDs.

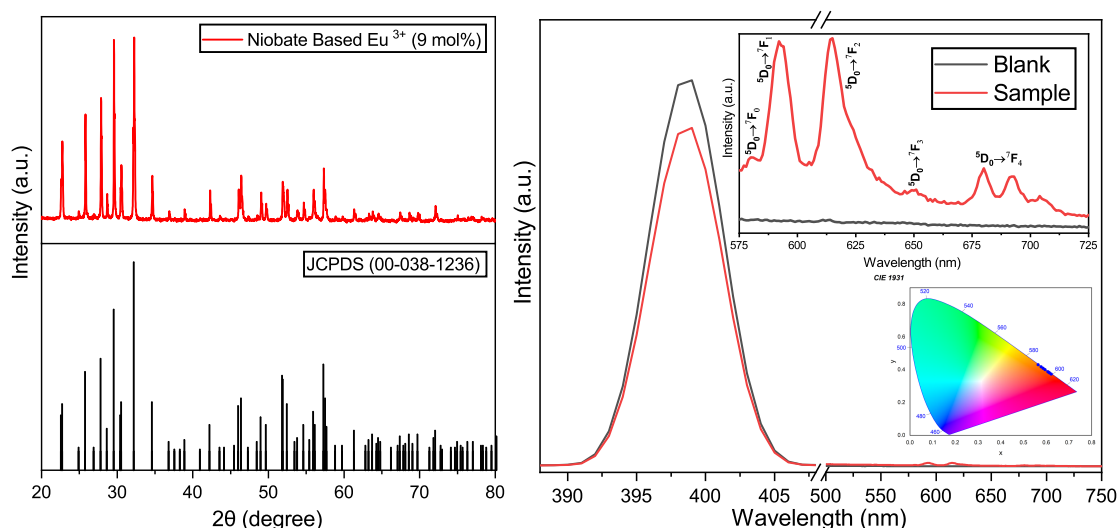


Figure 1: (a) XRD pattern for JCPDS and optimal phosphor. (b) Enhanced internal quantum yield for optimal phosphor (Inset: CIE chromaticity diagram)

- [1] Poria K, Lohan R, Bhatia S, Kumar A, Singh R, Deopa N, Punia R, Shahi JS, Rao AS., "Lumino-structural properties of  $\text{Dy}^{3+}$  activated  $\text{Na}_3\text{Ba}_2\text{LaNb}_{10}\text{O}_{30}$  phosphors with enhanced internal quantum yield for w-LEDs", RSC adv. **13** 11557-68 (2023).

# Probing Forbidden Low-Frequency Raman Modes in MoS<sub>2</sub> via Plasmonic Nanoparticle

Zhen Zong<sup>1</sup>, Ryosuke Morisaki<sup>1</sup>, Kanami Sugiyama<sup>2</sup>, Masahiro Higashi<sup>3</sup>, Takayuki Umakoshi<sup>1,4</sup>, Prabhat Verma<sup>1</sup>

<sup>1</sup> Dept. of Applied Physics, Osaka Univ., <sup>2</sup> Dept. of Molecular Engineering, Kyoto Univ., <sup>3</sup> Dept. of Complex Systems Science, Nagoya Univ., <sup>4</sup> Institute of Advanced Co-Creation Studies, Osaka Univ.

E-mail : verma@ap.eng.osaka-u.ac.jp

## 1. Introduction

Interlayer interaction through the van der Waals forces in two-dimensional (2D) materials like molybdenum disulfide (MoS<sub>2</sub>) determine most of the layer properties, which shows up as low-frequency modes (less than 50 cm<sup>-1</sup>) in Raman scattering. But the weak low-frequency signals are often obscured by background noise, requiring enhancement techniques [1]. Furthermore, detecting forbidden low-frequency Raman modes poses additional challenges. These modes, suppressed by symmetry selection rules, provide important information into molecular structures and electronic properties but are not observed in conventional Raman spectroscopy as they are symmetry forbidden. Our approach can detect forbidden low-frequency modes and achieve high-sensitivity through low-frequency surface-enhanced Raman spectroscopy (LF-SERS).

## 2. Result and discussion

We utilize silver nanoparticles to detect forbidden low-frequency Raman modes in MoS<sub>2</sub> by breaking the selection rules. The strong gradient of near-field light with sharply varying intensity within a nanometric volume near the nanoparticle causes selective symmetry breaking as shown in Fig.1. This breaks the Raman selection rules, allowing the observation of vibration patterns that are forbidden in Raman spectroscopy [2].

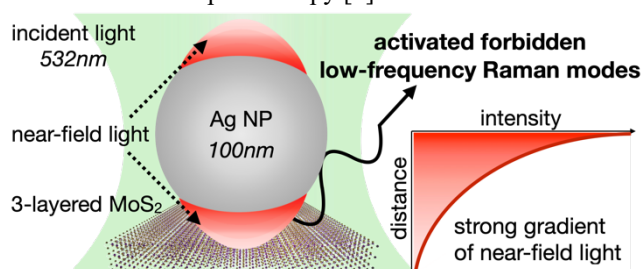


Figure 1. Gradient near-field light in the vicinity of a nanoparticle.

We used 3-layered MoS<sub>2</sub> as the sample and placed silver nanoparticles on its surface. We measured a LF-SERS image constructed with its breathing and shear modes at 28 cm<sup>-1</sup> and observed high-intensity Raman signals only around the nanoparticle, as shown by the bright areas in Fig. 2(a). MoS<sub>2</sub> has four vibration modes in the low-frequency range: the breathing and the shear modes, both appearing at 28 cm<sup>-1</sup>, are Raman-active, while the E'' (15 cm<sup>-1</sup>) and A<sub>2</sub>' (46 cm<sup>-1</sup>) modes are forbidden in Raman scattering. The forbidden Raman modes can only be activated near an iso-

lated single particle as seen in Fig. 2(b). An AFM image and a SERS image from one of the isolated single particles are shown in Figs. 2(c) and 2(d), respectively. We demonstrate how LF-SERS changes with the gradient near-field light around this nanoparticle, which are measured from the points marked in Fig. 2(d). The forbidden Raman modes only appear in region with a strong gradient, as shown in the spectrum by the blue areas in Fig.2(e).

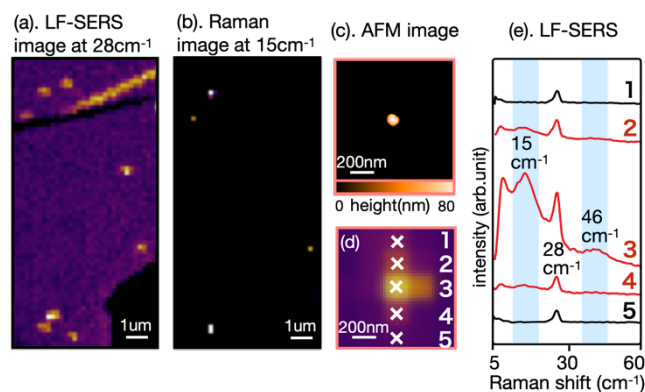


Figure 2. Forbidden LF-SERS image and spectrum.

To confirm our experimental results, we used calculations based on the density functional theory (DFT) to simulate Raman spectrum of a 3-layered MoS<sub>2</sub>. Our simulations confirm the existence of forbidden Raman modes in MoS<sub>2</sub>, with the vibration modes calculated by DFT matching the two forbidden Raman peaks detected in our experiments. Without the silver nanoparticles, these vibration modes are present but have zero intensity, indicating they are Raman-forbidden. The DFT calculations further reveal that the activation of these modes is not only due to the strong gradient near-field light but also involves physical contact deformation and charge transfer between the MoS<sub>2</sub> and the silver nanoparticles.

## 3. Conclusions

Our technique enables the first observation of LF-SERS and plasmonically activated forbidden low-frequency Raman modes in MoS<sub>2</sub>, providing more information into the material's vibrational properties and advancing material characterization methods.

## References

- [1] P. Verma et al., Sci Rep 10, 21227 (2020).
- [2] K. Ikeda et al., J. Am. Chem. Soc. 135 (2013).

4 JSAP-Optica Joint Symposia 2024 | 一般セッション(口頭講演) : 4.2 Photonics Devices, Photonic Integrated Circuit and Silicon Photonics

## **[17p-A25-2~11] 4.2 Photonics Devices, Photonic Integrated Circuit and Silicon Photonics**

[17p-A25-2]

[JSAP-Optica Joint Symposia Invited Talk] Integrated photonics for quantum computation

○Nobuyuki Matsuda<sup>1</sup> (1.Tohoku Univ.)

---

[17p-A25-3]

Performant Thin-Film Lithium Niobate Polarizer with an S-bend waveguide

○(M2)Fengyang Jin<sup>1,3</sup>, Tingting Lang<sup>2</sup>, Xiaowei Guan<sup>3</sup> (1.China Jiliang Univ., 2.ZJ Sci.&Tech Univ., 3.Jiaxing Inst. ZJU)

---

[17p-A25-4]

Modelling of CO<sub>2</sub> Gas Sensing using Spectral Envelope of Sol Integrated Racetrack Resonator

○(DC)Shalini Vardhan<sup>1</sup>, Naveen Kumar Gupta<sup>2</sup>, Aditya Kushwaha<sup>1</sup>, Priyanka Verma<sup>1</sup>, Ritu Raj Singh<sup>1</sup> (1.Netaji Subhas University of Technology, Dwarka, Sector-3, Delhi-110078, India, 2.Indian Institute of Information Technology, Ranchi- 831014, India)

---

[17p-A25-5]

Analysis of Ring Radius and Q-Factor for Enhanced Bandpass Filter performance in Racetrack Ring Resonators

○(DC)Shalini Vardhan<sup>2</sup>, Naveen Kumar Gupta<sup>1</sup>, Ritu Raj Singh<sup>2</sup> (1.IIT Ranchi- 831014, India, 2.NSUT, Delhi-110078, India)

---

[17p-A25-6]

[JSAP-Optica Joint Symposia Invited Talk] Diffraction-based on-chip optical neural network with high computational density

○Wencan Liu<sup>1</sup>, Yuyao Huang<sup>1</sup>, Run Sun<sup>1</sup>, Tingzhao Fu<sup>2</sup>, Hongwei Chen<sup>1</sup> (1.Tsinghua Univ., 2.National Univ. of Defense Technology)

---

[17p-A25-7]

[JSAP-Optica Joint Symposia Invited Talk] Two-Dimensional Broadband Silicon Optical Beam Scanning Device for Free-Space Optical Communication

○Yuki Atsumi<sup>1</sup>, Tomoya Yoshida<sup>1</sup>, Ryosuke Matsumoto<sup>1</sup>, Ryotaro Konoike<sup>1</sup>, Kazuhiro Ikeda<sup>1</sup>, Takashi Inoue<sup>1</sup>, Keihiro Suzuki<sup>1</sup> (1.AIST)

---

[17p-A25-8]

Cascading meta-devices for advanced functions and applications

○Jingcheng Zhang<sup>1</sup>, Din Ping Tsai<sup>1</sup> (1.CityU)

---

[17p-A25-9]

On-Chip Terahertz Polarization Control Enabled by Effective Medium

○(P)Weijie Gao<sup>1</sup>, Withawat Withayachumnankul<sup>2</sup>, Masayuki Fujita<sup>1</sup> (1.Osaka Univ., 2.Univ. Adelaide)

---

[17p-A25-10]

Multiband Frequency-Tunable Millimeter-Wave Absorber

A. Shahzad<sup>1</sup>, S. Ahmed<sup>1</sup>, Q. A. Naqvi<sup>1</sup>, Pankaj Kumar Choudhury<sup>2</sup> (1.Quaid-i-Azam Univ.,  
2.Zhejiang University)

---

[17p-A25-11]

Mode Switching in Few-Mode Fibers Using Electric Field Controlled Dynamic Offset Coupling

○(D)Isha Sharma<sup>1</sup>, Partha Roy Chaudhuri<sup>1</sup> (1.IIT Kharagpur)

---

# Performant Thin-Film Lithium Niobate Polarizer with an S-bend waveguide

Fengyang Jin<sup>1,3</sup>, Tingting Lang<sup>2</sup> and Xiaowei Guan<sup>3</sup>

<sup>1</sup> College of Optical and Electronic Technology, China Jiliang University, Hangzhou 310018, China, <sup>2</sup> School of Information and Electronic Engineering, Zhejiang University of Science and Technology, Hangzhou 310023, China, <sup>3</sup> Jiaxing Research Institute, Zhejiang University Jiaxing Key Laboratory of Photonic Sensing & Intelligent Imaging, Intelligent Optics and Photonics Research Center, Jiaxing Research Institute, Zhejiang University, Jiaxing 314000, China  
E-mail: guanxw@zju.edu.cn

## 1. Introduction

Thin-film lithium niobate (TFLN) is currently emerging as a popular photonic integration circuit (PIC) platform for its versatile material superiorities<sup>[1]</sup>. Diverse performant devices have been demonstrated in the TFLN PICs, such as modulators<sup>[2]</sup> and passive devices<sup>[3]</sup>. While polarizer is a fundamental building block for the PICs, it is not a trivial to realize it in the TFLN PICs attributed to the birefringence of the material (X-cut TFLN) and the temporarily unavoidable slant sidewalls of the TFLN waveguide. TFLN waveguide polarizers have been experimentally realized using long period gratings<sup>[4]</sup> or Eule bends<sup>[5]</sup> showing extinction ratios (ERs) of  $\sim 20$  dB and losses of  $\sim 1.5$  dB. In this work, we demonstrate TFLN polarizers using an S-bend waveguide where TM modes are leaked out, exhibiting ERs  $\sim 50$  dB and losses  $\sim 0.4$  dB.

## 2. Design and measurement

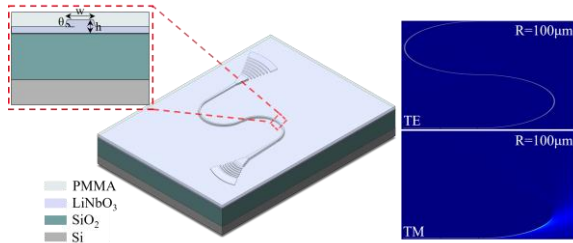


Fig. 2. 3D schematic of the proposed TFLN polarizer using an S-bend waveguide. Insets are for light propagations.

illustrates the structure of the proposed TFLN polarizer, where the commonly used ridge TFLN waveguide is employed with both the slab and ridge parts being 150 nm thick. The waveguide is initially tapered down from a 1.5- $\mu$ m width to a 0.6- $\mu$ m width and then successively connected to two 180° bend waveguides. As the transverse-magnetic (TM) mode is weakly confined in the 0.6- $\mu$ m-wide TFLN waveguide, it is easily leaked out to the silica substrate and the PMMA cladding. However, the transverse-electric (TE) mode can transmit through the S-bend waveguide with low loss. By adjusting the widths and the bending radii of the S-bend waveguide, it is possible to achieve TE-pass polarizers with large ERs and low losses.

As depicted in Fig. 2, FDTD simulations suggest that with a sufficiently large bending radius (e.g.,  $>40$   $\mu$ m), the polarizer's TE mode loss can be negligible. Conversely, the TM mode experiences increasing loss with larger bending

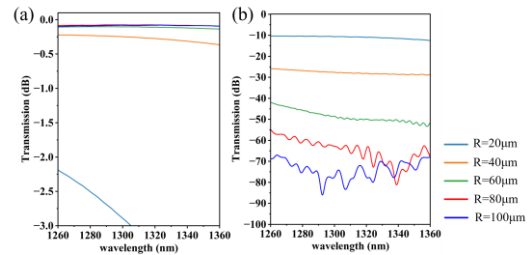


Fig. 1. Simulated transmissions for the TFLN polarizers with an S-bend waveguide. (a) TE mode. (b) TM mode.

radii, as even at 100  $\mu$ m, the S-bend waveguide weakly confines light, and the total loss depends primarily on the S-bend waveguide's total length. Fabricated polarizers were measured using an O-band laser, with grating couplers as the interface with the fiber. The results, shown in Fig. 3, generally align with the simulations. For a polarizer with a 100- $\mu$ m S-bend waveguide radius, the ERs exceed 50.6 dB and insertion losses are below 0.4 dB around a 1310 nm wavelength. Fabrication uniformity issues between the grating couplers for the polarizers and the straight waveguides for normalization posed some challenges. Extracting the bandwidth in terms of insertion loss was not straightforward. Nonetheless, the ERs generally exceed 30 dB for wavelengths from 1260 nm to 1340 nm.

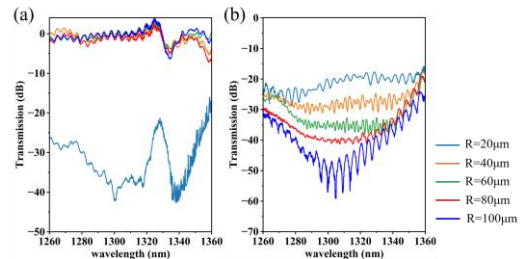


Fig. 3. Measured transmissions for the TFLN polarizers with an S-bend waveguide. (a) TE mode. (b) TM mode.

## 3. Conclusion

In conclusion, polarizers using an S-bend waveguide have been demonstrated for TFLN photonic circuits. The outstanding performances will potentially benefit many applications where pure polarization is required.

## References

- [1] Boes A, et al. Science. **379** (2023) 6627.
- [2] Wang C, et al. Nature, **562** (2018) 7725.
- [3] He J, et al. Opt. Express, **30** (2022) 19.
- [4] Wei Jin, et al. Optica. **8** (2021) 1624.
- [5] Weixi Liu, et al. Opt. Lett. **49** (2024) 2337.



# Modelling of CO<sub>2</sub> Gas Sensing using Spectral Envelope of SoI Integrated Racetrack Resonator

Shalini Vardhan<sup>1</sup>, Naveen Kumar Gupta<sup>2</sup>, Aditya Kushwaha<sup>1</sup>, Priyanka Verma<sup>1</sup>, Ritu Raj Singh<sup>1</sup>

<sup>1</sup>Department of Electronics and Communication Engineering, Netaji Subhas University of Technology, Delhi, India

<sup>2</sup>Department of Electronics and Communication Engineering, Indian Institute of Information Technology, Ranchi, India

E-mail: [shalini.vardhan.phd21@nsut.ac.in](mailto:shalini.vardhan.phd21@nsut.ac.in)

## 1. Introduction

Silicon on Insulator (SoI) technology has tantalized the photonics world in terms of integrated device modeling encountering with numerous applications. Many gas sensors can be designed using SoI technique with lower scaling factor and higher operational speed [1]. The emission of Carbon dioxide is a natural process but excess emission is a result of burning of fossil fuels, deforestation, increase in the use of automobiles [2]. People who work in automobile industries more likely face the respiratory problems, dizziness etc. To address these issues a gas sensor is designed to detect the excess of emitted CO<sub>2</sub>. In this manuscript an approach to sense CO<sub>2</sub> gas using microring racetrack resonator is demonstrated. The sensing analysis is done on the basis of change in the refractive index (RI) in the cavity region which will result in the envelope spectrum shift.

## 2. Structure and Sensing Methodology

The 3D schematic for CO<sub>2</sub> sensing is represented by Fig 1, where  $P_{in}$  is used to inject optical power and  $P_{out}$  is used for the transmittance spectrum. The materials used in the design of optical racetrack resonator are silicon (Si) as guiding material, silicon dioxide (SiO<sub>2</sub>) as substrate and cladding as a gas chamber. The refractive index of Si and SiO<sub>2</sub> is calculated using Sellmeier's equation [3]. The RI of CO<sub>2</sub> is 1.489 [4]. The width and height of Si is represented by  $x$  and  $y$  axis as shown Fig 1, which are 400 nm and 220 nm [5], [6]. For ease of simulation the coupling gap between straight waveguide and racetrack waveguide is 100 nm, the ring radius is 5  $\mu$ m and the coupling section inserted between the splitted ring is of 9.7  $\mu$ m. The operational wavelength range is from 1350 nm to 1850 nm.

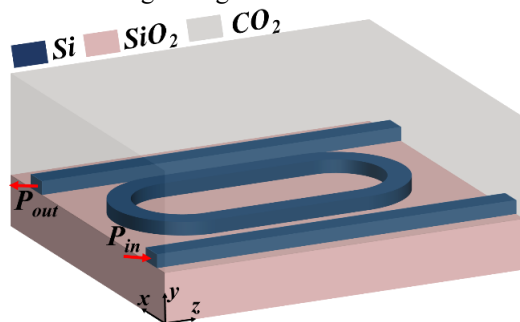


Figure 1. 3D schematic of Micro Racetrack Resonator for CO<sub>2</sub> gas sensing. For CO<sub>2</sub> sensing a gaseous chamber of glass is made for the concentration of air volume fraction. When the ppm in the gaseous chamber exceeds (concentration of CO<sub>2</sub> gas), the envelope spectrum of the optical racetrack resonator shifts from the referenced envelope spectrum. The RI of different percentage by volume of CO<sub>2</sub> – air mixture is obtained by Lorentz-Lorenz mixing rule [7].

## 3. Result and Discussion

The output obtained from the optical racetrack resonator is shown in Fig 2 expressed in the form of power transmittance. The envelope spectrum for SiO<sub>2</sub> and CO<sub>2</sub> gas sensor shows the

shift in the wavelength. To get the shifted spectrum, the refractive index of CO<sub>2</sub> gas is replaced with SiO<sub>2</sub>, in the cladding region of the racetrack waveguide. The sensor envelope spectrum shows the shift of 29.21 nm from the reference envelope spectrum. The sensitivity of the gas sensor is the fraction of change in resonant wavelength by the change in the refractive index expressed in nm/RIU mentioned in equation 1.

$$S = \frac{\Delta\lambda_c}{\Delta n} \text{ nm/RIU} \quad (1)$$

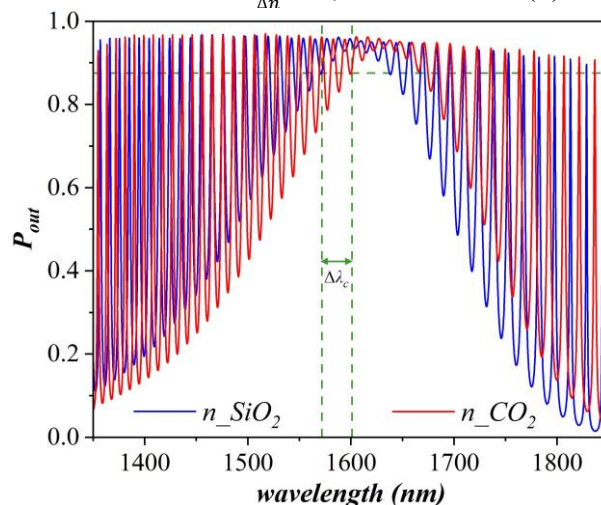


Figure 2. Envelope Spectrum for CO<sub>2</sub> gas sensor referenced with the silica glass cladding

## 4. Conclusion

A gas sensor is designed using optical racetrack resonator for 1350 nm to 1850 nm wavelength range. The practical application of CO<sub>2</sub> gas sensor is utilized at the industrial places where carbon emission poses the risk for the human health. The sensitivity obtained is 595.88 nm/RIU with a shift of 29.21 nm.

## REFERENCES

- [1] C. Ranacher *et al.*, "Characterization of Evanescent Field Gas Sensor Structures Based on Silicon Photonics," *IEEE Photonics J.*, vol. 10, no. 5, pp. 1–14, Oct. 2018, doi: 10.1109/JPHOT.2018.2866628.
- [2] R. Waheed, D. Chang, S. Sarwar, and W. Chen, "Forest, agriculture, renewable energy, and CO<sub>2</sub> emission," *J. Clean. Prod.*, vol. 172, pp. 4231–4238, Jan. 2018, doi: 10.1016/j.jclepro.2017.10.287.
- [3] S. Vardhan and R. R. Singh, "Design, simulation and performance comparison of SoI rectangular waveguide and SMF for methane detection," in *Integrated Photonics Platforms II*, May 2022, p. 32, doi: 10.1117/12.2621459.
- [4] C. Jesus Gouveia, A. Markovics, J. M. Baptista, B. Kovács, and P. A. S. Jorge, "Colorimetric and refractometric measurements of carbon dioxide," May 2011, p. 80013C, doi: 10.1117/12.892091.
- [5] S. Vardhan and R. R. Singh, "Optimization and Comparative Analysis of Rectangular and Slot Waveguide based Symmetric Ring and Racetrack Resonators for SoI Photonic Integrated Filters," *Silicon*, no. 0123456789, 2024, doi: 10.1007/s12633-024-02879-z.
- [6] S. Vardhan and R. R. Singh, "Poynting Vector Analysis of SoI based Hybrid Plasmonic Rectangular Waveguide," in *JSAP-Optica Joint Symposia 2022 Abstracts*, 2022, p. 20p\_C304\_13, [Online]. Available: [https://opg.optica.org/abstract.cfm?URI=JSAP0-2022-20p\\_C304\\_13](https://opg.optica.org/abstract.cfm?URI=JSAP0-2022-20p_C304_13).
- [7] R. R. Singh, N. Malviya, and V. Priye, "Parametric Analysis of Silicon Nanowire Optical Rectangular Waveguide Sensor," *IEEE Photonics Technol. Lett.*, vol. 28, no. 24, pp. 2889–2892, Dec. 2016, doi: 10.1109/LPT.2016.2624501.

# Analysis of Ring Radius and Q-Factor for Enhanced Bandpass Filter performance in Racetrack Ring Resonators

Naveen Kumar Gupta<sup>1</sup>, Shalini Vardhan<sup>2</sup>, Ritu Raj Singh<sup>2</sup>

<sup>1</sup>Department of Electronics and Communication Engineering, Indian Institute of Information Technology, Ranchi, India

<sup>2</sup>Department of Electronics and Communication Engineering, Netaji Subhas University of Technology, Delhi, India

E-mail: [naveenkumaar.ece@gmail.com](mailto:naveenkumaar.ece@gmail.com)

## 1. Introduction

There have been various studies on the racetrack ring resonators, which aimed to calculate various resonators parameters, Free Spectral Range (FSR), Full Width at Half Maximum (FWHM), Finesse (F), Quality (Q) factor [1], and Sensitivity. Optical Resonators have numerous applications in Photonic Integrated Circuits (PIC), from Optical filters to Sensors [2], Switches [3], Lasers [4], Modulators [5], Multiplexers [6]. In this research article, an optical Racetrack Ring Resonator (RTRR) is proposed as a band pass filter and the effect of ring radius (R) is demonstrated to optimize the Q-factor for bandpass filter (BPF) applications. The wavelength band for the study of band pass filter ranges from 1300 nm to 1900 nm.

## 2. Structure and Methodology

The RTRR is based upon the Silicon on Insulator (SoI) technology, in which a racetrack structure of Silicon material (Si) is mounted over a dielectric substrate, silicon dioxide (SiO<sub>2</sub>) as illustrated by Fig. 1. To design a RTRR, a ring of 'R' radius is splitted into two equal halves and a coupling section of 9.77  $\mu\text{m}$  is inserted. For Quasi TE [7] wave propagation, RTRR uses two straight waveguides and a racetrack waveguide and the gap between them is 100 nm. To design such optical resonators, the dimensional sizes of silicon wafers uses the cross section of 400 nm $\times$ 220 nm [8]. For the study of Q-factor, R is varied as 1  $\mu\text{m}$ , 2  $\mu\text{m}$ , 5  $\mu\text{m}$  and 10  $\mu\text{m}$ .

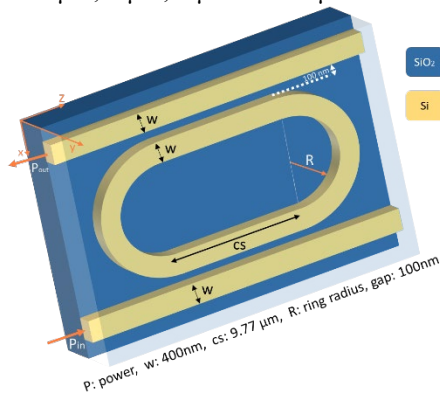


Fig. 1. 3D schematic of Racetrack Ring Resonator

Transverse Electric (TE) power propagates through the rectangular waveguide's input port  $P_{in}$ . The power injected through  $P_{in}$  gets coupled to the racetrack waveguide and circulates in it. Then power recouples to the upper straight waveguide and output is taken from  $P_{out}$  in the form of transmittance spectrum as shown in Fig. 2 and Fig. 3.

## 3. Result and Discussion

The RTRR with different R (1  $\mu\text{m}$ , 2  $\mu\text{m}$ , 5  $\mu\text{m}$  and 10  $\mu\text{m}$ ) is analyzed using finite element method (FEM). The results shown in Fig. 3 illustrates that on increasing R values the envelope spectrum shifts, the number of resonance notch increases, and the spectrum becomes more compressed, which results in the decrease of FSR and FWHM along with the blue shift. To examine the impact of R, the Q-factor is computed in terms of central wavelength ( $\lambda_c$ ) and FWHM, using the following formula.

$$Q = \frac{\lambda_c}{FWHM} \quad (1)$$

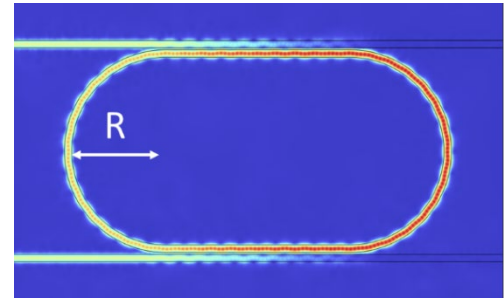


Fig. 2. Power propagation in RTRR

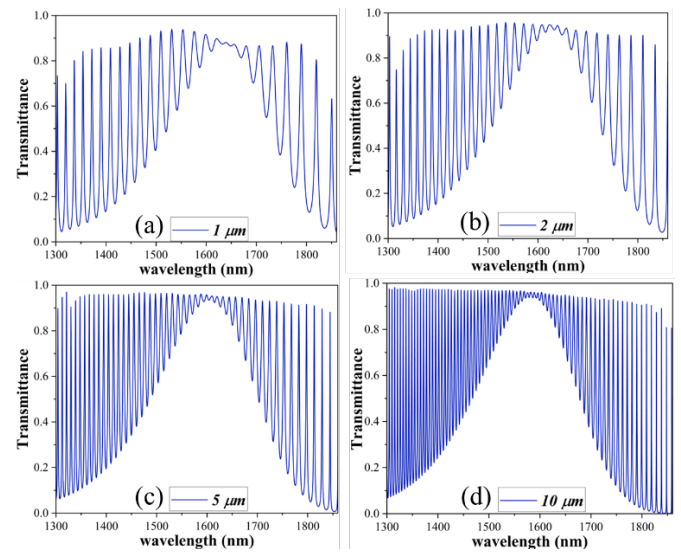


Fig. 3. Transmittance for R = (a) 1  $\mu\text{m}$ ; (b) 2  $\mu\text{m}$ ; (c) 5  $\mu\text{m}$ ; and (d) 10  $\mu\text{m}$

## 4. Conclusion

In this research work, the RTRR based filter has Q-factor of 7.304, 7.439, 7.616, 7.969 for R = 1  $\mu\text{m}$ , 2  $\mu\text{m}$ , 5  $\mu\text{m}$  and 10  $\mu\text{m}$ , respectively. The Q factor listed are not significantly varied on increasing R, but other dimensional parameters (i.e. 'cs' and gap) may have considerable impact on Q-factor. Hence, the proposed RTRR can be significantly utilized as an BPF.

## REFERENCES

- [1] T. Sun, W. Niu, and M. Xia, "Racetrack microring resonator with improved quality factor based on asymmetric waveguide bend," *Opt. Commun.*, vol. 529, p. 129092, Feb. 2023, doi: 10.1016/j.optcom.2022.129092.
- [2] Chung-Yen Chao and L. J. Guo, "Design and optimization of microring resonators in biochemical sensing applications," *J. Light. Technol.*, vol. 24, no. 3, pp. 1395–1402, Mar. 2006, doi: 10.1109/JLT.2005.863333.
- [3] S. Gulde, A. Jebali, and N. Moll, "Optimization of ultrafast all-optical resonator switching," *Opt. Express*, vol. 13, no. 23, p. 9502, 2005, doi: 10.1364/OPEX.13.009502.
- [4] X. Shen, H. Choi, D. Chen, W. Zhao, and A. M. Armani, "Raman laser from an optical resonator with a grafted single-molecule monolayer," *Nat. Photonics*, vol. 14, no. 2, pp. 95–101, Feb. 2020, doi: 10.1038/s41566-019-0563-7.
- [5] Y. Amemiya, T. Tokunaga, Y. Tanushi, and S. Yokoyama, "Optical modulator using metal-oxide-semiconductor type Si ring resonator," *Opt. Rev.*, vol. 16, no. 3, pp. 247–251, May 2009, doi: 10.1007/s10043-009-0046-z.
- [6] D. Wu, Y. Wu, Y. Wang, J. An, and X. Hu, "Four-channel optical add-drop multiplexer based on dual racetrack micro-ring resonators," *Opt. Commun.*, vol. 354, pp. 386–391, Nov. 2015, doi: 10.1016/j.optcom.2015.06.028.
- [7] F. Dell'Olio, V. M. N. Passaro, G. Z. Mashanovich, and F. De Leonardis, "Micro-racetrack coupled-resonator optical waveguides in silicon photonic wires," *J. Opt. A Pure Appl. Opt.*, vol. 10, no. 6, p. 064003, Jun. 2008, doi: 10.1088/1464-4258/10/6/064003.
- [8] S. Vardhan and R. R. Singh, "Optimization and Comparative Analysis of Rectangular and Slot Waveguide based Symmetric Ring and Racetrack Resonators for Sol Photonic Integrated Filters," *Silicon*, vol. 16, no. 7, pp. 2913–2926, May 2024, doi: 10.1007/s12633-024-02879-z.

# Diffraction-based on-chip optical neural network with high computational density

Wencan Liu<sup>1</sup>, Yuyao Huang<sup>1</sup>, Run Sun<sup>1</sup>, Tingzhao Fu<sup>2</sup> and Hongwei Chen<sup>1</sup>

Tsinghua University, China<sup>1</sup>, National University of Defense Technology, China<sup>2</sup>

E-mail: [chenhw@tsinghua.edu.cn](mailto:chenhw@tsinghua.edu.cn)

## 1. Introduction

The rapid advancement of artificial intelligence has led to substantial progress in various fields with deep neural networks (DNNs). However, complex tasks often require increasing power consumption and greater resources of electronics. On-chip optical neural networks (ONNs) are increasingly recognized for their power efficiency, wide bandwidth, and capability for light-speed parallel processing. In our previous work [1], we proposed on-chip diffractive optical neural networks (DONNs) to offer the potential to map a larger number of neurons and connections onto optics. To further improve the computational density and integration level, we proposed ultra-compact DONNs designed with the structure re-parameterization algorithm [2] and experimentally verified their performance [3], which increased the computational density by more than an order of magnitude.

## 2. Structure design and numerical modeling

The DONN chips developed consist of metalines, which represent the hidden layer of a neural network. These metalines consist of slots filled with SiO<sub>2</sub>, serving as trainable parameters, optimized in the training process. To accurately model the propagation process in the metaline, slot groups and extra length between adjacent layers are utilized, resulting in the relatively large chip scale [1].

Given the challenges in directly modeling on-chip DONNs, particularly in accurately depicting the interaction between the silicon slots and the optical field, a deep complex neural network (DCNN) is employed to simulate the complex interactions in each metaline. Consequently, this approach allows for a precise numerical representation of the on-chip light propagation [2]. The architecture of the DONN with two hidden layers is illustrated in Fig. 1(a) and the modeling process is depicted in Fig. 1(b). The dimensions of the structure are set to 53  $\mu\text{m}$  in length and 30  $\mu\text{m}$  in width, with distance between adjacent layers set as 15  $\mu\text{m}$ . The input and output layers consist of four input straight waveguides and three output taper waveguides, respectively. As a proof of the design method, the chip was fabricated based on the SOI platform. The SEM images in Fig. 1(c) illustrates the on-chip DONN with 2 hidden layers and diffractive units. The experimental result of the chip revealing an accuracy of 93.3% in Iris plants dataset, aligning with numerical predictions [3].

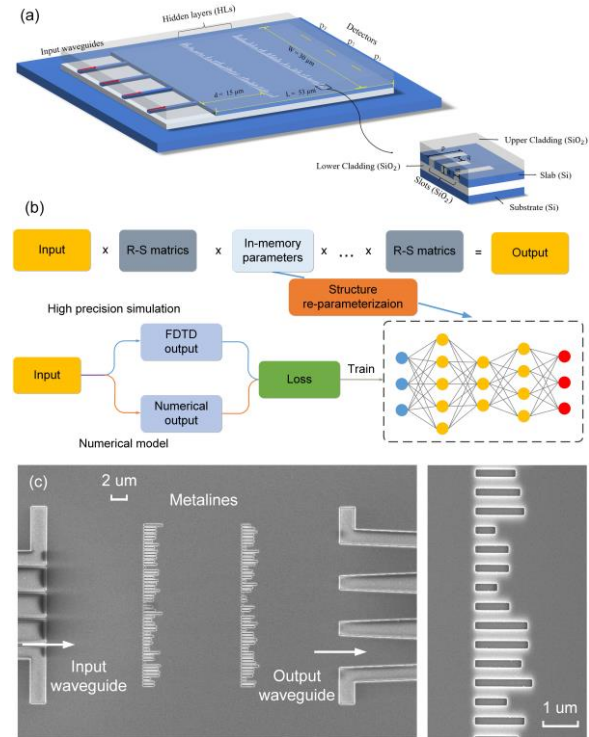


Fig. 1. (a) The architecture of the DONN. (b) Numerical modeling on structure re-parameterization algorithm. (c) SEM images of the DONN chip with 2 hidden layers and diffractive units.

## 3. Conclusions

In summary, DONN has significant advantage in mapping a large number of connections and trainable parameters on chip, allowing for passive computing on a compact structure. Furthermore, with utilization of the structure re-parameterization algorithm, we can greatly improve the parameter integration while achieving computational density of 18.6 POPS/mm<sup>2</sup>.

## Acknowledgements

This work was supported by the National Natural Science Foundation of China (62135009).

## References

- [1] T. Fu et al. "Photonic machine learning with on-chip diffractive optics," Nat. Commun. 14, 70 (2023).
- [2] W. Liu et al. "C-DONN: compact diffractive optical neural network with deep learning regression," Opt. Express 31, 22127–22143 (2023).
- [3] W. Liu et al. "Ultra-compact optical neural network chip," CLEO 2024, no. SM4M. 5



## Two-Dimensional Broadband Silicon Optical Beam Scanning Device for Free-Space Optical Communication

AIST<sup>1</sup>, <sup>○</sup>Yuki Atsumi<sup>1</sup>, Tomoya Yoshida<sup>1</sup>, Ryosuke Matsumoto<sup>1</sup>, Ryotaro Konoike<sup>1</sup>,

Kazuhiro Ikeda<sup>1</sup>, Takashi Inoue<sup>1</sup>, Keijiro Suzuki<sup>1</sup>

E-mail: y-atsumi@aist.go.jp

Silicon photonics-based beam scanning technology is expected to be introduced into short-distance free-space optical (FSO) communication applications such as inter/intra rack communications in data centers and indoor mobile communications in beyond-5G mobile communications [1]. In this report, we present our recent work about a broadband two-dimensional (2D) Si beam scanning device shown in Fig. 1 that integrates 128-port three-dimensionally-structured optical surface couplers known as “elephant couplers”[2-4]. This device can realize high-capacity FSO signal transmission by introducing wavelength-division multiplexing (WDM) technology. The fabricated device shows a fiber-to-fiber insertion loss of 5.6 dB and a 1-dB spectrum bandwidth of 40 nm. We obtained a beam scanning operation with the scannable beam-angle range and the resolution range of  $5.3 \text{ deg} \times 2.5 \text{ deg}$  and  $0.35 \text{ deg} \times 0.36 \text{ deg}$ , respectively, by introducing a commercial imaging lens. Using this system, we have demonstrated FSO transmission of a 10 Gbps non-return-to-zero on-off-keying signal successfully within a wavelength range from 1530 to 1590 nm with a fixed receiver position as shown in Fig. 2.

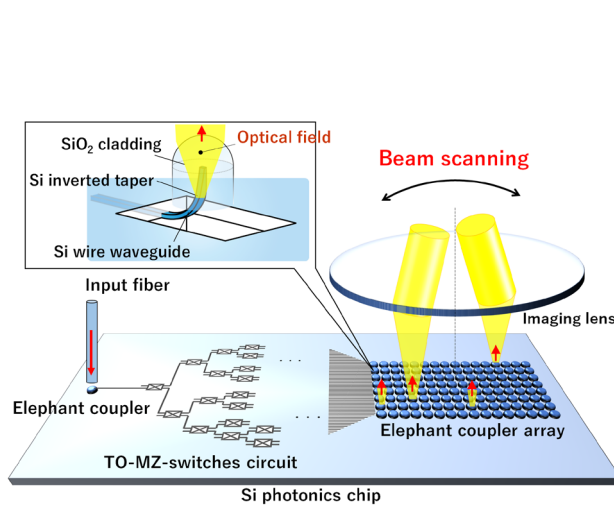


Fig. 1 Schematic images of silicon beam scanner.

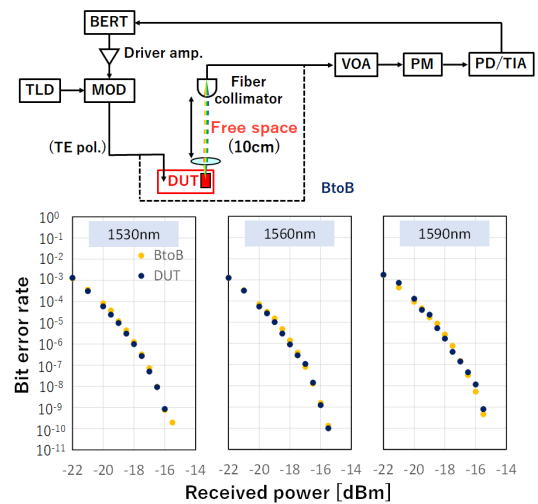


Fig. 2 FSO signal transmission

### Acknowledgment

These research results were obtained from commissioned research conducted by the National Institute of Information and Communications Technology (NICT), Japan with the grant number of JPY012368C08401.

### References

- [1] K. Wang, et al., J. Lightw. Technol., 37(2), pp. 619-626, 2019.
- [2] T. Yoshida, et al., IEEE Photon. Technol. Lett., 32(20), pp. 1319-1322, 2020.
- [3] Y. Atsumi, et al., Proc. Optical Fiber Communication Conf. (OFC), M3C.4, San Diego, CA, 2023.
- [4] Y. Atsumi, et al., IEICE trans. Electron., E106-C(11), pp. 739-747, 2023.

# Cascading meta-devices for advanced functions and applications

Jing Cheng Zhang<sup>1</sup> and Din Ping Tsai<sup>1</sup>

<sup>1</sup>Department of Electrical Engineering, City University of Hong Kong, Hong Kong SAR, CHINA

E-mail: jzhang2442-c@my.cityu.edu.hk

## 1. Introduction

Metasurfaces, recognized as subwavelength antenna collections, offer many possibilities for managing electromagnetic waves and streamlining the dimensions and intricacy of electromagnetic apparatus. These structures can govern diverse aspects of electromagnetic waves, encompassing amplitude, wavelength, polarization, phase, orbital angular momentum, and more. Multilayer meta-devices provide a greater degree of freedom to manipulate the light and have a better ability to perform various functions. In this thesis, various multilayer meta-devices have been systematically developed for advanced functions and applications, such as 6G communications, chiral imaging, and light field control for other advanced applications.

## 2. Methods and results

The polarization of light serves as a valuable information channel extensively explored in optical devices. We present an experimental demonstration of a chiral imaging meta-device featuring extensive area coverage and broadband chirality control, achieved through applying nanoimprint technology to create a centimeter-scale Moiré meta-device, as shown in Fig. 1(a) [1]. Tunable Airy beams with controllable propagation trajectories have garnered widespread interest in various fields. We present a novel method utilizing a dual metasurface system to overcome these limitations and significantly enhance the practical potential of the Airy beam, as shown in Fig. 1(b) [2]. Sixth-generation communication technology is currently undergoing active development, with expectations of surpassing its fifth-generation predecessor in speed and performance. To comprehensively govern the propagation direction and coverage area of terahertz beams, we have devised meta-devices featuring synthetic phase designs of rotary doublet Airy beams and triplet Gaussian beams with adjustable focal properties, as shown in Fig. 1(c) [3]. Our approach involves encoding a cubic phase profile and two off-axis Fresnel lens phase profiles across the two metasurfaces. Validation of the proposed strategy is achieved through simulation and experimental results. The proposed meta-device effectively addresses existing limitations and lays the foundation for expanding the applicability of Airy beams across diverse domains, including light-sheet microscopy,

laser fabrication, optical tweezers, and beyond.

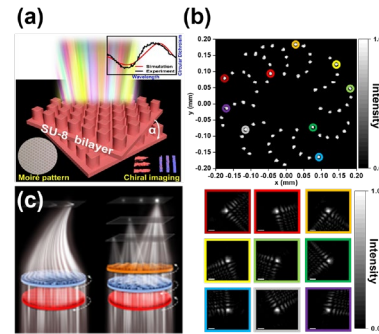


Fig. 1. (a) Chiral imaging meta-device, (b) Miniature tunable Airy beam optical meta-device, (c) A 6G meta-device for 3D varifocal

## 3. Conclusions

In summary, the exploration of metasurfaces and meta-devices in this thesis uncovers innovative possibilities, ranging from precise control over EM waves to communication, imaging, sensing, and beyond applications. The advancements presented hold significant promise for shaping the future of EM devices and technologies. To envision a broader perspective, metasurfaces exhibit numerous advantages over conventional devices, making them a promising avenue for developing new applications using established high-dimensional modulation principles.

## Acknowledgements

This work is supported by the University Grants Committee / Research Grants Council of the Hong Kong Special Administrative Region, China [Project No. AoE/P-502/20, CRF Project: C1015-21E; C5031-22G, GRF Project: CityU15303521; CityU11305223; CityU11310522; CityU11300123, and Germany/Hong Kong Joint Research Scheme: G-CityU 101/22], City University of Hong Kong [Project No. 9380131, 9610628, and 7005867], and National Natural Science Foundation of China [Grant No. 62375232].

## References

1. Zhang J C, et al. Miniature tunable Airy beam optical meta-device. *Opto-Electronic Advances*, 2024, 7(2): 230171-1-230171-8.
2. Zhang J C, et al. Nanoimprint meta-device for chiral imaging. *Advanced Functional Materials*, 2023, 33(49): 2306422.
3. Zhang J C, et al. A 6G meta-device for 3D varifocal. *Science Advances*, 2023, 9(4): eadf8478.



# 有効媒質によるオンチップテラヘルツ偏光制御

## On-Chip Terahertz Polarization Control Enabled by Effective Medium

阪大基礎工<sup>1</sup>, アデレード大<sup>2</sup>, <sup>○</sup>Weijie Gao<sup>1</sup>, Withawat Withayachumnankul<sup>2</sup>, 富士田 誠之<sup>1</sup>

Osaka Univ.<sup>1</sup>, Univ. Adelaide<sup>2</sup> <sup>○</sup>Weijie Gao<sup>1</sup>, Withawat Withayachumnankul<sup>2</sup>, Masayuki Fujita<sup>1</sup>

E-mail: gao.weijie.es@osaka-u.ac.jp

We have proposed a solution for terahertz wave on-chip transmission [1], filtering [2], and polarization manipulation [3] with unprecedented performance based on the concept of effective medium [4]. The effective medium is realized by periodically perforating the silicon slab with a period in the deep subwavelength region. As a result, the effective medium can be treated as a homogenous material within the operation frequency range with a tailorable anisotropic permittivity tensor that is only mildly frequency dependent. The unique characteristics of the effective medium play a critical role in enhancing the performance of various terahertz integrated devices. In particular, the anisotropy of the effective medium can significantly increase the polarization extinction ratio (PER) for polarization beam splitters and rotators. This study mainly focuses on the impacts on PER of a terahertz integrated polarization rotator enabled by the effective medium.

As shown in Figs. 1(a)-(b), the proposed polarization rotator consists of two inversely symmetric tapered cores based on silicon and effective medium, respectively. In-plane effective medium claddings are introduced to surround the cores, where the effective medium can be realized by creating holes in the silicon slab in a hexagonal lattice, as shown in Fig. 1(c). Given a perforation period of 100  $\mu\text{m}$ , the anisotropic relative permittivities can be obtained based on Maxwell-Garnett's effective medium theory [4], and they decrease with the hole diameter increasing, as shown in Fig. 1(d). Blind holes realize the effective medium core to rotate the optical axis, while the claddings are through holes. Here, the effective medium core is designed with an identical permittivity with that of the upper claddings realized with a hole diameter of 90  $\mu\text{m}$ . With such a configuration, the input mode with the  $E_y$  polarization can be gradually rotated to its orthogonal counterpart after a sufficiently long conversion length based on the mode evolution theory. Notably, the lower cladding is introduced, which can vary the polarization states by changing its permittivity, leading to different PERs. As shown in Fig. 1(f), by gradually changing  $\Delta d$ , i.e., by reducing the hole size of the lower cladding, PER can be increased over the operation frequency range, where  $\Delta d$  is defined as the difference in diameter of holes between the upper and lower claddings. This is mainly due to the optical axis's varying rotation angle determined by the asymmetric claddings' birefringence. The proposed method promises terahertz on-chip polarization control like half-wave and quarter-wave plates for free-space waves. This work was partly supported by JST CREST (JPMJCR21C4), the ARC Discovery Project (No. ARC DP220100489), and KAKENHI (24H00031).

参考文献

- [1]. W. Gao *et al.*, *Optics Express*, **27**, 26 (2019).
- [2]. W. Gao *et al.*, *APL Photonics*, **6**, 076105 (2021).
- [3]. W. Gao *et al.*, *Proceedings of APMC*, 100 (2021).
- [4]. A. V. Subashiev and S. Luryi, *Journal of Lightwave Technology*, **24**, 3(2006).

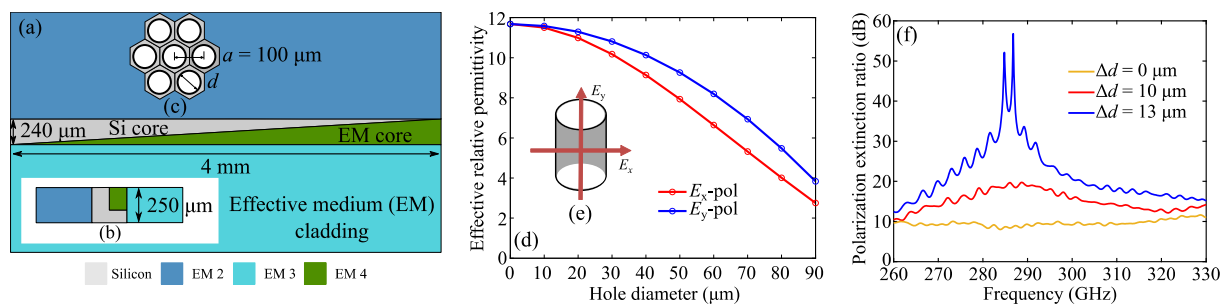


**Fig.1.** (a) Top view and (b) cross-section (center) view of terahertz integrated polarization rotator based on artificial homogeneous material. (c) Magnified view of the hexagonal lattice of the realized effective-medium cladding. (d) Effective relative permittivity as a function of the air hole diameter of the realized effective medium in (c). (e) 3D view of an air hole in silicon with an indication of polarization. (f) Polarization extinction ratio of the polarization rotator with different configurations of the asymmetric claddings.

# Multiband Frequency-Tunable Millimeter-Wave Absorber

A. Shahzad<sup>1,2</sup>, S. Ahmed<sup>1</sup>, Q. A. Naqvi<sup>1</sup>, and Pankaj K. Choudhury<sup>2\*</sup>

<sup>1</sup>Department of Electronics, Quaid-i-Azam University, Islamabad, 45320 Pakistan

<sup>2</sup>International Research Center for Advanced Photonics, Zhejiang University, Haining 314400, China

\*E-mail: pkchoudhury@ieec.org

## 1. Introduction

The use of wireless electronic devices, such as sensors, radar detectors and cell phones, has resulted in a complex electromagnetic (EM) environment that causes significant EM pollution [1]. To avoid these, absorbers with effective EM attenuation are indispensable [1–3]. Within the context, functional materials and structures having adjustable or adaptive absorption characteristics are of paramount importance to efficiently absorb EM radiation in challenging circumstances [4–6]. Frequency-tunable absorbers are commonly employed in microwave frequency bands. Herein, we present a multiband millimeter-wave absorber comprising a multi-layer hybrid structure of graphene-copper-FR4-copper to achieve multiband frequency-tunable millimeter-wave absorption. We emphasize on the theoretical framework, design methodology, and results based on simulations.

## 2. Device Modelling and Theory

Figure 1a illustrates the schematic of the absorber, which consists of a patterned graphene and copper layers, which are isolated by the PET dielectric medium. The structure is backed by a copper layer (of thickness slightly greater than the skin depth) acting as a reflective ground plane. Also, the FR4 dielectric substrate is placed between the patterned copper layer and the copper ground plane. We choose the unit cell size to be  $p = 2.5$  mm (fig. 1a). Figure 1b depicts the cross-sectional side view of the structure. In the design, the patterned graphene and copper have the same period as the unit cell structure. Also, the side lengths and strip widths of the patterned graphene and copper are identical, with their respective values as  $l = 1.5$  mm and  $w = 0.2$  mm (fig. 1a).

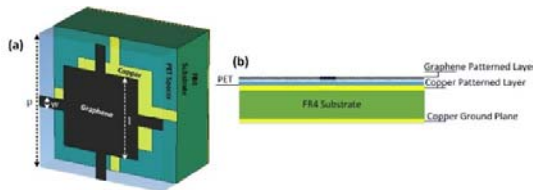


Fig. 1. Schematic of the multiband frequency tunable absorber; (a) top view, and (b) cross-sectional view.

We investigate the spectral properties using the finite integration technique implemented in the CST Microwave Studio platform. The spectral absorption characteristics are determined by

$$A(f) = 1 - |S_{11}|^2 - |S_{21}|^2. \quad (1)$$

Since copper as the ground plane makes almost vanishing transmission (i.e.,  $S_{21} \approx 0$ ), the absorptance will be

$$A(f) = 1 - |S_{11}|^2. \quad (2)$$

Thus, a single port network can be achieved with the input impedance

$$Z_{in} = Z_0(1 + S_{11})/(1 - S_{11}). \quad (3)$$

$Z_{in}$  is solely determined by  $S_{11}$ , and as  $S_{21} \approx 0$ , the impedance matching condition, given by  $[Re(Z_{in}) = Z_0 = 377\Omega, Im(Z_{in}) = 0]$ , is achieved. This condition marks the point where the nearly perfect absorption occurs.

## 3. Results and Discussion

Figure 2 illustrates the plots of reflection coefficients  $S_{11}$  for different values of graphene surface impedance. The simulated results exhibit shifts in reflection minima in three sub-bands (75.5–81GHz, 88–93GHz, and 101.8–106.5GHz) within the W-band as the graphene surface impedance varies from 1000  $\Omega/\text{Sq}$  to 180  $\Omega/\text{Sq}$ . Notably, the reflection minima consistently remain less than -17 dB (corresponding to absorptance  $\geq 98\%$ ). This is attributed to the impedance matching conditions met at different frequencies in the stated multiple frequency bands.

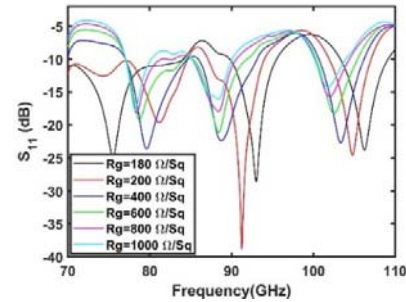


Fig. 2. Simulated reflection spectra of the absorber for variable graphene sheet impedance.

## 4. Conclusion

A multiband frequency-tunable millimeter-wave absorber comprising a patterned graphene-FR4-copper based hybrid structure has been studied, and the results yield tunability along with high absorption. The structure facilitates excellent frequency tunability range in three different bands, namely 75.5–81GHz, 88–93GHz, and 101.8–106.5GHz, within the W-band. It has been found that the millimeter wave absorber demonstrates over 98% absorptance throughout the frequency-tuning process.

## Acknowledgement

PKC acknowledges the financial support by Zhejiang University (China) through the grant 11133000\*194232301/002.

## References

- [1] E. F. Knott, J. F. Schaeffer, and M. T. Tulley, SciTech Publishing (2004).
- [2] C. M. Watts, X. Liu, and W. J. Padilla, Adv. Mater. **24** (2012).
- [3] S. Zhong and S. He, Sci. Rep. **3** (2013) 2083.
- [4] M. A. Baqir and P. K. Choudhury, J. Opt. Soc. Am. B **36** (2019) F123.
- [5] M. Pourmand, P. K. Choudhury, and M. A. Mohamed, Sci. Rep. **11** (2021) 3603.
- [6] M. Pourmand and P. K. Choudhury, IEEE Trans. Nanotechnol. **21** (2022) 586.

# Mode Switching in Few-Mode Fibers Using Electric Field Controlled Dynamic Offset Coupling

Isha Sharma<sup>1</sup>, Partha Roy Chaudhuri<sup>1\*</sup>

<sup>1</sup> Department of Physics, Indian Institute of Technology Kharagpur-721302, India

\*email : [roycp@phy.iitkgp.ac.in](mailto:roycp@phy.iitkgp.ac.in)

## I. INTRODUCTION

In recent years, there has been a significant R&D focus on developing optical fiber-based technologies in photonics and broadband communication systems. The surge in data communication and cloud computing has led to an exponential increase in communication traffic. To address this challenge, few-mode fibers and mode division multiplexing (MDM) have become promising solutions. Mode converters are essential components in MDM systems, and various types have been proposed and experimentally validated. These converters utilize a range of techniques, including acousto-optic transducers and structured optical waveguides, to achieve their functionality [1].

We have developed an all-fiber setup designed for selectively exciting and switching between higher-order modes in a few-mode fiber. Previously, we introduced a novel method utilizing cantilever beam deflection techniques to detect surrounding electric fields. In this study, we apply the cantilever technique to achieve mode switching by introducing a controlled perturbation in the input launching conditions. The fiber is coated with  $\text{BiFe}_{0.9}\text{Co}_{0.1}\text{O}_3$ , serving as a probe sample, and is placed within an electric field for testing.

## II. EXPERIMENTAL DETAILS AND RESULT

The light is coupled into one end of a single-mode fiber (SMF) from an input He-Ne laser source using a light coupling unit, shown in Fig. 1. The other end of the SMF is coated with our probe material (coated length 1.0 cm with coated thickness of 0.28 mm). A dual-mode fiber (DMF) is positioned directly in line with the exit of the input cantilever fiber, situated between two electric field plates. When an electric field is applied, the coated fiber deflects due to the induced polarization of the probe sample. This deflection modulates the input launching conditions, leading to changes in mode excitation within the fiber and resulting in the switching of the output mode.

Initially, light is coupled from SMF into the DMF through fiber-to-fiber transmission. This approach ensures close proximity between the fibers, establishing nearly ideal alignment to facilitate the excitation of the desired fundamental mode. Upon applying the electric field, we observe mode switching within the DMF. Figure 2 visually depicts the mode profiles and their transformations as the electric field intensity varies, specifically showing cases with different plate separations. In this scenario, we ob-

serve a transition from a circularly symmetric mode to an azimuthally asymmetric mode during the switching process.

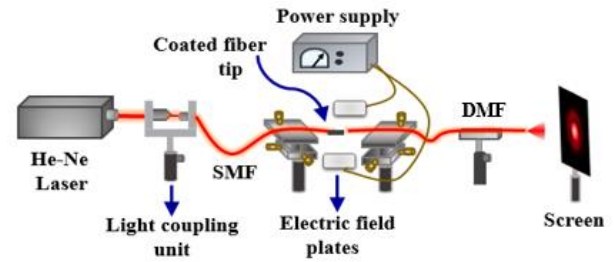


Fig. 1. Schematic of experimental set-up.

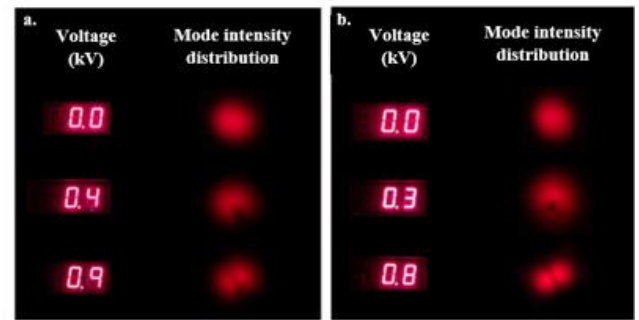


Fig.2. Real time monitoring of mode intensity distribution at different voltage values at fiber exit for varying plates distance at (a) 1.4 (b) 1.9 cm.

## III. CONCLUSIONS

We demonstrate a novel method to perform an automated mode switching within a few-mode fiber using an electric field-controlled fiber-to-fiber offset coupling. This innovative approach enables dynamic and controllable manipulation of modes by inducing deflection in the coated fiber through the electric field. This technology opens up possibilities for applications in sensing, communications, and beyond. By adjusting the experimental parameters, the sensitivity of the system can be tuned to meet specific requirements. This new automated mode-switching approach will be well-suited for field deployment in varying operational environments and should be useful in higher order applications in photonics and fiber circuits.

## IV. REFERENCES

- [1] A. K. Memon, and K. X. Chen, Opto-Electronics Review, 29 (2021).
- [2] Isha Sharma, Partha Roy Chaudhuri, Optical Fiber Technology, 62 (2021) 102472

4 JSAP-Optica Joint Symposia 2024 | 一般セッション(口頭講演) : 4.3 Laser sources and Laser applications

## [17a-A31-1~5] 4.3 Laser sources and Laser applications

[17a-A31-1]

3D Reconstruction of Veins Using NIR by Efficientnet Model

Phuong Anh Dam<sup>1</sup>, ○(M1)Hoang Nhut Huynh<sup>1</sup>, Tan Loc Huynh<sup>1</sup>, Kien Vinh Vuong<sup>1</sup>, Ngoc An Dang Nguyen<sup>1</sup>, Anh Tu Tran<sup>1</sup>, Trung Nghia Tran<sup>1</sup> (1.Ho Chi Minh City University of Technology (HCMUT), VNUHCM)

---

[17a-A31-2]

An Optical Approach for the Liquid Vortex Characterization

○(M1)Tien Danh Vu<sup>1,2</sup>, Phuong Hoang Le<sup>1</sup>, Thanh Nhu Nguyen<sup>1,2</sup>, Binh Xuan Cao<sup>1,2</sup> (1.Square Lab, Hanoi University of Science and Technology, 2.School of Mechanical Engineering, Hanoi University of Science and Technology)

---

[17a-A31-3]

Utilizing Near-Infrared Femtosecond Laser-Generated Gas Bubbles for Acellular Area Construction in Cell Monolayers

○Kazunori Okano<sup>1,4</sup>, Naomi Tanga<sup>1,2</sup>, Rieko Aida<sup>4</sup>, Hayato Suwa<sup>4</sup>, Hiromi Hagiwara<sup>4</sup>, Yalikun Yaxiaer<sup>1</sup>, Koichiro Kishima<sup>5</sup>, Yoichiro Hosokawa<sup>1,2,3</sup> (1.Mat. Sci, NAIST, 2.CDG, NAIST, 3.MediLux, NAIST, 4.Toin Yokohama Univ., 5.Pinpoint Photonics)

---

[17a-A31-4]

Evaluating Single Event Effects in Radiation-Tolerant Chips Using Short-Pulse Laser

○(M2)Chien Ping Hung<sup>1</sup>, Shih Bo Yu<sup>1</sup>, Jia Han Li<sup>1</sup> (1.National Taiwan Univ)

---

[17a-A31-5]

BREAKING OF PHONON BOTTLENECK IN CsPbI<sub>3</sub> NANOCRYSTALS DUE TO EFFICIENT AUGER RECOMBINATION

○(D)Ankit Sharma<sup>1</sup>, Samit K Ray<sup>2</sup>, K V Adarsh<sup>1</sup> (1.IISER Bhopal India, 2.IIT Kharagpur India)

---

## 3D Reconstruction of Veins Using NIR by Efficientnet Model

Phuong Anh Dam<sup>1,2</sup>, Hoang Nhut Huynh<sup>1,2</sup>, Tan Loc Huynh<sup>1,2</sup>, Kien Vinh Vuong<sup>1,2</sup>,  
Ngoc An Dang Nguyen<sup>1,2</sup>, Anh Tu Tran<sup>1,2</sup>, and Trung Nghia Tran<sup>1,2</sup>

<sup>1</sup> Laboratory of Laser Technology, Faculty of Applied Science, Ho Chi Minh City University of Technology (HCMUT), 268 Ly Thuong Kiet Street, District 10, Ho Chi Minh City 72409, Vietnam,

<sup>2</sup> Vietnam National University Ho Chi Minh City, Linh Trung Ward, Thu Duc, Ho Chi Minh City 71308, Vietnam

E-mail: [ttnggia@hcmut.edu.vn](mailto:ttnggia@hcmut.edu.vn)

### 1. Introduction

The study proposed a method for visualizing veins using near-infrared (NIR) transillumination imaging and reconstructing 3D structures with an EfficientNet CNN model and pixel-to-pixel technique. NIR imaging, despite being noninvasive, encounters issues with light scattering, resulting in blurry images with poor depth perception. The proposed method combines depth estimation and scatter deblurring to improve the clarity and accuracy of 3D reconstructions, specifically targeting veins on the back of the hand.

### 2. Method

The methodology for 3D vein reconstruction using NIR imaging and deep learning involves an image acquisition system that captures NIR images of hand vascular structures. Depth estimation and scatter deblurring are performed with an EfficientNet CNN model and pixel-to-pixel method. This includes preparing training data with blurred NIR images and corresponding depth maps, training the model to predict pixel depths, and generating a Depth Estimation Matrix (DEM) as shown in Figure 1.

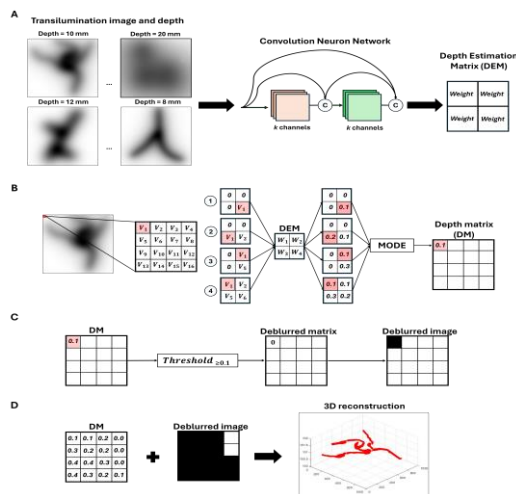


Figure 1. A. Depth estimation method, training data includes blurred images and depth, B. pixel-by-pixel method, C. deblurring method using depth matrix and depth thresholding, and D. reconstructing 3D structure from deblurred image and depth matrix.

The pixel-to-pixel method improves depth estimation by scanning the image, applying zero padding, and selecting the most common depth for each pixel. Scatter deblurring enhances clarity by using a depth threshold on the DEM, generating a deblurred image, and reconstructing the 3D structure using depth values on the x-y and z axes.

The model is trained with 100,000 images, a depth range of 0.1 to 50.0 mm, a batch size of 8, over 50 epochs, using the Adam optimizer and accuracy as the metric. Experiments, including simulations and real tissue tests capturing NIR images of the hand, show that the model effectively improves image clarity and depth estimation, leading to accurate 3D reconstructions of vascular structures as shown in Figure 2.

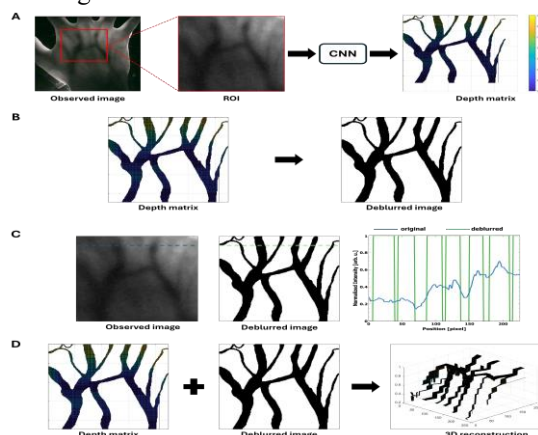


Figure 2. 3D reconstruction results of blood vessels using CNN model with A. Extracting ROI and estimating depth with CNN, B. Applying a depth matrix threshold to obtain a deblurred image, C. Comparing intensity profiles of observed and deblurred images, and D. Reconstructing the 3D blood vessel structure from the depth matrix and deblurred image.

### 3. Conclusion

The study proposed approach enhances 3D vein reconstruction through NIR imaging with the EfficientNet model and the pixel-to-pixel method, improving image clarity and depth estimation. Experimental results verify its accuracy and potential for noninvasive biomedical imaging, especially in vascular diagnostics and monitoring.

### Acknowledgements

We acknowledge Ho Chi Minh City University of Technology (HCMUT), VNU-HCM for supporting this study

### References

- [1] M. Tan and Q. Le, "Efficientnet: Rethinking model scaling for convolutional neural networks," in *International conference on machine learning*, pp. 6105–6114, PMLR, 2019.
- [2] N. A. Dang Nguyen et al. "Improvement of the performance of scattering suppression and absorbing structure depth estimation on transillumination image by deep learning," *Applied Sciences*, vol. 13, no. 18, p. 10047, 2023.



# An Optical Approach for the Liquid Vortex Characterization

Tien Danh Vu<sup>1,2</sup>, Phuong Le Hoang<sup>1</sup>, Thanh Nhu Nguyen<sup>1,2</sup>, Binh Xuan Cao<sup>1,2</sup>

<sup>1</sup> Square Lab, Hanoi University of Science and Technology, Hanoi 100000, Viet Nam,

<sup>2</sup> School of Mechanical Engineering, Hanoi University of Science and Technology, Hanoi 100000, Viet Nam

E-mail: [binh.caoxuan@hust.edu.vn](mailto:binh.caoxuan@hust.edu.vn)

## 1. Introduction

Research on liquid vortices is integral to fluid mechanics and is applied in various fields, including the manufacturing of optical elements [1]. To discover liquid vortex surfaces, contact methods [2], though simple, damage surface structures. Noncontact methods offer high-speed and accurate measurements but require complex systems [3]. Most experimental setups are suboptimal.

This paper proposes a straightforward approach combining the optical system and image processing techniques to investigate liquid vortex surfaces by light reflection. Collimated laser beams directed onto liquid surfaces provide vortex parameters through reflected beam profile analysis. The method is validated by the parabolic shape of liquid vortices in a rotary cylinder, showing promise for liquid characterization using simple optical elements.

## 2. Experimental Method

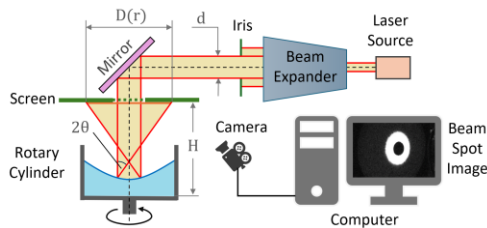


Figure 1 Experiment Setup

Liquid vortices are examined in real-time through surface reflection. The axially symmetric liquid surface is described by  $z = z(r)$ . A collimated, expanded laser beam shines perpendicular to the rotating liquid surface, with its axis aligned with the rotation axis. An iris diaphragm creates various beam radii, and the diameter of the incoming beam  $d$  equals the iris aperture. The reflected beam profile is recorded with its spot width monitored by a camera with image processing techniques and an observation screen with a central hole for the collimated beam. The optical path of two symmetric boundary rays of the collimated beam is illustrated in Fig. 1. Given the tangent slope at the reflection point is  $\theta$ , the angle between reflected and incoming beams is  $2\theta$ . The beam width on the screen  $D(r)$  is calculated:

$$D(r) = 2(H - z) \tan(2\theta) - d = 4z'(H - z) \left(1 - z'^2\right)^{-1} - 2r \quad (1)$$

where  $r$  is the incident beam radius ( $r = d/2$ ), and  $H$  is the distance from the cylinder bottom to the observation screen. A rotatable cylindrical liquid container

driven by a rotor is precisely controlled by the encoder feedback signal with a PID controller. When the container rotates with liquid inside, it creates vortices.

## 3. Results and Discussion

The following parameters were investigated in this study. Two 150 ml liquid samples were used in the experiment including a saline solution (NaCl; 0.9) and a propylene glycol solution (C<sub>3</sub>H<sub>8</sub>O<sub>2</sub>; 99). The viscosities of the saline and glycol solutions, at standard experimental conditions (25°C, 1 atm), are 0.9 cp and 57 cp, respectively, and their approximate densities are 1 mg/l. The container angular velocity is  $15 \pm 0.12$  rad/s. The iris aperture is adjusted to investigate incident beam diameters in the range of 10–19 mm.

The parabolic shape of the liquid vortex surface has been demonstrated in previous research [1,2]. Initial results with 10 incident beam diameters for both solutions show similar vortex surface profiles by the data on reflected beam spots. A detailed analysis with 37 iris aperture values further examines the relationship between the reflected spot size and the incoming beam radius  $D(r)$ , described as a quadratic function of  $z(r)$  (Eq. 3). The vortex surface shape, as determined by fitting the plots, closely matches a parabola, with  $R^2 \geq 99\%$ . The proposed method effectively investigates liquid vortices.

## 4. Conclusion

This method analyzes liquid vortices by light reflection. A collimated laser beam directed onto liquid surfaces determines vortex parameters from reflected beam data. Studying vortices in a rotating cylinder with propylene glycol and saline solutions at 15 rad/s, we determine similar vortex shapes. Curve fitting shows the vortex surface is nearly parabolic. The method offers a technique to characterize liquid dynamics.

## References

- [1] Wattering, M., Gordon, P., Ghorayshi, M. & Coté, G. Method and system for the centrifugal fabrication of low cost, polymeric, parabolic lenses. *Opt Express* 27, 21405 (2019).
- [2] Menker, P. & Herczyński, A. Form of spinning liquids in diverse geometries. *Am J Phys* 88, 475–482 (2020).
- [3] Arshad, M., Rowland, E. M., Riemer, K., Sherwin, S. J. & Weinberg, P. D. Improvement and validation of a computational model of flow in the swirling well cell culture model. *Biotechnol Bioeng* 119, 72–88 (2022).

## Utilizing Near-Infrared Femtosecond Laser-Generated Gas Bubbles for Acellular Area Construction in Cell Monolayers

Kazunori Okano<sup>1,4</sup>, Naomi Tanga<sup>1,2</sup>, Rieko Aida<sup>4</sup>, Hayato Suwa<sup>4</sup>, Hiromi Hagiwara<sup>4</sup>, Yalikus Yaxiaer<sup>1</sup>, Koichiro Kishima<sup>5</sup>, Yoichiro Hosokawa<sup>1,2,3</sup>

<sup>1</sup> Division of Materials Science, Nara Institute of Science and Technology, <sup>2</sup> Center for Digital Green-innovation, Nara Institute of Science and Technology, <sup>3</sup> MediLux Research Center, Nara Institute of Science and Technology, <sup>4</sup> Faculty of Biomedical Engineering, Toin Yokohama University, <sup>5</sup> Pinpoint Photonics, Inc.  
E-mail: k-okano@ms.naist.jp

The focused irradiation of near-infrared femtosecond laser (NIR fs laser) pulses in biological solvents efficiently induces molecular breakdown, generating vaporous gas micro bubbles [1]. Such irradiation on live cells induces apoptosis and necrosis depending in pulse energy [2]. Here we examined the relation bubble size and numbers and pulse energy in cells. Further, the NIR fs laser bubbling-formed cell-removed acellular area was used for assaying antimotility effects of the plant flavonoid apigenin.

### Gas bubble generation

An acellular rectangular area was pre-formed by NIR fs laser scanning (Fig. 1). The same laser was then scanned across the cell monolayer at a right angle, intersecting the acellular region. The gas bubble observed at cell monolayer area while no bubbles at acellular area, indicating that required pulse energy for the bubble generation was different at live cell and medium.

Series of experiments at different energy condition estimated that pulse energy threshold was 35 and 80 nJ for cell monolayer and medium, respectively (Fig. 2). The pulse irradiation condition ranging from 30 to 80 nJ could ablate cells without medium bubbling. The bubbles remained in cells for several to more than 10 s at 100 nJ pulse irradiation while immediate decayed at irradiation to medium. Below 30 nJ, gas bubbles were never generated, and cells receive no lethal damage. Above 80 nJ, the bubbles vigorously generated in both cells and medium.

### Application in biology

The NIR fs laser-based bubbling was employed to demonstrate its effectiveness in evaluating the motility of a lung cancer cell line A549, particularly in the context of assessing the antimotility effects of the plant flavonoid apigenin (Fig. 3). The acellular area closed completely within 6 h in the regular medium, whereas in the apigenin containing medium, it persisted beyond the 6 h mark. Quantitative analysis revealed a significant and dose-dependent reduction in the motility rate of A549 cells with apigenin treatment. The 50% effective apigenin concentration (ED50) was observed at 60  $\mu\text{M}$ .

### Methods

A549 cell line (RCB3677) was cultured in DMEM containing 9% FBS and antibiotics until making cell monolayer on a glass-bottom dish. NIR fs laser ablation (800 nm, 1 kHz) was executed at a speed of 600  $\mu\text{m/s}$  over an area of

50  $\times$  250  $\mu\text{m}$ . The laser pulse energy was measured with a laser power meter after the objective lens. Throughout the laser scanning process, bubble generation and cell monolayer conditions were recorded with a CMOS camera.

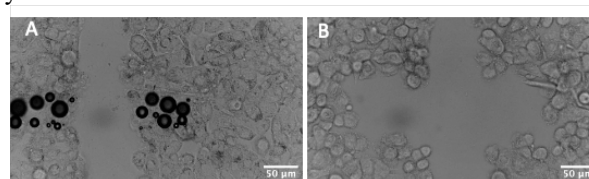


Fig. 1 Bright field micrographs of A549 cell monolayer (A) during and (B) after NIR fs laser scanning (60 nJ).

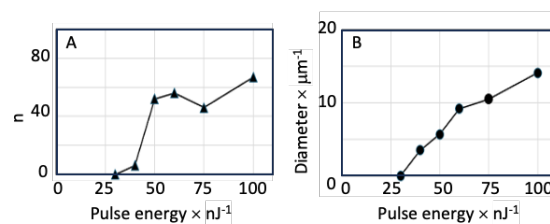


Fig. 2 Pulse energy response of micro bubbles generation in a cell monolayer. Number of bubbles (A) and bubble diameter (B) vs. pulse energy.

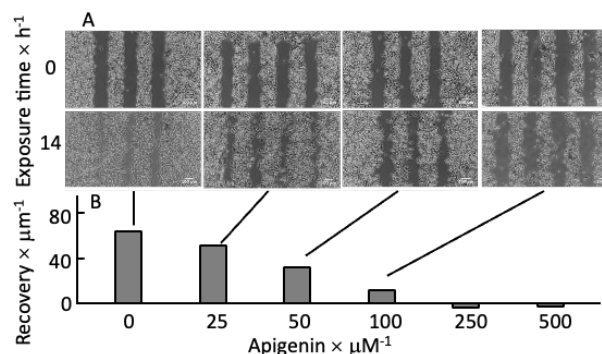


Fig. 3 Apigenin dose response in acellular area recovery. Micrographs before and 14 h after apigenin treatment (A) and the width of recovery area after 14 h of treatment (B).

### Acknowledgements

This study was supported with Pinpoint Photonics, Inc.

### References

- [1] R. Yasukuni, A. Koyanagi, Y. Tanaka, K. Okano, Y. Hosokawa, Sci. Rep. **12** 19001 (2022).
- [2] K. Okano, C.-H. Wang, Z.-Yi Hong, Yoichiro Hosokawa, Ian Liao, Biochem. Biophys. Res. **24** 199817 (2020).

# Evaluating Single Event Effects in Radiation-Tolerant Chips Using Short-Pulse Laser

Chien-Ping Hung, Shih-Bo Yu, and Jia-Han Li\*

Department of Engineering Science and Ocean Engineering, National Taiwan University, Taipei 10617, Taiwan

Email: R11525065@ntu.edu.tw, R10525092@ntu.edu.tw, \*: jiahan@ntu.edu.tw

## 1. Introduction

Radiation-tolerant chips are essential for high-reliability applications in aerospace, military, and nuclear industries, as they withstand high radiation levels without performance degradation. Short pulse lasers are used to test these chips, offering high precision and the ability to simulate various radiation effects in a controlled setting, providing valuable insights into their performance and reliability.

We test radiation-tolerant chips using 800 nm and 1060 nm lasers. Each wavelength interacts differently with the chip's material, allowing for a comprehensive analysis of their behavior under diverse conditions. This approach identifies the strengths and weaknesses of different circuit designs and materials. Additionally, these lasers can induce Single Event Effects (SEE) in the chips, enabling further analysis of their vulnerability and resilience.

## 2. Method

Our short-pulse laser platform involves two laser sources operating at wavelengths of 800 nm and 1060 nm, each with varying camera modules. Because the 1060 nm laser spectrum is entirely in the non-visible range, it is necessary to use an IR camera module to observe the irradiation position.

The figure below shows a block diagram of the experimental setup, detailing the different modules within the system.

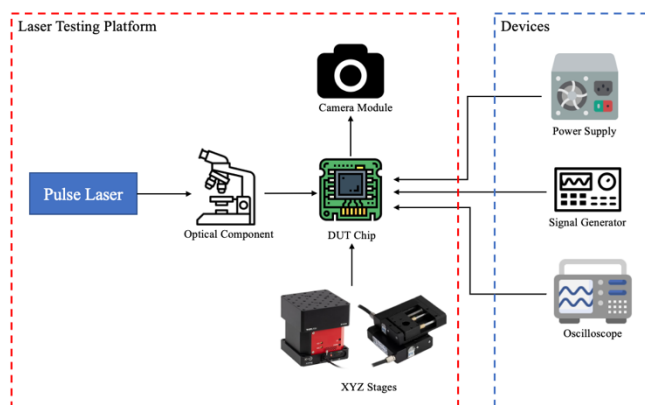


Figure 1. Block Diagram of Laser Testing Platform [1][2]

Objective of each experiment is to detect SEE in each DUT, which includes identifying SET (Single Event Transient), SEU (Single Event Upset), or bit errors in the memory. Next, based on the different DUTs, we analyze the data to assess their radiation resistance and identify sensitive areas.

## 3. Results and Discussion

The current optical path structure used in the experiments maintains a laser spot size of approximately 5  $\mu\text{m}$ . This fine spot size, combined with a minimum step size of 50 nm on the motorized platform, is essential for high-resolution scanning and accurate detection of radiation effects on the chip.

The scanning path used in the experiments follows established protocols, ensuring that the entire chip surface is systematically scanned. [3]

The analysis of irradiation results includes both front and back illumination scenarios. The observed SEE in these experiments are documented and compared. The findings indicate that the proportion of sensitive areas relative to the entire chip is very small, underscoring the importance of precise positioning and scanning during the tests.

## 4. Conclusions

The experiments demonstrate that both 800 nm and 1060 nm lasers can induce SEE in the DUT. However, it is noted that the 1060 nm laser is more suitable for back illumination experiments, likely due to its higher penetration rate compared to the 800 nm laser. [4]

The cross-section analysis of the chip can be compared with particle experiments to validate the findings. This comparison provides a more comprehensive understanding of the chip's behavior under different radiation conditions.

Additionally, the bit error rate (BER) for memory components within the chip is analyzed for its correlation with the observed SEE. This analysis helps assess the overall reliability of the memory under radiation exposure and guides the design of more robust radiation-tolerant chips.

## Acknowledgements

This research was funded by the Ministry of Science and Technology of Taiwan MOST 113-NU -E-002 -001 -NU, and financial support and technical support from the Taiwan Space Agency and Nuclear Safety Commission.

## References

- [1]<https://www.thorlabs.com/thorproduct.cfm?partnumber=KVS0>
- [2]<https://www.physikinstrumente.com/en/products/linear-stages/stages-with-stepper-dc-brushless-dc-blcd-motors/m-110-m-111-m-112-compact-linear-stage-412418433>
- [3] Lei, Zhifeng, et al. "Single Event Effects test for CMOS devices using 1064nm pulsed laser." 2011 International Conference on Quality, Reliability, Risk, Maintenance, and Safety Engineering. IEEE, 2011.
- [4] Buchner, Stephen P., et al. "Pulsed-laser testing for single-event effects investigations." IEEE Transactions on Nuclear Science 60.3 (2013): 1852-1875.

# BREAKING OF PHONON BOTTLENECK IN CsPbI<sub>3</sub> NANOCRYSTALS DUE TO EFFICIENT AUGER RECOMBINATION

**Ankit Sharma\***<sup>1</sup>, Samit K Ray<sup>2</sup>, K V Adarsh\*<sup>1</sup>

<sup>1</sup> Department of Physics, Indian Institute of Science Education and Research, Madhya Pradesh, India, 462066

<sup>2</sup> Department of Physics, Indian Institute of Technology Kharagpur, West Bengal, India, 721302,

Email id: [ankits19@iiserb.ac.in](mailto:ankits19@iiserb.ac.in) and [adarsh@iiserb.ac.in](mailto:adarsh@iiserb.ac.in)

## ABSTRACT

Inorganics lead halide perovskite (LHP) have been become appropriate system for demonstrating light-matter interaction due to their flexible bandgap tunability, defect tolerance and high photoluminescence quantum yield nature. Although, LHPs have many hallmark properties which can support highly efficient photovoltaic devices, but they lost lot of energy in carriers-phonon scattering which slow down the recombination process and decrease the efficiency. Faster thermalization time of hot carriers support electron-hole recombination at band-edge which can be exploited in optoelectronic devices either by incorporating electrons/holes transport layer for photovoltaic or fast recombination for LED. Recently, efficient photovoltaic and light emitting devices are immediate requirement for high-speed quantum technologies. Here, we have chosen CsPbI<sub>3</sub> and Cu-doped CsPbI<sub>3</sub> nanocrystals (NCs) and addressed both issues simultaneously by using transient absorption spectroscopy. Our sample can be classified as an intermediate confinement as the size of NCs is 16 nm (32 nm) for CsPbI<sub>3</sub> (Cu-doped CsPbI<sub>3</sub>) NCs which are higher than Bohr's radius (~12 nm), and give sharp excitonic peaks in ground state optical absorption with excitonic position at ~2.1 eV. Further, by femtosecond laser excitation with 400 nm and 120 fs pulse width, which is generated by second harmonic of fundamental wavelength 800 nm. The fluence-dependent measurement revealed the many-body interaction and hot carriers dynamics. At higher fluence, say 150  $\mu\text{J}/\text{cm}^2$  and above, pristine CsPbI<sub>3</sub> NCs shows breaking of phonon bottleneck effect by fast decay while Cu-doped NCs showed slow thermalization. To get insight, we have calculated Auger recombination (non-radiative) lifetime by subtractive method. The lifetime measurements clearly distinguished the appearance of contrast results due to efficient Auger process associated with pristine CsPbI<sub>3</sub> NCs. Thus, our results provide insight to incorporate metal doping and understanding about hot carrier dynamics for solar energy harvesting.

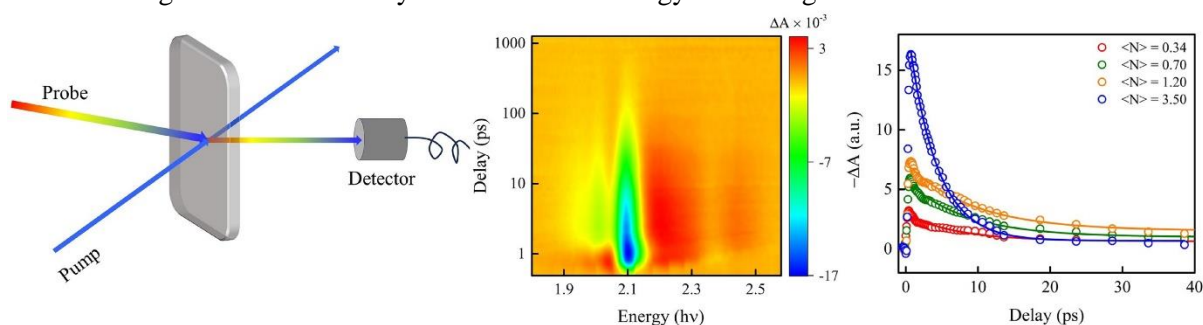


**Figure 1:** From right to left; pump-probe technique, 2D contour plot and calculated Auger recombination time.

## References:

1. H. Baker, C. M. Perez, C. Sonnichsen, D. Strandell, O. V. Prezhdo, and P. Kambhampati, ACS Nano, 17 (2023) 3913.
2. A. Dutta, R. K. Behera, P. Pal, S. Baitalik, and N. Pradhan, Angew. Chem. Int. Ed., 58 (2019) 5552.
3. Y. Yang, D. P. Ostrowski, R. M. France, K. Zhu, J. Van De Lagemaat, J. M. Luther, and M. C. Beard, Nat. Photonics., 10 (2016) 53.
4. K. Miyata, D. Meggiolaro, M. T. Trinh, P. P. Joshi, E. Mosconi, S. C. Jones, F. De Angelis, and X.-Y. Zhu, Sci. Adv., 3 (2017) e1701217.

**[17p-A31-1~11] 4.3 Laser sources and Laser applications**

[17p-A31-1]

[JSAP-Optica Joint Symposia Invited Talk] High-repetition-rate soliton frequency combs in ultrahigh-Q microresonators

○Shun Fujii<sup>1</sup> (1.Keio Univ.)

---

[17p-A31-2]

All-PM, Soliton mode-locked, dual-comb fiber laser with single-walled carbon nanotubes for high-precision spectroscopy

○(M2)Yifei Zhu<sup>1</sup>, Norihiko Nishizawa<sup>1</sup>, Shotaro Kitajima<sup>1</sup> (1.Nagoya Univ)

---

[17p-A31-3]

Applied spectroscopic measurement and analysis of gases using dual comb spectroscopy

○(M1)Naoki Takeshi<sup>1</sup>, Ryusei Uchiyama<sup>1</sup>, Kousuke Kubota<sup>1</sup>, Toshiyuki Miyazaki<sup>1</sup>, Yohei Sugiyama<sup>2</sup>, Feng-Lei Hong<sup>2</sup>, Yoshiaki Nakajima<sup>1</sup> (1.Toho Univ., 2.Yokohama Natl. Univ.)

---

[17p-A31-4]

Detection of ultrafast pulse profiles at telecom wavelength using dispersion-compensated chirped-pulse spectroscopy

○(M1)Miho Fukuoka<sup>1</sup>, Ryo Tamaki<sup>1,2</sup>, Isao Morohashi<sup>3</sup>, Ikufumi Katayama<sup>1</sup> (1.Yokohama National University, 2.KISTEC for Kanagawa Institute of Industrial Science and Technology, 3.NICT for National Institute of Information and Communications Technology)

---

[17p-A31-5]

[JSAP-Optica Joint Symposia Invited Talk] A microresonator frequency comb as a low phase-noise terahertz-wave oscillator

○Tomohiro Tetsumoto<sup>1</sup> (1.NICT)

---

[17p-A31-6]

[JSAP-Optica Joing Symposia Invited Talk] Ion Clustering Model of a Highly Er<sup>3+</sup>-doped ZBLAN Fiber Laser at 2.8  $\mu\text{m}$

○Ju Han Lee<sup>1</sup> (1.University of Seoul)

---

[17p-A31-7]

[JSAP-Optica Joint Symposia Invited Talk] mW-class broadband mid-infrared comb generation using a waveguide-type PPLN crystal and its application to dual-comb spectroscopy

○Kazumichi Yoshii<sup>1</sup>, Ryo Mitsumoto<sup>2</sup>, Naoya Kuse<sup>1</sup>, Yoshiaki Nakajima<sup>3</sup>, Takeshi Yasui<sup>1,2</sup>, Kaoru Minoshima<sup>1,4</sup> (1.pLED, Tokushima Univ., 2.Tokushima Univ., 3.Toho Univ., 4.Univ. of Electro-Commun.)

---

[17p-A31-8]

Er: fiber Comb System Optimized for mW-class Mid-infrared Light Generation Using a Waveguide-type Periodically Poled Lithium Niobate Crystal

○(D)Ryo Mitsumoto<sup>1</sup>, Naoya Kuse<sup>2</sup>, Yoshiaki Nakajima<sup>3</sup>, Takeshi Yasui<sup>1,2</sup>, Kaoru Minoshima<sup>2,4</sup>, Kazumichi Yoshii<sup>2</sup> (1.Tokushima Univ., 2.Institute of Post-LED Photonics, Tokushima Univ., 3.Toho Univ., 4.Univ. of Electro-Commun.)

---

[17p-A31-9]



## Generation of Frequency Comb Spanning 5.0-12.0 $\mu\text{m}$ Based on a Bidirectional Dual-comb Fiber Laser

○Kousuke Kubota<sup>1</sup>, Ryusei Uchiyama<sup>1</sup>, Wataru Kokuyama<sup>2</sup>, Peter G. Schunemann<sup>3</sup>, Yoshiaki Nakajima<sup>1</sup> (1.Toho Univ., 2.AIST, 3.BAE Systems)

---

[17p-A31-10]

## Development of Broadband Fiber-Based Frequency Comb Light Sources Using Nonlinearity in a Laser Cavity

○Ryusei Uchiyama<sup>1</sup>, Wataru Kokuyama<sup>2</sup>, Yoshiaki Nakajima<sup>1</sup> (1.Toho Univ., 2.NMIJ/AIST)

---

[17p-A31-11]

## [JSAP-Optica Joint Symposia Invited Talk] Highly efficient and aberration-corrected spectrometer and monochromator for extreme ultraviolet high harmonic light source

○Jie Li<sup>1,2</sup>, Hao Xu<sup>1</sup>, Kui Li<sup>1,2</sup>, Yutong Wang<sup>1</sup>, Jiyue Tang<sup>1,2</sup>, Yongjun Ma<sup>1</sup>, Ruixuan Li<sup>1,2</sup>, Jin Niu<sup>1,2</sup>, Guangyin Zhang<sup>1,2</sup>, Changjun Ke<sup>1,2</sup>, Zhongwei Fan<sup>2</sup> (1.Aerospace Information Research Institute, Chinese Academy of Sciences, 2.School of Optoelectronics, University of the Chinese Academy of Sciences)

---

# High-repetition-rate soliton frequency combs in ultrahigh-Q microresonators

Shun Fujii

<sup>1</sup> Department of Physics, Faculty of Science and Technology, Keio University, 223-8522, Japan  
E-mail: shun.fujii@phys.keio.ac.jp

Ultrahigh-Q optical microresonators are receiving intense interest as an attractive platform for miniature, high-repetition-rate frequency comb sources [1]. By leveraging the resonantly enhanced parametric gain and cascaded four-wave mixing processes, a mode-locked optical frequency comb has been discovered in anomalous dispersion regime, referred to as ‘dissipative Kerr soliton’ [2]. Recent progress in nano- and microphotronics also allows us to integrate such a microresonator into a tiny chip or a compact module that would open a possibility of practical applications including high-capacity telecommunication [3], LiDAR [4], spectroscopy [5], and low-noise microwave generation [6]. Moreover, intriguing phenomena introduced by a nonlinear resonator are an ideal target to study optical soliton physics.

In this talk, recent advances in soliton frequency combs will be given while highlighting the generation method and its applications. We show some examples of microresonators as a promising platform of microcombs and discuss the resonator fabrication techniques [7]. A soliton frequency comb with a gigahertz (GHz) repetition rate in ultrahigh-Q crystalline microresonators will be mainly featured in the light of the broadband, high-speed frequency tunability by utilizing thermal effects and a piezoelectric effect [8,9]. A high-capacity optical communication utilizing dense frequency comb components of microcombs has also been demonstrated not only in a lab-environment but also at the on-field experiment [10]. A future outlook on the soliton frequency comb technology and the cutting-edge research will be briefly overviewed.

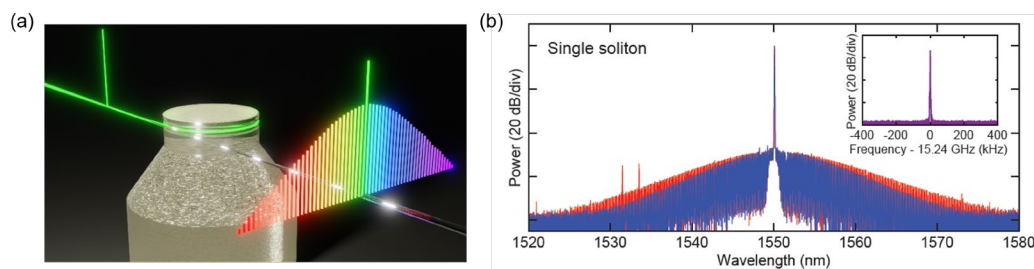


Fig. 1 (a) Schematics of frequency comb generation in an ultrahigh-Q microresonator. (b) Optical spectrum of a soliton comb with a repetition rate of 15 GHz.

## Acknowledgements

This work is supported by JSPS KAKENHI (24K17624); SCOPE (JP225003008); JST A-STEP (JPMJTR23RF); Mizuho Foundation for the Promotion of Sciences; The Murata Science Foundation; Keio University Program for the Promotion of Next Generation Research Projects.

## References

- [1] K. J. Vahala, *Optical Microcavities*, Nature **424**, 839 (2003).
- [2] T. Herr, V. Brasch, J. D. Jost, C. Y. Wang, N. M. Kondratiev, M. L. Gorodetsky, and T. J. Kippenberg, *Temporal Solitons in Optical Microresonators*, Nat. Photonics **8**, 145 (2013).
- [3] P. Marin-Palomo et al., *Microresonator-Based Solitons for Massively Parallel Coherent Optical Communications*, Nature **546**, 274 (2017).
- [4] J. Riemensberger, A. Lukashchuk, M. Karpov, W. Weng, E. Lucas, J. Liu, and T. J. Kippenberg, *Massively Parallel Coherent Laser Ranging Using a Soliton Microcomb*, Nature **581**, 164 (2020).
- [5] M.-G. Suh, Q.-F. Yang, K. Y. Yang, X. Yi, and K. J. Vahala, *Microresonator Soliton Dual-Comb Spectroscopy*, Science **354**, 600 (2016).
- [6] I. Kudelin et al., *Photonic Chip-Based Low-Noise Microwave Oscillator*, Nature **627**, 534 (2024).
- [7] S. Fujii, Y. Hayama, K. Imamura, H. Kumazaki, Y. Kakinuma, and T. Tanabe, *All-Precision-Machining Fabrication of Ultrahigh-Q Crystalline Optical Microresonators*, Optica **7**, 694 (2020).
- [8] S. Fujii, K. Wada, R. Sugano, H. Kumazaki, S. Kogure, Y. K. Kato, and T. Tanabe, *Versatile Tuning of Kerr Soliton Microcombs in Crystalline Microresonators*, Communications Physics **6**, 1 (2023).
- [9] S. Fujii, K. Wada, S. Kogure, H. Kumazaki, and T. Tanabe, *Mechanically Actuated Kerr Soliton Microcombs*, Laser Photon. Rev. (2024).
- [10] S. Fujii et al., *Dissipative Kerr Soliton Microcombs for FEC-Free Optical Communications over 100 Channels*, Opt Express **30**, 1351 (2022).

# All-PM, Soliton mode-locked, dual-comb fiber laser with single-walled carbon nanotubes for high-precision spectroscopy

Nagoya Univ, °Zhu Yifei, Shotaro Kitajima, Norihiko Nishizawa

E-mail: zhu.yifei.s6@s.mail.nagoya-u.ac.jp

## 1. Introduction

In this study, we successfully implemented an all-polarization maintaining, soliton mode-locked, fiber laser using single-walled carbon nanotubes (SWNTs)[1]. The laser employs a mechanical sharing concept to achieve high mutual coherence[2]. It has a repetition frequency of 70.9 MHz and a frequency difference of approximately 100 Hz. We conducted the experiments of dual comb spectroscopy for hydrogen cyanide (HCN) gas and observed the corresponding absorption spectra[3].

## 2. Experimental setup and results

The experimental setup, as shown in Fig. 1 for the all-PM dual comb soliton fiber laser, involved a 980nm pump laser diode (LD) providing the necessary power to the erbium-doped fiber (EDF) via a wavelength-division multiplexing (WDM) coupler. The EDF served as the gain medium. A 50:50 optical coupler split the pump beam into two paths, and single-walled carbon nanotubes (SWNTs) were used as a saturable absorber to achieve passive mode-locking. An optical isolator prevented back reflections, and a delay line fine-tuned the cavity length. Two outputs were overlapped, and used for dual comb spectroscopy.

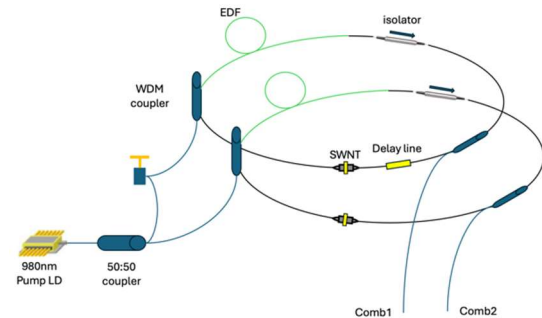


Fig.1. Configuration of All-Soliton Fiber Laser

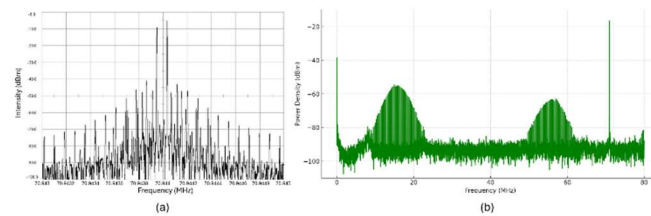


Fig.2. (a)Frequency spectrum (b) RF beat spectra

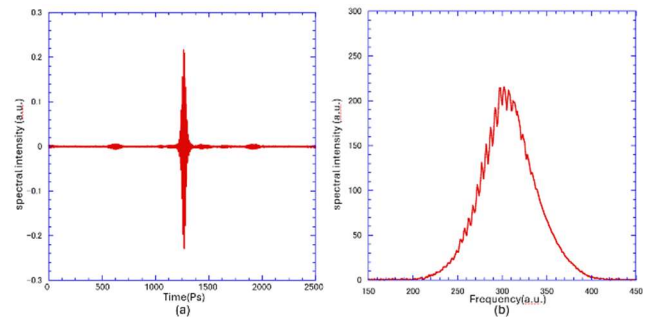


Fig.3. Temporal and Spectral Characteristics after HCN absorption

The results presented in Fig. 2(a) shows the RF spectra of the all-PM dual comb soliton fiber laser. The repetition frequencies were 70.94 MHz and the frequency difference was  $\sim 100$  Hz. Figure 2(b) shows RF beat spectra. The RF beat signals corresponding to the pulse spectral shapes were observed clearly without overlapping, which confirms the usefulness for dual comb spectroscopy.

Figure 3(a) shows the observed temporal interferogram when hydrogen cyanide (HCN) gas was used as the sample. The intense center burst and FID signals were observed clearly. Figure 3(b) shows the spectra after FFT. The absorption features corresponding to HCN gas can be observed as small dips in the spectral intensity, indicating the good stability and resolution of the developed dual comb system.

## 3.Reference

- [1] Y. Saito, M. Yamanaka, Y. Sakakibara, E. Omoda, H. Kataura, and N. Nishizawa, Opt. Express 27, 17868-17875 (2019).
- [2] Y. Nakajima, Y. Kusumi, K. Minoshima, Opt. Lett. 46(21), 5401-5404 (2021).
- [3] N. Nishizawa et al., Conf. on Lasers Electro-Optics (CLEO) 2020, SW4R.52.

# Applied spectroscopic measurement and analysis of gases using dual comb spectroscopy

Toho Univ.<sup>1</sup>, Yokohama National Univ.<sup>2</sup>, °Naoki Takeshi<sup>1</sup>, Ryusei Uchiyama<sup>1</sup>, Kousuke Kubota<sup>1</sup>,  
Toshiyuki Miyazaki<sup>1</sup>, Yohei Sugiyama<sup>2</sup>, Feng-Lei Hong<sup>2</sup>, Yoshiaki Nakajima<sup>1</sup>  
E-mail: yoshiaki.nakajima@sci.toho-u.ac.jp

In recent years, laser spectroscopy has been used in a wide range of fields, including environmental science, and industry, owing to its non-contact and remote gas sensing capabilities. Several spectroscopic techniques have been reported for measuring gas temperature and concentration. In particular, Rotational-state Distribution Thermometry(RDT) has demonstrated to date, taking advantage of the broadband and high accuracy of DCS technique<sup>1)</sup>.

In this research, gas temperature and concentration were measured by dual comb spectroscopy (DCS). A DCS system employing two mode-locked Erbium fiber lasers with a repetition rate ( $f_{\text{rep}}$ ) of 100 MHz was used to measure acetylene( $^{12}\text{C}_2\text{H}_2$ ) gas and hydrogen cyanide(HCN) gas. To simultaneously measure ro-vibration transition of two gases, the  $f_{\text{rep}}$  difference( $\Delta f_{\text{rep}}$ ) was set to 407 Hz. Each frequency combs were amplified using Er-doped fiber amplifiers (EDFAs), and a spectral bandwidth of approximately 100 nm around 1550 nm was achieved. The baseline for normalizing the spectra was obtained by FFT on the interferograms, which were separated into a central burst signal and free-induced decay (FID) on the time axis. Fig. 1(a) shows transmittance spectra obtained by the proposed technique. We calculated the gas temperature of acetylene by analyzing this spectrum. The technique for measuring gas temperature has been reported as RDT, and we calculated the temperature using the proposed method based on RDT. The proposed method obtaining the temperature from linear fit by plotting the profile by RDT on a logarithmic scale. Fig. 1(b) shows a log scale plot of R branch. The presentation will report on the analysis results and validity.

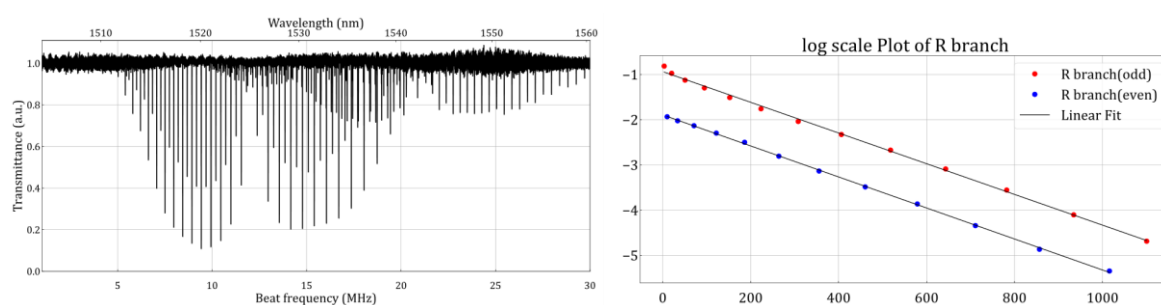


Fig. 1(a) Transmittance spectra (acetylene, hydrogen cyanide)

(b) log scale plot of R branch (acetylene)

## References

- 1) Y. Shimizu, et al., Appl. Phys. B **124**, 71 (2018)

# Detection of ultrafast pulse profiles at telecom wavelength using dispersion-compensated chirped-pulse spectroscopy

Miho Fukuoka<sup>1</sup>, Ryo Tamaki<sup>1,2</sup>, Isao Morohashi<sup>3</sup>, Ikufumi Katayama<sup>1</sup>

<sup>1</sup> Yokohama National University, <sup>2</sup> KISTEC, <sup>3</sup> NICT

E-mail: fukuoka-miho-cp@ynu.jp

## 1. Introduction

Chirped-pulse spectroscopy [1] has been developed as a single-shot measurement technique to visualize ultrafast dynamics of irreversible phenomena that are difficult to investigate with repeated measurements. Dispersion-compensated chirped-pulse spectroscopy, or the time-lens technique [2], were proposed to improve the waveform distortions that appears in the conventional method [3], and near-infrared pump-probe and terahertz waveform detection were demonstrated [4]. In this study, we aimed to use this technique to detect ultrafast intensity profiles of telecom wavelength lasers. We demonstrated asynchronous single-shot detection of femtosecond pulse profiles at telecom wavelength with the time resolution higher than 1 ps. Our method to measure the ultrafast intensity profiles of modulated light sources at telecom wavelength is very promising for developing high-speed optical fiber communication technology.

## 2. Experiment

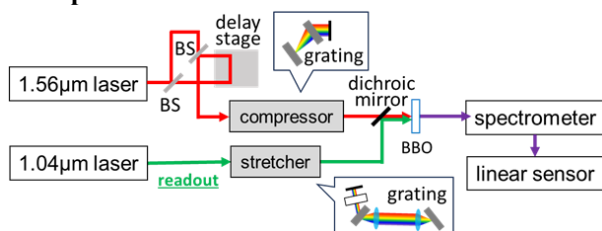


Fig.1 Schematic of the experiment.

Figure 1 shows a schematic of the experimental system. Two light sources were used asynchronously: An Yb fiber laser (center wavelength 1.04  $\mu\text{m}$ , pulse width 394 fs, repetition rate 100 kHz) as the readout light and an Er fiber laser (center wavelength 1.56  $\mu\text{m}$ , pulse width 98 fs, repetition rate 50 MHz) as the telecom wavelength light to be measured. The readout light was positively chirped with a group delay dispersion (GDD) of 0.71  $\text{ps}^2$  by a grating pair stretcher, and the target light was negatively chirped with a GDD of -0.71  $\text{ps}^2$  by a grating pair compressor for dispersion compensation. The target 1.56  $\mu\text{m}$  light was divided into two pulses by a Mach-Zehnder interferometer to control the relative delay of them. The chirped readout light and the target light were coaxially focused onto a  $\beta\text{-BaB}_2\text{O}_4$  (BBO) crystal by a dichroic mirror and an achromatic lens. Sum-frequency generation spectra were

measured by a spectrometer with a CMOS line sensor.

## 3. Results and discussion

The sum-frequency spectra for the case where the target light was dispersion-compensated by the compressor (red) and without compensation (blue) are shown in Figure 2. The delay time between double pulses was set to  $\Delta t = 3$  ps, which was used to calibrate the horizontal axis of the linear sensor from frequency domain to time domain. While the waveform distortion was observed without compensation, we detected sharp peaks of the double pulses with compensation, and found that the temporal resolution was less than 1 ps because their full width at half maximum were estimated to be 0.92 ps and 0.97 ps, respectively. Because the two lasers are asynchronous, the detection probability is determined by the coincidence ratio of laser with chirped readout pulses, which was in good agreement with the observed rate of about 1/1000.

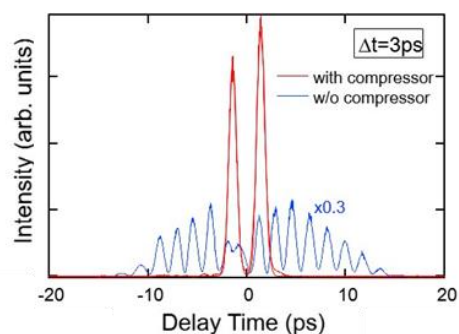


Fig.2 Single-shot pulses obtained from sum-frequency spectrum with and without dispersion compensation.

## 4. Summary

We demonstrated that dispersion-compensated chirped-pulse spectroscopy can be used for asynchronous single-shot detection of femtosecond pulse profiles at telecom wavelength in time domain. This technique may be applied to the real-time detection of ultrafast modulation of telecom wavelength band lasers.

## References

- [1] Z. Jiang and X.-C. Zhang, Opt. Lett. **23**, 1114 (1998).
- [2] P. Suret, Nat. Commun. **7**, 13136 (2016).
- [3] J. R. Fletcher, Opt. Exp. **10**, 1425 (2002).
- [4] R. Tamaki, *et al.*, Opt. Exp. **31**, 40142 (2023).



## A microresonator frequency comb as a low phase-noise terahertz-wave oscillator

National Institute of Information and Communications Technology, Tomohiro Tetsumoto

E-mail: ttetsumo@nict.go.jp

Optical frequency combs have been essential tools in fields such as time-keeping, metrology, and spectroscopy. Traditionally, these combs are generated using bulky mode-locked lasers, which are primarily employed in scientific laboratories due to their complexity and size. However, advancements in microresonator fabrication technologies have enabled the generation of optical frequency combs in a more compact and accessible manner. These microresonator frequency combs, or microcombs, have opened up various potential civilian applications, including optical communication and LiDAR [1]. Among these applications is the generation of low phase-noise millimeter- and terahertz-waves. The repetition frequency of a microcomb typically falls within the millimeter- and terahertz-wave domains (10 GHz to 1 THz), owing to the small dimensions of a microresonator. Generating radio waves in this frequency range is achievable by detecting a microcomb with an ultrafast photodiode. In recent years, there has been significant research interest in implementing these generation systems in a compact form and with ultralow phase noise levels [2-5]. In this talk, I will present research background, general methods and recent our activities related to low phase-noise terahertz-wave generation using microcombs.

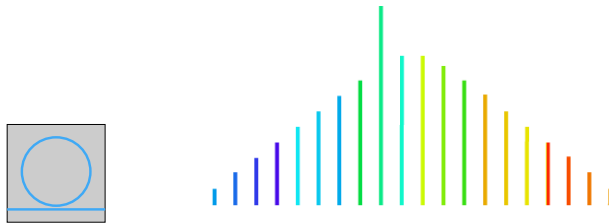


**Fig. 1: Schematic illustration of microcomb generation and its application in terahertz-wave generation. A microcomb is excited with a continuous-wave laser via cascaded four-wave mixing in a microresonator. A terahertz wave is generated by detecting a microcomb with a repetition frequency located in the terahertz-wave domain.**

- [1] T. J. Kippenberg, et al., “Dissipative Kerr solitons in optical microresonators,” *Science* **361**, eaan8083 (2018).
- [2] T. Tetsumoto, et al., “Optically referenced 300 GHz millimetre-wave oscillator,” *Nature Photonics* **15** (7), 516-522 (2021).
- [3] Kudelin, I., Groman, W., Ji, QX. et al. Photonic chip-based low-noise microwave oscillator. *Nature* **627**, 534–539 (2024).
- [4] Y. Zhao, et al., “All-optical frequency division on-chip using a single lase,” *Nature* **627**, 546–552 (2024).
- [5] S. Sun, et al., “Integrated optical frequency division for microwave and mmWave generation,” *Nature* **627**, 540–545 (2024).

# Ion Clustering Model of a Highly Er<sup>3+</sup>-doped ZBLAN Fiber Laser at 2.8 μm

Ju Han Lee

School of Electrical and Computer Engineering, University of Seoul, Seoul 02504, South Korea  
E-mail: j.h.lee@ieee.org

Soft glass-based mid-infrared (MIR) fiber lasers have garnered significant attention in the field of laser technology, owing to their substantial potential for diverse applications such as environmental monitoring, defense countermeasures, and medical uses [1-5]. Among these soft glass materials, ZBLAN (ZrF<sub>4</sub>-BaF<sub>2</sub>-BaF<sub>2</sub>-LaF<sub>3</sub>-AlF<sub>3</sub>-NaF) has emerged as a promising host material for rare-earth-doped fibers operating in the MIR spectral range [7]. A number of investigations on MIR fiber lasers have been conducted using ZBLAN fibers doped with ions such as Er<sup>3+</sup>, Dy<sup>3+</sup>, and Ho<sup>3+</sup> [8-10]. One issue in high power rare-earth-doped ZBLAN fiber lasers or amplifiers is that the output efficiencies are lower than the theoretically expected quantum limit [11-13].

This issue has been investigated by various research groups and they proposed modified theoretical models to account for the reduced quantum efficiency. Gorjan *et al.* proposed an approach called “Weakly Interaction” (WI) [13] and this approach has been developed by various research groups. The WI approach assumes that the energy transfer processes such as cross relaxation (CR) and homogeneous up-conversion (HUC) are significantly weaker within optical fiber than within bulk glass. In this model, the CR and HUC parameters, which are obtained by iterative numerical calculation followed by comparison with experimental data, adopted rather than the parameters obtained from bulk material measurements [13]. This approach induced various fundamental concerns: First, the reason why the energy transfer processes in ZBLAN fiber should be an order weaker than those in bulk, is unclear from a viewpoint of physics. Second, ion clustering is not included in the WI approach. The WI approach assumes that all of Er<sup>3+</sup> ions are isolated ones without clustering.

Bisson *et al.* recently proposed an energy transfer model with a cubic atomic population dependence [14]. They empirically found that HUC and CR rates from the assumption that the excited ions are uniformly distributed in the material system without considering ion clustering. They verified that the proposed model gives better agreement with experimental data for multiple erbium concentrations.

Srinivasan *et al.* proposed an Er:ZBLAN fiber model with ion clustering effect [15]; however, the model assumed that all the clustered ions are in the ground state due to rapid de-excitation caused by fast cross relaxation and thus is believed to have overestimated the ion clustering effect.

In this presentation, I review our recent investigation

results on modeling of a highly Er<sup>3+</sup>-doped ZBLAN fiber laser with ion clustering effect. Unlike previous WI-based models, our model does not employ any WI energy transfer parameters but use conventional ionic interaction parameters. Our model assumes that the ion population at each energy level is governed by two separate rate equations: one is for single ions and the other for clustered ions [16, 17]. The efficacy of our proposed model an Er:ZBLAN fiber laser is verified by comparing the numerically calculated output curves with the experimentally measured ones in a Fabry-Pérot laser setup based on commercially available Er<sup>3+</sup>-doped ZBLAN fiber for two different pumping wavelengths of 790 and 970 nm. The calculation results from our model were in good agreement with the experimentally measured ones under a relative clustering level of 18.1%, indicating that ion clustering needs to be considered for theoretical performance prediction in highly Er<sup>3+</sup>-doped ZBLAN fiber lasers [18].

## Acknowledgements

This work was supported by the National Research Foundation of Korea (NRF) grant funded by the Korea government (MSIP) (NRF-2021R1A2C1004988, NRF-2021R1A5A1032937), Republic of Korea.

## References

- [1] S. D. Jackson, *Nature Photonics* **6** (2012) 423–431 (2012).
- [2] B. I. Vasil'ev et al., *Quantum Electronics*, **36**, (2006) 801-820.
- [3] J. J. Scherer et al., *Applied Physics B*, **110**, (2013) 271-277.
- [4] H. H. P. T. Bekman et al., *Proc. in European symposium on optics and photonics for defence and security* **5615**, (2004) 27-38.
- [5] D. Halmer et al., *Appl. Phys. B, Lasers Opt.*, **85**, (2006) 437–443.
- [6] S. D. Jackson and R. K. Jain, *Opt. Express* **28** (2020) 30964–31019.
- [7] X. Zhu and N. Peyghambarian, *Adv. OptoElectronics* **2010** (2010). Art. ID 501956.
- [8] O. Henderson-Sapir et al., *Opt. Lett.* **41**, (2016) 1676–1679.
- [9] M. Z. Amin et al., *J. Light. Technol.* **38** (2020) 5801-5808.
- [10] S. D. Jackson, *Opt. Lett.* **34** (2009) 2327–2329.
- [11] V. Petrov, *Prog. Quantum Electron.*, **42** (2015) 1–106 (2015).
- [12] M. Gorjan et al., *IEEE J. Quantum Electron.*, **47**, (2011) 262–273.
- [13] J. Li and S. D. Jackson, *IEEE J. Quantum Electron.*, **48** (2012) 454–464.
- [14] W. Bisson et al., *IEEE Journal of Quantum Electronics*, **60** (2024) 1-9.
- [15] B. Srinivasan et al., *J. Opt. Soc. Amer. B*, **17** (2000) 178–181.
- [16] J. Jung, J. Lee, K. Lee, and J. H. Lee, *J. Lightwave Technol.* **41**, (2023) 265-274.
- [17] J. Nilsson et al., *J. Lightwave Technol.* **13** (1995) 341–349.
- [18] J. Jung, K. Lee, J. Kim, and J. H. Lee, *Opt. Quant. Electron.* **56**, (2023) 79.

## **[17p-A31-1~11] 4.3 Laser sources and Laser applications**

**[17p-A31-7] [JSAP-Optica Joint Symposia Invited Talk] mW-class broadband mid-infrared comb generation using a waveguide-type PPLN crystal and its application to dual-comb spectroscopy**

○Kazumichi Yoshii<sup>1</sup>, Ryo Mitsumoto<sup>2</sup>, Naoya Kuse<sup>1</sup>, Yoshiaki Nakajima<sup>3</sup>, Takeshi Yasui<sup>1,2</sup>, Kaoru Minoshima<sup>1,4</sup> (1.pLED, Tokushima Univ., 2.Tokushima Univ., 3.Toho Univ., 4.Univ. of Electro-Commun.)

キーワード : mid-infrared comb、waveguide-type PPLN crystal、dual-comb spectroscopy

We generated a broadband mid-infrared comb of 2.7-4.5  $\mu\text{m}$  with an output of 2.7 mW based on an Er: fiber comb as a fundamental light using a waveguide-type PPLN crystal. A dual-comb spectrometer using these combs was developed.

---

# Er:fiber Comb System Optimized for mW-class Mid-infrared Light Generation Using a Waveguide-type Periodically Poled Lithium Niobate Crystal

○(D)Ryo Mitsumoto<sup>1,†</sup>, Naoya Kuse<sup>2</sup>, Yoshiaki Nakajima<sup>3</sup>, Takeshi Yasui<sup>1,2</sup>,  
Kaoru Minoshima<sup>2,4</sup>, Kazumichi Yoshii<sup>2,†</sup>

Tokushima Univ.<sup>1</sup>, Institute of Post-LED Photonics, Tokushima Univ.<sup>2</sup>,  
Toho Univ.<sup>3</sup>, Univ. of Electro-Commun.<sup>4</sup>

†) Present affiliation: Ryukoku Univ.

E-mail: y24d001@mail.ryukoku.ac.jp

## 1. Introduction

The mid-infrared (MIR) region is rich in molecular absorption lines that can be used to identify trace gases and other substances. The 3-5  $\mu\text{m}$  wavelength region, which is called the first MIR atmospheric window, is of particular interest because it contains the fingerprints of many hydrocarbons, nitrogen oxides, and greenhouse gases. In the near-infrared region, new spectroscopic techniques using optical frequency combs have been actively studied, and particularly, dual-comb spectroscopy using two optical combs is attracting attention as a broadband, high-precision, and high-speed Fourier spectroscopy method. Against this background, dual-comb spectrometers in the 3-5  $\mu\text{m}$  range are expected to be a new real-time and open-pass measurement method for environmental measurements and breath analysis.

Previous works [1,2] have successfully generated broadband MIR combs over 2.5-5  $\mu\text{m}$  in a single-pass configuration in which light from a broadened Er:fiber comb is injected into a waveguide-type periodically poled lithium niobate crystal (PPLN WG). However, the output power of the MIR comb was limited to a few hundred  $\mu\text{W}$ , which was insufficient for practical applications. In this work, we report the generation of a single-pass configuration broadband MIR comb with an output power of mW-class in the 2.4 - 4.5  $\mu\text{m}$  range using a PPLN WG of the same type as in the previous works [1].

## 2. Experimental setup

An Er:fiber comb with a repetition rate of  $f_{\text{rep}} = 100$  MHz was used as the fundamental light source. The output from the oscillator is amplified to 390 mW with a polarization-maintaining Er-doped fiber amplifier (PM EDFA) pumped both forward and backward by three laser diodes, and spectrally broadened in a polarization-maintaining highly nonlinear fiber (PM HNLF). The output beam from the PM HNLF was then coupled into a PPLN WG using butt coupling to generate the MIR comb.

## 3. Results

The dependences of MIR comb output on polarization-maintaining fiber (PMF) length between PM EDFA and PM HNLF, PM HNLF length, PPLN WG crystal length, and fundamental light output power, respectively, were measured. Figure 1 (a) shows the measured MIR comb output power versus PMF length between PM EDFA and PM HNLF when the PM-HNLF length and PPLN WG length are fixed. MIR comb with power greater than 1 mW is generated when the PMF is shorter than 110 cm (472 mm is the cutback limit). From these results, for a fixed set of PPLN WG crystal lengths and PM HNLF lengths, we are able to determine the range of Er:fiber comb light dispersion values required for mW-class MIR comb generation. Figure 1 (b) shows the spectra of the MIR combs measured over a long time by optimizing the setup. A broadband MIR comb of 2.4 to 4.5  $\mu\text{m}$  is stably generated over a long time due to the difference frequency generation of the PPLN WG.

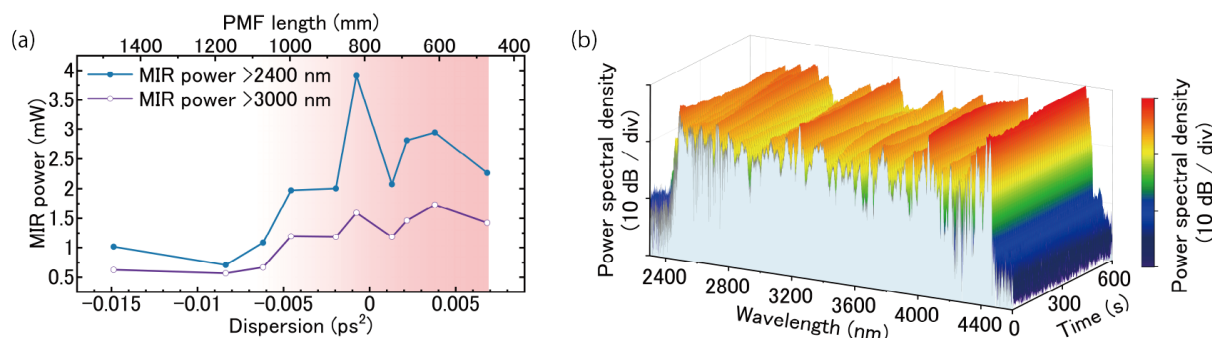


Fig. 1 (a) Measured MIR comb power 2.4-4.5  $\mu\text{m}$  and 3.0-4.5  $\mu\text{m}$  as a function of PMF length between PM EDFA and PM HNLF. The red region indicates the range of MIR power above 1 mW. (b) Long-term stability of MIR comb spectra obtained by optimizing the setup.

## References

- [1] K. Iwakuni, *et al.*, Opt. Lett., **41**, 3980 (2016).
- [2] A. S. Kowligy, *et al.*, Opt. Lett., **43**, 1678 (2018).
- [3] R. Mitsumoto, *et al.*, Conference on Lasers and Electro-Optics, JTh2A.91 (2023).

## Generation of Frequency Comb Spanning 5.0-12.0 $\mu\text{m}$ Based on a Bidirectional Dual-comb Fiber Laser

Toho Univ.<sup>1</sup>, AIST.<sup>2</sup>, BAE Systems<sup>3</sup> <sup>○</sup>Kousuke Kubota<sup>1</sup>, Ryusei Uchiyama<sup>1</sup>,

Wataru Kokuyama<sup>2</sup>, Peter G. Schunemann<sup>3</sup>, Yoshiaki Nakajima<sup>1</sup>

E-mail: yoshiaki.nakajima@sci.toho-u.ac.jp

Long-wavelength infrared (LWIR) spectroscopy has relied on Fourier transform spectroscopy (FTS) with incoherent thermal light sources. The thermal sources with low-brightness limit focusing ability, long-distance propagation, and spectroscopic sensitivity. Moreover, the FTS systems use mechanical moving stages, leading to a trade-off between spectral resolution and acquisition time. On the contrary, dual-comb spectroscopy (DCS) [1] surpasses conventional FTS in terms of bandwidth coverage, resolution, acquisition time, and sensitivity. However, DCS necessitates a complex laser source system to generate two optical combs with high relative frequency stability. To address this challenge, we have developed a bidirectional dual-comb fiber laser [2] capable of generating dual optical frequency combs from a single laser source.

In this research, we have developed an LWIR comb generation system based on our high-coherence, ultra-broadband bidirectional dual-comb fiber laser. Figure 1(a) shows a schematic illustration of our experimental setup for LWIR comb generation using a bi-directional dual-comb fiber laser. We operated the laser within a single-laser cavity in both clockwise (CW) and counter-clockwise (CCW) directions simultaneously. The outputs of CW direction from the laser were coupled into a bi-directionally pumped EDFA and increased output power by the EDFA. The amplified frequency comb underwent spectral broadening through a normal dispersion highly nonlinear fiber (ND-HNLF). The ND-HNLF output pulses were collimated using the first off-axis parabolic mirror and compensated for using fused silica glasses. After compression, the second off-axis parabolic mirror focused the pulses into an OP-GaP crystal. Finally, the output from the crystal was collimated once more by the third off-axis parabolic mirror. Figure 2(a) shows the spectrum of the generated LWIR optical frequency comb, spanning the range of 5.0 to 12.0  $\mu\text{m}$ . This work was supported by the New Energy and Industrial Technology Development Organization (NEDO), the Paloma Foundation.

1) I. Coddington, et al., *Optica* **3**, 414 (2016).

2) Y. Nakajima, et al., *Optics Express* **27**, 5931 (2019).

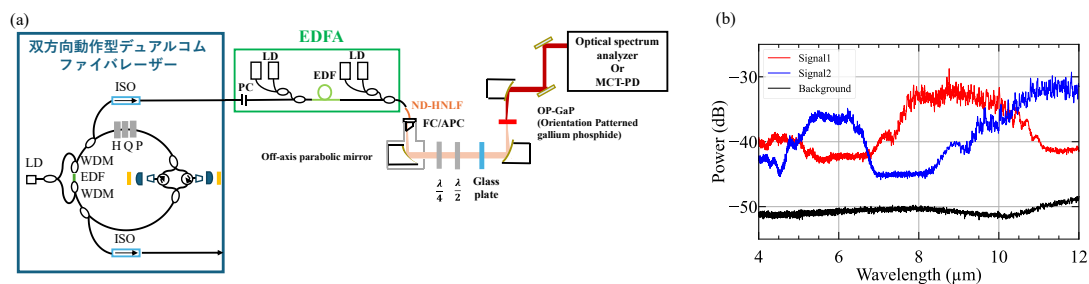


Fig. 1 (a) Experimental setup of bi-directional dual-comb fiber laser and LWIR comb generation system.  
(b) Optical spectra of OP-GaP output.



## Development of Broadband Fiber-Based Frequency Comb Light Sources Using Nonlinearity in a Laser Cavity

Toho Univ.<sup>1</sup>, NMIJ/AIST<sup>2</sup>, <sup>○</sup>Ryusei Uchiyama<sup>1</sup>, Wataru Kokuyama<sup>2</sup>, Yoshiaki Nakajima<sup>1</sup>

E-mail: yoshiaki.nakajima@sci.toho-u.ac.jp

Optical frequency combs play a vital role in spectroscopic measurements, serving as an array of continuous-wave (CW) lasers with precisely aligned modes at equidistant frequency intervals across a broadband spectrum. Broadening the spectral bandwidth is essential for conducting precise spectroscopic measurements across various wavelength ranges. A technique for achieving a broadband spectrum directly at the laser direct output has been reported, which involves integrating a nonlinear medium distinct from the gain medium in the laser cavity<sup>1</sup>. This technique exploits the high optical power stored in the cavity to generate a broadband spectral bandwidth surpassing that of the gain spectrum from 600 to 1350 nm.

In this study, we attempted the direct generation of a broadband frequency comb by integrating an optical fiber with a small core size into a fiber laser cavity to enhance nonlinearity. Figure 1(a) illustrates the experimental setup of the broadband fiber-based frequency comb developed in this study. A single mode fiber (SMF) optimized at 1  $\mu\text{m}$  (1  $\mu\text{m}$  SMF) is utilized as the nonlinear medium. The SMF has a smaller mode field diameter (MFD) than the SMF optimized for operation at 1.5  $\mu\text{m}$ , enhancing nonlinearity in the cavity. Owing to the influence of group velocity dispersion in fibers, the optical pulses propagating within the cavity exhibit variations in pulse width and peak power. To enhance the nonlinearity, we strategically inserted a 1  $\mu\text{m}$  SMF at the position where the peak power reached its maximum between the WDM and 10/90 couplers. Figure 1(b) shows the optical spectra of the output when a 1  $\mu\text{m}$  SMF of 10 cm length is inserted at each position shown in Fig. 1(a). Notably, position 2 exhibits the most broadened spectrum, featuring a full width at half maximum (FWHM) of 50 nm and a 10-dB width of 95 nm, an output power of 0.62 mW.

This work was supported by the New Energy and Industrial Technology Development Organization (NEDO), the Japan Science and Technology Agency Adaptable and Seamless Technology Transfer Program through Target-driven R&D (A-STEP) Grant Number JPMJTM22B6, the Paloma foundation.

1) R. Ell, et al., Opt. Lett. **26**, 373–375 (2001).

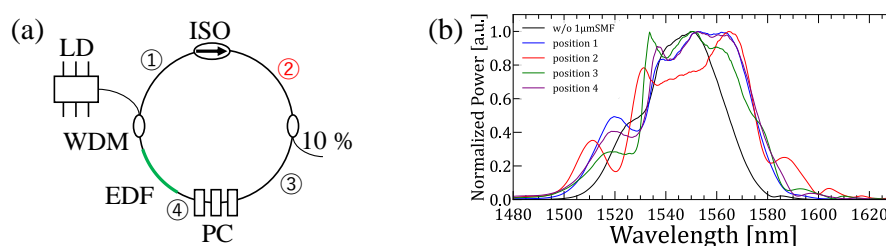


Fig. 1(a) Experimental setup for laser resonators. (b) Optical spectra of the output when a 1  $\mu\text{m}$  SMF of 10 cm length is inserted at each position shown in Fig. 1(a).

# Highly efficient and aberration-corrected spectrometer and monochromator for extreme ultraviolet high harmonic light source

Jie Li<sup>1,2</sup>, Hao Xu<sup>1</sup>, Kui Li<sup>1,2</sup>, Yutong Wang<sup>1</sup>, Jiyue Tang<sup>1,2</sup>, Yongjun Ma<sup>1</sup>, Ruixuan Li<sup>1,2</sup>, Jin Niu<sup>1,2</sup>,  
Guangyin Zhang<sup>1,2</sup>, Changjun Ke<sup>1,2</sup>, Zhongwei Fan<sup>2</sup>

<sup>1</sup>Aerospace Information Research Institute, Chinese Academy of Sciences, Beijing 100094, China

<sup>2</sup>School of Optoelectronics, University of Chinese Academy of Sciences, Beijing 100049, China

Email: lijie430@aircas.ac.cn

The unique EUV and soft X-ray light sources based on high harmonic generation have been successfully utilized for probing femtosecond-to-attosecond dynamics in atomic, molecular, and solid-state systems in the EUV and soft X-ray spectral regions. However, due to the relatively low conversion efficiency of the high harmonic generation process, the applicability of these sources has been predominantly limited to spectroscopy, where fewer photons are required. Here, we report on the development of a spectrometer optimized for EUV light sources to address the low throughput efficiency over a broad spectral range, and to achieve a tunable, monochromatic, aberration-free mode of operation. Our approach combines high efficiency, high spectral resolution, broad spectral range, and polarization-maintaining at the same time. This simple design is also cost-effective and easy to use for a vast range of EUV and soft X-ray wavelengths.

The spectrometer consists of a grazing angle toroidal mirror and a single grating in a conical diffraction geometry, where the aberrations are eliminated for a single high harmonic beam (see Fig. 1). We show experimentally and theoretically that the total throughput efficiency can be greater than 40% across a very broad wavelength range. Furthermore, to achieve the best possible spectral resolution and aberration-free imaging, we optimize the parameters and the relative orientation of a single toroidal mirror and a grating to cancel the aberration caused by each optical element at a specific EUV wavelength, without compromising the diffraction efficiency of the grating. All these experimental results agree extremely well with our theoretical design considerations.

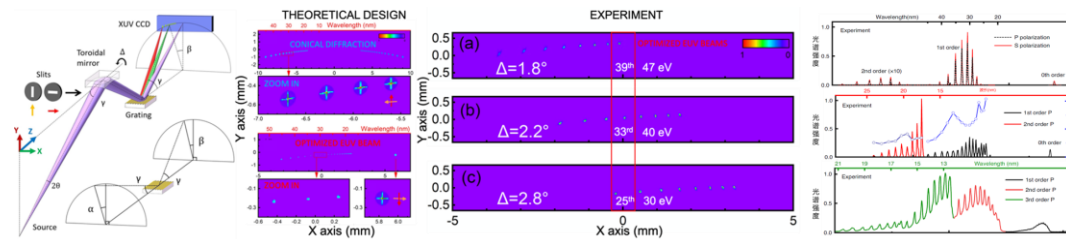


Figure 1. (Left) Experimental setup: EUV beam optimization using a dual-optic imaging spectrometer achieved through a simple axial rotation of a toroidal focusing mirror with respect to a grating operating in a conical diffraction mode. Theoretical ray tracing of aberration uncorrected and corrected EUV beam. (Right) Experimental well-focused, aberration-free, EUV beams of the 39<sup>th</sup>, 33<sup>th</sup>, and 25<sup>th</sup> harmonics optimized at the center of the CCD at toroidal angles  $\Delta$  of 1.8° (a), 2.2° (b) and 2.8° (c), respectively.

**[17a-A35-1~9] 4.5 Nanocarbon and 2D Materials**

[17a-A35-1]

[JSAP-Optica Joint Symposia Invited Talk] Shift current photovoltaics in single domain ferroelectric SnS

○Kosuke Nagashio<sup>1</sup> (1.UTokyo)

[17a-A35-2]

Absorption Enhancement of Excitons in WS<sub>2</sub> by Silicon Huygens' Metasurface○(D)Dingwei Chen<sup>1</sup>, Junichi Takahara<sup>1,2</sup> (1.GSE. Osaka Univ., 2.PC. Osaka Univ.)

[17a-A35-3]

Magnetic brightening and its dynamics of defect-localized excitons in monolayer WSe<sub>2</sub>○(DC)Yubei Xiang<sup>1</sup>, Keisuke Shinokita<sup>1</sup>, Kenji Watanabe<sup>2</sup>, Takashi Taniguchi<sup>3</sup>, Kazunari Matsuda<sup>1</sup> (1.Institute of Advanced Energy, Kyoto Univ., 2.Research Center for Electronic and Optical Materials, NIMS, 3.Research Center for Materials Nanoarchitectonics, NIMS)

[17a-A35-4]

[JSAP-Optica Joint Symposia Invited Talk] Electronic and excitonic properties of semiconductor bilayer moiré system revealed by optical spectroscopy

○Yuya Shimazaki<sup>1,2</sup> (1.RIKEN, CEMS, 2.Univ. of Tokyo, Eng.)

[17a-A35-5]

Exciton-driven Floquet-Bloch States in 2D Semiconductors

Vivek Pareek<sup>1</sup>, David Bacon<sup>1</sup>, ○(DC)XING ZHU<sup>1</sup>, Yang-Hao Chan<sup>2</sup>, Fabio Bussolotti<sup>3</sup>, Nicholas S Chan<sup>1</sup>, Joel Perez Urquiza<sup>1</sup>, Kenji Watanabe<sup>4</sup>, Takashi Taniguchi<sup>4</sup>, Michael K. L. Man<sup>1</sup>, Julien Madeo<sup>1</sup>, Diana Qiu<sup>5</sup>, Kuan Eng Johnson Goh<sup>3,6,7</sup>, Felipe H. da Jornada<sup>8,9</sup>, Keshav M. Dani<sup>1</sup> (1.FSU, OIST, 2.IAMS, Academia Sinica, 3.IMRE, A\*STAR, 4.NIMS, 5.Yale Univ., 6.NUS, 7.NTU, 8.Stanford Univ., 9.SLAC)

[17a-A35-6]

[JSAP-Optica Joint Symposia Invited Talk] Exciton transfer and interface excitons in mixed-dimensional heterostructures

○Nan Fang<sup>1</sup>, Yih-Ren Chang<sup>1</sup>, Shun Fujii<sup>1,2</sup>, Daiki Yamashita<sup>1,3</sup>, Mina Maruyama<sup>4</sup>, Yanlin Gao<sup>4</sup>, Chee Fai Fong<sup>1</sup>, Daichi Kozawa<sup>1,5</sup>, Keigo Otsuka<sup>1,6</sup>, Kosuke Nagashio<sup>6</sup>, Susumu Okada<sup>4</sup>, Yuichiro Kato<sup>1</sup> (1.RIKEN, 2.Keio Univ., 3.AIST, 4.Univ. of Tsukuba, 5.NIMS, 6.UTokyo)

[17a-A35-7]

Identification and manipulation of valley coherence in monolayer WSe<sub>2</sub>○(D)Wang Haonan<sup>1</sup>, Kenji Watanabe<sup>2</sup>, Takashi Taniguchi<sup>2</sup>, Kazunari Matsuda<sup>1</sup> (1.IAE, Kyoto Univ., 2.NIMS)

[17a-A35-8]

Dry transfer and optical properties of CVD-grown transition metal dichalcogenides

○Wenjin Zhang<sup>1</sup>, Tomoya Ogawa<sup>1</sup>, Takahiko Endo<sup>1</sup>, Kenji Watanabe<sup>2</sup>, Takashi Taniguchi<sup>2</sup>, Takumi Sannomiya<sup>3</sup>, Kazunari Matsuda<sup>4</sup>, Yasumitsu Miyata<sup>1</sup> (1.Tokyo Metropolitan Univ., 2.NIMS, 3.Tokyo Tech., 4.Kyoto Univ.)

[17a-A35-9]

Structural and Electrical Properties of Millimeter Scale CVD Graphene

○(P)Sengottaiyan Chinnasamy<sup>1</sup>, Kazunori Hirose<sup>1</sup>, Yuta Kurachi<sup>1</sup>, Masanori Hara<sup>1</sup>,  
Masamichi Yoshimura<sup>1</sup> (1.Toyota Tech. Inst.)

---

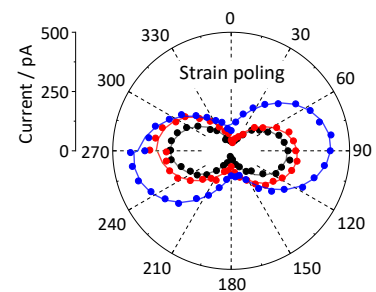
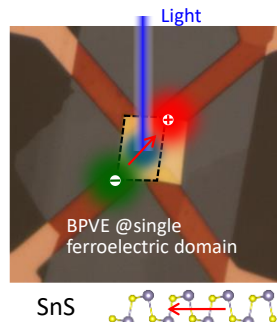
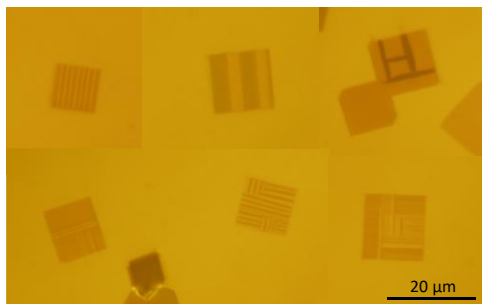
## Shift current photovoltaics in single domain ferroelectric SnS

Kosuke Nagashio

Department of Materials Engineering, The University of Tokyo, Japan

nagashio@material.t.u-tokyo.ac.jp

The bulk photovoltaic effect (BPVE) in ferroelectrics, wherein spontaneous polarization can be reversed within crystals lacking centrosymmetry, encompasses the significant contribution of ferroelectric domain walls (DWs), known as DW-PVE. Nevertheless, the separation between intrinsic BPVE within the domain and DW-PVE remains unexplored in two-dimensional (2D) ferroelectrics, notwithstanding its significant importance. In this study, we have successfully grown sizable crystals of 2D ferroelectric SnS, facilitating comprehensive yet intricate examination of domain configurations utilizing polarized optical microscopy and piezoresponse force microscopy. By properly selecting the large ferroelectric single domain within SnS crystals, uniform intrinsic BPVE across the domain was unequivocally demonstrated. Furthermore, to further enhance intrinsic BPVE, manipulation of strain poling increased photocurrent, suggesting that locally distributed polarizations due to imperfection introduced in SnS crystals are aligned by strain. These results will offer a new avenue for rigorous comprehension of DW-PVE in 2D ferroelectrics.



### References:

- [1] Ferroelectric domain: Adv. Funct. Mater. 2024, (in revision).
- [2] Shift current: Adv. mater. 2023, 35, 2301172.
- [3] FET: ACS appl. mater. interfaces 2022, 14, 19928.
- [4] Spiral growth: Chem. mater. 2021, 33, 186.
- [5] Phase stability: ACS appl. mater. interfaces 2021, 13, 43282.
- [5] Monolayer growth: Nanoscale 2020, 12, 23274.
- [6] Ferroelectricity: Nature commun. 2020, 11, 2428.
- [7] Electrical transport: Nanoscale 2018, 10, 22474.
- [8] Mechanical exfoliation: MRS Advances 2018, 3, 2809.



# Absorption Enhancement of Excitons in WS<sub>2</sub> by Silicon Huygens' Metasurface

Dingwei Chen<sup>1</sup> and Junichi Takahara<sup>1,2</sup>

<sup>1</sup> Graduate School of Engineering, Osaka University, 2-1 Yamadaoka, Suita, Osaka 565-0871, Japan

<sup>2</sup> Photonics Center, Graduate School of Engineering, Osaka University, 2-1 Yamadaoka, Suita, Osaka 565-0871, Japan

E-mail: takahara@ap.eng.osaka-u.ac.jp

## 1. Introduction

Strong visible absorption of light in semiconducting two-dimensional transition-metal dichalcogenides (TMDCs) is essential for improving the photocarrier extraction efficiency in optoelectronic devices [1,2]. However, their ultrathin thickness leads to limited optical absorption [3]. To accomplish adequate light absorption, a dielectric-based Silicon (Si) Huygens' metasurface (HMS) based on degenerate critical coupling (DCC) can realize superimposed modes enhancement effects on WS<sub>2</sub> [4, 5].

In this study, we design and fabricate Si HMS to enhance the absorption of WS<sub>2</sub>. The enhancement is as high as 0.56 in simulation. Meanwhile, we demonstrate that small monolayer WS<sub>2</sub> fragment is successfully transferred to the metasurface utilizing poly (propylene) carbonate (PPC) films.

## 2. Results and Discussion

First, we designed and fabricated Si metasurface. In our design, the degenerate of Electric Dipole (ED) and Magnetic Dipole (MD) modes was realized (namely, the so-called HMS). Figure 1a shows the designed structure and Scanning Ion Microscope (SIM) image of the sample. The Si metasurface was comprised by cylindrical resonator arrays with period  $d = 334$  nm, radius  $r = 112$  nm, and thickness  $h = 89$  nm.

As shown in Fig. 1b, we simulated and measured the absorption spectra of the metasurface. Because the height and radius of prepared sample was different from designed, the degenerate was not completely achieved. However, we partially realized DCC with ED/MD modes shown as the fitting curve 1 and 2.

Without background, the simulated absorption of WS<sub>2</sub> on metasurface is increased by about 0.52 (15.5 times) under DCC condition compared with WS<sub>2</sub> on Si substrate as shown in Fig. 1c. The inset shows the raw absorption spectrum of WS<sub>2</sub> on metasurface and the corresponding fitting curve.

Furthermore, we tried to transfer monolayer WS<sub>2</sub> on the metasurface by dry release transfer method with PPC films. The optical microscope photo is shown in Fig. 1d. Due to the thermoplastic properties of PPC

film, the adhesion between WS<sub>2</sub> and PPC decreases at about 70 °C. With temperature control, WS<sub>2</sub> flakes on PPC can be easily dry-transferred.

Our observations undeniably establish the groundwork for a material platform enabling high-efficiency photodetection, energy harvesting, and thermal emission based on TMDCs.

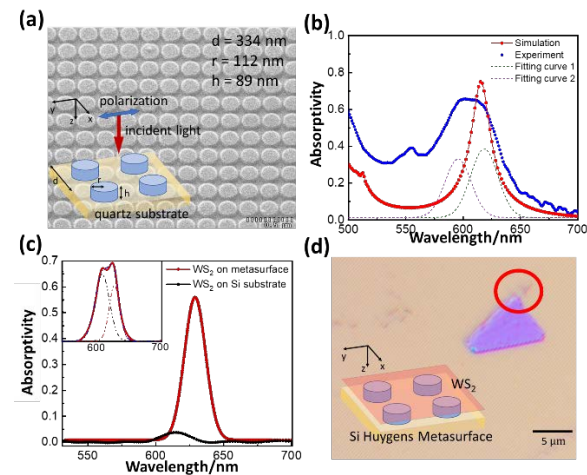


Figure 1. (a) The SIM image of the sample and the schematic illustration of Si HMS, which was constituted by Mie resonator arrays with  $h = 89$  nm,  $d = 334$  nm and  $r = 112$  nm, and (b) experimental and simulated [6] absorptivity for the metasurface, and MD /ED mode fitting curves with the experimental spectrum. (c) Simulated absorptivity subtracting background for WS<sub>2</sub> on Si substrate and HMS. (d) Optical microscope image of monolayer WS<sub>2</sub> transferred on the metasurface. The scale bar is 5  $\mu$ m.

## Acknowledgements

This work was supported by JSPS KAKENHI 23H00274. DW. C. was supported by CSC (No. 202204910108).

## References

- [1] H. Li *et al.*, Phys. Rev. B. **105** 165305 (2022).
- [2] W. Xu *et al.*, Nature **541** 62 (2017).
- [3] E. Buhara *et al.*, Plasmonics **16** 687 (2021).
- [4] D. Chen and J. Takahara, The 84th JSAP Autumn Meeting, 20a-A602-4 (2023).
- [5] D. Chen, J. Takahara, OPIC, ICNN5-02 (2024).
- [6] J. Gwang-Hun *et al.*, Nanophotonics. **8** 2 (2019).

# Magnetic brightening and its dynamics of defect-localized excitons in monolayer WSe<sub>2</sub>

Yubei Xiang<sup>1</sup>, Keisuke Shinokita<sup>1</sup>,  
Kenji Watanabe<sup>2</sup>, Takashi Taniguchi<sup>3</sup> and Kazunari Matsuda<sup>1</sup>

<sup>1</sup> Institute of Advanced Energy, Kyoto University, <sup>2</sup> Research Center for Electronic and Optical Materials, NIMS, <sup>3</sup> Research Center for Materials Nanoarchitectonics, NIMS  
E-mail: xiang.yubei.86h@st.kyoto-u.ac.jp

## 1. Introduction

Quantum light sources, in particular solid-states single-photon emitters have attracted considerable attention due to their crucial roles in the field of quantum information technologies. Recently, defects in two-dimensional monolayer transition metal dichalcogenides, such as tungsten diselenide (WSe<sub>2</sub>), have been demonstrated to be promising candidates for stable and bright quantum light sources [1,2]. However, the external controllability of single-photon emission has not been fully understood.

## 2. Results

In this study, we have investigated the nature and dynamics of defect-localized exciton emissions in monolayer WSe<sub>2</sub> under magnetic fields for novel single-photon emitters with external tunability. Figure 1(a) depicts the typical photoluminescence (PL) spectra of monolayer WSe<sub>2</sub> at low temperature. The strong and sharp PL peaks are clearly observed and can be attributed to defect-localized exciton emissions. Figure 1(b) shows the photon statistics obtained from defect-localized exciton emissions using the Hanbury-Brown and Twiss experimental setup, demonstrating photon antibunching behavior. This indicates that the observed defect-localized exciton emission functions as a single-photon emitter. Moreover, the polarization-resolved PL spectra with an in-plane magnetic field are shown in Figure 1(c), where each PL spectrum is normalized by the peak intensity of the higher energy states for each magnetic field. The PL intensity of the lower energy states significantly

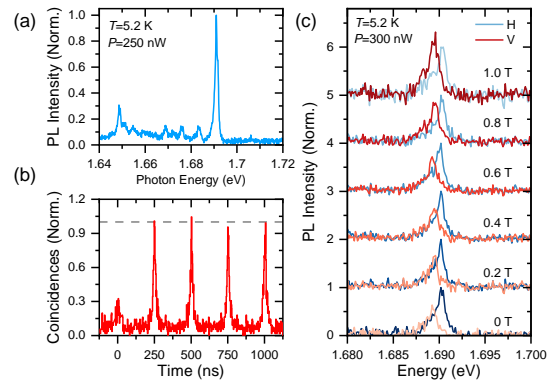


**Figure 1** (a) Typical low temperature PL spectra of monolayer WSe<sub>2</sub>. (b) Second-order correlation measurement of the localized exciton emission. The cross-talk signals in the histogram are removed. (c) Polarization-resolve PL spectra with the increasing in-plane magnetic fields.

increases with increasing magnetic field within a small range below 1 T. We discuss the dynamics of the magnetic brightening from the defect-localized exciton emission in monolayer WSe<sub>2</sub>.

## 3. Conclusions

Our findings on the physical nature of defect-localized exciton states in monolayer WSe<sub>2</sub> and the dynamics of the magnetic brightening offer a novel approach to manipulating single-photon emitters using an external magnetic field in the field of quantum optics application.

## References

- [1] Linhart, L. et al. *Phys. Rev. Lett.*, **123**, 146401 (2019).
- [2] Jadczyk, J. et al. *ACS Nano.*, **15**, 19165–19174 (2021).

## Electronic and excitonic properties of semiconductor bilayer moiré system revealed by optical spectroscopy

RIKEN CEMS<sup>1</sup>, Univ. of Tokyo, Eng.<sup>2</sup>, °Yuya Shimazaki<sup>1, 2</sup>

E-mail: yuya.shimazaki@riken.jp

The recent discovery of many-body physics such as strongly correlated electrons, superconductivity and magnetism in precisely twist angle-controlled bilayer graphene at a magic angle revived enormous interest on moiré lattice system. Many-body physics in bilayer moiré system is not limited to graphene, but rather robustly appears in 2D semiconductor materials such as transition metal dichalcogenides (TMDs). Monolayer semiconductor TMDs have conduction and valence bands with relatively large effective mass which enhances the influence of Coulomb interactions, also resulting in formation of strongly bound excitons with optical excitations. In twisted bilayer semiconductor TMDs, the superlattice effect due to the formation of moiré lattice further enhances the influence of Coulomb interaction for electrons and expected to show many-body electronic phases. On the other hand, it has been a long-standing issue that semiconductor TMDs have poor electrical contact properties due to the formation of Schottky barriers, which has been hindering the observation of those many-body electronic phases in moiré system via transport measurement. Instead, we performed optical microscopic spectroscopy experiments of a bilayer TMD moiré system which revealed many-body electronic phase, quantum coupled excitonic states, and novel quantum mixture of exciton – hole states.

Here we studied a twisted bilayer MoSe<sub>2</sub> system with monolayer hBN tunnel barrier (Figure 1). The combination of the top and bottom gates allows to control the chemical potential and the perpendicular electric field independently. The energy shifts of excitonic resonances (exciton polarons) probe the carrier densities of the top and bottom layers independently, which revealed the formation of moiré sub bands in the system. By changing the energy detuning between layers via control of the perpendicular electric field, we observed an abrupt charge transfer at  $\nu = 1$  (1 electron per moiré lattice) and a stabilized charge transfer plateau at  $\nu = 2$  around zero detuning point, which evidences the existence of strongly correlated electrons [1]. We further observed the existence of charge order at these fillings from the Umklapp scattering of excitons [2]. Last but not least, we figured out that the tunnel coupling of holes through the monolayer hBN barrier results in formation of hybrid exciton states [1] and electric field-controlled exciton – hole Feshbach resonances [3].

### References

- [1] Y. Shimazaki et. al., *Nature* **580**, 472 (2020)
- [2] Y. Shimazaki et. al., *Phys. Rev. X* **11**, 021027 (2021)
- [3] I. Schwartz\*, Y. Shimazaki\* et. al., *Science* **374**, 336 (2021)

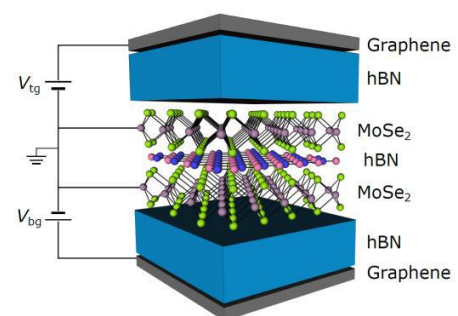


Figure 1: Schematic sketch of MoSe<sub>2</sub>/hBN / MoSe<sub>2</sub> heterostructure

## Exciton-driven Floquet-Bloch States in 2D Semiconductors

Vivek Pareek<sup>1†</sup>, David Bacon<sup>1†</sup>, Xing Zhu<sup>1†</sup>, Yang-Hao Chan<sup>2</sup>, Fabio Bussolotti<sup>3</sup>, Nicholas S Chan<sup>1</sup>, Joel Pérez Urquiza<sup>1</sup>, Kenji Watanabe<sup>4</sup>, Takashi Taniguchi<sup>5</sup>, Michael K. L. Man<sup>1</sup>, Julien Madéo<sup>1</sup>, Diana Qiu<sup>6</sup>, Kuan Eng Johnson Goh<sup>3,7,8</sup>, Felipe H. da Jornada<sup>9,10\*</sup>, Keshav M. Dani<sup>1\*</sup>

<sup>1</sup>Femtosecond Spectroscopy Unit, Okinawa Institute of Science and Technology Graduate University; Onna, Okinawa, Japan 904-0495, <sup>2</sup>Institute of Atomic and Molecular Sciences, Academia Sinica, and Physics Division, National Center of Theoretical Sciences; Taipei, Taiwan, <sup>3</sup>Institute of Materials Research and Engineering (IMRE), Agency for Science, Technology and Research (A\*STAR); 2 Fusionopolis Way, Singapore, 138634 Singapore, <sup>4</sup>Research Center for Functional Materials, National Institute for Materials Science; 1-1 Namiki, Tsukuba, Ibaraki 305-0044, Japan, <sup>5</sup>International Center for Materials Nanoarchitectonics, National Institute for Materials Science; 1-1 Namiki, Tsukuba, Ibaraki 305-0044, Japan, <sup>6</sup>Department of Mechanical Engineering and Materials Science, Yale University; New Haven, CT, USA, <sup>7</sup>Department of Physics, National University of Singapore; 2 Science Drive 3, Singapore, 117551 Singapore, <sup>8</sup>Division of Physics and Applied Physics, School of Physical and Mathematical Sciences, Nanyang Technological University; 50 Nanyang Avenue, Singapore 639798, Singapore, <sup>9</sup>Department of Materials Science and Engineering, Stanford University; Stanford, CA, USA <sup>10</sup>Stanford PULSE Institute, SLAC National Accelerator Laboratory; Menlo Park, CA, USA († equal contribution)

\*Email address: jornada@stanford.edu, kmdani@oist.jp

### 1. Introduction

Floquet engineering, in which a temporal periodic drive breaks the continuous temporal symmetry and dynamically engineers the electronic structure, has attracted enormous attention in condensed matter physics. However, only a handful of studies have experimentally demonstrated Floquet effects driven by optical fields [1-4], which are limited by weak light-matter interactions. Meanwhile, theoretically it is predicted that an internal oscillating field, such as phonons and excitons, could also drive giant Floquet effects without the undesirable aspects of the optical case [5,6]. In this talk, we will discuss the experimental observation of the Floquet-Bloch states induced by the excitons in 2D semiconductors.

and angle-resolved photoemission spectroscopy (Tr-ARPES). The experimental setup, as employed in our previous studies [7,8], consists of a home-built table-top beamline generating 21.7-eV XUV probe to photoemit the electrons from the sample. The electrons are further analyzed by a momentum microscope to map the 3D band-structure of the material ( $E$ ,  $k_x$ ,  $k_y$ ).

To study Floquet effects driven by excitons, a pump pulse resonant with the  $\text{WS}_2$  A exciton (2.1 eV) is used to excite the sample. As shown in figure 1(b), we observe the striking change of dispersion around the center of valence band top, transforming from ground-state parabolic dispersion to Mexican-hat dispersion. This change results from the hybridization of the valence band and the conduction band replica dressed by excitons. Similar change is also observed in the replica of valence band at 2.1 eV.

### 3. Conclusions

Using Tr-ARPES, we studied the Floquet-Bloch states in 2D semiconductors, driven by the excitonic field internally.

### Acknowledgements

This work was supported in part by JSPS Kakenhi grant number 21H01020. Funding was also provided in part by the Femtosecond Spectroscopy Unit of the Okinawa Institute of Science and Technology Graduate University. We thank the OIST engineering support section for their support.

### References

- [1] Y. H. Wang et al., Science 342, 453 (2013).
- [2] S. Ito et al., Nature 616, 696 (2023).
- [3] S. Zhou et al., Nature 614, 7946 (2023).
- [4] S. Aeschlimann et al., Nano Lett. 21, 5028 (2021).
- [5] Y.-H. Chan et al., PNAS 120, e2301957120 (2023).
- [6] H. Hübener et al., Nano Lett. 18, 1535 (2018).
- [7] J. Madéo et al., Science 370, 1199 (2020).
- [8] M. K. L. Man et al., Science Advances 7, eabg0192 (2021).

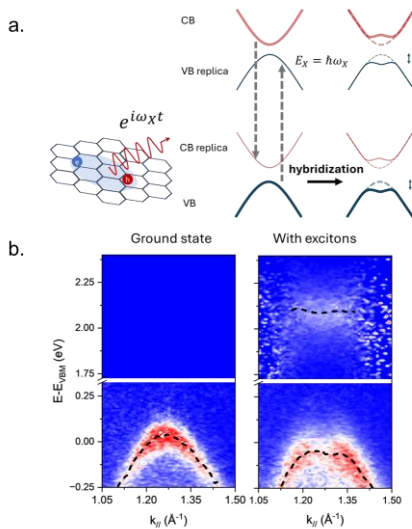


**Figure 1. a.** Schematics of Floquet effects driven by excitons. The bands are replicated by energy of exciton. The original valence band hybridize with the conduction band replica, transforming to Mexican-hat dispersion. **b.** ARPES spectrum of (left) ground state of valence band, (right) the valence band and its replica with excitons ( $N_X = 3 \times 10^{12} \text{ cm}^{-2}$ ).

### 2. Experiment

We perform experiments on monolayer  $\text{WS}_2$  using time-

## Exciton transfer and interface excitons in mixed-dimensional heterostructures

○N. Fang<sup>1,2</sup>, Y. R. Chang<sup>1</sup>, S. Fujii<sup>2,3</sup>, D. Yamashita<sup>2,4</sup>, M. Maruyama<sup>5</sup>, Y. Gao<sup>5</sup>, C. F. Fong<sup>1</sup>,  
D. Kozawa<sup>1,2,6</sup>, K. Otsuka<sup>1,7</sup>, K. Nagashio<sup>8</sup>, S. Okada<sup>5</sup>, Y. K. Kato<sup>1,2</sup>

<sup>1</sup> *Nanoscale Quantum Photonics Laboratory, RIKEN Cluster for Pioneering Research, Saitama, Japan*

<sup>2</sup> *Quantum Optoelectronics Research Team, RIKEN Center for Advanced Photonics, Saitama, Japan*

<sup>3</sup> *Department of Physics, Keio University, Kanagawa, Japan*

<sup>4</sup> *Platform Photonics Research Center, National Institute of Advanced Industrial Science and Technology (AIST), Ibaraki, Japan*

<sup>5</sup> *Department of Physics, University of Tsukuba, Ibaraki, Japan*

<sup>6</sup> *Research Center for Materials Nanoarchitectonics, National Institute for Materials Science, Ibaraki, Japan*

<sup>7</sup> *Department of Mechanical Engineering, The University of Tokyo, Tokyo, Japan*

<sup>8</sup> *Department of Materials Engineering, The University of Tokyo, Tokyo, Japan*

E-mail: nan.fang@riken.jp

Two-dimensional van der Waals heterostructures have introduced unconventional phenomena that emerge at atomically precise interfaces, and further development is expected in mixed-dimensional heterostructures. Here we discuss exciton physics in 1D-2D heterostructures consisting of one-dimensional carbon nanotubes and two-dimensional tungsten diselenide. Both the chirality and the layer number are identified before assembling the clean and free-standing heterostructures, allowing for investigation of the band alignment effects. For small band gap nanotubes corresponding to type I band alignment, exciton transfer is observed [1]. The mixed-dimensional heterostructures display a remarkable exciton reservoir effect where the longer-lifetime excitons within the two-dimensional semiconductor are funneled into carbon nanotubes through diffusion. With increasing the nanotube band gap, the transfer efficiency shows a pronounced enhancement indicating a resonance in the band alignment. For large band gap nanotubes corresponding to type II band alignment, exciton transfer diminishes whereas bright emission peaks originating from the interface are identified [2]. We assign the peaks to interface excitons as they only appear in type-II heterostructures. Localization of low-energy interface excitons is indicated by extended lifetimes as well as small excitation saturation powers, and photon correlation measurements confirm room-temperature quantum emission. With mixed-dimensional van der Waals heterostructures where band alignment can be engineered, new opportunities for quantum photonics are envisioned.

This work is supported by JSPS (KAKENHI JP22K14624, JP22K14625, JP21K14484, JP22K14623, JP22H01893, JP21H05233, JP22F22350, JP23H00262, JP20H02558, JP24K08296) and MEXT (ARIM JPMXP1222UT1135). Y.R.C. is supported by JSPS (International Research Fellow). N.F. and C.F.F. are supported by the RIKEN Special Postdoctoral Researcher Program. We thank the Advanced Manufacturing Support Team at RIKEN for technical assistance.

### References

- [1] N. Fang, Y. R. Chang, D. Yamashita, S. Fujii, M. Maruyama, Y. Gao, C. F. Fong, K. Otsuka, K. Nagashio, S. Okada, and Y. K. Kato, [Nat. Commun. 14, 8152 \(2023\)](#).
- [2] N. Fang, Y. R. Chang, S. Fujii, D. Yamashita, M. Maruyama, Y. Gao, C. F. Fong, D. Kozawa, K. Otsuka, K. Nagashio, S. Okada, and Y. K. Kato, [Nat. Commun. 15, 2871 \(2024\)](#).



# Identification and manipulation of valley coherence in monolayer WSe<sub>2</sub>

Haonan Wang<sup>1</sup>, Kenji Watanabe<sup>2</sup>, Takashi Taniguchi<sup>3</sup>, and Kazunari Matsuda<sup>1</sup>

<sup>1</sup>Institute of Advanced Energy, Kyoto University, <sup>2</sup>Research Center for Electronic and Optical Materials, NIMS, <sup>3</sup>Research Center for Materials Nanoarchitectonics, NIMS

E-mail: wang.haonan.36t@st.kyoto-u.ac.jp

## 1. Introduction

The monolayer transition metal dichalcogenide (TMDs) are granted with valley degree of freedom due to broken inversion symmetry, and strong spin-orbit coupling. The degenerated states at band-edges of K(K') valley possess information of valley pseudospin, which experiences intervalley decoherence process during emission [1]. With valley decoherence not coupling to any radiative dipole, direct probing or manipulation of valley coherence in the time domain has remain a challenge. Here we propose a method of optically exploring the valley coherence time in the time-domain measurement.

## 2. Results

We have developed a method of direct measuring valley coherence time of the free exciton in monolayer WSe<sub>2</sub>. By employing polarized interferometer, the decoherence process between K and K' valley excitons under various temperature and excitation power are directly measured. **Figure 1(a)** shows the typical interferogram arising from valley coherence. The exacted valley coherence times from the interferogram are plotted in **Figure 1(b)**. It can be seen that the values of valley coherence time remain stable under temperature from 4 to 30 K, which is consistent with the previous result [2]. Moreover, the valley coherence time gradually decreases due to increased exciton-exciton collision with increasing excitation power condition. We also explored the valley coherence of monolayer (1L) WSe<sub>2</sub> device with changing carrier density in the spectral and time domain. A wide tuning range of degree of linear polarization

(DOLP) is observed, with the values ranging from nearly 0% under heavily positive doping, to 50% under heavily negative doping conditions. The measured valley coherence time shows the similar trend as the DOLP, which will be further discussed in detail.

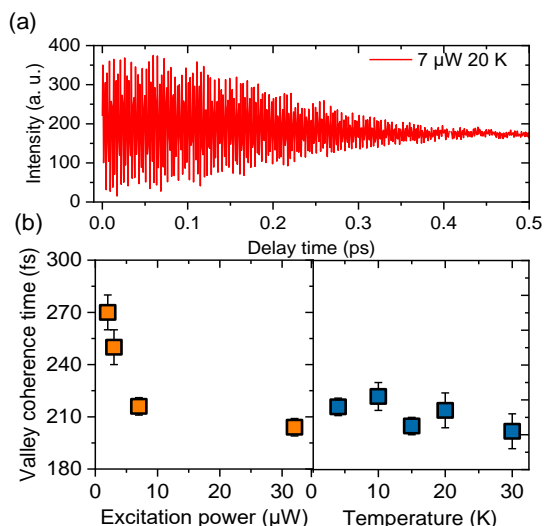


**Figure 1** (a) Interferogram of intervalley decoherence process of free exciton in 1L-WSe<sub>2</sub> under 7  $\mu$ W and 20 K. (b) Extracted valley coherence time of free exciton in 1L-WSe<sub>2</sub> under various temperature and excitation power

## 3. Conclusions

A new direct method of exciton valley coherence has been applied to 1L-WSe<sub>2</sub> in the time-domain. The detail of intervalley decoherence process is explored under various temperature, excitation power and carrier doping condition, which will facilitate further understanding of valleytronics in 1L-TMDs.

## References

- [1] A. Jones, et al. *Nat. Nanotech* **8**, 634–638 (2013).
- [2] K. Hao, et al. *Nat. Phys* **12**, 677–682 (2016).

# Dry transfer and optical properties of CVD-grown transition metal dichalcogenides

Wenjin Zhang<sup>1</sup>, Tomoya Ogawa<sup>1</sup>, Takahiko Endo<sup>1</sup>, Kenji Watanabe<sup>2</sup>, Takashi Taniguchi<sup>2</sup>, Takumi Sannomiya<sup>3</sup>, Kazunari Matsuda<sup>4</sup>, Yasumitsu Miyata<sup>1</sup>

<sup>1</sup> Tokyo Metropolitan University, <sup>2</sup> National Institute for Materials Science, <sup>3</sup> Tokyo Institute of Technology, <sup>4</sup> Institute of Advanced Energy, Kyoto University

E-mail: ymiyata@tmu.ac.jp; wjzhang@tmu.ac.jp

Improving the transfer technique of 2D materials is an important issue for their fundamental study and future applications. Even though much progress has been made, the search for exfoliated thin and sufficiently large flakes of 2D materials is still very time-consuming. In contrast, the use of triangular single crystals of transition metal dichalcogenides (TMDCs) allows for easy determination of crystal orientation and thus easy control of twist angles. However, there have been only a few reports on dry transfer and its effect on the optical properties of CVD-grown TMDCs. One of the major technical difficulties is the efficient peeling of CVD-grown monolayers from growth substrates. In general, CVD-grown monolayers are known to adhere strongly to growth substrates compared to exfoliated flakes. Compared with the solution or chemical assisted transfer of CVD grown TMDCs, the dry transfer should keep the intrinsic properties of as grown TMDCs because the solution processes induce physical or chemical property modulations of TMDCs. To expand the versatility of this growth-assisted approach, it is highly desirable to demonstrate the dry transfer and investigate its effects on physical properties.

Here, we report the dry transfer and optical properties of CVD-grown TMDCs using a simple acrylic resin stamp [1]. We introduced the melting and solidification process of an acrylic resin stamp in contact with the sample to improve the adhesion of the stamp. This improvement allows us to efficiently pick up the single crystals of various TMDC monolayers with desired grain size and density from the SiO<sub>2</sub> surface, and to perform high-throughput and continuous dry transfer. Furthermore, we also fabricated the hBN-encapsulated TMDC monolayers and various twisted bilayers including MoSe<sub>2</sub>/MoS<sub>2</sub>, MoSe<sub>2</sub>/WSe<sub>2</sub>, and MoSe<sub>2</sub>/WS<sub>2</sub>. The interlayer interaction and quality of dry-transferred, CVD-grown TMDCs were characterized by using photoluminescence (PL), cathodoluminescence (CL) spectroscopy, and cross-sectional electron microscopy. The prominent PL peaks of interlayer excitons can be observed for the MoSe<sub>2</sub>/MoS<sub>2</sub> with small twist angles at room temperature (Fig.1). We also found that the optical spectra were locally modulated due to the nanosized bubbles, which are formed by the presence of interface carbon impurities (Fig.2). The present findings provide a widely applicable potential of the present method and enable an efficient search of the emergent optical and electrical properties of TMDC-based vdW heterostructures.

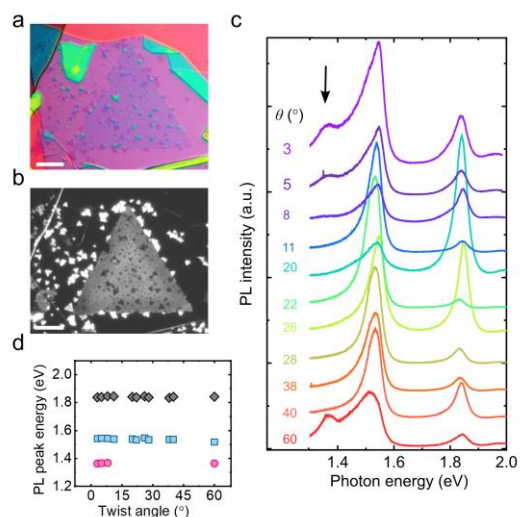


**Figure 1.** (a) Optical and (b) PL images of hBN encapsulated MoS<sub>2</sub>/MoSe<sub>2</sub> heterobilayers. Scale bars are 10  $\mu\text{m}$ . (c) Room-temperature PL spectra of twisted area with various twist angle. (d) PL peak positions of intralayer exciton from MoS<sub>2</sub> and MoSe<sub>2</sub>, and interlayer exciton from MoSe<sub>2</sub>/MoS<sub>2</sub> heterobilayer with different twist angles.

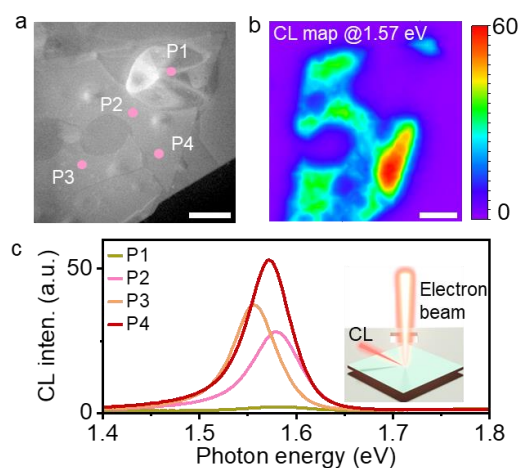


**Figure 2.** (a) CL analysis of hBN-encapsulated monolayer MoSe<sub>2</sub>. (b) STEM image of hBN-encapsulated monolayer MoSe<sub>2</sub>. (c) CL map at 1.57 eV of the same area as (a). Scale bars in (a) and (b) are 1  $\mu\text{m}$ . (d) CL spectra recorded at the positions in (a).

## References

- [1] H. Naito, W. Zhang, Y. Miyata et al., *Nanoscale Adv.* **2023**, 5, 5115.

## Structural and Electrical Properties of Millimeter Scale CVD Graphene

Toyota Technological Institute, Surface Science Lab., Chinnasamy Sengottaiyan, Kazunori Hirose,

Yuta Kurachi, Masanori Hara, Masamichi Yoshimura\*

\*Email: yoshi@toyota-ti.ac.jp

Despite the large single-crystal graphene is highly desired and important for the applications of graphene in electronics, it is still a challenge to precisely control the nucleation site of graphene to develop wafer-scale high-quality graphene. Herein, we synthesized millimeter-scale high-quality graphene on Cu-foil by chemical vapor deposition (CVD). To synthesize graphene, a copper foil was annealed in Ar and H<sub>2</sub> atmosphere to remove impurities and increase grain size. Then, methane (CH<sub>4</sub>) was introduced at 1035 °C for 200 min to grow high-quality graphenes on the copper surface (**Figure a**). Graphene was transferred from Cu-foil to SiO<sub>2</sub>/Si substrate by the bubble transfer method (**Figure b**). The synthesized graphenes before and after transfer are studied for structural and electrical properties by AFM (**Figure c**) and Kelvin probe force microscope (**Figure d**). The Raman spectra specify the quality and defects structure in the graphene lattice, while energy dispersive spectroscopy shows oxidation on the graphene/Cu surface. Investigate a deeper understanding of the structural and electrical properties of hexagon graphene structure to meet future developments in the research relevant to the scalable growth of high-quality graphene.

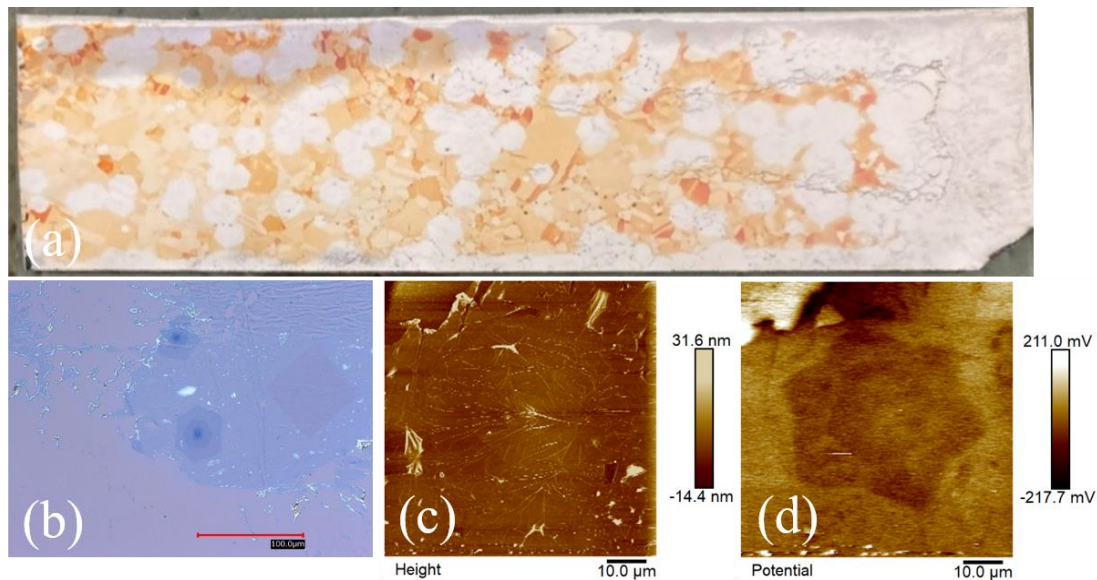


**Figure:** (a) Photograph of a synthesized hexagonal graphene/Cu-foil. The transferred graphene on SiO<sub>2</sub>/Si substrate for (b) Optical, (c) AFM, and (d) Surface potential images.

### References:

- [1] S. Suzuki *et al.*, *Jpn. J. Appl. Phys.* **2013**, 52, 125102. [2] S. Suzuki *et al.*, *Sci Rep.* **2017**, 7, 14851.
- [3] S. Suzuki *et al.*, *Adv. Funct. Mater.* **2021**, 31, 2007038.

4 JSAP-Optica Joint Symposia 2024 | 一般セッション(口頭講演) : 4.6 Terahertz Photonics

**[18p-B2-1~15] 4.6 Terahertz Photonics**

[18p-B2-1]

[JSAP-Optica Joint Symposia Invited Talk] High-power and compact terahertz signal sources using resonant tunneling diodes

○Safumi Suzuki<sup>1</sup> (1.Tokyo Tech)

[18p-B2-2]

[JSAP-Optica Joint Symposia Invited Talk] Strongly coupled terahertz magnons and chiral phonons in antiferromagnets

○Qi Zhang<sup>1</sup> (1.Nanjing Univ.)

[18p-B2-3]

A fast and sensitive THz rectenna detector working with zero-bias based on the 2D Dirac-Semimetal/Insulator heterostructure

○Chao Tang<sup>1,2</sup>, Koichi Tamura<sup>1,3</sup>, Aoi Hamada<sup>1,3</sup>, Hiroyoshi Kudo<sup>1,3</sup>, Shinnosuke Uchigasaki<sup>1,3</sup>, Yuma Takida<sup>4</sup>, Hiroaki Minamide<sup>4</sup>, Tsung-Tse Lin<sup>1,4</sup>, Akira Satou<sup>1</sup>, Taiichi Otsuji<sup>1</sup> (1.RIEC, Tohoku Univ., 2.FRIS, Tohoku Univ., 3.School of Eng. Tohoku Univ., 4.RAP, RIKEN)

[18p-B2-4]

Negative curvature annulus core fiber for transmission of orbital angular momentum modes in THz regime

○(D)Ishani De<sup>1</sup>, Vipul Rastogi<sup>1,2</sup> (1.Dept. of Physics, Indian Institute of Technology Roorkee, 2.Center of Photonics and Quantum Communication Technology, Indian Institute of Technology Roorkee)

[18p-B2-5]

Temperature Dependence Analysis for  $\beta$ -Ga<sub>2</sub>O<sub>3</sub> Studied by Terahertz Time-Domain Spectroscopy○(D)Shuang Liu<sup>1</sup>, Verdad C. Agulto<sup>1</sup>, Toshiyuki Iwamoto<sup>1,2</sup>, Kosaku Kato<sup>1</sup>, Hisashi Murakami<sup>3</sup>, Yoshinao Kumagai<sup>3</sup>, Masashi Yoshimura<sup>1</sup>, Makoto Nakajima<sup>1</sup> (1.Osaka Univ. ILE, 2.Nippo Prec., 3.TAT Appli. Chem.)

[18p-B2-6]

Study of c- and m-plane properties of ZnO via terahertz time-domain ellipsometry

○(D)Zixi Zhao<sup>1</sup>, Verdad C. Agulto<sup>1</sup>, Toshiyuki Iwamoto<sup>1,2</sup>, Kosaku Kato<sup>1</sup>, Kohei Yamanoi<sup>1</sup>, Toshihiko Shimizu<sup>1</sup>, Nobuhiko Sarukura<sup>1</sup>, Takashi Fujii<sup>2,3</sup>, Tsuguo Fukuda<sup>4</sup>, Masashi Yoshimura<sup>1</sup>, Makoto Nakajima<sup>1</sup> (1.ILE, Osaka Univ., 2.PNP, 3.Ritsumeikan Univ., 4.Fukuda Crystal Lab.)

[18p-B2-7]

Identification of calcium oxalate hydrates by terahertz spectroscopy

○(D)Wangxuan Zhao<sup>1</sup>, Haruto Kobashi<sup>1</sup>, Verdad C. Agulto<sup>1</sup>, Kosaku Kato<sup>1</sup>, Mihoko Maruyama<sup>2</sup>, Masae Takahashi<sup>3</sup>, Yutaro Tanaka<sup>2</sup>, Yusuke Mori<sup>2</sup>, Masashi Yoshimura<sup>1</sup>, Makoto Nakajima<sup>1</sup> (1.ILE Osaka Univ., 2.GSE Osaka Univ, 3.GSS Tohoku Univ.)

[18p-B2-8]

## Low and High Spatial Frequency Periodic Surface Structure Formation under Terahertz Free Electron Laser Irradiation

○(D)Youwei Wang<sup>1</sup>, Zihao Yang<sup>1</sup>, Kosaku Kato<sup>1</sup>, Verdad C. Agulto<sup>1</sup>, Kotaro Makino<sup>2</sup>, Junjii Tominaga<sup>2</sup>, Goro I soyama<sup>3</sup>, Makoto Nakajima<sup>1</sup> (1. ILE, Osaka Univ., 2. AIST, 3. SANKEN, Osaka Univ.)

---

[18p-B2-9]

## Terahertz micrometer-scale imaging based on spintronic emitters

○(D)Ruochen Dai<sup>1</sup>, Shinya Isosaki<sup>1</sup>, Jiaming Zhang<sup>1</sup>, Kosaku Kato<sup>1</sup>, Verdad C. Agulto<sup>1</sup>, Shojiro Nishitani<sup>1</sup>, Mikihiro Nishitani<sup>1</sup>, Masashi Yoshimura<sup>1</sup>, Makoto Nakajima<sup>1</sup> (1. Osaka Univ. ILE)

---

[18p-B2-10]

## [JSAP-Optica Joint Symposia Invited Talk] Low-temperature-grown dilute bismide III-V compound semiconductors towards fabrication of photoconductive antenna for terahertz-wave emission and detection

○Yoriko Tominaga<sup>1</sup>, Fumitaro Ishikawa<sup>2</sup>, Noriaki Ikenaga<sup>3</sup>, Osamu Ueda<sup>4</sup> (1. Hiroshima Univ., 2. Hokkaido Univ., 3. Kanazawa Inst. Tech., 4. Meiji Univ.)

---

[18p-B2-11]

## [JSAP-Optica Joint Symposia Invited Talk] Terahertz spin currents resolved with nanometer spatial resolution

○Xiaojun Wu<sup>1</sup> (1. Beihang University)

---

[18p-B2-12]

## 3D-printed Packaging for Terahertz Silicon Waveguides

○(P)Ngo Hoai Nguyen<sup>1</sup>, Weijie Gao<sup>1</sup>, Mingxiang Li<sup>2</sup>, Daiki Ichikawa<sup>1</sup>, Yoshiharu Yamada<sup>3</sup>, Hidemasa Yamane<sup>3</sup>, Shuichi Murakami<sup>3</sup>, Withawat Withayachumnankul<sup>2</sup>, Masayuki Fujita<sup>1</sup> (1. Osaka University, 2. Univ. of Adelaide, 3. ORIST)

---

[18p-B2-13]

## New Composition Signal Among Comb-Like Terahertz Spectrum Generated Using Dual Multimode Laser Diodes

○(D)Yuanhao Zeng<sup>1</sup>, Kosaku Kato<sup>1</sup>, Verdad C. Agulto<sup>1</sup>, Fumiyoshi Kuwashima<sup>2</sup>, Masahiko Tani<sup>1,3</sup>, Masashi Yoshimura<sup>1</sup>, Makoto Nakajima<sup>1</sup> (1. ILE, Osaka Univ., 2. Fukui Univ. of Tech., 3. FIR-UF)

---

[18p-B2-14]

## Terahertz spectroscopy and imaging of circular dichroism in chiral metasurfaces

○Takumi Yoichi<sup>1</sup>, Uina Chiba<sup>1</sup>, Rinpei Sasaki<sup>1</sup>, Takeo Minari<sup>2</sup>, Seigo Ohno<sup>3</sup>, Katsuhiko Miyamoto<sup>1,4</sup> (1. Chiba Univ., 2. NIMS, 3. Tohoku Univ., 4. Chiba Univ. MCRC)

---

[18p-B2-15]

## Kinetics analysis of anti-CD9 antibody and H1299 EV using terahertz chemical microscope

○(M2)YUCHEN MA<sup>1</sup>, Changjiang Liu<sup>1</sup>, Xue Ding<sup>1</sup>, Jin Wang<sup>1</sup>, Toshihiko Kiwa<sup>1</sup> (1. Okayama Univ.)

---



## High-power and compact terahertz signal sources using resonant tunneling diodes

Tokyo Tech., °Safumi Suzuki

E-mail: safumi@ee.e.titech.ac.jp

The use of terahertz (THz) electromagnetic waves is anticipated for high-capacity communications, sensing, imaging, and spectroscopic analysis. However, the output power of semiconductor THz signal sources remains low, limiting THz applications. Resonant tunneling diodes (RTDs) are promising candidates for THz sources due to their compactness and high-frequency operation [1]. For high-power operation, RTD oscillator arrays have been studied for power combination. Recently, a very high output power of 11.8 mW at 450 GHz was achieved by a 36-element coherent array using mutual injection locking [2]. In addition to power combination using arrays, attempts to increase the output power of a single oscillator have also been conducted. In this presentation, recent studies on high-power RTD THz oscillators will be introduced.

RTDs have negative differential conductance characteristics, which can be used as gain for THz oscillators. Synchronous operation of the RTD oscillator array is necessary for coherent power combination, requiring coupling of each array element and control of operating modes in the arrayed oscillator. For slot-antenna integrated RTD oscillators, we proposed a strong coupling structure via a resistor that allows coherent operation even with some frequency variation in each element. Theoretical analysis and experiments achieved coherent operation [3]. A high-power oscillation exceeding 1 mW with high radiation directivity was obtained at 400 GHz using a double slot-ring structure [4].

We proposed a cavity resonator structure to improve the output power of a single oscillator. This cavity resonator has low loss and low inductance, achieving high output power while maintaining the oscillation frequency even with large-area RTDs. However, large-area RTDs generate significant heat, leading to thermal destruction issues. Therefore, by using InP, which has high thermal conductivity, for the lower electrical conduction layer of the RTD instead of low-thermal conductive InGaAs, we achieved operations without thermal destruction due to improved heat dissipation [5]. Furthermore, a device combining a cavity resonator and an array technique achieved 0.24 mW at the very high frequency of 925 GHz [6].

This work was partially supported by a scientific grant-in-aid (24H00031) from JSPS, CREST (JPMJCR21C4) from JST, X-NICS (JPJ011438) and ARIM (JPMXP1224IT0018, JPMXP1224IT0019) from MEXT, and the ROHM Company.

- [1] M. Asada and S. Suzuki, *Sensors*, 21, 1384 (2021).
- [2] Y. Koyama, et al., *IEEE Trans. Terahertz Sci. Technol.* 12, 510 (2022).
- [3] T. V. Mai, M. Asada, T. Namba, Y. Suzuki, and S. Suzuki, *IEEE Trans. Terahertz Sci. Technol.*, 13, 405 (2023).
- [4] S. Endo and S. Suzuki, *Appl. Phys. Express*, 17, 044001 (2024).
- [5] H. Tanaka, H. Fujikata, F. Han, and S. Suzuki, *Jpn. J. Appl. Phys.*, 63, 011004 (2023)
- [6] F. Han, T. Shimura, H. Tanaka, and S. Suzuki, *Appl. Phys. Express*, 16, 064003 (2023)

**Strongly coupled terahertz magnons and chiral phonons in antiferromagnets****Nanjing University, China<sup>1</sup>, Qi Zhang<sup>1</sup>****E-mail: zhangqi@nju.edu.cn**

In quantum materials, collective excitations in the terahertz (THz) regime govern the low-energy responses of ground states to external stimuli, which is crucial in understanding various correlated phenomena. The hybridization of distinct collective modes offers a pathway for coherent manipulation of coupled degrees of freedom and quantum phases. Particularly in antiferromagnets, the strong coupling between angular momentum-carrying spin and lattice excitations, i.e., magnons and chiral phonons, leads to the formation of chiral magnon polarons in the THz regime, exhibiting intriguing novel properties. This presentation showcases the observation of magnon polarons with THz and Raman spectroscopy in antiferromagnetic insulators. We reveal a unique angular momentum-selective hybridization between THz magnons and chiral phonons. Additionally, we report findings of phonon Zeeman splitting and fluctuation-enhanced phonon magnetic moments in a polar antiferromagnet,  $\text{Fe}_2\text{Mo}_3\text{O}_8$ , attributed to phonon-(para)magnon interactions.

[1] Fangliang Wu, Song Bao, Jin Zhou, Yunlong Wang, Jian Sun, Jinsheng Wen, Yuan Wan, and Qi Zhang, Nat. Phys. 19, 1868 (2023).

[2] Jun Cui, Emil Vinas Bostrom, Mykhaylo Ozerov, Fangliang Wu, Qianni Jiang, Jiun-Haw Chu, Changcun Li, Fucai Liu, Xiaodong Xu, Angel Rubio, and Qi Zhang, Nat. Comm. 14, 3396 (2023).

## A fast and sensitive THz rectenna detector working with zero-bias based on the 2D Dirac-Semimetal/Insulator heterostructure

<sup>1</sup>Research Institute of Electrical Communication, Tohoku University, <sup>2</sup>Frontier Research Institute for Interdisciplinary, Tohoku University, <sup>3</sup>Department of Communication Eng., Graduate School of Tohoku University, <sup>4</sup>RIKEN Center for Advanced Photonics, RIKEN, Chao Tang<sup>1,2</sup>, Koichi Tamura<sup>1,3</sup>, Aoi Hamada<sup>1,3</sup>, Hiroyoshi Kudo<sup>1,3</sup>, Shinnosuke Uchigasaki<sup>1,3</sup>, Yuma Takida<sup>4</sup>, Hiroaki Minamide<sup>4</sup>, Tsung-Tse Lin<sup>1,4</sup>, Akira Satou<sup>1</sup> and Taiichi Otsuji<sup>1</sup>  
E-mail: tang.chao.c4@tohoku.ac.jp

In this study, we developed a fast and sensitive terahertz (THz) detector using a Bi<sub>2</sub>Se<sub>3</sub>/h-BN heterostructure rectenna that enables detection without a cathode-anode bias. The fabrication process involved synthesizing  $\beta$ -Bi<sub>2</sub>Se<sub>3</sub> via vapor-controlled liquid phase growth and h-BN via chemical vapor deposition [1]. The Bi<sub>2</sub>Se<sub>3</sub> flake were cleaved and transferred onto a Si/SiO<sub>2</sub> substrate, followed by the deposition of anode electrodes and the hot transfer method to stack an h-BN flake, completing the fabrication with cathode and anode electrodes and a bow-tie antenna with metal pads. For THz detection, we employed a 0.95-THz, 500-mW-peak injection-seeded THz parametric generator (is-TPG) as the light source [2], with anode and cathode electrodes connected through a bias tee using a GSG RF probe (Fig. 1). We observed a THz photovoltage peak of 20 mV at an applied electric field of 0.25 V/nm, with a 200-ps full width at half maximum (FWHM). This resulted in a responsivity of 40 mV/W under a 50- $\Omega$  load (equivalent to 400 V/W under a 50-k $\Omega$  load) and a response time of 100 ps (equivalent to 10 Gbps) at room temperature. Remarkably, we also achieved a responsivity of 20 mV/W at zero bias with the same response speed (Fig. 2). The asymmetry in the peak photovoltage with respect to the applied bipolar electric field is attributed to the asymmetric Dirac conical dispersions of Bi<sub>2</sub>Se<sub>3</sub>, highlighting the potential for passive, high-speed THz detection using 2D semimetal devices.

A part of this research was supported by Creative Interdisciplinary Collaboration Program, Frontier Research Institute for Interdisciplinary Science, Tohoku University, Hirose Foundation, NICT Grant No. JPJ012368C01301, ROHM joint research program, The Telecommunications Advancement Foundation, Support Center for Advanced Telecommunications Technology Research, Iketani Science and Technology Foundation, Murata Science and Education Foundation.

[1] C. Tang, Y. Sato, K. Watanabe, et al., Results in Materials 13, 100253 (2022).

[2] Y. Takida, K. Nawata, T. Notake, et al., Opt. Express 30, 11217 (2022).

[3] C. Tang, K. Tamura, A. Hamada, et al., DRC2024, at Maryland, USA (2024).

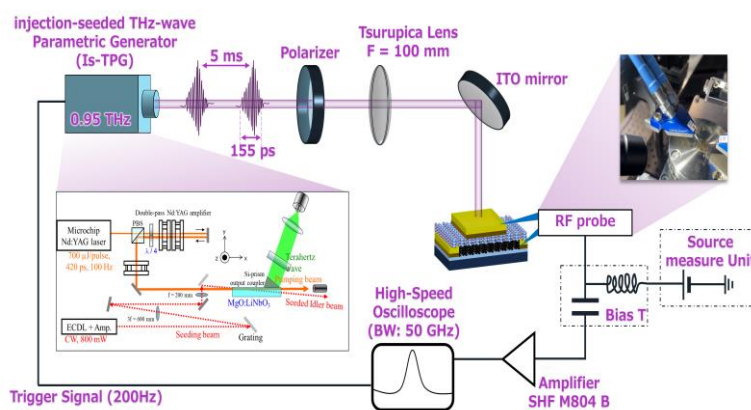


Fig. 1. THz detection experimental system

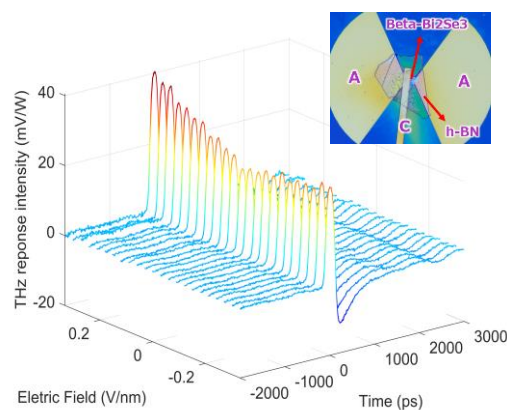


Fig. 2. THz response of Bi<sub>2</sub>Se<sub>3</sub> antenna

# Negative curvature annulus core fiber for transmission of orbital angular momentum modes in THz regime

Ishani De<sup>1</sup>, Vipul Rastogi<sup>1,2\*</sup>

<sup>1</sup> Department of Physics, Indian Institute of Technology Roorkee, Roorkee, Uttarakhand-247667, India,

<sup>2</sup> Center of Photonics and Quantum Communication Technology, Indian Institute of Technology Roorkee, Uttarakhand-247667, India

\*E-mail: [vipul.rastogi@ph.iitr.ac.in](mailto:vipul.rastogi@ph.iitr.ac.in)

## 1. Introduction

In the electromagnetic spectrum terahertz band lies between microwave and infrared bands. By convention, the terahertz window is generally considered from a frequency range of 0.1 THz to 10 THz. For this terahertz window, the development of sources and detectors has resulted in research interest in low-loss communication channels. Propagation of THz radiation in free space is lossy due to water vapor content. So, designing a guided wave medium, especially fiber, is the need of the hour [1].

It has been predicted that there will be a capacity crunch in the existing fiber network in the next decade or so. Different degrees of freedom of multiplexing are being used to address this problem. One of them is mode division multiplexing (MDM) in which data is sent independently in different orthogonal modes. Orbital angular momentum (OAM) modes is one of the modal basis sets used for MDM. OAM modes have helical phase fronts because of azimuthal phase dependence, quantified by topological charge  $l$ , but uniform annular intensity profile irrespective of the value of  $l$ . In fiber, OAM modes can be represented by orthogonal superposition of vector modes [2].

We have proposed the design of a negative curvature annulus-core fiber for transmission of 14 OAM modes from 0.3 THz to 1.1 THz frequency range. The supported vector modes have extremely low values of confinement losses between  $10^{-8} - 10^{-11}$  dB/m and effective mode area nearly up to  $10 \text{ mm}^2$ .

## 2. Fiber design

The cross-section of the designed negative curvature annulus core fiber is shown in Fig 1. The background material (shown by the blue shade in Fig. 1) is cyclo olefin polymer, commercially known as Zeonex, which has low losses in the THz band and the rest is air [3]. The central annulus core supports OAM modes surrounded by seven cladding tubes of thickness  $t$ . In the absence of the cladding tubes the fiber supports OAM modes, including second-order radial modes upto  $l = 2$  at 0.4 THz frequency. On the introduction of cladding tubes of a certain thickness  $t$ , the confinement loss of the undesirable second-order radial modes (they cause difficulty in multiplexing and demultiplexing) increases as the light leaks from the annulus core into the cladding tubes when the condition of resonance is met. This can be observed from Fig. 2, that for  $t = 0.4 \text{ mm}$  onwards, the confinement

loss of the second order radial vector modes increases to  $3.5 \times 10^{-7}$  dB/m and at  $t = 0.5 \text{ mm}$ , the loss further increases to 0.1 dB/m. Since the loss for vector modes constituting OAM mode  $l = 4$  is less than  $3.1 \times 10^{-10}$  dB/m for  $t = 0.5 \text{ mm}$ , this thickness can be used as it filters out the second order radial vector modes without compromising the purity of OAM modes.

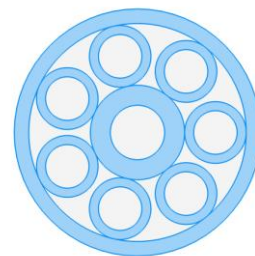


Fig 1. Cross-section of the proposed fiber

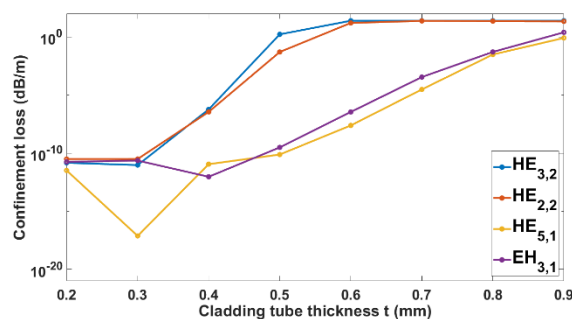


Fig. 2. Variation of confinement loss with cladding tube thickness at 0.4 THz frequency.

## 3. Conclusion

A negative curvature annulus core fiber based on Zeonex for transmission of 14 OAM modes in the THz band has been proposed. With a cladding tube thickness 0.5 mm, the second order radial will not be guided stably by the designed fiber. All the supported vector modes have an effective mode area greater than  $9.0 \text{ mm}^2$  and confinement losses between  $10^{-8} - 10^{-11}$  dB/m.

## References

- [1] M. S. Islam et. al, Opt. Express, **28** (2020), 16089
- [1] Z. Zhu et. al., IEEE J. Sel. Top. Quantum Electron., **30** (2024), 1-10
- [2] J. Anthony et. al, J. Opt. Soc. Am. B, **28**, (2011) 1013-1018

## Temperature Dependence Analysis for $\beta$ -Ga<sub>2</sub>O<sub>3</sub> Studied by Terahertz Time-Domain Spectroscopy

Shuang Liu<sup>1</sup>, Verdad C. Agulto<sup>1</sup>, Toshiyuki Iwamoto<sup>1,2</sup>, Kosaku Kato<sup>1</sup>, Hisashi Murakami<sup>3</sup>, Yoshinao Kumagai<sup>3</sup>, Masashi Yoshimura<sup>1</sup>, and Makoto Nakajima<sup>1</sup>

<sup>1</sup>Institute of Laser Engineering, Osaka University

<sup>2</sup>Nippo Precision Co., Ltd.

<sup>3</sup>Department of Applied Chemistry, Tokyo University of Agriculture and Technology

E-mail: u885580a@ecs.osaka-u.ac.jp

In recent years, beta-gallium oxide ( $\beta$ -Ga<sub>2</sub>O<sub>3</sub>) has attracted attention as an emerging ultrawide-bandgap semiconductor material. For  $\beta$ -Ga<sub>2</sub>O<sub>3</sub> semiconductor application, it requires a thorough study of its temperature dependence to determine its performance under multiple temperature environments. THz-TDS is a powerful technique [1-5] for accurately measuring the refractive index of semiconductors. By analyzing the transmitted THz field, we can calculate the refractive index of the sample in the THz region. Subsequently, the obtained data can be fitted with the Drude-Lorentz model to analyze the transport properties of the material. This study aims to provide valuable insights into the study of  $\beta$ -Ga<sub>2</sub>O<sub>3</sub>, which is essential for advancing its application prospects in various fields.

A 647- $\mu$ m-thick Fe-doped semi-insulating (001)  $\beta$ -Ga<sub>2</sub>O<sub>3</sub> substrate and a 4.5- $\mu$ m-thick Si-doped n-type homoepitaxial  $\beta$ -Ga<sub>2</sub>O<sub>3</sub> film grown on the substrate were prepared. We employed a THz-TDS system (Tera Prospector, Nippo Precision, Co., Ltd.), and the temperature was varied from 100 K to 400 K. The THz polarization was parallel to the [100] axis. The complex refractive index of the sample was extracted by Fourier transforming the acquired time-domain data.

Figure 1 shows the refractive index of semi-insulating  $\beta$ -Ga<sub>2</sub>O<sub>3</sub> substrate. The refractive index increases with increasing temperature, and it can be fitted using the Lorentz model. Phonon scattering increases with increasing temperature, so the refractive index in the terahertz region increases. The complex refractive index of the epilayer is determined using the complex refractive index obtained for the substrate, considering multiple reflections in the film, and fitting with the Drude-Lorentz model to obtain the carrier transport properties. The obtained carrier density and mobility at different temperatures are shown in Fig. 2. At low temperatures, the carrier density initially increased and then slowly plateaued as the temperature was further increased. On the other hand, the mobility reached a maximum near 100 K and then decreased at higher temperatures. This shows that within the measurement temperature range, the ionization of dopant atoms makes the carrier density increase. While the temperature rises to the saturation region, the carrier density cannot increase significantly. For ultrawide bandgap semiconductor, in a long temperature range, it is difficult for carriers to achieve the transition from the valence band to the conduction band. The mobility

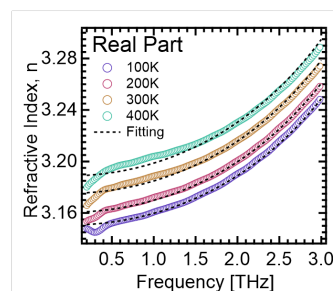


Fig.1 Real part (refractive index) of the complex refractive index spectra of semi-insulating  $\beta$ -Ga<sub>2</sub>O<sub>3</sub> substrate at different temperatures.

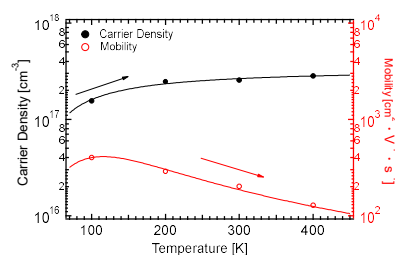


Fig. 2. Temperature dependence of the carrier density and mobility of the  $\beta$ -Ga<sub>2</sub>O<sub>3</sub> epilayer.

decreases at high temperature due to the temperature-dependent enhancement of lattice scattering. At low temperatures, the mobility is affected by both impurity scattering and lattice scattering.

In summary, we investigated the temperature dependence of the complex refractive index and the carrier transport properties of  $\beta$ -Ga<sub>2</sub>O<sub>3</sub> in the THz region. The fundamental parameters of  $\beta$ -Ga<sub>2</sub>O<sub>3</sub> are elucidated through THz-TDS measurements with a high accuracy, providing valuable information for the applications of  $\beta$ -Ga<sub>2</sub>O<sub>3</sub>.

### Acknowledgements

The authors are grateful to Dr. Ken Goto for his support in the sample fabrication. This work was partly supported by JKA and its promotion funds from AUTORACE.

### References

- [1] J. Wang et al., Nature (2024).<https://doi.org/10.1038/s41586-024-07513-x>.
- [2] M.Ota et al., Nature Physics, 18, 1436 (2022).
- [3] V. C. Agulto et al., Appl. Phys. Lett. 118, (2021).
- [4] V.C.Agulto et al.,Scientific Reports 11, 18129 (2021).
- [5] T. Iwamoto et al., Jpn. J. Appl. Phys. 62, SF1011 (2023).



# Study of c- and m-plane properties of ZnO via terahertz time-domain ellipsometry

Zixi Zhao<sup>1</sup>, Verdad C. Agulto<sup>1</sup>, Toshiyuki Iwamoto<sup>1,2</sup>, Kosaku Kato<sup>1</sup>, Kohei Yamanoi<sup>1</sup>, Toshihiko Shimizu<sup>1</sup>, Nobuhiko Sarukura<sup>1</sup>, Takashi Fujii<sup>2,3</sup>, Tsuguo Fukuda<sup>4</sup>, Masashi Yoshimura<sup>1</sup>, Makoto Nakajima<sup>1</sup>

<sup>1</sup> Institute of Laser Engineering, Osaka University, <sup>2</sup> Nippo Precision Co., Ltd.,

<sup>3</sup> Ritsumeikan University, <sup>4</sup> Fukuda Crystal Laboratory Co., Ltd.

E-mail: nakajima.makoto.ile@osaka-u.ac.jp

## 1. Introduction

The terahertz region has recently attracted much attention as the next-generation communication (Beyond 5G, 6G) band, meanwhile, material characterization techniques in the terahertz region have also emerged to meet the needs of 6G devices development [1-3]. Currently, the most widely used characterization technique in the THz band is terahertz time-domain spectroscopy (THz-TDS). However, THz-TDS faces challenges in characterizing high carrier density semiconductors and its phase precision needs improvement.

On the other hand, zinc oxide (ZnO) possesses characteristics such as wide-bandgap and high mobility, making it a promising material for terahertz photonic applications. Additionally, ZnO, as an anisotropic semiconductor, exhibits different optical properties in different orientations, offering more innovative possibilities for device design.

Herein we present the characterization of two ZnO samples using terahertz time-domain ellipsometry (THz-TDE), an emerging semiconductor characterization technique that combines THz-TDS and ellipsometry. THz-TDE measurement is very sensitive to phase and amplitude information that changes with orientation, while also achieving high phase precision, making it promising for the characterization of anisotropic semiconductors.

ZnO crystal typically exhibits a hexagonal wurtzite structure. Here we studied two ZnO crystals with different surface orientations: the c-plane perpendicular to the c-axis or [0001] growth direction, and the m-plane perpendicular to the [1 $\bar{1}$ 00] direction.

## 2. Experiment

Two bulk ZnO single crystals with different orientations were prepared by hydrothermal growth method. By measuring the c-plane ZnO sample, the refractive index perpendicular to the c-axis,  $n_{\perp c}$ , can be obtained. For the m-plane ZnO sample, the sample was first placed with the c-axis perpendicular to the plane of incidence so as to measure  $n_{\perp c}$ , and was then rotated 90° along the sample plane so that the refractive index parallel to the c-axis,  $n_{\parallel c}$ , can be measured.

THz-TDE characterization of the ZnO samples was performed using Tera Evaluator, developed by Nippo Precision, Co., Ltd., with a spectral range of 1-3 THz [4, 5]. Time-domain waveforms of the p and s polarizations reflected from the samples were measured and Fourier transformed to obtain the amplitude ratio and phase difference known as the ellipsometric parameters.

## 3. Results

Using the measured ellipsometric parameters, the complex refractive index spectra were obtained as shown in Fig. 1. Then by fitting the real and imaginary parts of the complex refractive index to the Drude model, the carrier density and mobility can be deduced. For the c-oriented sample (Fig. 1a), the obtained carrier density and mobility are  $\sim 4.8 \times 10^{16} \text{ cm}^{-3}$  and  $\sim 210 \text{ cm}^2/\text{V}\cdot\text{s}$ , respectively.

Similar analysis was implemented for the m-oriented ZnO sample for both  $n_{\perp c}$  and  $n_{\parallel c}$ . The experimental results and the best-fit curves are shown in Fig. 1b. The real parts of  $n_{\perp c}$  and  $n_{\parallel c}$  are close to 2.8 and 3.0 respectively, which are consistent with the  $n_{\perp c}$  obtained for the c-oriented sample. Furthermore, the imaginary parts of  $n_{\perp c}$  and  $n_{\parallel c}$  show increasing behavior toward the low frequency region, indicating free-carrier absorption. The best-fit parameters obtained for the m-oriented sample along the two directions are similar, with a carrier density of  $\sim 2.9 \times 10^{16} \text{ cm}^{-3}$  and a mobility of  $\sim 260 \text{ cm}^2/\text{V}\cdot\text{s}$ .

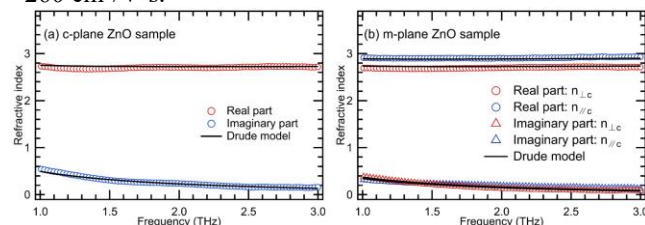


Fig. 1(a) refractive index  $n_{\perp c}$  spectra of c-plane ZnO sample and (b) refractive index  $n_{\perp c}$  and  $n_{\parallel c}$  spectra of m-plane ZnO sample.

## 4. Conclusions

Two ZnO single crystals with different orientations were characterized by THz-TDE, successfully obtaining the anisotropic refractive index,  $n_{\perp c}$  and  $n_{\parallel c}$ . Additionally, the carrier density and mobility were obtained using the Drude model, implying that THz-TDE can be effectively applied to the characterization of semiconductors with anisotropy and with high carrier densities above  $10^{16} \text{ cm}^{-3}$ .

## Acknowledgements

This work was partly supported by JKA and its promotion funds from AUTORACE.

## References

- [1] J. Wang et al., Nature (2024). <https://doi.org/10.1038/s41586-024-07513-x>.
- [2] M. Ota et al., Nature Physics, 18, 1436 (2022).
- [3] V. C. Agulto et al., Appl. Phys. Lett. 118, (2021).
- [4] V. C. Agulto et al., Scientific Reports 11, 18129 (2021).
- [5] T. Iwamoto et al., Jpn. J. Appl. Phys. 62, SF1011 (2023).

# Identification of calcium oxalate hydrates by terahertz spectroscopy

Wangxuan Zhao<sup>1</sup>, Haruto Kobashi<sup>1</sup>, Verdad C. Agulto<sup>1</sup>, Kosaku Kato<sup>1</sup>, Mihoko Maruyama<sup>2</sup>, Masae Takahashi<sup>3</sup>, Yutaro Tanaka<sup>2</sup>, Yusuke Mori<sup>2</sup>, Masashi Yoshimura<sup>1</sup>, Makoto Nakajima<sup>1</sup>

<sup>1</sup>ILE Osaka Univ., <sup>2</sup>GSE Osaka Univ., <sup>3</sup>GSS Tohoku Univ.  
E-mail: nakajima.makoto.ile@osaka-u.ac.jp

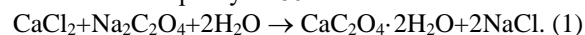
## 1. Introduction

Although kidney stones come in various types, approximately 80% are composed of either calcium oxalate or phosphate [1]. Calcium oxalate, the primary component of kidney stones, undergoes a phase transition from calcium oxalate dihydrate (COD) to calcium oxalate monohydrate (COM) during the stone formation process. Therefore, analyzing stone components is crucial for both diagnosis and subsequent treatment strategies for urolithiasis.

Terahertz spectroscopy [2-7] is valuable for identifying proteins and organic molecular constituents and exploring higher-order structures since it is safe for biological samples and sensitive to molecular fingerprints. Additionally, it can be operated at room temperature, enabling the simulation of phase transitions at low energies. This study utilizes terahertz time-domain spectroscopy (THz-TDS) and Fourier transform infrared (FTIR) spectroscopy to examine the optical properties of synthetic COD and COM pellet samples within the terahertz and far-infrared regions.

## 2. Methodology

Given that COM was the stable phase, commercially available powder with a purity of over 95% was utilized to produce COM pellet samples. The synthesis of COD entailed the addition of 300 ml of sodium oxalate solution ( $\text{Na}_2\text{C}_2\text{O}_4$ ) to 500 ml of calcium chloride solution ( $\text{CaCl}_2$ ) at 4 °C, leading to a precipitation reaction as described by chemical equation (1). The resulting crystals were isolated, characterized using powder X-ray diffraction (PXRD), and demonstrated a purity of 86%.



The preparation of COD and COM pellet samples included mixing COD and COM powder with a matrix material known for its high transparency in the THz band. The powder mixture was then pressed using a hydraulic press under the conditions of 20 MPa pressure and 20 s duration time. The concentration of all pellet samples was maintained at 10 wt%. Calcium oxalate pellet samples of suitable thickness were measured by THz-TDS and FTIR, respectively.

## 3. Results

Both COD and COM exhibit absorption peaks at 3.0, 4.1, 5.0, and 5.4 THz. However, COM shows two distinct absorption peaks at approximately 1.9 and 2.0 THz. Additionally, both COM and COD demonstrate a broad absorption peak centered around 8.4 THz, but COD exhibits a relatively narrower absorption peak compared to COM. Consequently, we can distinguish between COD and COM in the terahertz region.

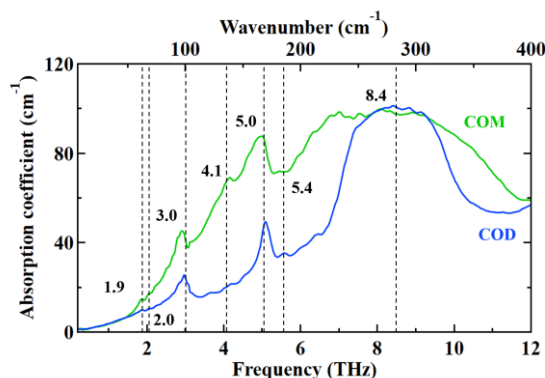


Fig. 1. Absorption coefficient spectra of COM and COD 10 wt% pellet samples in the THz and far-infrared regions.

In future studies, THz spectroscopy will be utilized to analyze the composition of human urinary stones by utilizing the spectral characteristics of COM and COD, with the goal of distinguishing their distribution in imaging research.

## References

- [1] M. J. Chung, JAAPA **30**, 49–50 (2017).
- [2] M. Takahashi, Crystals **4**, 74–103 (2014).
- [3] J. Wang et al., Nature (2024).  
doi.org/10.1038/s41586-024-07513-x.
- [4] M. Ota et al., Nature Phys. **18**, 1436 (2022).
- [5] V. C. Agulto et al., Appl. Phys. Lett. **118**, (2021).
- [6] V. C. Agulto et al., Sci. Rep. **11**, (2021).
- [7] T. Iwamoto et al., Jpn. J. Appl. Phys. **62**, SF1011 (2023).

# Low and High Spatial Frequency Periodic Surface Structure Formation under Terahertz Free Electron Laser Irradiation

You Wei Wang<sup>1</sup>, Zihao Yang<sup>1</sup>, Kosaku Kato<sup>1</sup>, Verdad C. Agulto<sup>1</sup>, Kotaro Makino<sup>2</sup>, Junjii, Tominaga<sup>2</sup>, Goro Isoyama<sup>3</sup>, Makoto Nakajima<sup>1</sup>

<sup>1</sup>ILE, Osaka Univ., <sup>2</sup>AIST, <sup>3</sup>SANKEN, Osaka Univ.  
E-mail: u596103i@ecs.osaka-u.ac.jp

## 1. Introduction

Terahertz (THz) technology has recently seen significant advancements and applications in several fields, including ultrafast electric field measurement[1], semiconductor diagnostics[2], and magnetic material control[3]. Ablation phenomena in the terahertz range have been relatively underexplored due to the limited availability of powerful THz sources. However, recent progress in laser technology has opened up opportunities for the development of high-intensity THz sources, thereby facilitating investigations into ablation processes [4] and nonlinear effects [5]. These advancements have also made it possible to generate high-intensity pulses capable of inducing laser induced periodic surface structures (LIPSS) on materials, offering a promising avenue for surface nanostructuring. In this study, we investigated LIPSS formation on Ge<sub>2</sub>Sb<sub>2</sub>Te<sub>5</sub> (GST), a material renowned for its phase-change recording properties [6], by the irradiation of a high-intensity THz free electron laser (FEL). We observed the emergence of two types of LIPSS through laser ablation. These LIPSS can be categorized as either low spatial frequency LIPSS (LSFL) or high spatial frequency LIPSS (HSFL) depending on their periodicity.

## 2. Experiment

To produce powerful THz pulses, we utilized the THz-FEL situated at SANKEN, Osaka University. This system is renowned for generating exceptionally robust THz pulses, boasting a macropulse energy of approximately 40 mJ at a frequency of 4 THz. Such configuration furnished us with the requisite intense THz pulses vital for our experimental inquiries. The THz-FEL beam transmitted through two metal wire grid polarizers to regulate intensity and polarization direction. Subsequently, the transmitted beam was focused onto the sample surface via a 90° off-axis parabolic mirror with an effective focal length of 25.4 mm, yielding a spot size of 0.6 mm in radius. The maximum energy density within the irradiated area reached 35 J/cm<sup>2</sup>. For our specimen, we employed a 100-nm-thick GST thin film deposited on a 500 μm thick Al<sub>2</sub>O<sub>3</sub> substrate via DC magnetron sputtering at ambient temperature. A stoichiometric Ge<sub>2</sub>Sb<sub>2</sub>Te<sub>5</sub> target served as the sputtering source. To prevent oxidation, a 20-nm SiO<sub>2</sub> protective layer was deposited atop the sample. Notably, the as-grown film remained amorphous and did not undergo any annealing processes [6].

## 3. Result

Figure 1 illustrates the outcomes obtained from

irradiating GST with 5 pulses, each possessing an energy density of 18 J/cm<sup>2</sup>. The incident polarization  $E$  is denoted by the vertical red arrow. A periodic structure aligned parallel to the polarization direction emerged, exhibiting an average periodicity of 18.9 μm, equivalent to 1/4 of the incident wavelength. This structure is categorized as LSFL-II, induced by excitation with an energy smaller than the bandgap. Additionally, surrounding the ablation mark reveals the presence of HSFL structures with a spacing of 4 μm (1/18 of the wavelength), perpendicular to the polarization direction.

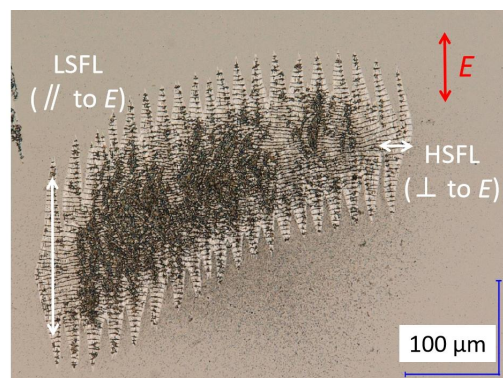


Fig 1. Microscope image of the GST film after 5-shots THz pulse irradiation.

## 4. Conclusions

Our study demonstrated the formation of laser-induced periodic surface structures (LIPSS) on Ge<sub>2</sub>Sb<sub>2</sub>Te<sub>5</sub> a phase change recording material, using a terahertz (THz) free electron laser with a fluence up to 35 J/cm<sup>2</sup>. Two types of LIPSS emerged: one running parallel and the other perpendicular to the direction of laser polarization. The spacings of the former and of the latter corresponded to approximately 1/4 wavelength and 1/18 wavelength, respectively. The formation of the two types of LIPSS provides the possibility of a new approach to surface nanostructuring.

## References

- [1] M. Ota, et al., *Nat. Phys.* **18** (2022) 1436.
- [2] T. Kurihara, et al., *Sci Rep* **10** (2020) 7321.
- [3] J. Wang, et al., *Nature* (2024).  
<https://doi.org/10.1038/s41586-024-07513-x>
- [4] Y.W. Wang, et al., *Appl. Phys. A* **128** (2022) 836.
- [5] T. N. K. Phan, et al., *Opt. Lett.* **49** (2024) 1073.
- [6] K. Makino, et al., *Sci. Rep.* **8**, (2018) 2914.

## Terahertz micrometer-scale imaging based on spintronic emitters

Ruochen Dai<sup>1</sup>, Shinya Isosaki<sup>1</sup>, Jiaming Zhang<sup>1</sup>, Kosaku Kato<sup>1</sup>, Verdad C. Agulto<sup>1</sup>,  
Shojiro Nishitani<sup>1</sup>, Mikihiro Nishitani<sup>1</sup>, Masashi Yoshimura<sup>1</sup>, Makoto Nakajima<sup>1</sup>

<sup>1</sup> Institute of Laser Engineering, Osaka University

E-mail: u974561d@ecs.osaka-u.ac.jp

In recent years, the terahertz (THz, 0.1–10 THz) region has attracted significant research attention, which can be exploited for nondestructive applications such as biomedical, materials inspection, and security [1-3]. Therefore, high spatial resolution imaging at THz region of interest is a highly desirable capability in imaging applications. Due to the Abbe diffraction limit, the minimum spatial resolution of microscopy at a given wavelength is  $\lambda/2$ . For imaging in the THz band, this limit is on the order of hundreds of microns. To go beyond this limit, we propose in this study a THz imaging method in which the object is set directly on top of a spintronic THz emitter (STE) made of ferromagnetic/non-magnetic heterojunction, which emits a terahertz signal with a peak frequency of 1 THz. A femtosecond laser beam to excite an STE can be focused into a spot size with a diameter of a few microns. Therefore, the excited THz radiation is confined in a few microns just above the STE, which enables the micrometer-scale imaging of an object on top of the STE. Our results demonstrate a spatial resolution of 2.5  $\mu\text{m}$ , below  $\lambda/100$  for 1 THz.

The optical platform for THz super-resolution imaging employs a Ti:sapphire laser with a pulse duration of 100 fs and a repetition rate of 80 MHz. The laser beam is divided into a pump beam and a probe beam. The pump beam excites the spintronic terahertz emitter, generating THz radiation, while the probe beam samples the THz pulses. A photoconductive antenna detects the THz radiation. The setup includes a two-dimensional (2D) scanning motorized stage, enabling high-resolution imaging.

The sample used to demonstrate THz super-resolution imaging mainly consists of two parts, shown in Figure 1a. The first part is an STE of Pt/Fe heterojunction [4,5], which can emit terahertz radiation when excited by femtosecond pulse laser. The second part is deposited aluminum (Al) layer with a thickness of more than 100 nm using photolithography and magnetron sputtering methods. The Al layer is used for resolution measurement and imaging.

The THz spot size on top of the STE was determined from the one-dimensional (1D) scan across the edge of an

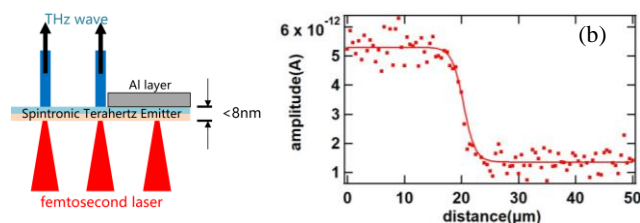


Fig.1 (a) Imaging structure of partially sputtered Al layer on STE (side view) (b) THz emission peak-to-peak amplitude scan results

Al pattern in a manner of the knife-edge method. The markers in Figure 1b shows the scan result of the peak-to-peak amplitude of the emitted THz signal when the laser irradiation spot was moved from left to right in the configuration of Figure 1a with a step of 0.5  $\mu\text{m}$ . The Al layer does not exist on the left side and thus the terahertz radiation can be fully transmitted. When the pump laser spot begins to contact the deposited Al pattern, the terahertz radiation is partially blocked, and the amplitude of the detected terahertz signal begins to decrease until it is completely blocked. The data were fitted by a sigmoid function (solid curve), and from this fit the diameter of the terahertz radiation spot was estimated to be about 2.5  $\mu\text{m}$ .

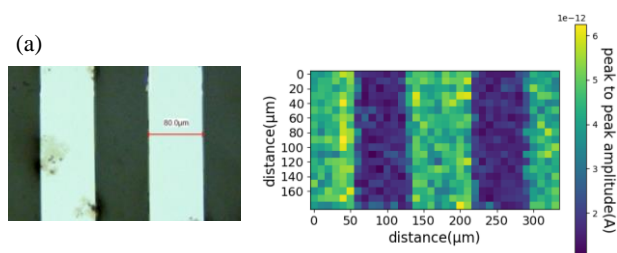


Fig.2 (a) Optical photo of strip imaging structure (b) 2D image extracted from THz scanning measurements

For the demonstration of 2D imaging, we used a test pattern of Al deposited on the STE. Figure 2a depicts an optical microscopy image of the sample. The bright area is Al layer with a width of 80  $\mu\text{m}$ , that blocks terahertz radiation, while three gaps are bare STE that can emit terahertz radiation unhindered. Figure 2b presents two-dimensional image extracted from THz scanning measurements. Pixel color denotes the intensity of terahertz radiation while high-intensity terahertz radiation spots show bright colors. The scanning step is 10  $\mu\text{m}$  in both  $x$  and  $y$  directions. The dark areas indicate regions blocked by the Al layer, with clearly defined boundaries. The dimensions observed in the figure 2b correspond well to the actual dimensions of the Al test patterns.

Our results illustrate the potential of utilizing spintronic terahertz emitters for super-resolution imaging, with a spatial resolution below  $\lambda/100$ .

### References

- [1] J. Wang et al., Nature (2024).  
<https://doi.org/10.1038/s41586-024-07513-x>
- [2] M. Ota et al., Nature Physics **18** (2022) 1436.
- [3] Verdad C. Agulto et al., Scientific Reports **11** (2021) 18129.
- [4] H. Qiu et al., Optics Express. **26** (2018) 15247.
- [5] H. Qiu et al., Applied Physics Express **11** (2018) 092101.



## Low-temperature-grown dilute bismide III-V compound semiconductors towards fabrication of photoconductive antenna for terahertz-wave emission and detection

AdSE, Hiroshima Univ.<sup>1</sup>, RCIQE, Hokkaido Univ.<sup>2</sup>, Kanazawa Inst. Tech.<sup>3</sup>, Meiji Univ.<sup>4</sup>

°Yoriko Tominaga<sup>1</sup>, Fumitaro Ishikawa<sup>2</sup>, Noriaki Ikenaga<sup>3</sup>, Osamu Ueda<sup>4</sup>

E-mail: ytominag@hiroshima-u.ac.jp

Towards the 6<sup>th</sup> generation mobile communications system (6G), it is considered to expand a frequency band higher than that for 5G, 95 GHz–3 THz, and electromagnetic waves up to approximately 300 GHz are under consideration[1]. Therefore, developing and realizing devices that can operate in these frequency bands is an urgent issue. It is essential to elucidate the dielectric, magnetic, and electrical properties of semiconductors and other electronic materials, which constitute the development and manufacturing processes, in these frequency bands. It is said that 6G will be in operation in 2030, the demand for material property measurement systems for the frequency range from the high-frequency band of millimeter waves to the THz wave region (300 GHz up to 3 THz) is expected to significantly increase in the next decade. The authors are focusing particularly on dilute bismide (Bi) III-V compound semiconductors grown at low temperatures as a candidate material for photoconductive antenna (PCA) that is a device often used for generating and detecting THz wave in these frequency bands as a drive source of ultrashort laser pulses in the THz time-domain spectroscopy system.

Dilute Bi-III-V compound semiconductors such as GaAsBi and InAsBi are relatively new semiconductor materials that show unique properties: the band gap is rapidly reduced; the energy of the valence band maximum shifts to a higher one; and the temperature dependence of the band gap is reduced; when a few percent of Bi atoms are incorporated into the parent semiconductor crystal[2-4]. From the viewpoint of crystal growth, it is interesting that low-temperature growth at  $\leq 400^\circ\text{C}$  is necessary to incorporate Bi atoms into matrix crystals such as GaAs[5]. Because the band gap energy of (In)GaAsBi shifts to near-infrared region when Bi atoms are incorporated into crystals of (In)GaAs, and incorporating In and Bi into GaAs affects the conduction and valence band edges, respectively, one may locate the Fermi levels at mid-gap in the semiconductors for PCAs activated by 1.5- $\mu\text{m}$  wavelength lasers by controlling the defect levels.

In this presentation, the authors report molecular beam epitaxial growth of GaAsBi and InGaAsBi at low temperatures of  $\leq 250^\circ\text{C}$  towards fabrication of the PCAs[6]. The kinds of defects within the crystals will be discussed[7], and the authors provide an outlook on how to obtain the three characteristics of ultrashort carrier lifetimes, high resistivity, and relatively good carrier mobility which are required for the operation of the PCAs.

Acknowledgments: This study was partially supported by JSPS KAKENHI 19H04548, 21H01829, 21H05566, 21K04910, and a research grant from the Iketani Science and Technology Foundation.

[1] “5G sophistication and 6G” NTT DOCOMO White paper, November 2022 (Version 5.0). (in Japanese)

[2] K. Oe, Jpn. J. Appl. Phys., **41**, 2801 (2002). [3] A. Janotti et al., Phys. Rev. B, **65**, 115203 (2002). [4] Y. Zhang et al., Phys. Rev. B, **71**, 155201 (2005). [5] M. Yoshimoto et al., Jpn. J. Appl. Phys. **42**, L1235 (2003). [6] Y. Tominaga et al., Appl. Phys. Express, **15**, 045504 (2022). [7] O. Ueda et al., J. Cryst. Growth, **601**, 126945 (2023).



## Terahertz spin currents resolved with nanometer spatial resolution

Xiaojun Wu

School of Electronic and Information Engineering, Beihang University, Beijing, 100191,  
China, [xiaojunwu@buaa.edu.cn](mailto:xiaojunwu@buaa.edu.cn)

The ability to generate, detect, and control coherent terahertz (THz) spin currents with femtosecond temporal and nanoscale spatial resolution has significant ramifications. The diffraction limit of concentrated THz radiation, which has a wavelength range of 5  $\mu\text{m}$ -1.5 mm, has impeded the accumulation of nanodomain data of magnetic structures and spintronic dynamics despite its potential benefits. Contemporary spintronic optoelectronic apparatuses with dimensions 100 nm presented a challenge for researchers due to this restriction. In this study, we demonstrate the use of spintronic THz emission nanoscopy (STEN), which allows for the efficient injection and precise coherent detection of ultrafast THz spin currents at the nanoscale. Furthermore, STEN is an effective method that does not require invasion for characterising and etching nanoscale spintronic heterostructures. The cohesive integration of nanophotonics, nanospintronics, and THz-nano technology into a single platform is poised to characterize the spin state at the micro-to-nanoscale density, accelerate the development of high-frequency spintronic optoelectronic nanodevices and other revolutionary technical applications.

### Reference:

- [1] Jiahua Cai, et al., Appl. Phys. Rev. 10, 041414 (2023).
- [2] Xiaojun Wu, et al., Adv. Mater. 35, 2208947 (2023).
- [3] Xiaojun Wu, et al., Adv. Mater. 34, 2204373 (2022).
- [4] Xinhou Chen, et al., Adv. Mater. 34, 2106172 (2022).



**Xiaojun Wu** received his PhD degree in the Institute of Physics, Chinese Academy of Sciences. She joined in Beihang University in the May of 2017 after she completed his Humboldt postdoctoral research at DESY in Germany. In the past 10 years, she has been engaged in researches on ultrafast THz science, technology, and applications, especially focusing on generating high-energy high-field THz radiation and its applications, spintronic THz devices and systems. She has published >80 academic papers on top journals including Nature Photonics, Nature Communications, Optica, Advanced Materials etc, and given >40 keynote and invited talks on FiO, IRMMW-THz, UP, OTST, ISUPTW, POEM and so on. She was awarded the first Zhenyi Wang Award for Excellence for achievements in the development of high-power THz sources and the generation and manipulation of chiral THz waves by International Society of Infrared, Millimeter, and THz Waves: IRMMW-THz, the first Women in Ultrafast Science Global Award, and the first prize of the first China Science and Technology Youth Forum, and she becomes Optica Fellow in 2023.

## 3D-printed Packaging for Terahertz Silicon Waveguides

Nguyen H. Ngo<sup>1</sup>, Weijie Gao<sup>1</sup>, Mingxiang Li<sup>2</sup>, Daiki Ichikawa<sup>1</sup>, Yoshiharu Yamada<sup>3</sup>,  
Hidemasa Yamane<sup>3</sup>, Shuichi Murakami<sup>3</sup>, Withawat Withayachumnankul<sup>2</sup>, Masayuki Fujita<sup>1</sup>

<sup>1</sup> Graduate School of Engineering Science, Osaka University, Japan

<sup>2</sup> Terahertz Engineering Laboratory, The University of Adelaide, Australia

<sup>3</sup> Osaka Research Institute of Industrial Science and Technology, Japan

Email: [ngo.h-nguyen.es@osaka-u.ac.jp](mailto:ngo.h-nguyen.es@osaka-u.ac.jp)

### 1. Introduction

In recent years, the rapid development of terahertz (THz) devices has necessitated the utilization of waveguides for coupling signals to the devices under test. Metallic hollow waveguides have been widely adopted for coupling purposes owing to their high coupling efficiency and compatibility with the equipment. As the frequency approaches 300 GHz and higher, the hollow core's size shrinks to less than 1 mm, complicating micromachining and gold plating processes and leading to high fabrication costs. With the advancement of additive manufacturing technology, 3D-printed metallic waveguides have been developed with high accuracy and high coupling efficiency [1]. Nevertheless, the optimization of post-process for metallization is required, and hence, increases the finishing complexity. All-dielectric waveguides are featured for their low loss, low dispersion, and flexible design [2,3]. A drawback of this waveguide is the requirement of supporting frames. To address these problems, we propose non-metallic 3D-printed packages for all-silicon waveguides, targeting the WR-3.4 band (220–330 GHz).

### 2. Fabrication

The packages are printed using a commercial 3D printer with polylactic acid (PLA) as the printing filament. Figure 1 shows the model of the 3D-printed package with UG-387/UM flange for the WR-3.4 band. An effective-medium (EM)-clad silicon waveguide, of which the mechanism is based on total internal reflection, was employed owing to its ultra-low loss and broad bandwidth [3]. The waveguides were fabricated on a 200- $\mu\text{m}$ -thick high-resistivity ( $> 10 \text{ k}\Omega\cdot\text{cm}$ ) silicon wafer. The waveguide width ( $w$ ) is 225  $\mu\text{m}$  with a taper length ( $TL$ ) of 2.5 mm. An air hole's period ( $a$ ) and radius ( $r$ ) are 100  $\mu\text{m}$  and 45  $\mu\text{m}$ , respectively. Four corners of the waveguide are cut for alignment purposes. The upper lid is then capped, and the silicon waveguide is locked in place.

### 3. Results

The samples were evaluated using a vector network analyzer with WR-3.4 extenders. Figure 2 shows the transmittances of the 2-cm sample for the bare waveguide in simulation (blue) and experiment (orange) and the 3D-package measurement (yellow). The results agree well with each other at a high-frequency range, i.e., 270 – 330 GHz, while a discrepancy is observed at a low-frequency range. The difference is likely due to the misalignment of the waveguide in the package, while the bare waveguide can be freely adjusted at the interface of the hollow waveguide to achieve the highest transmittance. In addition, the wave at the low-frequency range is prone to strong interaction with the lossy package material due to a weaker wave confinement.

### 4. Conclusion

Despite the discrepancy, the 3D package shows a broad bandwidth of 110 GHz in the WR-3.4 band. Such 3D-printed packages for silicon waveguides promisingly show low-loss and low-cost solutions for terahertz applications in high-speed communications and non-destructive imaging and sensing.

**Acknowledgement** This work was supported in part by CREST, JST (JPMJCR21C4), KAKENHI (24H00031), and AJF, Australia (AJF2021044).

### References

- [1] G. Xu *et al.*, *J. of Appl. Phys.*, 133 (2023) 210901. [2] K. Tsuruda *et al.*, *Opt. Express*, 23 (2015) 31977.  
[3] W. Gao *et al.*, *Opt. Express*, 27 (2019) 38721.

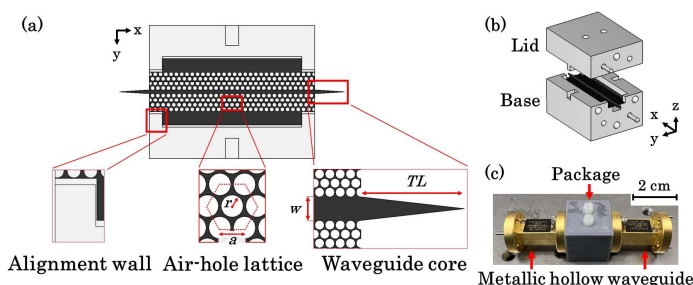


**Fig. 1** (a) EM waveguide inside the package, (b) 3D-printed package model, (c) fabricated package with two supportive metallic hollow waveguides.

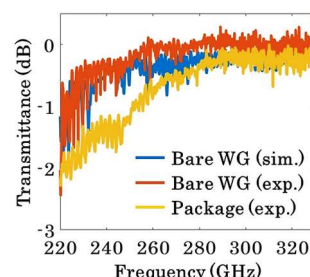


**Fig. 2** Transmittances of a 2-cm sample in simulation, experiment, and 3D-package.

# New Composition Signal Among Comb-Like Terahertz Spectrum Generated Using Dual Multimode Laser Diodes

Yuanhao Zeng<sup>1</sup>, Kosaku Kato<sup>1</sup>, Verdad C. Agulto<sup>1</sup>, Fumiyoshi Kuwashima<sup>2</sup>, Masahiko Tani<sup>1,3</sup>  
Masashi Yoshimura<sup>1</sup>, Makoto Nakajima<sup>1</sup>

<sup>1</sup> ILE, Osaka Univ., <sup>2</sup> Dept. of EEE, Fukui Univ. of Tech., <sup>3</sup> FIR, Univ. of Fukui  
E-mail: u326341i@ecs.osaka-u.ac.jp

## 1. Introduction

The application of sub-THz technology in material evaluation is gaining traction. As sub-THz frequencies are expected to be used in "beyond the 5th generation" (B5G) and 6G wireless communication bands, there is a need for material testing technology in this region. [1-3] A

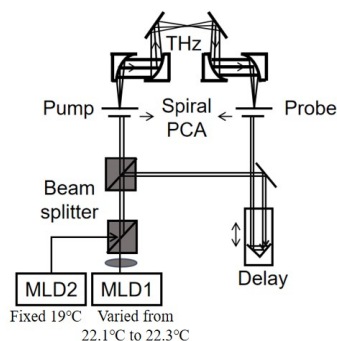


**Fig. 1.** Experiment setup of the dual-MLD THz-TDS system.

continuous wave multi-mode laser diode (CW-MLD) based THz time-domain spectroscopy (TDS) [4-6] system offers a cost-effective alternative to systems using femtosecond lasers. A 660 nm MLD can generate sub-terahertz spectra from 25 GHz to 200 GHz. However, the THz spectra produced by a single MLD have a comb-like structure with fixed THz peaks, leading to gaps in spectral information. In this work we demonstrate that using two MLDs can generate new signal components to fill these spectral gaps.

## 2. Experiment and Results

The schematic diagram of the dual-MLD-THz-TDS system is shown in Fig. 1. We used two CW-MLDs with a central wavelength about 660 nm. The central wavelength and output power of the MLDs were regulated by manipulating their excitation current and operational temperature. We fixed the operation temperature of MLD2 at 19°C, so that we can only adjust the temperature of MLD1 to match the wavelength. The total laser power supplied to the PCAs was around 9 mW for pump and about 8 mW for probe, which were the same power used in the single MLD system.

The THz spectra generated using only 1 MLD and dual MLDs are shown in Fig. 2. The peak spacing in the spectrum is determined by the separation value between the longitudinal modes of the MLD, which is 0.025 THz, as shown by the blue dashed lines. The colored curves show the THz spectra generated using two MLDs at different MLD1 temperatures. In addition to the 0.025-THz-period peaks observed from a single MLD, beat-frequency THz signals, indicated by arrows, are generated when two MLDs are used. These beat-THz signals are typically paired, and their frequencies can be adjusted by changing the MLD operating temperature. The successful generation

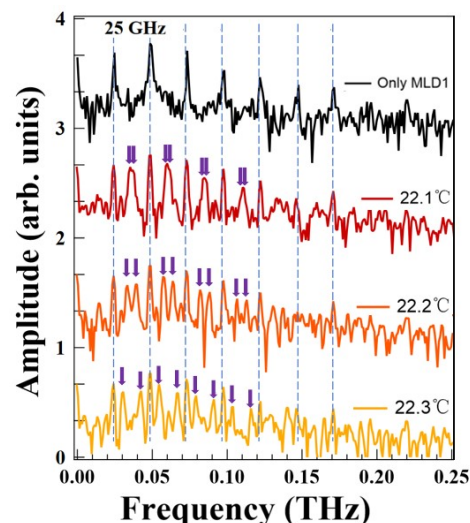


**Fig. 2.** THz spectra signals. MLD1 operated with temperatures varying from 22.1 °C to 22.3 °C, while the temperature of MLD2 was fixed.

of beat-THz signals has enabled us to overcome the limitation of single MLD-TDS, which emits fixed-frequency THz signals constrained by the MLD's longitudinal modes. In contrast, the CW-THz signals and their beat-THz signals from our dual MLDs CW-THz-TDS system can continuously cover the frequency range from 0.025 THz to 0.2 THz. This provides the possibility for CW THz spectral measurement within this frequency range.

## 3. Conclusions

We confirmed that using two MLDs in an MLD-based THz-TDS system generates new spectral components known as beat-frequency THz signals. These new components enhance the potential of MLD-based THz-TDS systems for spectroscopic applications. The dual-MLD THz-TDS system is expected to be widely used in the future, particularly for testing of semiconductor materials and evaluating communication materials.

## References

- [1] V.C.Agulto et al., Sci. Rep., **11** (2021) 18129.
- [2] M.Ota et al., Nat. Phys., **18** (2022) 1436.
- [3] J. Wang et al., Nat. (2024)  
<https://doi.org/10.1038/s41586-024-07513-x>.
- [4] O. Morikawa et al., Jpn. J. Appl. Phys., **59** (2020) 082003.
- [5] M. Tani et al., Semicond. Sci. Technol., **20** (2005) S151.
- [6] F. Kuwashima et al., Opt. Express, **28** (2020) pp. 24833-24844.

# Terahertz spectroscopy and imaging of circular dichroism in chiral metasurfaces

Takumi Yoichi<sup>1</sup>, Uina Chiba<sup>1</sup>, Rinpei Sasaki<sup>1</sup>, Takeo Minari<sup>2</sup>, Seigo Ohno<sup>3</sup>, Katsuhiko Miyamoto<sup>1,4</sup>

<sup>1</sup> Chiba University, <sup>2</sup> National Institute for Materials Science, <sup>3</sup> Tohoku University,

<sup>4</sup> Molecular Chirality Research Center Chiba University

E-mail: k-miyamoto@faculty.chiba-u.jp

## 1. Introduction

Optical metamaterial elements that break mirror symmetry, such as swastika-shaped lattice structures, have been shown to exhibit chirality in the terahertz (THz) region, which is due to the spiral character of their hierarchical three-dimensional structure. However, in ordinary THz imaging with a linearly polarized beam, it has been difficult to quantify chiral optical characteristics, limiting the ideal design of metamaterials.

The aim of our research is to develop a circularly polarized THz imaging system that has not before been investigated in the THz frequency range. The system combines a tunable frequency THz source [1] and a circularly polarized cross-Nicol arrangement. Its purpose is to visualize the structural chirality of metasurfaces created using printed electronics techniques [2], specifically twisted-layered moiré metasurfaces (TLMMS) [3].

## 2. Experiments and results

The THz light source is formed of a 4'-dimethylamino- N-methyl- 4-stilbazolium tosylate difference frequency generator (DAST-DFG) pumped by a 1.5  $\mu\text{m}$  dual-wavelength picosecond source (pulse width:  $\sim 8$  ps, PRF: 1 MHz). A linear polarized THz beam was converted into circular polarized beam by using a quarter wave plate (QWP: TYDEX, WP-CQ), and it was focused to a diameter of  $\sim 170$   $\mu\text{m}$  on the TLMMS. A circular polarized crossed-Nicol setup including a QWP, and a wire-grid analyzer is utilized to specifically detect the polarization component modulated by the samples.

A triangular lattice configuration of metal (Ag) disk (radius of 11.25  $\mu\text{m}$ ) array was fabricated on a Zeonor film sheet (50  $\mu\text{m}$  thick). The TLMMS was fabricated by layering two film sheets with a twist angle of roughly 1.5 degrees, either right-handed or left-handed, as shown in Fig.1. The two singularities labeled as A and B in Fig. 1 represent the specific points of structural chirality in the TLMMS. THz CD spectroscopy measurements were conducted at either point A or B, revealing an imaging frequency of 4.35 THz, which was then used for THz CD imaging.

Figure 2 (a) shows the experimentally achieved two-dimensional imaging at 4.35 THz for the TLMMS with a left-hand twist. The images are 60 x 60 pixels with a resolution of 100  $\mu\text{m}$  per pixel, covering a scanning area of 6 x 6 mm. The circular dichroism factor,  $g$ , was calculated using the formula,  $g = (I_R - I_L)/(I_R + I_L)$ , where  $I_{R,L}$  is the transmitted signal intensity of left- and right-handed circular polarizations. It is interesting to note that the sign of the  $g$  factor at points A and B is reversed, manifesting the structural chirality of TLMMS.

Figure 2(b) compares the results of THz CD imaging with scaled-layered moiré metasurface. Scale moiré was created by superimposing two kind of Ag disk array with differing lattice constants. The results reveal that, unlike the TLMMS experimental results, singularities A and B are not identifiable, and there is no clear  $g$ -value inversion. In principle, the scale moiré has no structural chirality, which supports the experimental results.

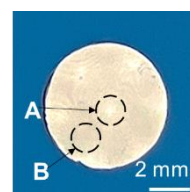


Fig. 1. TLMMS optical image with a left-handed twist.

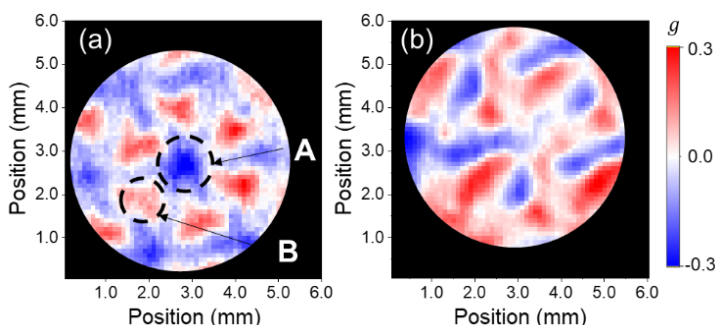


Fig. 2. THz circular dichroism imaging at a frequency of 4.35 THz. (a) TLMMS with a left-handed twist, (b) Scale moiré.

## 3. Conclusion

We have successfully shown the application of THz CD spectroscopic imaging on a TLMMS using a DAST-DFG THz source and circular polarization crossed-Nicol configuration detection. The singularities of TLMMS, resulting from its structural chirality, can be easily distinguished as left- and right-handed. The implementation of our suggested THz CD spectroscopic imaging will enhance the progress of THz research and technology by enabling precise evaluation of optical properties, including chiral molecules and structures.

## Acknowledgements

The authors are grateful to Prof. T. Omatsu in Chiba University for the insightful discussion. This work was supported by JSPS KAKENHI Grant Number JP22H01980 and JP23K17885, JST FOREST Program, Grant Number JPMJFR2036.

## References

- [1] K. Miyamoto et al., Opt Express, **27**, (2019), 31840.
- [2] L. Li et al., Small, **17**, (2021), 2101754.
- [3] S. Ohno, Appl Phys Lett, **108**, (2016), 251104.



## Kinetics analysis of anti-CD9 antibody and H1299 EV using terahertz chemical microscope

Okayama Univ. °(M2)Yuchen Ma, (D2)Changjiang Liu, (D1)Xue Ding, Jin Wang and Toshihiko Kiwa

E-mail: [pa835s36@s.okayama-u.ac.jp](mailto:pa835s36@s.okayama-u.ac.jp)

### 1. Introduction

In recent years, hospitals have used PET-CT scans and pathology to detect lung cancer, but PET-CT scans involve the use of radioactive tracers as well as X-rays from the CT scan, frequent scans can increase long-term health risks, and pathology requires advanced technology. Recent studies have shown that exosomes released from cells can provide the information needed to detect and diagnose cancer. Exosomes play an important role in tumourigenesis, cancer invasion, angiogenesis, tumour microenvironment formation and cancer metastasis. Currently, exosome detection methods include SPR and ELISA, but both have limitations and cannot quickly detect small samples. To address these problems, our research group developed terahertz chemical microscope (TCM) [1,2,3]. Through TCM detection, we found that the concentration of exosomes is proportional to the intensity of terahertz waves. This demonstrates TCM can be used for the quantitative analysis of exosomes.

### 2. Experimental and Results

TCM is a system that measures the surface potential of a sensing plate as the THz amplitude emitted from the sensing plate. In this study, anti-CD9 antibodies were used and immobilized on the sensing plate. Then, the exosomes from the H1299 lung cancer cell line (H1299 EV) were interacted anti-CD9 antibodies. The sensing plate was irradiated with a femtosecond laser to excite charge carriers in the valence band of the silicon layer, and the terahertz wave amplitude was proportional to the potential of the sensor surface. When exosomes are added to the sensor surface, a chemical reaction occurs, changing the electron distribution in the molecule and the surface potential of the silicon dioxide film. By comparing the terahertz wave intensity measurements before and after the reaction, the reaction of the exosome with the antibody can be detected.

The methodology of the study was as follows. First, phosphate buffer solution (PBS) was added as a reference for TCM imaging, then the surface solution was removed and 0.4 µg/mL H1299 EV solution was added. The reaction was allowed to proceed on a shaker (45 rpm) at room temperature for 45 minutes. TCM imaging was then performed again. Finally, the 0.4 µg/mL H1299 EV solution was removed. TCM imaging of 0.8 µg/mL, 1.2 µg/mL, 1.6 µg/mL and 2.0 µg/mL H1299 EV solutions was performed as described above.

Figure 1 shows the reference imaging and the imaging of the reaction of each concentration of H1299 EV with the antibody CD9. The measurement range is 6 mm × 6 mm as shown in the black square. It can be seen that the colour of

the image representing the intensity of the terahertz wave deepens as the concentration of H1299 EV increases. Figure 2 shows the concentration of H1299 EV as a function of the variation in terahertz intensity. The vertical axis represents the THz intensity, the horizontal axis represents the concentration of H1299 EV and the error bar represents the standard deviation of the THz intensity obtained from four measurements. The dissociation constants ( $K_d$ ) were determined from the curve fitting and Hill equation in Figure 2.

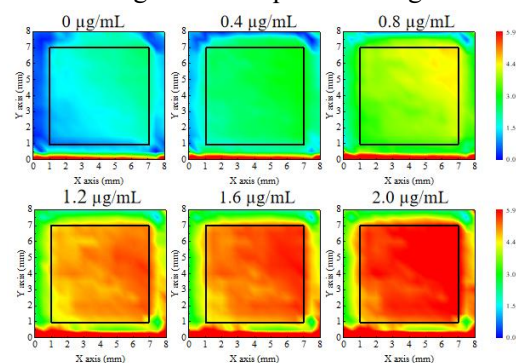


Figure 1. Terahertz intensity distribution with changing concentration of H1299 EV.

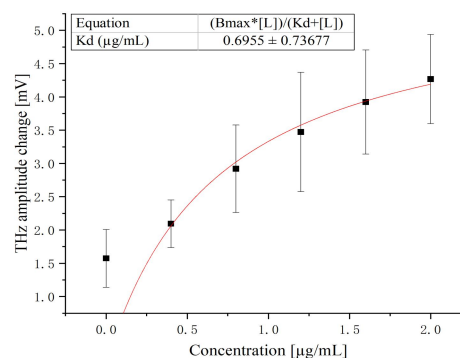


Figure 2. Determination of  $K_d$  using terahertz chemical microscope.

### 3. References

- [1] T. Kiwa et al., "A terahertz chemical microscope to visualize chemical concentrations in microfluidic chips," *Jpn. J. Appl. Phys.*, vol. 46, no. 11L, p. L1052, 2007.
- [2] T. Kiwa, J. Kondo, S. Oka, I. Kawayama, H. Yamada, M. Tonouchi, and K. Tsukada: "Chemical biosensor with a laser-terahertz monitoring system," *Appl. Opt.* 47, 18, pp. 3324-3327 (2008)
- [3] Liu, C.; Wang, J.; Negishi, R.; Inuzuka, T.; Kiwa, T. Label-Free Measurement of CD63 Positive Extracellular Vesicles Using Terahertz Chemical Microscopy. *ACS sensors* 2024.



4 JSAP-Optica Joint Symposia 2024 | 一般セッション(口頭講演) : 4.7 Quantum Optics, Nonlinear Optics and Structured Optics

## **[19p-C43-1~15] 4.7 Quantum Optics, Nonlinear Optics and Structured Optics**

[19p-C43-1]

[JSAP-Optica Joint Symposia Invited Talk] Nonlinear mode converted with multi-color spectral composites

K.-H. Chang<sup>1,2</sup>, J.-H. Lai<sup>1</sup>, T.-F. Pan<sup>1</sup>, H.-H. Chiu<sup>3</sup>, A. Boudrioua<sup>2</sup>, C.-M. Lai<sup>4</sup>, H. Yokoyama<sup>5</sup>, E. Higurashi<sup>5</sup>, H. Akiyama<sup>6</sup>, OLung-Han Peng<sup>1,3</sup> (1.Graduate Institute of Photonics and Optoelectronics, National Taiwan University, 2.Laboratoire de Physique de Lasers CNRS UMR 7538, Universite Sorbonne Paris Nord, 3.Dept. Elec. Eng. National Taiwan University, 4.Electronic and Optoelectronic System Research Laboratories, Industrial Technology Research Institute, 5.Graduate School of Engineering, Tohoku University, 6.The Institute for Solid State Physics, The University of Tokyo)

[19p-C43-2]

[JSAP-Optica Joint Symposia Invited Talk] Optical skyrmion beam generation based on integrated photonics

OSatoshi Iwamoto<sup>1,2</sup>, Wenbo Lin<sup>3</sup>, Yasutomo Ota<sup>4</sup> (1.RCAST, The Univ. of Tokyo, 2.IIS, The Univ. of Tokyo, 3.Tokyo Institute of Technology, 4.Keio University)

[19p-C43-3]

Green Skyrmion fiber laser

O(P)Srinivasa Rao Allam<sup>1,2,3</sup>, Yuto Yoneda<sup>1</sup>, R. Kerridge-Johns William<sup>4</sup>, Yasushi Fujimoto<sup>5</sup>, Takashige Omatsu<sup>1,2</sup> (1.GSE, Chiba Univ., 2.MCRC, Chiba Univ., 3.IAAR, Chiba Univ., 4.Univ. Southampton, 5.Chiba Inst. Tech.)

[19p-C43-4]

High-speed atomic force microscopy combined with optical vortex for in-situ real-time observation of twisting azo-polymer

OKota Kojimoto<sup>1</sup>, Rihito Tamura<sup>2</sup>, Chan Feng-Yueh<sup>3</sup>, Keishi Yang<sup>1</sup>, Takayuki Uchihashi<sup>3,4</sup>, Prabhat Verma<sup>1</sup>, Takashige Omatsu<sup>2,5</sup>, Takayuki Umakoshi<sup>1</sup> (1.Osaka Univ., 2.Chiba Univ., 3.Nagoya Univ., 4.ExCELLS, Nagoya Univ., 5.MCRC, Chiba Univ.)

[19p-C43-5]

[JSAP-Optica Joint Symposia Invited Talk] High-order Laguerre- and Hermit-Gaussian laser generated from laser cavity incorporating aberrated cat-eye optics

OQuan Sheng<sup>1</sup>, Shijie Fu<sup>1</sup>, Wei Shi<sup>1</sup>, Jianquan Yao<sup>1</sup>, Yuanyuan Ma<sup>2</sup>, Takashige Omatsu<sup>2</sup> (1.Tianjin University, 2.Chiba University)

[19p-C43-6]

Electron Dynamics of Ultrafast Vector Vortex Laser Irradiation

O(M2)JIAMING ZHANG<sup>1</sup>, Morita Ken<sup>2</sup>, Verdad C. Agulto<sup>1</sup>, Kosaku Kato<sup>1</sup>, Makoto Nakajima<sup>1</sup> (1.ILE., Osaka Univ., 2.Chiba Univ.)

[19p-C43-7]

Controlled Generation of White-Light Filaments in BK-7 Glass using Ultrafast Vector Pulses

OMaruthi Manoj Brundavanam<sup>1</sup>, Yuuki Uesugi<sup>2</sup>, Yuichi Kozawa<sup>2</sup> (1.IIT Kharagpur, 2.IMRAM, Tohoku Univ.)

[19p-C43-8]

Real-time movies of photo-induced azo-polymer motions obtained by high-speed atomic force microscopy

○Keishi Yang<sup>1</sup>, Feng-Yueh Chan<sup>2</sup>, Yasushi Inouye<sup>1,4</sup>, Prabhat Verma<sup>1</sup>, Takayuki Uchihashi<sup>2,3</sup>, Hidekazu Ishitobi<sup>1,4</sup>, Takayuki Umakoshi<sup>1,5</sup> (1.Dept. Applied Physics, Osaka Univ., 2.Dept. of Physics, Nagoya Univ., 3.ExCELLS, 4.FBS, Osaka Univ., 5.Inst. Adv. Co-creation Studies, Osaka Univ.)

---

[19p-C43-9]

Soliton evolution under the perturbative effects of Raman scattering in Highly Nonlinear Materials

○(D)Abhisek Roy<sup>1</sup>, Partha Roy Chaudhuri<sup>1</sup> (1.IIT Kharagpur)

---

[19p-C43-10]

Third Harmonic Generation at THz Frequencies: Utilizing a Frequency Selective Metasurface Approach with Complementary Split Ring Resonators

○(D)Mitali Sahu<sup>1</sup>, Partha Roy Chaudhuri<sup>1</sup> (1.IIT Kharagpur)

---

[19p-C43-11]

Broadband Optical Frequency Comb Generation by Employing dual lasers with Dual-Drive Mach Zehnder modulator and Frequency Modulator

○(DC)PRIYANKA VERMA<sup>1</sup>, SUKHBIR SINGH<sup>1</sup> (1.NETAJI SUBHAS UNIVERSITY OF TECHNOLOGY)

---

[19p-C43-12]

Closed-form solutions in Lugiato-Lefever Equation for Frequency Comb Applications

○(D)Sanjana Bhatia<sup>1</sup>, C.N. Kumar<sup>1</sup> (1.Panjab University, Chandigarh, India)

---

[19p-C43-13]

Transmitted Wave Frequency Shift on a Moving Media Interface: between the Doppler and the Photon Recoil Effects

○(D)Valentyn Ivan Lyman<sup>1</sup>, Evhen Makovetskyi<sup>1</sup>, Ruslan Vovk<sup>1</sup> (1.Kharkiv Univ.)

---

[19p-C43-14]

A Numerical Study on the Sensing Characteristics of Raman-Induced Frequency Shift

○(DC)Protik Roy<sup>1</sup>, Partha Roy Chaudhuri<sup>1</sup> (1.IIT Kharagpur)

---

[19p-C43-15]

Metal-Insulator-Metal (MIM) Waveguide Based Fano Resonance Sensor for Human Sperm Detection

○(B)ANIRUDH YASHOVARDHAN<sup>1</sup>, LOKENDRA SINGH<sup>1</sup> (1.Department of Electronics and Communication Engineering, Graphic Era (Deemed to be University), Dehradun, India - 248001)

---

# Nonlinear mode converted with multi-color spectral composites

K.-H. Chang<sup>1,2</sup>, J.-H. Lai<sup>1</sup>, T.-F. Pan<sup>1</sup>, H.-H. Chiu<sup>3</sup>, A. Boudrioua<sup>2</sup>, C.-M. Lai<sup>4</sup>, H. Yokoyama<sup>5</sup>,  
E. Higurashi<sup>5</sup>, H. Akiyama<sup>6</sup> and L.-H. Peng<sup>1,3</sup>

<sup>1</sup>Graduate Institute of Photonics and Optoelectronics, National Taiwan University, Taipei 106, Taiwan, R.O.C

<sup>2</sup>Laboratoire de Physique de Lasers CNRS UMR 7538, Université Sorbonne Paris Nord, Villetaneuse, France

<sup>3</sup>Dept. Elec. Eng. National Taiwan University, Taipei 106, Taiwan, R.O.C.

<sup>4</sup>Electronic and Optoelectronic System Research Laboratories, Industrial Technology Research Institute, Hsinchu, 310401, Taiwan, R.O.C.

<sup>5</sup>Graduate School of Engineering, Tohoku University, Aramaki Aza Aoba, Aoba-ku, Sendai, Miyagi 980-8579, Japan

<sup>6</sup>The Institute for Solid State Physics, The University of Tokyo, 5-1-5 Kashiwanoha, Kashiwa, Chiba 277-8581, Japan

E-mail: peng1@ntu.edu.tw

## 1. Introduction

Structured light beams constitute emerging light sources which are beneficial to fundamental studies as well as practical applications. Structured light is conventionally shaped in a monochromatic format either in the linear- or nonlinear-optics regime. Most of the related reports, by far, seek the assistance of  $\pi/2$  cylindrical optics, spiral phase plate, q-plate, spatial light modulator, or meta-structures to achieve beam shaping either in phase or amplitude.

Based upon the principle of beam partition and spatial tunneling in the gain modulated quasi-phase-matching nonlinear photonic crystal bi-grating QPM-NPC structures, we demonstrate nonlinear mode conversion characterized by multi-spectral contents with the spectral intensity, phase, and polarization states determined by the individual QPM NPC in action with the partitioned pump laser.

## 2. Theory and Experiments

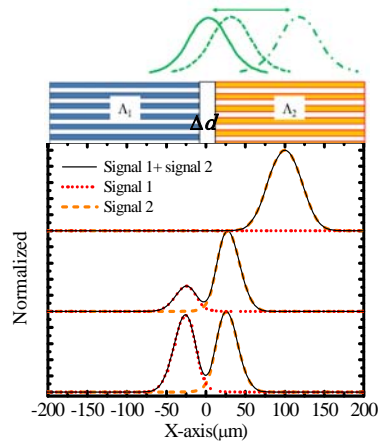


Fig.1 Theory: Calculated Spatial distribution of dual OPG-signal waves from bi-grating OPM-NPC

Overlaid in Fig.1 are the calculated spectral distributions for the dual signal waves at (960, 980) nm arisen from optical parametric generation (OPG) due to NLO interaction of the partitioned 532nm pump beam with a bi-grating QPM-NPC device with period of  $\Lambda_1=7.66$  and  $\Lambda_2=7.68$   $\mu\text{m}$ . These data delineate a feasibility to concurrently oscillate dual-OPOs with a mode pattern composed of multi-spectral contents. Note that the spacer of width  $\Delta d$ , separating the bi-grating QPM gain regions, plays a role like potential

barrier in the Schrödinger equation where continuity of the OPG waves generated from the NLO gain region can assure spatial tunneling. These data present an interesting beam shaping mechanism to incorporate multi-spectral as well as spatial composites due to NLO gain modulation.

Using a HG<sub>10</sub> mode of 532nm pump laser, In Fig. 2 we display the spectrally- and spatially-resolved cavity mode patterns generated from the intra-cavity OPO-SHG/SHG. These data verify a feasibility to achieve NLO mode conversion with multi-spectral composites upon which the spectral contents (intensity, phase, and polarization) are determined by the partitioned pump beam in action to the individual QPM-NPC structure.

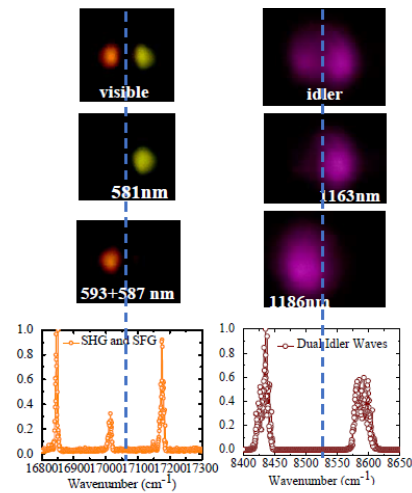


Fig.2 Experiments: Spectrally- and Spatially-resolved mode images from intra-cavity OPO-SHG/SFG processes pumped by HG<sub>10</sub> mode of 532nm pulse laser.

**3. Conclusions:** NLO mode conversion with multi-spectral contents (intensity, phase, and polarization) can be resolved from QPM-NPC which may serve as a building block to realize complex multi-colored vector beams in the future.

**Acknowledgements** LP acknowledged support from National Science and Technology Council (NSTC) R.O.C. by Grant No. 110-2221-E-002-137-MY3, 107-2221-E-002-154-MY3, 104-2221-E-002-071-MY3, and NTU Sister University programs of 109-L203302 106-R203309. HY acknowledged support from AMED (Japan Agency for Medical Research and Development) Grant No. JP21dm0207078, and JSPS (Japan Society for the Promotion of Science) KAKENHI Grant No. JP20H05669. KC acknowledged scholarship from Labex SEAM of France.

# Optical skyrmion beam generation based on integrated photonics

Satoshi Iwamoto<sup>1,2</sup>, Wenbo Lin<sup>3</sup>, and Yasutomo Ota<sup>4</sup>

<sup>1</sup> RCAST, <sup>2</sup> IIS, The University of Tokyo, <sup>3</sup> Tokyo Institute of Technology, <sup>4</sup> Keio University  
E-mail: iwamoto@iis.u-tokyo.ac.jp

## 1. Introduction

Structured light characterized by unique optical fields in space and time has been studied from the viewpoints of fundamental science and applications [1,2]. In addition to widely studied optical vortices and polarization vector beams, optical skyrmion and related optical states, a family of optical fields that have more complex optical fields, have started to get attention recently [3]. Optical skyrmion beams having all polarization states of light in their beam cross-section are one of the family members. Some applications of optical skyrmion exploiting their unique polarization distribution and topological character have been investigated [4,5].

Optical skyrmion beams have been generated mainly using free-space optics setups [5, 6]. Integrated photonics offers an approach for generating optical skyrmion beams in a chip-scale device, enabling the efficient and stable generation of the beams. This would expand the horizon of skyrmion photonics. Here, we will introduce our challenge for creating optical skyrmion beams based on integrated photonics technologies.

## 2. Optical skyrmion beam generator using a silicon micro-ring resonator.

We have proposed a scheme to generate optical skyrmion beams using a micro-ring resonator, an essential device component in integrated photonics [8]. Figure 1 schematically shows the device. The ring resonator is equipped with two surface gratings. The gratings are designed so that each diffracts the cavity mode circulating in the ring into a beam with opposite circular polarization and different orbital angular momentum. An optical skyrmion beam is generated as the superposition of the two diffracted beams. Changing the orders of gratings or exciting a cavity mode with a different order allows the generation of a skyrmion beam with a different skyrmion number.

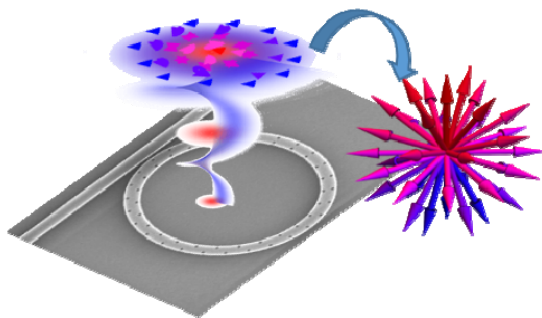


Fig. 1: Ring-resonator-based on-chip skyrmion beam generator

We have realized the devices using a silicon ring resonator and succeeded in generating beams with different skyrmion numbers [9]. In the presentation, the details of the generation mechanism and the experiment will be discussed. If time allows, we will quickly touch our attempts to realize a skyrmion laser [10] and a generator of a skyrmion-crystal beam [11] in integrated photonic platforms.

## Acknowledgements

We would like to express sincere thanks to all the collaborators who are contributing to the work discussed here. The work here was supported by JST-CREST (JPMJCR19T1).

## References

- [1] Y. Shen, X. Wang, Z. Xie, C. Min, X. Fu, Q. Liu, M. Gong, and X. Yuan: *Light Sci. Appl.* **8**, 90 (2019).
- [2] C. He, Y. Shen, and A. Forbes: *Light Sci. Appl.* **11**, 205 (2022).
- [3] Y. Shen, Q. Zhang, P. Shi, L. Du, X. Yuan, and A. V. Zayats: *Nat. Photon.* **18**, 15 (2024).
- [4] R. Tamura, P. Kumar, A. Srinivasa Rao, K. Tsuda, F. Getzlaff, K. Miyamoto, N. M. Litchinitser, T. Omatsu: *APL Photon.* **9**, 046104 (2024).
- [5] A. Wang, Z. Zhao, Y. Ma, Y. Cai, T. Marozsak, B. Chen, H. He, L. Luo, M. J Booth, S. J Elston, S. M Morris, and C. He: *arXiv: 2403.07837* (2024).
- [6] A. M. Beckley, T. G. Brown, and M. A. Alonso: *Opt. Express* **18**, 10777 (2010).
- [7] W. R. Kerridge-Johns, A. Srinivasa Rao, and T. Omatsu: *Optica* **11**, 769 (2024).
- [8] W. Lin, Y. Ota, Y. Arakawa and S. Iwamoto, *Phys. Rev. Research* **3**, 023055 (2021).
- [9] W. Lin, Y. Ota, Y. Arakawa, and S. Iwamoto: "Demonstration of on-Chip Optical Skyrmionic Beam Generators," The 2022 CLEO Conference and Exhibition, SM2N.4 (2022).
- [10] Z. Dai, W. Lin, S. Ji, H. Sakamoto, M. Takenaka, and S. Iwamoto: "Unidirectional Lasing in a Ring Resonator with an S-shaped Waveguide," The 29th MOC, submitted (2024).
- [11] W. Lin, T. Yoshida, H. Atsumi, Y. Sakakibara, T. Amemiya, Y. Ota, and S. Iwamoto: "An optical skyrmion crystal beam generator based on elephant couplers", 2023 JSAP Fall Meeting, 22P-A308-13 (2023).

## Green Skyrmion fiber laser

Srinivasa Rao Allam<sup>1,2,3</sup>, Yuto Yoneda<sup>1</sup>, William R. Kerridge-Johns<sup>1,4</sup>, Yasushi Fujimoto<sup>5</sup>, and Takashige Omatsu<sup>1,2\*</sup>

<sup>1</sup>Graduate School of Engineering Chiba University Chiba 263-8522, Japan

<sup>2</sup>Molecular Chirality Research Centre, Chiba University, Chiba 263-8522, Japan

<sup>3</sup>Institute for Advanced Academic Research, Chiba University, Chiba, 263-8522, Japan

<sup>4</sup>Optoelectronics Research Centre, University of Southampton, SO171BJ, UK

<sup>5</sup>Chiba Institute of Technology, 2-17-1 Tsudanuma, Narashino, Chiba 275-0016, Japan

E-mail: \*[tomatsu@faculty.chiba-u.jp](mailto:tomatsu@faculty.chiba-u.jp)

Optical skyrmions are topologically stable quasiparticles with variegated polarization textures [1], formed by the mixture of quantized spin and orbital angular momentum. In recently, their topological polarization textures have been successfully imprinted on polarization sensitive materials, such as azo-polymers [2], and they have also been utilized in nonlinear frequency conversion [3], and quantum entanglement [4].

The optical skyrmions can be easily produced by the coherent superposition of two circularly polarized Laguerre Gaussian (LG) modes with different azimuthal indices. In fact, the generation of optical skyrmions has been successfully demonstrated by employing diffractive optical elements such as a spatial light modulator, and a digital micro mirror device, however, it exhibits many limitations in mode purity, mode conversion efficiency, output power, and wavelength range. In recent years, we have proposed the direct generation of high quality optical skyrmions from a diode-pumped  $\text{Pr}^{3+}$  ions doped  $\text{YLiF}_4$  solid-state laser with a double output coupler formed of an intra-cavity wedge-plate shearing interferometer (WPSI) [5].

In this paper, we report on the direct generation of green (523 nm) optical skyrmions from a diode-pumped  $\text{Pr}^{3+}$  ions doped water-proof fluoro-aluminate glass (WPFG) fiber laser with an intracavity WPSI dual output coupler configuration.

Figure 1 shows the experimental laser cavity configuration used for the generation of optical skyrmions. A  $\text{Pr}^{3+}$ : WPFG fiber used as an active laser medium possessed a 8  $\mu\text{m}$  core and a 40 mm length. The laser was operated at a fundamental Gaussian mode, and its output was coupled out as a first order LG mode by an intracavity wedge-plate. The Gaussian and LG modes were then coherently superposed by a polarizing beam splitter (PBS) and a quarter-wave plate, thereby generating a first order optical skyrmions. The Néel, Bloch and anti-optical skyrmions were generated at 523 nm, as provided in the inset of Fig. 1.

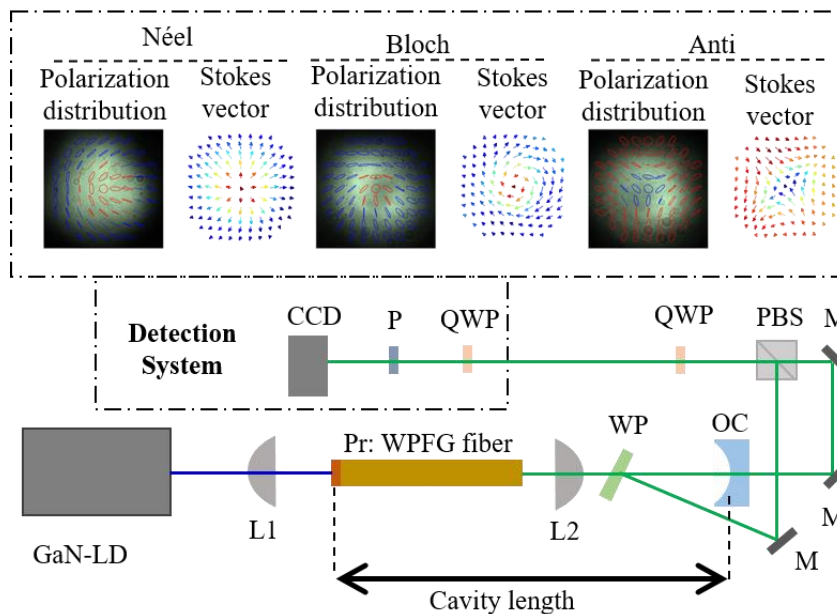


Fig. 1. Experimental configuration used for the generation of optical skyrmions: pump source GaN-LD, plano-convex lens (L1,2), laser gain medium (Pr:WPFG), wedge plate (WP), output coupler (OC), mirror (M), polarizing beam splitter (PBS), polarizer (P), quarter-wave plate (QWP), and charge coupled device camera (CCD).

### References

- [1] S. Gao, F. C. Speirits, F. Castellucci, S. Franke-Arnold, S. M. Barnett, and J. B. Götte, *Phys. Review A* **102**(5), 053513 (2020).
- [2] R. Tamura, P. Kumar, A. S. Rao, K. Tsuda, F. Getzlaff, K. Miyamoto, N. M. Litchinitser, and T. Omatsu, *APL Photonics* **9**(4) (2024).
- [3] A. Karnieli, S. Tsesses, G. Bartal, and A. Arie, *Nat. Commun.* **12**(1), 1092 (2021).
- [4] P. Ornelas, I. Nape, R. de Mello Koch, and A. Forbes, *Nat. Photonics*, **18**, 258–2661 (2024).
- [5] W. R. Kerridge-Johns, A. S. Rao, and T. Omatsu, *Optica* **11**(6), 769-775 (2024).



# High-speed atomic force microscopy combined with optical vortex for *in-situ* real-time observation of twisting azo-polymer

Kota Kojimoto<sup>1</sup>, Rihito Tamura<sup>2</sup>, Feng-Yueh Chan<sup>3</sup>, Keishi Yang<sup>1</sup>, Takayuki Uchihashi<sup>3,4</sup>,  
Prabhat Verma<sup>1</sup>, Takashige Omatsu<sup>2,5</sup>, Takayuki Umakoshi<sup>1,6</sup>

<sup>1</sup>Dept. of Applied Physics, Osaka Univ., <sup>2</sup>Graduate School of Engineering, Chiba Univ., <sup>3</sup>Dept. of Physics, Nagoya Univ.,

<sup>4</sup>ExCELLS, <sup>5</sup>MCRC, Chiba Univ., <sup>6</sup>Inst. Adv. Co-creation Studies, Osaka Univ.

E-mail : umakoshi@ap.eng.osaka-u.ac.jp

## 1. Introduction

An azo-polymer film is a photoactive material forming unique surface reliefs through photoisomerization reactions under light irradiation, which is promising for various optical applications such as optical memory. Moreover, by irradiating the azo-polymer film with optical vortex, a complex twisting structure was formed due to the orbital angular momentum of optical vortex[1]. However, the deformation dynamics and mechanisms have not been fully elucidated.

Recently, we demonstrated that high-speed atomic force microscopy (HS-AFM) is capable of capturing azo-polymer motions in real-time at the nanoscale[2]. Although a simple linear polarization of incident light was used in this study, HS-AFM will be a powerful tool to study more complex dynamics, such as azo-polymer twisting under optical vortex. Therefore, in this study, we constructed HS-AFM combined with optical vortex, as illustrated in Fig. 1, to observe the deformation process of azo-polymer induced by optical vortex.

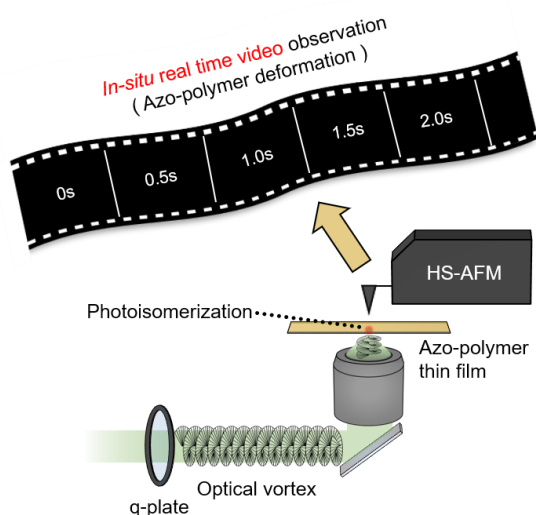


**Figure 1** Schematic diagram of HS-AFM and optical vortex combined system.

## 2. Results and Discussion

HS-AFM is a fast operation AFM that can capture sample motions with high temporal (<10 frames/s) and spatial (~1nm) resolutions. To observe azo-polymer deformation

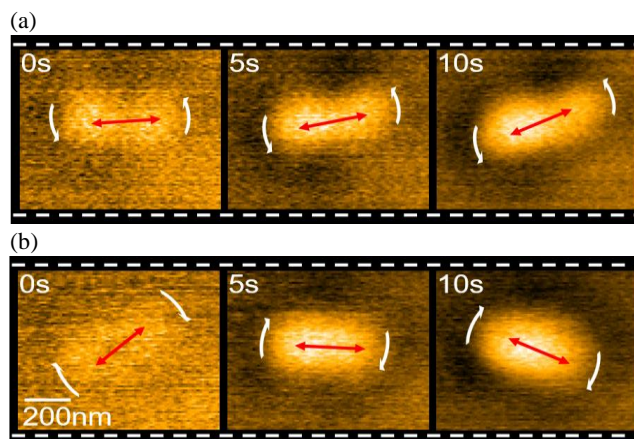


**Figure 2** (a), (b) HS-AFM images of azo-polymer surface deformation induced by optical vortex irradiation with reversed total angular momentum.

occurring at a local focused spot, we employed the setup of a tip-scan HS-AFM installed on an inverted optical microscope, as previously reported [2]. To generate optical vortex, we used a q-plate that can convert circularly polarized light into optical vortex. The direction of optical vortex between clockwise and counter-clockwise can be controlled using right- and left- circularly polarized light.

Using this setup, we illuminated the azo-polymer film with optical vortex while observing it with HS-AFM, as shown in Fig. 2(a). We found that an elliptical structure appeared in the beginning, and subsequently started to rotate counter-clockwise. By changing the optical vortex direction, the rotation became clockwise (Fig. 2(b)). The twisting motions by optical vortex were successfully visualized by HS-AFM. Further details of the experimental setup and HS-AFM movie analysis will be discussed in the presentation.

## 3. Conclusions

We successfully demonstrated the *in-situ* real-time HS-AFM observation of azo-polymer twisting deformation caused by optical vortex.

## References

- [1] M. Watabe, et al., *Sci. Rep.*, **4**, 4218, (2014)
- [2] K. Yang, et al., *Nano Lett.*, **24**, 9, 2805, (2024)

# High-order Laguerre- and Hermit-Gaussian laser generated from laser cavity incorporating aberrated cat-eye optics

Quan Sheng<sup>1</sup>, Shijie Fu<sup>1</sup>, Wei Shi<sup>1</sup>, Jianquan Yao<sup>1</sup>, Yuanyuan Ma<sup>2</sup>, Takashige Omatsu<sup>2</sup>

<sup>1</sup> Tianjin University, China    <sup>2</sup> Chiba University, Japan  
E-mail: shengquan@tju.edu.cn

## 1. Introduction

By introducing mode-dependent laser gain and loss, structured laser field in eigen cavity modes can be generated directly from a laser [1]. Here we present the high-order Laguerre-Gaussian (LG) and Hermit-Gaussian (HG) mode laser output of a Nd:YVO<sub>4</sub> laser cavity incorporating cat-eye optics. The aberration of the cat-eye optics, including the intrinsic spherical aberration (SA) of the spherical lens and the artificially introduced astigmatism via misaligning the cavity, enabled the modal discrimination for high-order mode output. The angular indices of the LG mode laser output could be extended to over 350. High-order two-dimension HG mode output was also obtained.

## 2. Method and results

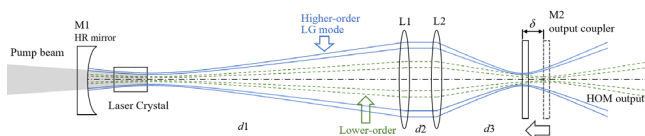


Fig. 1. Cavity arrangement of the high-order mode laser based on aberrated cat-eye optics.

As shown in fig. 1, the laser cavity was consisted of a concave input mirror M1, two lenses L1 and L2 which collimate and refocus the beam, and a flat output coupler M2. A Nd:YVO<sub>4</sub> crystal end-pumped at 878.6 nm provided the laser gain. Here the lens L2 and the mirror M2 located near the focus of the lens made a cat-eye optics, which usually utilized to retroreflect the incident light.

The cat-eye retroreflector could only provide good retroreflection for the on-focus beam incident through its pupil [2]. The ring-like intensity profile of the higher-order LG modes tend to be larger, which experiences stronger focusing given the intrinsic SA of the spherical lens L2. This means, different orders of modes have different focus (beam waist) after being focused by L2, and only the mode with proper size (mode order) so that being focused on the flat M2 can be well-retroreflected to have the smallest loss and win the competition. Therefore, the selection of high-order mode can be realized by simply adjusting the distance between the L2 and M2. Moving M2 towards L2, the laser would trend to operate in higher-order mode with larger beam size and experience stronger focusing, and vice versa.

In the experiment, lenses with different focal lengths were used as L2. Short-focal lens with stronger SA would enhance the modal discrimination, so that single-mode LG output with small angular indices can be obtained. For high-order mode with hundred-level angular indices, we need to use long-focal lens with weaker SA to diminish the loss of the oscillating beam. The LG<sub>0,m</sub> mode output with angular indices  $m$  selectable from 1 to up to 355 have been obtained under the incident diode pump power of 1-3 W, higher order mode requires higher pump power to reach the lasing threshold due to the lower overlap between oscillating beam and the pump beam. The mode order can be selected across a large range by moving the mirror M2 in several millimeters. No customized element is needed for high-order mode generation.

To generate high-order HG mode, we tried to off-axis pump the laser and misalign the cavity slightly via tilting the mirror M2, to change the cavity symmetry from cylindrical to rectangle. Since the cat-eye optics was adopted to provide the cavity feedback, the unwanted deflection loss of the beam was minimized, so that high-order HG mode could be obtained more conveniently than with a linear cavity. In the experiment we obtained the one-dimension HG<sub>m,0</sub> mode output with  $m$  over 60, as well as the two-dimension HG<sub>m,n</sub> mode output with both  $m$  and  $n$  over 20. There two-dimension HG modes facilitate the multi-annular orbital angular momentum beam generation [3].

## 3. Conclusions

In summary, with laser cavity consisted by cat-eye retroreflector, the selection of high-order mode structured field via SA and astigmatism became convenient. LG modes with angular indices up to 355 and two-dimension HG modes output were generated directly from a Nd:YVO<sub>4</sub> laser, without necessity of any customized devices.

## References

- [1] Andrew Forbes, Light Mkhumbuzi, Liang Feng, Orbital angular momentum lasers, *Nature Reviews Physics*, **6** (2024) 352.
- [2] Quan Sheng, Jingni Geng, Zheng Chang et al., Adaptive wireless power transfer via resonant laser beam over large dynamic range, *IEEE Internet of Things Journal*, **10** (2023) 8865.
- [3] Johannes Courtial, Miles J. Padgett, Performance of a cylindrical lens mode converter for producing Laguerre-Gaussian laser modes, *Optics Communications*, **159** (1999) 13.

# Electron Dynamics of Ultrafast Vector Vortex Laser Irradiation

Jiaming Zhang<sup>1</sup>, Ken Morita<sup>2</sup>, Verdad C. Agulto<sup>1</sup>, Kosaku Kato<sup>1</sup>, Makoto Nakajima<sup>1</sup>

<sup>1</sup> ILE., Osaka Univ., <sup>2</sup> Chiba Univ.  
E-mail: u081044i@ecs.osaka-u.ac.jp

## 1. Introduction

The dynamical effects of lasers have garnered widespread attention, holding significant research value in fields such as optical tweezers (optical trapping), laser processing, and photonic nanojets [1,2]. Studies related to optical dynamical effects primarily focus on dielectric materials [3,4]. On the other hand, research on interactions between optical light and single-charged electrons is mainly focused on the conduction electron excitations in the semiconductors involving the quantum transitions, leaving their dynamics insufficiently explored. Recently, we reported an experiment using ultrafast lasers to observe electron relativistic effects [5], demonstrating the enormous potential of optoelectronic interactions. Studying the dynamic effects of lasers on electrons in free carriers in simple materials rather than in dielectric materials, which are assemblies of dipoles, provides a deeper understanding of the dynamics of lasers and the photon-electron interactions.

In this study, we simulated the motion of nearly free electrons in a GaAs under an external laser field of vector vortex beams. Through this research, we aim to derive the macroscopic light-driven force on electrons and find the trace how the spin angular momentum (SAM) and orbital angular momentum (OAM) of the laser affects the specific motion of electrons in the semiconductors.

## 2. Calculation Result

In simulations of the motion of electrons in the semiconductor, the electrons are assumed to be independent of each other and the following electromagnetic force equations are used:

$$m^* \ddot{\mathbf{r}}_i = q(\mathbf{E} + \dot{\mathbf{r}}_i \times \mathbf{B}),$$

where  $m^*$  is the effective mass of electrons in GaAs,  $\mathbf{E}$  and  $\mathbf{B}$  are the electric and magnetic field of laser. In the calculation, we independently calculate the electrons located at different initial positions. These initial positions are in a plane perpendicular to the direction of laser propagation, and  $\mathbf{r}_i$  refers to the positions of different electrons. Electric field of laser beams are described by,

$$\mathbf{E} = f(r, \varphi, z, t) e^{il\varphi} J_x \hat{\mathbf{x}} + f(r, \varphi, z, t) e^{il\varphi} J_y \hat{\mathbf{y}}.$$

where,  $f(r, \varphi, z, t)$  represents the spatial and temporal variations of the electric field, with the term  $e^{il\varphi}$  representing the spiral phase unique to vortex beam.  $\hat{\mathbf{x}}$  and  $\hat{\mathbf{y}}$  represent the unit vectors in the  $x$  and  $y$  directions, we use normalized Jones matrix  $\hat{\mathbf{J}}$  to represent the polarization component, which is  $\hat{\mathbf{J}} = J_x \hat{\mathbf{x}} + J_y \hat{\mathbf{y}}$  and  $|\hat{\mathbf{J}}| = 1$ .

As FIG 1. shows, in the case that the laser intensity is relatively low and  $l=0$ , it can be seen the electron motion is affected by the ponderomotive force, i.e.,  $\mathbf{F} \propto \nabla E^2$  under the irradiation of the light beam.

In the case that the laser intensity is relatively high, as shown in the FIG 2., we notice that the ponderomotive force model is no longer applicable, and the electron displacement exhibits a special pattern. It can also be observed that the number of lobes in this pattern is directly matches to the total

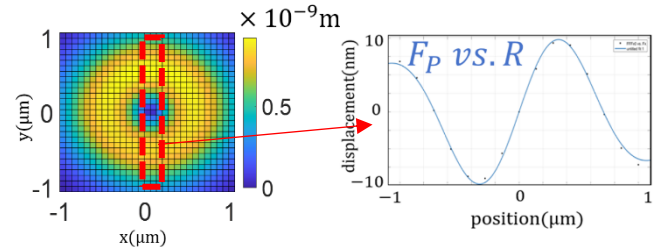


**FIG 1.** The electronic displacement and the fitting results based on ponderomotive force  $F_P$  and displacement  $R$ . The laser here is a circularly polarized Gaussian beam ( $l=0$ ) with an electric field amplitude of  $E = 10^6$  V/m and a wavelength  $\lambda = 800$  nm. The electron displacement  $R$  is the distance traveled after the end of the laser pulse (pulse width 100 fs)

angular momentum  $J$ . In FIG 2. a), for  $l = 2$  and  $\sigma = -1$  ( $J = l + \sigma = 1$ ), matches the number of lobes in the graph. Here,  $\sigma$  represents the SAM and  $l$  represents the OAM of laser photons, respectively. On the other hand, in FIG 2. b), for  $l = 1$  and  $\sigma = 1$  ( $J = l + \sigma = 2$ ), we also find that this rule still holds. We believe that this represents the effect of angular momentum on the dynamics in macroscopic regions.

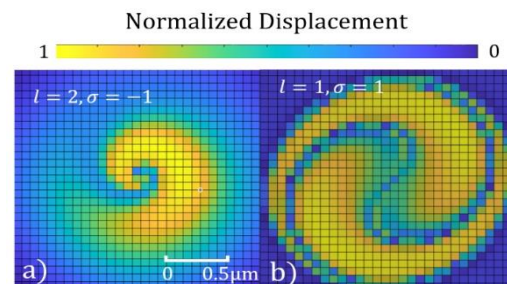


**FIG 2.** Electron motion driven by high-intensity vector vortex laser, where  $E=10^{11}$  V/m and wavelength  $\lambda = 800$  nm,  $\sigma$  is defined by Jones vector which is  $\sigma = 2\text{Im}(J_x J_y^*)$ .

## 3. Conclusions

This study primarily simulates and calculates the behavior of electron motion in a GaAs sample under laser irradiation, particularly with vector vortex lasers. Our results show that under low-intensity laser conditions, the ponderomotive force model is applicable. However, under high-intensity conditions, the electron displacement exhibits a special topological pattern, which is directly related to the orbital angular momentum of the laser electromagnetic field. The specific mechanism behind this phenomenon remains to be clarified.

## References

- [1] M. Piccardo, M. de Oliveira, A. Toma, et al, Nat. Photon. **16** (2022) 359.
- [2] Z. Shen, L. Su, X.-C. Yuan, Y.-C. Shen, Appl. Phys. Lett, **109** (2016) 241901.
- [3] J. Wang et al., Nature (2024).doi:10.1038/s41586-024-07513-x.
- [4] V.C.Agulto et al.,Scientific Reports 11 (2021) 18129.
- [5] M.Ota et al., Nature Physics, 18 (2022) 1436.



# Controlled Generation of White-Light Filaments in BK-7 Glass using Ultrafast Vector Pulses

Maruthi M Brundavanam<sup>1</sup>, Yuuki Uesugi<sup>2</sup>, Yuichi Kozawa<sup>2</sup>

<sup>1</sup> Department of Physics, IIT Kharagpur, Kharagpur, West Bengal, India, <sup>2</sup> Institute of Multidisciplinary Research for Advanced Materials (IMRAM), Tohoku University, Sendai, Japan  
E-mail: bmmanoj@phy.iitkgp.ac.in

## 1. Introduction

One of the fascinating mechanisms caused by the intense light-matter interaction is the generation of the filaments in optical media using ultrafast femtosecond lasers [1]. The filamentation using femtosecond laser pulses is of great interest due to its scientific vigor and practical applications [2]. The control of the filamentation and properties of the output optical field has gained large interest since its discovery [3].

Recently, there has been an increased interest in the generation of the filamentation using femtosecond vector pulses [4, 5] due to their fascinating intensity and polarization structures [5]. The existing experimental and numerical studies on filamentation with femtosecond vector pulses, such as radial or azimuthal polarization, are done in air [4, 5].

In the present work, we demonstrate experimentally the generation and control of white-light filaments in BK-7 glass using ultrafast vector pulses.

## 2. Experimental Details

Ultrafast femtosecond pulses with a peak wavelength of 800 nm, pulse width of 100 fs and repetition rate of 1 kHz from a Ti:Sapphire laser with a regenerative amplifier (Spitfire Pro, Spectra Physics) are used for the present studies. The power of the pulses is controlled using a variable attenuator. The pulses are passed through a segmented half wave plate to generate femtosecond vector pulses with radial or azimuthal polarization, depending on the incident polarization direction. The generated vector pulses are focused into a BK-7 glass using a lens with a focal length of 100 mm. The cross-sectional images of the generated filaments are produced using a bi-convex lens and recorded by a beam profiler, located at the image position, after filtering out the incident laser pulses.

The spatial profiles of the radially (R) and azimuthally (A) polarized femtosecond pulses are shown in the figures 1(a) and 1(g) respectively. The power of the incident pulses is adjusted to observe the multiple filaments for radially and azimuthally polarized beams as shown in the figure 1 (b) and (h), respectively, which are in close match with the proposed numerical model [5].

A linear polarizer is inserted just before the focusing lens to control the spatial structure and polarization of

the incident pulses. By rotating the polarizer, we can control the spatial structure of the vector pulses focused into the BK-7 glass and there by controlling the position of the filaments along the azimuthal directions as shown in the figures from 1 (c) to 1(f) for radial polarization and 1(i) to 1(l) for azimuthal polarization. The control of the filament position and the polarization simply by rotating a linear polarizer during filamentation is very useful in laser patterning of chiral structures.

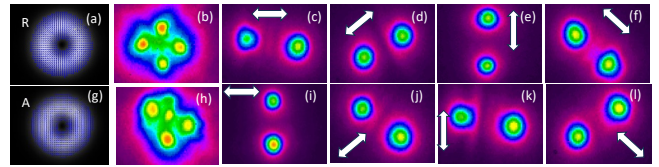


**Fig. 1:** (a) to (f) corresponds to radial polarization; (g) to (l) corresponds to azimuthal polarization. White arrow corresponds to the polarizer angle

## 3. Conclusions

Experimental generation and imaging of white-light filaments in BK-7 glass using radially and azimuthally polarized ultrafast vector pulses were presented. The azimuthal position of the filaments inside the bulk BK-7 was controlled using the polarization and intensity properties of the ultrafast vector pulses. The present studies are potentially applicable to the laser patterning of chiral structures based on controlled filamentations.

## Acknowledgements

MMB would like to express sincere thanks to Japan Society for Promotion of Science (JSPS) for short term fellowship at IMRAM, Tohoku University.

## References

- [1] T. Yan, L. Ji, *Ultrafast Sci.* **3** (2023) 0023.
- [2] A. Houaoud, A. Mysyrowicz, *Light Filaments: Structures, challenges and applications* (IET, 2021), Chap. 1.
- [3] A. Braun, G. Korn, X. Liu, *et al.*, *Opt. Lett.* **20** (1995) 73.
- [4] A. Sadeghpour, D. Abdollahpour, *arXiv:2311.00098* (2023)
- [5] L. Lu, Z. Wang, R. Lin and Y. Cai, *Front. Phys.* **10** (2022) 892581.
- [6] H. Kawauchi, Y. Kozawa, S. Sato, *et al.*, *Opt. Lett.* **33** (2008) 399.

# Real-time movies of photo-induced azo-polymer motions obtained by high-speed atomic force microscopy

○Keishi Yang<sup>1</sup>, Feng-Yueh Chan<sup>2</sup>, Yasushi Inouye<sup>1,4</sup>, Prabhat Verma<sup>1</sup>, Takayuki Uchihashi<sup>2,3</sup>, Hidekazu Ishitobi<sup>1,4</sup>, Takayuki Umakoshi<sup>1,5</sup>

<sup>1</sup>Dept. Applied Physics, Osaka Univ., <sup>2</sup>Dept. of Physics, Nagoya Univ., <sup>3</sup>ExCELLS, <sup>4</sup>FBS, Osaka Univ.,

<sup>5</sup>Inst. Adv. Co-creation Studies, Osaka Univ.

E-mail: [yang@ap.eng.osaka-u.ac.jp](mailto:yang@ap.eng.osaka-u.ac.jp)

## 1. Introduction

Azo-polymer thin film, containing azo-benzene molecules, forms unique surface reliefs due to photoisomerization reaction under light irradiation [1]. It has been considered to be a promising material for various optical application. In addition, the formation of complex reliefs by optical vortex and skyrmion has recently attracted much attention in topological and quantum optics [2]. In previous, the formation process of azo-polymer has been studied by observing distinct deformed structures at different irradiation times using atomic force microscopy (AFM). To reveal the formation mechanisms, real-time nanoscale visualization of the azo-polymer deformation process is highly desirable.

## 2. Experimental results

In this study, we achieved the real-time observation of the deformation process of azopolymer thin films using high-speed atomic force microscopy (HS-AFM) [3]. HS-AFM can capture AFM image with a high spatial resolution ( $\sim 1$  nm) and temporal resolution ( $\sim 10$  frames per second) by rapidly scanning a cantilever [4]. We applied tip-scan HS-AFM that can be combined with an inverted optical microscope. As shown in Fig. 1, we constructed HS-AFM combined with the optical setup to observe the laser focused area on azo-polymer thin film by HS-

AFM. By focusing laser light on the azo-polymer thin film and observing the same area with HS-AFM, we succeeded *in-situ* real-time observation of azo-polymer deformation process (Fig.2(a)). Here, linear polarization was applied as a demonstration, indicated by the arrow. Moreover, as shown in Figs.2 (b, c), height line profiles allowed detailed analysis of the temporal evolution of the surface reliefs. We further confirmed that different surface structures formed depending on the orientation of the incident polarized light.

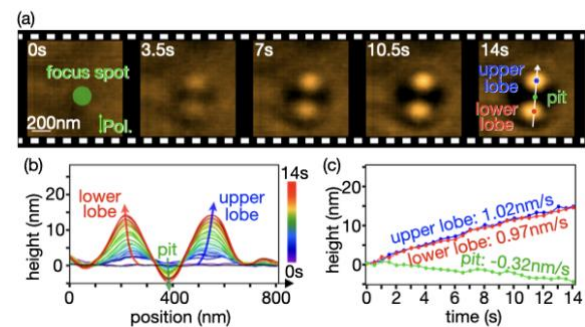


Figure2: (a) High-speed AFM images of azo polymer surface deformation. (b) Height line-profiles of azo-polymer surface along the white line on (a). (c) Height changes of azo-polymer structures, analyzed from (b).

## 3. Conclusion

We succeeded in real time imaging of azo-polymer deformation process. Through HS-AFM observations under various conditions like the twisted surface relief using optical vortex, the deformation mechanism of azo-polymer can be further understood in the future.

## References

- [1] H. Ishitobi et al., *Opt. Express*, **15** (2007), 652.
- [2] R. Tamura et al., *APL Photonics*, **9** (2024), 046104.
- [3] K. Yang et al., *Nano Letters*, **24** (2024), 2805.
- [4] T. Ando et al., *Proc. Nat. Acad. Sci. U. S. A.*, **98** (2001), 12468.

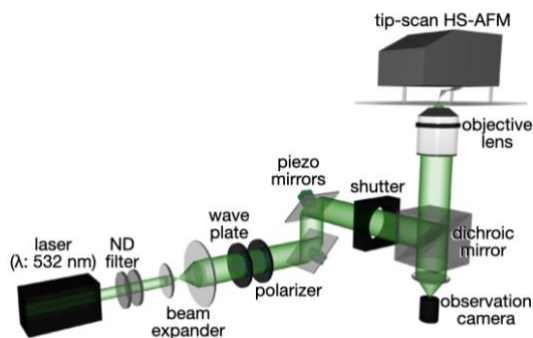


Figure1: Experimental setup that we constructed. HS-AFM was combined with the optical setup.



# Soliton evolution under the perturbative effects of Raman scattering in Highly Nonlinear Materials

Abhisek Roy<sup>1</sup> and Partha Roy Chaudhuri<sup>1\*</sup>

<sup>1</sup>Department of Physics, Indian Institute of Technology Kharagpur

\*E-mail: roycp@phy.iitkgp.ac.in

We have examined the propagation of temporally separated soliton pulses in single-mode optical fibers under the influence of Stimulated Raman Scattering (SRS), focusing on chalcogenide materials. Our study investigates the interplay of Kerr nonlinearity, Raman effects, and material-dependent collision length, demonstrating significant differences from typical soliton interactions. The findings from our research offers insights into nonlinear effects in high-power soliton transmission, suggesting potential applications in optical switches and mode-locked lasers.

## I. MATHEMATICAL MODEL FOR TWO-SOLITON INTERACTION

We have considered a single-mode optical fiber and used the Generalized NLSE as [21],

$$\frac{\partial}{\partial z} A + \frac{\alpha}{2} A + \left( \sum_{k \geq 2} \beta_k \frac{i^{k-1}}{k!} \frac{\partial^k}{\partial T^k} \right) A = i\gamma \left( 1 + \frac{1}{\omega_0} \frac{\partial}{\partial T} \right) \times \left( (1 - f_R) |A|^2 + f_R \int_0^\infty h_R(\tau) |A(z, T - \tau)|^2 d\tau \right) A \quad (1)$$

The Raman scattering is represented by the Raman response function  $R(T)$  as,

$$R(T) = (1 - f_R) \delta(T) + f_R h_R(T) \quad (2)$$

where  $f_R$  denotes the delayed Raman response's fractional contribution to nonlinear polarization and  $h_R$  is the Raman response term related to the molecular vibrations.

We considered two incident pump pulses having a hyperbolic secant (sech) shape, as follows,

$$A(0, T) = \sqrt{P_0} \operatorname{sech} \left( \frac{T - 2t_0}{T_0} \right) + \sqrt{P_0} \operatorname{sech} \left( \frac{T + 2t_0}{T_0} \right) \quad (3)$$

where  $P_0$  and  $T_0$  are the peak input power and the pulse duration respectively.

For all computations, we opt for  $N = 1$ , ensuring that every pulse propagates as a fundamental soliton independently of the other. To initiate the interactions, we set the Raman term on and off using the the parameter  $f_R$ . The computations were performed in MATLAB assuming a femtosecond laser as our pumping source. We have used the Split Step Fourier Method (SSFM) for our computation, in MATLAB.

## II. NUMERICAL RESULTS

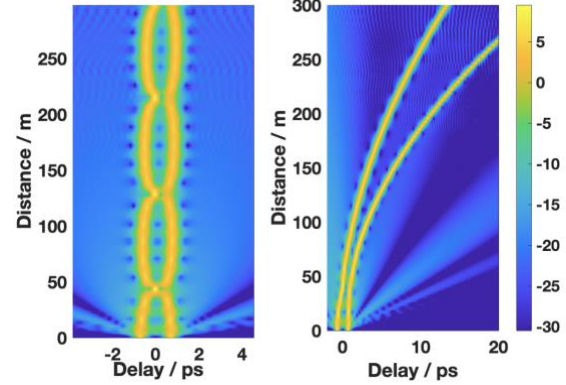


Fig.1 Temporal evolution of two identical solitons in the absence (left) and presence (right) of a Raman interaction term, in  $\text{As}_2\text{S}_3$  glass.

The left side of Fig. 1 shows that soliton pulse interactions occur earlier in chalcogenide ( $\text{As}_2\text{S}_3$ ) than in silica [2] due to its nonlinear refractive index being about 100 times greater. This high nonlinearity results in complex soliton behaviors, such as fusion and fission, occurring at a shorter distance of around 45 meters.

The collision length of the materials was theoretically deduced and compared to the collision length observed in the simulations as follows,

TABLE 1. Collision length value.

Material	$L_{\text{col}}$ (theoretical)	$L_{\text{col}}$ (observed)
$\text{As}_2\text{S}_3$	90.20	90.05

## III. CONCLUSION

Our comprehensive investigation into soliton interactions within arsenic trisulphide reveals significant material-dependent dynamics, exhibiting pronounced nonlinear effects and energy transfer under Raman interaction. The study underscores the critical role of material selection and initial relative phases in optimizing soliton-based optical systems. These insights advance the development of advanced optical communication and ultrafast signal processing technologies.

## REFERENCES

- [1] G. P. Agrawal, *Nonlinear Fiber Optics*, 1989, Chap. 6.
- [2] P. Balla, S. Buch, G.P. Agarwal. *Effect of Raman scattering on soliton interactions in optical fibers*. J. Opt. Soc. Am. B Lett., vol. 34, No. 6, pp. 1247-1254, 2017.
- [1] K.Ogusu, K. Shinkawa, "Optical nonlinearities in  $\text{As}_2\text{Se}_3$  chalcogenide glasses doped with Cu and Ag for pulse durations on the order of nanoseconds" Opt. Exp., vol. 17, no. 10, 2009.

# Third Harmonic Generation at THz Frequencies: Utilizing a Frequency Selective Metasurface Approach with Complementary Split Ring Resonators

Mitali Sahu<sup>1</sup>, Partha Roy Chaudhuri<sup>1\*</sup>

<sup>1</sup> Department of Physics, Indian Institute of Technology Kharagpur-721 302, INDIA  
E-mail : [roycp@phy.iitkgp.ac.in](mailto:roycp@phy.iitkgp.ac.in)

## Abstract:

we report our investigation on third harmonic generation (THG) in the terahertz (THz) regime using double resonant frequency selective metasurface composed of square-shaped periodic complementary single split ring resonators.

## 1. Introduction

Metamaterials with sub-wavelength structuring are used to manipulate nonlinear interactions, driving significant R&D in nonlinear optics. One key response is THG, with applications in photonics, biosensing, signal processing, and materials research. Our study focuses on THG using a metasurface with square-shaped complementary split ring resonators (c-SRR) for efficient THz frequency conversion. In optics, SRR resonances correspond to plasmonic eigenmodes, and c-SRRs offer an enhanced mechanism. We propose c-SRR metasurfaces engineered for effective THG, revealing odd modes at 3.9 THz and 11.5 THz under TM mode incidence, aligning with fundamental (FF) and third harmonic (TH) frequencies.

## 2. Theoretical Model and Results

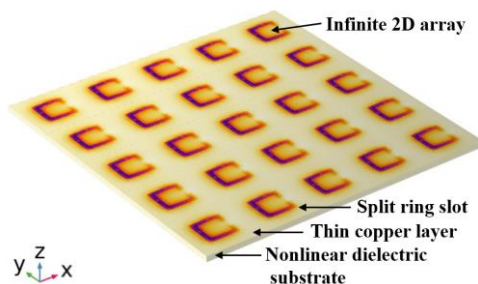


**Fig. 1.** Schematic illustration showing the design of the suggested nonlinear FS metasurface.

The proposed frequency-selective (FS) metasurface (Fig. 1) features a single square split ring slot on a thin copper layer, placed on a  $1.45 \mu\text{m}$  dielectric spacer with a Kerr-type nonlinear material, like amorphous chalcogenide glass, suitable for low THz frequencies. Stimulated by strong magnetic resonance at the fundamental wavelength and a defined mode at the harmonic wavelength, effective THG occurs under a normally incident TM-polarized plane wave with the magnetic field along the y-axis. The resonant response caused by the proposed FSS is shown in Fig. 2. Aligning the FF ( $\omega = 3.9 \text{ THz}$ ) and TH ( $3\omega = 11.5 \text{ THz}$ ) frequencies with the metasurface resonances confines en-

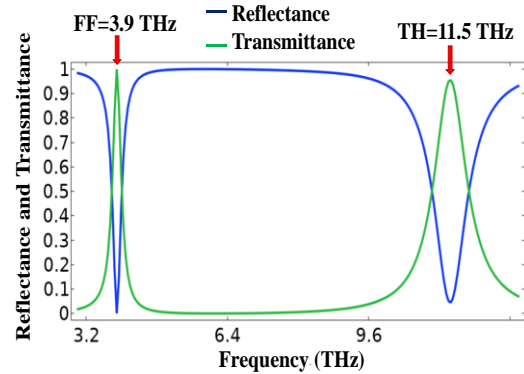


**Fig. 2.** The calculated reflectance and transmittance of the FF mode and TH mode at the c-SRR frequency selective surface are shown as a function of the incident wave frequency.

ergy during excitation and radiation at  $0.4 \text{ MW/cm}^2$  input intensity. SRRs enhance electromagnetic sensitivity, boosting the FF mode electric field by 60 times and the TH mode by 25 times (Fig. 3).

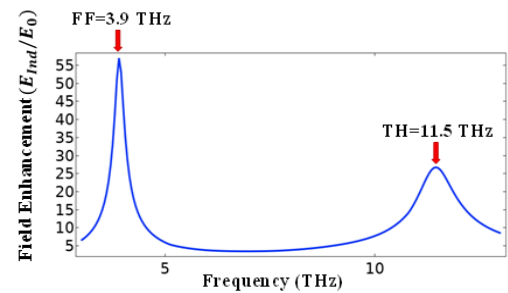


**Fig. 3.** The enhancement of field in FF and TH modes at the suggested metasurface varies with the incident frequency.

## 3. Conclusions

We demonstrate the performance of a new design of nonlinear thin FS c-SSR metasurface with periodic structure for efficient THG at THz frequencies which yields high efficiency with low input intensities showing a marked advancement in the field.

## References

- [1] B. Jin, T. Guo, and C. Argyropoulos. J. Opt. **19** (2017) 094005. (11pp) (2017).
- [2] B. Y. Jin, and C. Argyropoulos. Sci. Rep. **6** (2016) 28746.
- [3] J. Lee, and M. Belkin. Nature. **511** (2014) 65.

# Broadband Optical Frequency Comb Generation by Employing dual lasers with Dual-Drive Mach Zehnder modulator and Frequency Modulator

Priyanka Verma<sup>1</sup>, Sukhbir Singh<sup>1</sup>

<sup>1</sup>Department of Electronics and Communication Engineering, Netaji Subhas University of Technology, Delhi, India

E-mail: [priyanka.verma.phd21@nsut.ac.in](mailto:priyanka.verma.phd21@nsut.ac.in)

## 1. Introduction

Currently, there is a high demand for communication networks that provide large bandwidth and high efficiency without any interference for various users. One of the traditional ways to increase spectral efficiency is to use individual laser sources. To overcome these issues, optical frequency comb (OFC) [1] has emerged as a popular and effective approach that can improve spectral gain and reduce unwanted interference in communication systems. Researchers find optical frequency combs interesting because of their numerous applications such as precise optoelectronics instrumentation, ultra-short pulse generation [2] and dense wavelength division multiplexing (DWDM)[3] in optical communication networks [4]. In this manuscript an approach is designed for generation of broadband optical frequency comb (OFC) which is characterized by various parameters of laser sources, Dual-drive Mach Zehnder modulator (DD-MZM) and frequency modulator (FM). This approach is effective to achieve 159 optical comb lines with bandwidth of 541 GHz. The generated setup performance is analyzed by optical spectrum analyzer (OSA).

## 2. Operating principle of proposed OFC generation

The proposed system setup in Figure 1 employs two laser sources CW<sub>1</sub> and CW<sub>2</sub> with specification 193.1 THz and 193.2 THz having linewidth 10 MHz respectively. Two laser sources are optically coupled with DD-MZM which is based on electro-optic effect [1]. The DD-MZM is biased at voltage of -2.8 V and -1.1 V accompanied with 12 V modulation voltage. DD-MZM is followed by FM which is driven by RF source of 32 GHz having frequency deviation 200 GHz. The initial frequency for generated OFC is provided by coupling of two laser sources. When a signal is passing through DD-MZM subcarriers are generated which exhibits broadness and flatness in generated comb lines. The performance of generated comb lines get analysed with equation (1) [5]. Furthermore, in order to enhance the spectral subcarriers, flatness as well as broadness in generated OFC, DD-MZM is followed by FM which is driven directly by RF source without any need of phase shifters and amplifiers.

$$E_{out}(t) = \frac{E_{in}}{2} \left[ \gamma e^{j\pi \left( \frac{V_{RF}(t)}{V_{\pi RF}} + \frac{V_{dc}}{V_{\pi dc}} \right)} + (1-\gamma) e^{j\pi \frac{-V_{RF}(t)}{V_{\pi RF}}} \right] \quad (1)$$

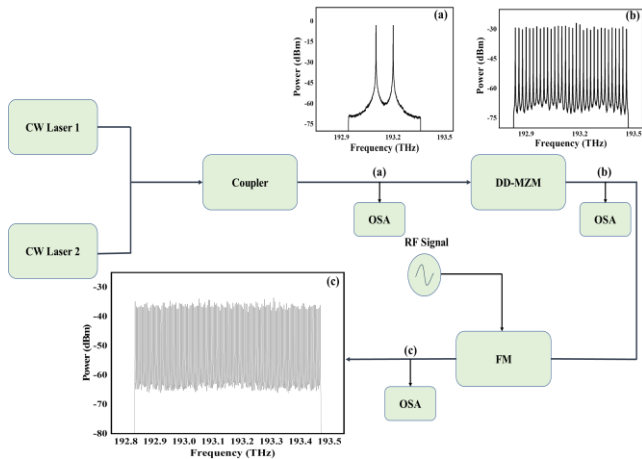


Figure 1. System Setup Proposed for generating Optical Frequency Comb (OFC) based on DD-MZM and FM

Here equation (1) depicts MZM output and input ports which produces electric field intensity  $E_{out}(t)$  and  $E_{in}$  respectively whereas  $\gamma$  depicts power splitting ratio. Whereas  $V_{RF}(t)$  and  $V_{\pi RF}(t)$  represents biasing voltages while  $V_{DC}$  and  $V_{\pi dc}$  represents modulated voltages of two arms of MZM.

## 3. Results and discussion

The generated OFC performance can be determined with parameters that includes number of optical spectral lines, flatness, bandwidth and adjacent spacing between the generated comb lines. Figure 2(a) and 2(b) depicts the output spectrum at optical spectrum analyzer (OSA) obtained at output of DD-MZM and FM respectively. Figure 2(a) depicts the optical carriers produced at output of DD-MZM are 32 with 2 dB flatness in frequency band of 642 GHz. The comb spacing between the adjacent lines are 20 GHz which has significant impact on resulting OFC.

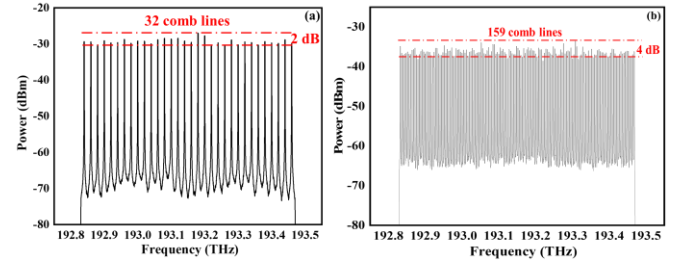


Figure 2. Optical frequency comb generation at (a) DD-MZM (b) FM

Whereas Figure 2(b) demonstrates generated OFC having 159 optical comb lines, 4 dB maximum power deviation with spectral band of 541 GHz in frequency region 192.8 THz to 193.47 THz.

## 4. Conclusion

This manuscript presents the generation of OFC by employing DD-MZM followed by FM. At initial stage DD-MZM is proficient to generate 32 carriers are 32 with 2 dB flatness but FM act as subcarrier booster. The proposed OFC achieves 159 optical spectral lines with 4 dB flatness that occupies bandwidth of 541 GHz. The generated OFC is proficient in telecommunication network, high precision spectroscopy and quantum optics.

## Acknowledgement

The authors are thankful to the science and engineering research board (SERB), New Delhi for their funding to research project no. SRG/2023/001522. One of the author Ms. Priyanka Verma is thankful to the authorities of NSUT to provide research fellowship facilities.

## REFERENCES

- [1] P. Verma and S. Singh, "Optical Frequency Comb Generation by using Higher Order Susceptibility in SOA," in *2023 2nd Edition of IEEE Delhi Section Flagship Conference (DELCON)*, 2023: IEEE, pp. 1-4.
- [2] T. Yang, J. Dong, S. Liao, D. Huang, and X. Zhang, "Comparison analysis of optical frequency comb generation with nonlinear effects in highly nonlinear fibers," *Optics express*, vol. 21, no. 7, pp. 8508-8520, 2013.
- [3] H. Zhang *et al.*, "Coherent optical frequency combs: from principles to applications," *Journal of Electronic Science and Technology*, vol. 20, no. 2, p. 100157, 2022.
- [4] P. Verma and S. Singh, "Enhanced ultra-wideband optical frequency comb generation based on cross-polarization modulation effect of semiconductor optical amplifier," *Optical and Quantum Electronics*, vol. 56, no. 6, p. 1043, 2024.
- [5] J. Cartledge, C. Rolland, S. Lemerle, and A. Solheim, "Theoretical performance of 10 Gb/s lightwave systems using a III-V semiconductor Mach-Zehnder modulator," *IEEE photonics technology letters*, vol. 6, no. 2, pp. 282-284, 1994.



# Closed-form solutions in Lugiato-Lefever Equation for Frequency Comb Applications

Sanjana Bhatia<sup>1</sup>, and C. N. Kumar<sup>1</sup>

<sup>1</sup>*Department of Physics, Panjab University, Chandigarh-160014, India*

E-mail: sanjana.bhatia577@gmail.com

## 1. Introduction

In this study, we explore solitary wave solutions of the ac-driven nonlinear Schrödinger equation also known as Lugiato-Lefever Equation supported by localized gain-loss. By modifying the master equation to incorporate distributive loss, we derive exact analytical solutions for both localized and wave-train patterns, considering cases with trivial and non-trivial chirping. Our findings enhance the theoretical framework for dissipative solitons, revealing significant potential for real-world applications in high-capacity telecommunications and optical frequency combs. This work contributes to the precise control and design of nonlinear optical systems, advancing the understanding of Kerr-frequency comb dynamics.

## 2. Methodology

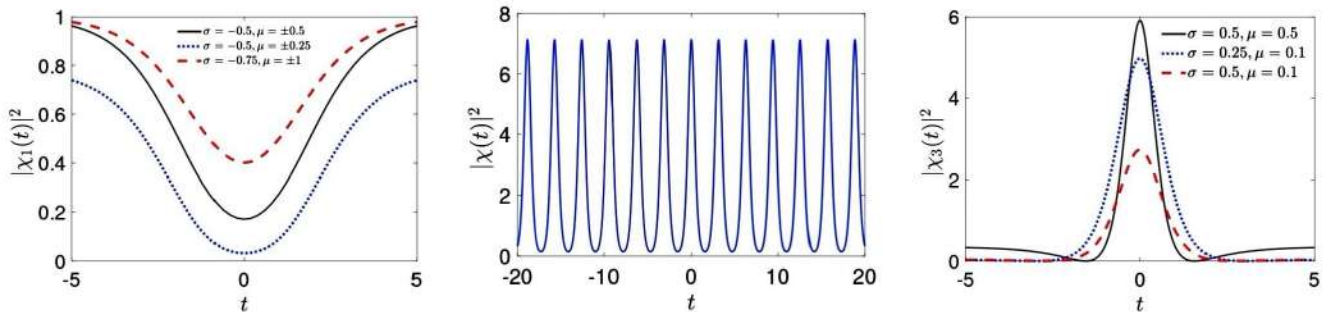
To capture the diversity of nonlinear effects enclosed in Kerr-comb dynamics, Renninger and Rakich have developed a single closed-form analytical solution of the driven NLSE that reproduces a large class of patterns in Kerr-comb systems, including solitons and periodic wavetrains [1, 2] using damped-driven NLSE in linear loss settings given by:

$$i\frac{\partial E}{\partial z} = -i\frac{\alpha}{2}E + \delta E - \frac{\beta}{2}\frac{\partial^2 E}{\partial t^2} - \sigma|E|^2E + i\mu e^{i\phi}, \quad (1)$$

where  $E(z, t)$  is the electric field inside the cavity,  $\alpha$  is the linear cavity loss,  $\delta$  represents the pump detuning,  $\beta$  is the dispersion,  $\sigma$  signifies the Kerr-nonlinearity,  $\mu$  is the external drive strength, and  $\phi(z, t)$  is the phase of the drive. As pointed out in [1], this equation does not have any known exact solutions when the loss term is linear. Inspired by the stable dissipative solitons observed in the models with nonlinear and localized gain-loss terms, we propose a modified version of the master equation to model the dynamics of Kerr-frequency combs in a microring with  $\alpha \rightarrow \alpha_{NL}(t)$ , where the latter is now distributive or nonlinear function of  $t$ , while all other parameters retain the same physical meanings as in Eq. (1).

## 3. Conclusions

We find exact dark, periodic, and bright solitons as shown in Fig. (1) with various chirping functions.



- [1] W.H. Renninger, P.T. Rakich, "Closed-form solutions and scaling laws for Kerr frequency combs", Sci. Rep. **6** 24742 (2016).
- [2] T.S. Raju, C.N. Kumar, P.K. Panigrahi, "On exact solitary wave solutions of the nonlinear Schrödinger equation with a source", J. Phys. A: Math. Gen. **38**, L271 (2005).

# Transmitted Wave Frequency Shift on a Moving Media Interface: between the Doppler and the Photon Recoil Effects

Valentyn Lymar<sup>1</sup>, Yevhen Makovetskyi, Ruslan Vovk

<sup>1</sup> OPTICA

E-mail: lymar@univer.kharkov.ua

## 1. Introduction

A broad range of well-known nonlinear optics phenomena demonstrates feasibility of managing the substance by means of the optical field influence. But, in addition to the manifestation of nonlinear optical properties, the radiation-substance system may be brought into a state far from thermodynamic equilibrium forming so-called “optically induced dissipative structure”. Obviously, light absorption is important in this case. The combination of optical and thermodynamic nonlinearities becomes a characteristic property of the system, and studying it is mutually enriching.

## 2. Physical Mechanisms and Signal Analysis on Frequency Shifts for the Photon Interacting with the Moving Interface

An example of optical dissipative structure is a gas bubble which is thermo-capillary trapped by a continuous laser beam passing through an absorbing liquid. The captured bubble expands because of elevated temperature of the liquid in the laser beam path. Moving interference patterns have been observed in both reflected and transmitted laser light, and these movements are attributable to manifestation of Doppler effect on the gas bubble walls [1, 2].

In Fig. 1 the simplest scheme is shown for a photon transmission through the moving interface between two contiguous homogeneous and transparent media. At our experimental conditions, the first medium is gaseous one with refractive index close to unity. By applying the energy-momentum conservation laws in the case of infinitely large and constant media masses, we obtain the frequency shift  $\delta\omega$  of the transmitted or reflected photon:

$$\delta\omega = \mathbf{v} \cdot \delta\mathbf{k}, \quad (1)$$

$\mathbf{v}$  is the velocity vector of the moving surface;  $\delta\mathbf{k}$  is the wave vector alteration for the light transmitted through the surface or reflected from it. Eq. (1) describes classical Doppler effect (CDE) as a consequence of the exchange of

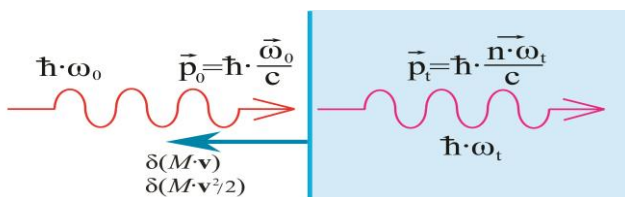


Figure 1. The principal scheme of the photon refraction on a moving interface. Momentum-energy conservation laws must be fulfilled. A collinear geometry is not obligatory.

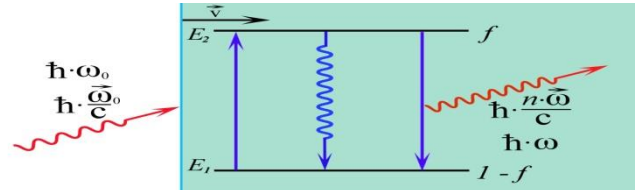


Figure 2. The principal scheme of the photon refraction on a moving interface with resonant absorption. Straight blue arrows correspond to stimulated transitions, while waving blue – to spontaneous one.

energy and momentum between the photon and the moving surface.

Within the frames of the same model of Fig. 1 it is appropriate to consider another way of photon-surface interaction. If the photon momentum alteration  $\hbar \cdot \delta\mathbf{k}$  is provided in the process by a change of mass of the moving medium by some “defect mass”  $\delta M$ , then Eq. (1) is replaced by the following:

$$-\mathbf{v}^2 \cdot \delta M / 2 = \hbar \cdot \delta\omega; \quad \delta\omega = \mathbf{v} \cdot \delta\mathbf{k} / 2. \quad (2)$$

Naturally, a process described by Eqs. (2) should be referred to as photon recoil effect (PRE) in the context of the moving surface-photon interaction.

And finally, dissipative properties of our experimental system are caused by some resonant absorption of the laser light. This absorption is taken into account if, instead of the initial model in Fig. 1, the photon interaction with a surface of a resonant two-level quantum system is considered (Fig. 2). In the context of this model, it can be shown that the frequency shift  $\delta\omega$  of the transmitted photon is determined by:

$$\delta\omega = \mathbf{v} \cdot \delta\mathbf{k} \cdot (1 - f), \quad (3)$$

$f$  is the upper-level population in fractions of a unit. It makes sense to call the process of Eq. (3) a stimulated Doppler effect (SDE) because of an important role of stimulated transitions in it.

Intensities' time dependences were examined experimentally both of the light transmitted through an expanding laser trapped gas bubble at near-zero observation angle and of the light specularly reflected from it. The frequency spectrum analysis of the transmitted signal indicates occurrence of both CDE and SDE, but input of PRE cannot be excluded.

## References

- [1] V. Lymar et al., **BS-23** in *Proceedings of 13<sup>th</sup> Int. Conf. Ser. on Laser-light and Interactions with Particles LIP-2022, August 21-26<sup>th</sup>, 2022, Warsaw, Poland.*
- [2] V. Lymar et al., *Visnyk KhNU, Ser. “Physics”* **25** (2016) 26-29



# A Numerical Study on the Sensing Characteristics of Raman-Induced Frequency Shift

Protik Roy<sup>1</sup>, Partha Roy Chaudhuri<sup>1</sup>

Indian Institute of Technology Kharagpur, 721302, India

Email - royecp@phy.iitkgp.ac.in

We present here an analysis of the sensing properties associated with the Raman-induced frequency shift (RIFS). By employing a conventional step index chalcogenide fiber and utilizing the thermo-optic properties of the material, we investigate the temperature-sensing capabilities facilitated by RIFS.

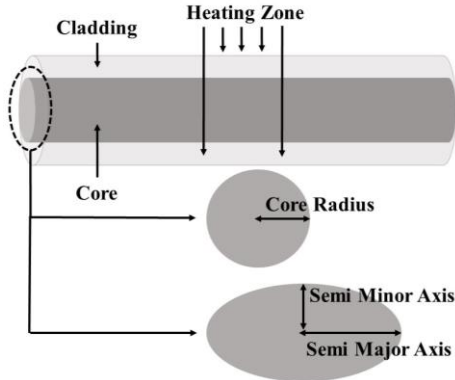


Fig. 1 Sensor schematic

To determine the temperature of the external medium, we perform computations to compute the dispersion parameters of the proposed model as shown in Figure 1. The simulations are conducted using the MATLAB platform and involve utilizing a standard step index fiber with core and cladding materials of As<sub>40</sub>S<sub>60</sub> and As<sub>42</sub>S<sub>58</sub>, respectively. The refractive indices of these materials are determined using the Sellmeier equation [1]. For the case of a circular core cross-section, we set the core radius as 3  $\mu\text{m}$  and the cladding radius as 60  $\mu\text{m}$ . In the case of an elliptical core, the semi-major axis is chosen as 3  $\mu\text{m}$ , the semi-minor axis as 1  $\mu\text{m}$ , and the cladding radius as 60  $\mu\text{m}$ . By incorporating these typical parameters, we simulate the propagation of ultrafast pulses using a generalized nonlinear Schrödinger equation (GNLSE) [2]. The equation governing the pulse propagation through the fiber is expressed as follows:

$$\frac{\partial}{\partial z} A + \frac{\alpha}{2} A + \left( \sum_{k \geq 2} \beta_k \frac{i^{k-1}}{k!} \frac{\partial^k}{\partial T^k} \right) A = i\gamma \left( 1 + \frac{1}{\omega_0} \frac{\partial}{\partial T} \right) \times \left( (1 - f_R) |A|^2 + f_R \int_0^\infty h_R(\tau) |A(z, T - \tau)|^2 d\tau \right) A \quad (1)$$

The left-hand side of (1) represents the linear effects during pulse propagation. It incorporates the slowly varying pulse envelope,  $A(z, T)$ , which evolves along the fiber structure in a time frame referred to as  $T = t - \beta_1 z$ , where  $\beta_1$  represents the group velocity. The parameter  $\alpha$  represents the transmission loss. On the other hand, the right-hand side of the (1) accounts for nonlinear effects, with  $\gamma$  representing the nonlinear coefficient. The response function  $R(T)$  of a system, which describes its

nonlinearity, incorporates both immediate and delayed Raman effects. It can be expressed as,

$$R(T) = (1 - f_R) \delta(T) + f_R h_R(T) \quad (2),$$

where  $f_R$  represents the fractional contribution of the delayed Raman response to the system's nonlinear polarization. In the case of chalcogenide materials,  $f_R$  takes the values of 0.148 [15]. The Raman response term,  $h_R$ , is given by the expression

$$h_R = \frac{\tau_1^2 + \tau_2^2}{\tau_1 \tau_2} \exp(-\tau/\tau_2) \sin(-\tau/\tau_1) \quad (3)$$

For Chalcogenide materials, these are 23 fs and 164.5 fs, respectively [15]. To solve the GNLSE, we utilize a split-step Fourier method implemented in MATLAB. The incident pump pulse is assumed to be a hyperbolic secant pulse, which can be represented as follows:

$$A(0, T) = \sqrt{P_0} \operatorname{sech} \left( \frac{T}{T_0} \right) \quad (4),$$

where  $P_0$  and  $T_0$  are the peak input power and the pulse duration (1/1.763 of the full width at half maxima duration for the input pulse) respectively.

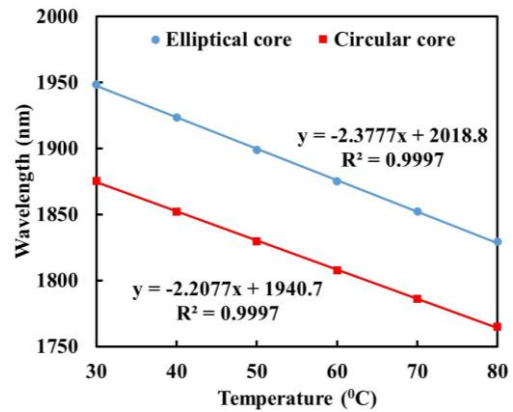


Fig. 2 Wavelength shifting due to temperature variation.

Figure 2 provides detailed information on the variation of the central wavelength of the pulse with respect to the ambient temperature. As discussed in the previous section, the dispersion parameters can be varied due to the thermo-optic coefficient of the chalcogenide material with changes in the ambient temperature. In our analysis, the central wavelength shifts by 118.91 nm and 110.40 nm with a total temperature change of 50  $^{\circ}\text{C}$  for the elliptical and circular core cross-sections, respectively. These correspond to a sensitivity of 2.38 nm/ $^{\circ}\text{C}$  and 2.21 nm/ $^{\circ}\text{C}$ , respectively.

## References

1. J. S. McCloy, B. J. Riley, S. K. Sundaram, H. A. Qiao, J. V. Crum, and B. R. Johnson, "Structure-optical property correlations of arsenic sulfide glasses in visible, infrared, and sub-millimeter regions," *J. Non-Cryst. Solids*, vol. 356, pp. 1288–1293, 2010.
2. G. P. Agrawal, *Nonlinear Fiber Optics*, 1989, Chap. 6.

# Metal–Insulator–Metal (MIM) Waveguide Based Fano Resonance Sensor for Human Sperm Detection

Anirudh Yashovardhan, Lokendra Singh

Department of Electronics and Communication Engineering, Graphic Era (Deemed to be University), Dehradun, India - 248001

\*E-mail: [anirudhyashovardhanlt@gmail.com](mailto:anirudhyashovardhanlt@gmail.com)

## 1. Introduction

When a light ray is incident on the metal surface, the free electron capture energy and generates a form of collective oscillation, called Surface Plasmonic Polaritons (SPPs) [1]. SPP gets confined to a deep subwavelength scale in metal-insulator-metal (MIM) waveguides with the advantages of high restraint, low loss, long transmission distance, and simple fabrication [2]. SPP-based MIM waveguides have been used in different applications such as refractive index sensing, wavelength division multiplexing [2].

rectangular resonating cavity (RRC) is used with three nano rods defects (NRD) in the bus waveguide as shown in Fig. 1. The proposed structure of the FR sensor is used for the detection of concentration and mobility of human sperm, by using its corresponding refractive index (RI). The detected concentration of 17, 23, 62, 79, 104, 197 million/ml having mobility of 64, 41, 44, 75, 48, 71 carries a RI of 1.3461, 1.3385, 1.3459, 1.342, 1.3465, 1.344, respectively [4].

Figure 1 (a) shows the schematic of the proposed FR sensor, where the length ( $l$ ) and width ( $h$ ) of the RRC are  $3\ \mu\text{m}$  and  $1\ \mu\text{m}$ , respectively. 's' is a separation between nanorod defects (NRD) and RRC,  $d$  is the diameter of NRD,  $p$  is the distance between the center of two NRD's, and  $w$  is the width of bus waveguide. Thereafter, the designed FR sensor is used to detect the human sperm concentration and mobility by varying its RI in NRD's and RRC. The coupling of field between the bus waveguide and RRC at an RI of 1.3459 is shown in the inset of Fig. 1 (a). For the tested RI of human sperm samples the output power is recorded and an autocorrelation curve is plotted in Fig. 1 (b). The result shows that the proposed sensor is capable of detecting human sperm samples with an autocorrelation coefficient of 99.97 %. For the tested RI values the sensitivity of the proposed FR sensor is 587.5 nm/RIU.

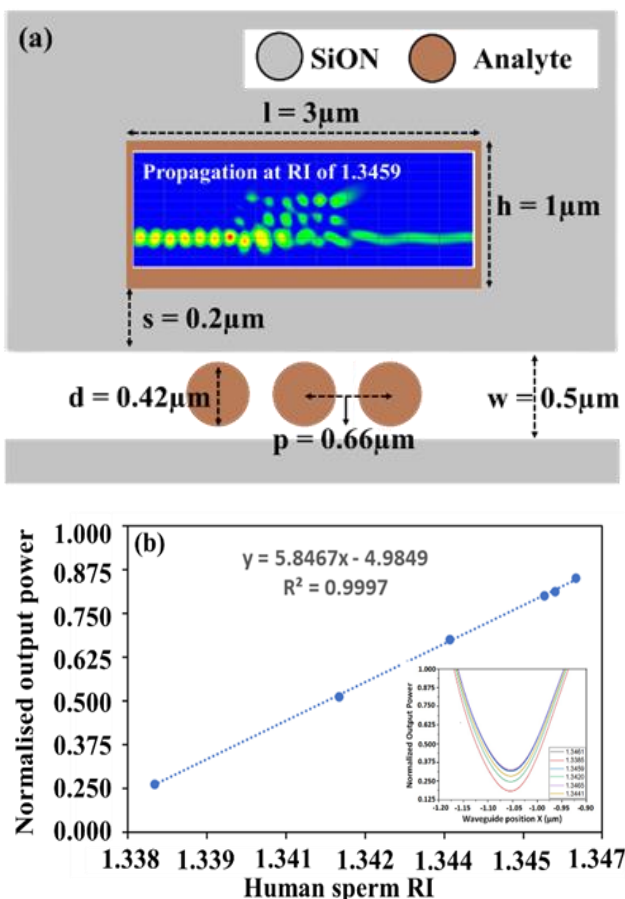


Fig. 1. (a) Schematic of the proposed FR sensor and (b) autocorrelation curve.

Sensing performance improvements were observed when a square ring was proposed with an MIM Waveguide structure and termed Fano resonance (FR) sensors [3]. Therefore, a

## 2. Conclusions

This work presented a MIM waveguide-based FR sensor for RI-based detection of human sperm in terms of its concentration and mobility. Three NRD were created in the bus waveguide to attain the FR effect. For the tested RI of human sperm, the autocorrelation coefficient and sensitivity of 99.97 % and 587.5 nm/RIU are obtained.

## References

- [1] Z. Chen et al. IEEE Photonic Technol Lett 27 (2015) 1695.
- [2] K. Ren et al. J. Phys. D: Appl. Phys. 53 (2020) 135107.
- [3] Y. Chen, Y. Xu, J. Cao. Results in Physics 14 (2019) 102420.
- [4] L. Singh et al. Optics and Lasers in Engineering 169 (2023) 107727.

4 JSAP-Optica Joint Symposia 2024 | 一般セッション(口頭講演) : 4.7 Quantum Optics, Nonlinear Optics and Structured Optics

## **[20a-C43-1~5] 4.7 Quantum Optics, Nonlinear Optics and Structured Optics**

[20a-C43-1]

[JSAP-Optica Joint Symposia Invited Talk] Femtosecond Region Photon Echo with Quantum Dots via Up-conversion Single-photon Detector

○Yuta Kochi<sup>1,2</sup>, Sunao Kurimura<sup>3</sup>, Kouichi Akahane<sup>4</sup>, Junko Ishi-Hayase<sup>1,2</sup> (1.Keio Univ., 2.Keio CSRN, 3.NIMS, 4.NICT)

[20a-C43-2]

Optimizing Spontaneous Parametric Down Conversion in Metasurfaces with In-verse Design

○Marcus Cai<sup>1</sup>, Neuton Li<sup>1</sup>, Tongmiao Fan<sup>1</sup>, Jihua Zhang<sup>1,2</sup>, Jinyong Ma<sup>1</sup>, Dragomir Neshev<sup>1</sup>, Andrey Sukhorukov<sup>1</sup> (1.ARC Centre of Excellence for Transformative Meta-Optical Systems (TMOS), Dept. of Electronic Materials Engineering, Research School of Physics, Australian National Univ., Australia, 2.Songshan Lake Materials Lab., China)

[20a-C43-3]

Spectral resolution of quantum Fourier transform infrared spectroscopy using pulsed laser excitation

○(DC)Jasleen Kaur<sup>1</sup>, Yu Mukai<sup>1</sup>, Ryo Okamoto<sup>1</sup>, Shigeki Takeuchi<sup>1</sup> (1.Kyoto University)

[20a-C43-4]

All-fiber broadband photon pair generation in dispersion flattened highly non-linear fiber

○(D)Anadi Agnihotri<sup>1</sup>, Pradeep kumar Krishnamurthy<sup>1</sup> (1.IIT Kanpur)

[20a-C43-5]

Quantum Antibunching in Nonlinear Coupler Using Wigner Representation

Mohd Syafiq M. Hanapi<sup>1</sup>, Abel-Baset M. A. Ibrahim<sup>1</sup>, ○Pankaj Kumar Choudhury<sup>2</sup> (1.Univ. Teknologi MARA, 2.Zhejiang University)

# Femtosecond Regime Photon Echo with Quantum Dots Evaluated by Up-conversion Single-photon Detector

Yuta Kochi<sup>1,2</sup>, Sunao Kurimura<sup>3</sup>, Kouichi Akahane<sup>4</sup> and Junko Ishi-Hayase<sup>1,2</sup>

<sup>1</sup> School of Fundamental Science and Technology, Keio University

<sup>2</sup> Center for Spintronics Research Network, Keio University

<sup>3</sup> National Institute for Materials Science

<sup>4</sup> National Institute of Information and Communications Technology

E-mail : yuta.kouchi@keio.jp

## Introduction

Recently, quantum information processing and communications using photons have been attracting attention. To increase the density of transmitted photonic qubits, it is necessary to develop broadband quantum memories and detectors that can handle ultrashort pulses. Although rare-earth-ion doped quantum memories [1] have been widely studied, due to their storage bandwidth of  $\sim$ GHz, they are incapable of storing ultrashort pulses. In our group, we used the photon echo (PE) method with quantum dots (QDs) to realize ultrashort femtosecond pulse storage. However, we encountered many difficulties in realizing this method such as low PE efficiency from the QDs and the insufficient temporal resolution of the avalanche single-photon detectors. To solve these problems, we have applied a new quantum control method and utilized an up-conversion single-photon detector (UCSPD) [2]. In this presentation, we will introduce the techniques “1. Time-resolving measurement by UCSPD,” “2. PE quantum memory using QDs” and “3. enhancement of PE signals.”

### 1. Time-resolving measurement by UCSPD

To enable femtosecond regime time-resolving measurements, we developed a UCSPD. This single-photon detector uses the frequency up-conversion technique and signal photons are converted to visible photons by sum-frequency generation (SFG). For this process, we used a femtosecond pulse laser as the pump light. Since SFG occurs only when the signal photons and the pump pulse overlap, we can perform time-gating the signal waveforms with femtosecond order temporal resolution. Fig. 1(a) shows the schematic setup of the UCSPD. The up-conversion efficiency in the femtosecond regime strongly depends on crystal length because of the group delay between signal and pump pulses in a crystal. Despite much research on up-conversion with CW laser, SFG between femtosecond pulses has rarely been investigated. Hence, we evaluated the crystal length dependence of UCSPD performances theoretically and experimentally and achieved the temporal resolution of 415 fs. Our results provide a guideline for optimizing crystal length for femtosecond up-conversion.

### 2. PE quantum memory using QDs

As a demonstration of our UCSPD, we detected femtosecond PE from InAs QDs with an inhomogeneous broadening of 7.2 THz. By applying the PE method, we can use these QDs as a medium for broadband quantum memory. We successfully stored 200 fs time-bin pulse in our QDs, read-out

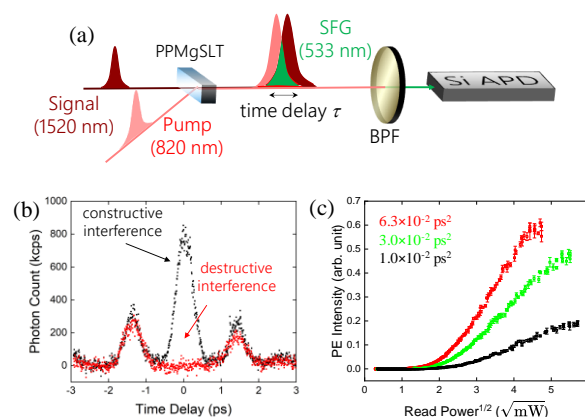


Fig. 1 (a) Optical setup of UCSPD. (b) Temporal waveforms of time-bin PE with different phase. (c) Chirped amount dependence of PE signal intensity.

the stored signals, and measured the waveforms by UCSPD for the first time (Fig. 1(b)). We also succeeded in evaluating the relative phase of time-bin PE signals with a visibility of over 90 %.

### 3. Enhancement of PE signal using chirped pulses

Since we applied a rephasing pulse to read-out stored signals as an echo signal for the PE method, the accuracy of quantum control directly affects memory efficiency. Extending the bandwidth of QDs to THz is complicated because large detuning makes it difficult to accurately control the system through single-frequency pulses. To solve this problem, we introduced the adiabatic rapid passage (ARP) method [3], which uses chirped pulses for read-out and enables robust control. Although this method has been demonstrated only for rare-earth-ion-doped materials, we have demonstrated that ARP is also effective for QDs with inhomogeneous broadening more than 100 times wider than in conventional methods. Fig. 1(c) shows the chirped amount dependence of PE intensity. These results are a great achievement for advancing into the femtosecond regime of quantum communications.

This work was partly supported by CSRN, Keio University. The QDs sample was fabricated at Advanced ICT Laboratory, NICT. The authors would like to thank Prof. R. Shimizu, Y. Kinoshita, M. Hornauer, Y. Takahashi, and T. Shoji for their useful discussion.

## References

- [1] Z. Q. Zhou, *et al.*, *Laser Photonics Rev.*, **17**, 2300257 (2023).
- [2] Y. Kochi, *et al.*, arXiv, 2205.06957 (2022).
- [3] G. Demeter, *et al.*, *Phys. Rev. A*, **88**, 052316 (2013).

# Optimizing Spontaneous Parametric Down Conversion in Metasurfaces with Inverse Design

Marcus Cai<sup>1</sup>, Neuton Li<sup>1</sup>, Tongmiao Fan<sup>1</sup>, Jihua Zhang<sup>1,2</sup>, Jinyong Ma<sup>1</sup>,  
Dragomir N. Neshev<sup>1</sup>, Andrey A. Sukhorukov<sup>1</sup>

<sup>1</sup> ARC Centre of Excellence for Transformative Meta-Optical Systems (TMOS), Department of Electronic Materials Engineering, Research School of Physics, Australian National University, Canberra, Australia

<sup>2</sup> Songshan Lake Materials Laboratory, Dongguan, Guangdong, P.R. China

E-mail: marcus.cai@anu.edu.au

Spontaneous parametric down conversion (SPDC) is one of the most versatile techniques for the generation of correlated photon pair, whose quantum state is essential for photon entanglement that underpins many quantum applications like secure communication, quantum metrology and lithography and quantum imaging [1]. Inverse design of effective SPDC has been achieved by structured crystals with shaped pump beams [2]. Another popular platform for SPDC is nanofabricated structures with sub-wavelength thickness called metasurfaces, as they could achieve drastic enhancement of nonlinear light-matter interactions [3]. There remains the possibility to use inverse design to optimize metasurfaces for SPDC.

In this work, we report a method for optimizing metasurfaces' SPDC performance by building on an existing inverse design optimization framework [4]. Our method employs a gradient-based optimization method called adjoint optimization and the quantum-classical correspondence between SPDC and Sum Frequency Generation [5]. By strategically setting our desired output function in the algorithm, we can control the degree of polarization entanglement we optimize for. We create patterns for unidirectional SPDC that outperform the thin film of the same material and thickness by more than 10 times in brightness while ensuring the almost maximal polarization entanglement of the signal and idler states.

Our results show the possibility of inversely designing metasurfaces with good SPDC that produce strongly entangled signal and idler states, allowing various quantum applications like secure communication and quantum metrology. By building on our work, we can further explore the direction of the signal, idler and pump photons.

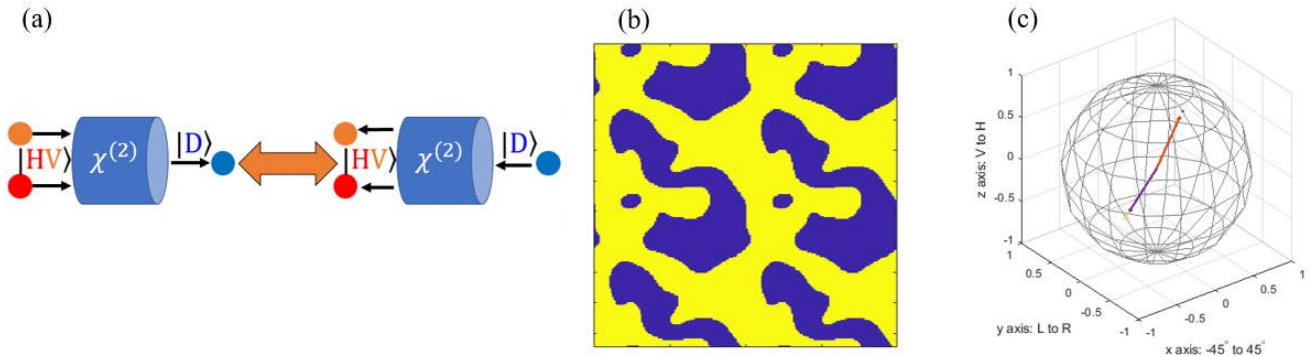


Fig. 1. (a) Diagram of the quantum-classical correspondence of SPDC and SFG: Signal (idler) photon is horizontally (vertically) polarized while the pump photon is diagonally polarized. The second-order nonlinear material is InGaP in our case. (b) Optimized pattern that provides good SPDC performance while trying to maximize the entanglement of the signal and idler states. (c) Poincaré-sphere representation of the signal and idler states from SPDC: Each axis represents the corresponding polarization from negative 1 to positive 1. For example,  $y=-1$  represents left-handed circular polarization while  $y=1$  right-handed circular polarization [6]. Vectors pointing in opposite directions means maximal entanglement.

## References

- [1] J. L. O'Brien, A. Furusawa, and J. Vučković, *Nature Photon.* 3, 687–695 (2009).
- [2] E. Rozenberg, A. Karnieli, O. Yesharim, J. Foley-Comer, S. Trajtenberg-Mills, D. Freedman, A. M. Bronstein, and A. Arie, *Optica* 9, 602–615 (2022).
- [3] A. H. Dorrah and F. Capasso, *Science* 376, 367 (2022).
- [4] N. Li, J. Zhang, D. N. Neshev, and A. A. Sukhorukov, *Nanophotonics*, 137 (2024).
- [5] A. N. Poddubny, I. V. Iorsh, and A. A. Sukhorukov, *Phys. Rev. Lett.* 117, 123901 (2016).
- [6] M. V. Chekhova and M. V. Fedorov, *J. Phys. B* 46, 095502 (2013).



# Spectral resolution of quantum Fourier transform infrared spectroscopy using pulsed laser excitation

Jasleen Kaur, Yu Mukai, Ryo Okamoto, Shigeki Takeuchi\*

Kyoto University

\*E-mail: takeuchi@kuee.kyoto-u.ac.jp

## 1. Introduction

In recent years, nonlinear quantum interferometry has been widely explored for applications like spectroscopy, optical coherence tomography, and imaging [1]. Quantum infrared spectroscopy (QIRS) uses quantum interference of generation processes of frequency-entangled visible-IR photon pairs to perform infrared spectroscopy using visible light sources and silicon-based detectors [2]. This technique utilizes a nonlinear quantum interferometer configuration where the generated IR photons pass through the sample, and the correlated visible photons are detected. The change in the detected visible photon flux with and without the sample helps extract the complex transmittance of the sample in the IR region.

It is commonly assumed that perfect frequency correlation between visible and IR photons is essential for achieving high spectral resolution in QIRS. Therefore, continuous wave (cw) lasers with negligible linewidth are predominantly used in most QIRS experiments. Conversely, when using pulsed lasers, the inherent finite spectral linewidth is generally thought to degrade the spectral resolution. Recently, we reported that the visibility of spectral-domain quantum interference decreases for pulsed pumping [3], confirming that spectral resolution of dispersive QIRS method degrades, wherein a dispersive spectrometer is used for detection. However, pulsed pumping is attractive as it enables high generation efficiency of visible-IR photons and time-resolved measurements.

Here, we investigate whether high spectral resolution can be obtained with a pulsed pump of finite spectral linewidth using the quantum Fourier-transform infrared (QFTIR) spectroscopy method. In this method, interferogram of visible photons is recorded while scanning the optical path difference between nonlinear interferometer arms. Taking the ratio of Fourier amplitudes of interferograms with and without sample, we can extract the spectrum of sample in IR region [4]. In this presentation, we will report the theoretical framework of QFTIR with pulsed pumping. We also plan to experimentally show whether high-resolution spectra of samples can be observed with pulsed pumping.

## 2. Experimental setup

Figure 1 shows the experimental setup consisting of both pulsed and cw lasers to allow a fair comparison under the same experimental conditions. The cw pump has center wavelength of 532.37 nm, average power of 150 mW, and negligible linewidth ( $<1$  MHz). The pulsed laser source of 532 nm centroid wavelength has linewidth of  $\sim 0.6$  nm

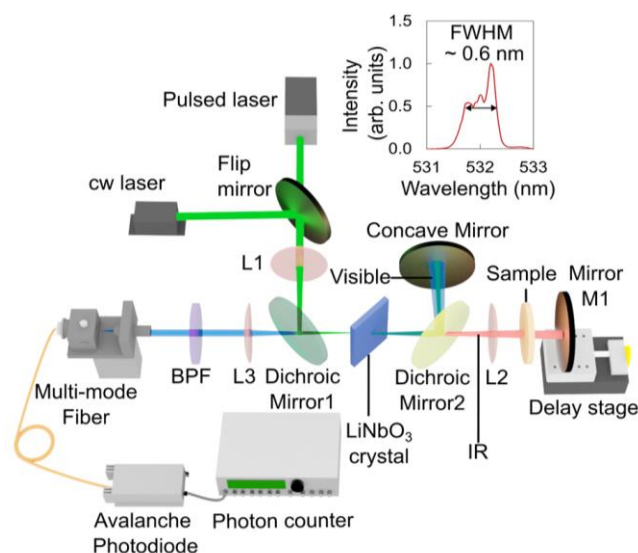


Fig. 1: Experimental setup of QFTIR method

(pulsed laser spectrum in inset of Fig. 1) and an average power of 150 mW. The visible photon interferograms are recorded for both pump sources. The pump beam passes through 0.5 mm thick MgO:LiNbO<sub>3</sub> crystal, generating visible-IR photon pairs of about 816 nm and 1.53  $\mu$ m. Quantum interference occurs between generation processes and visible photon interferogram is detected by Si photodiode while scanning mirror M1 placed on delay stage.

## 3. Conclusion

We will present a theoretical and experimental investigation of the effect of pulsed laser linewidth on the spectral resolution of the QFTIR method. Our results will be useful for performing high-resolution ultrafast infrared spectroscopy using a visible light source and detector.

## Acknowledgments

This work is supported by MEXT Quantum Leap Flagship Program Grant Number JPMXS0118067634; Cabinet Office, Government of Japan, Public/Private R&D Investment Strategic Expansion Program (PRISM); JSPS KAKENHI Grant Number 21H04444; and WISE Program, MEXT.

## References

- [1] A. Hochrainer, M. Lahiri, M. Erhard, M. Krenn, and A. Zeilinger, Rev. Mod. Phys. 94, 025007 (2022).
- [2] D. A. Kalashnikov, A. V. Paterova, S. P. Kulik, and L. A. Krivitsky, Nature Photonics 10, 98 (2016).
- [3] J. Kaur, Y. Mukai, R. Okamoto, and S. Takeuchi, Phys. Rev. A 108, 063714 (2023).
- [4] Y. Mukai, M. Arahata, T. Tashima, R. Okamoto, and S. Takeuchi, Phys. Rev. Applied 15, 034019 (2021).

# All-fiber broadband photon pair generation in dispersion flattened highly non-linear fiber

Indian Institute of Technology Kanpur,<sup>1</sup>, °Anadi Agnihotri<sup>1</sup>, Pradeep Kumar Krishnamurthy<sup>1</sup>

E-mail: anadi@iitk.ac.in

We report on a spontaneous four-wave mixing (SFWM) based broadband correlated photon pair generation using a dispersion flattened highly-nonlinear fiber (DF-HNLF). The DF-HNLF is pumped by a stable mode-locked laser (MLL) which generates pump pulses of 250 ps FWHM at a repetition rate of 94.509 MHz. The joint spectral intensity (JSI) data indicates photon pair generation across entire S, C, and L bands. The intrinsic photon pair generation rate, after accounting for spontaneous Raman scattering (SpRS), system loss, and detector dark counts, is  $\approx 100$  kHz although due to detection gating limit we measured the rate to be 1 kHz at peak pump power of 70 mW. The use of an arbitrary waveform generator for establishing pump MLL and gating of the single-photon detectors (SPDs) allows for precise synchronization of generation and detection of photon pairs.

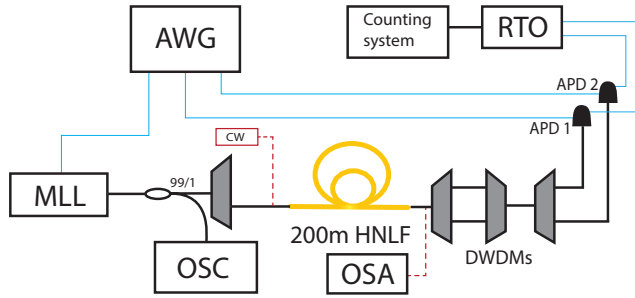


Figure 1: Schematic diagram of experimental setup for broadband photon pair generation.

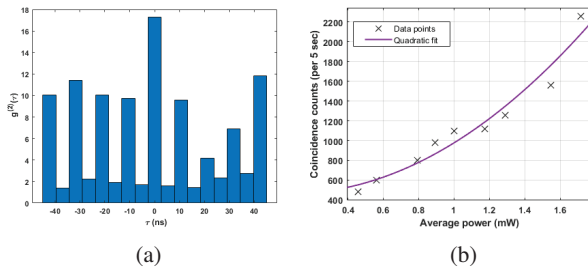


Figure 2: Photon pair measurement results for signal at 1552.52 nm and idler at 1547.72 nm (a) Cross-correlation measurement for 1 mW of average pump power, (b) Coincidence counts vs pump power.

Fig. 1. shows the schematic diagram of our experimental setup. The pulses from the MLL is coupled into a 200 m DF-HNLF from OFS. For the JSI measurement as in [1], a CW laser output from a tunable laser diode is coupled along with the pump as shown in dashed lines. At the output of the HNLF, the signal and idler wavelengths are filtered out and

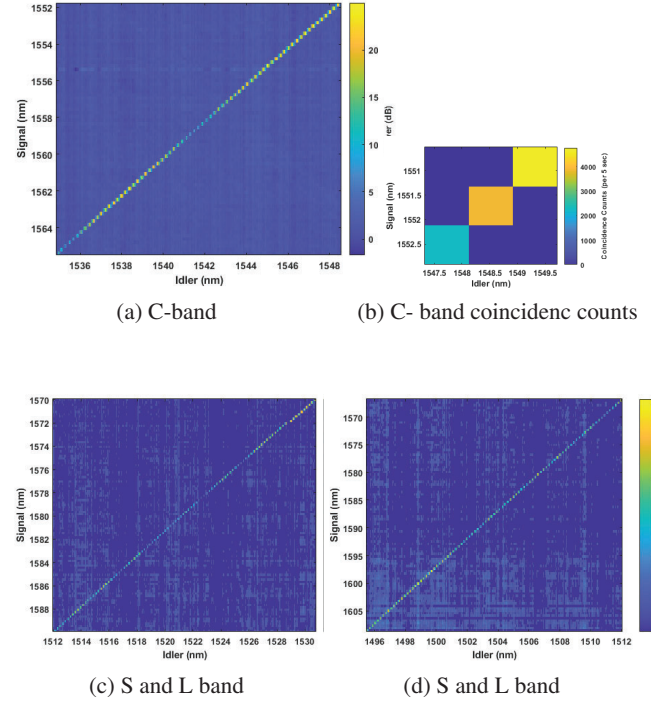


Figure 3: Measured Joint Spectral Intensity of photon pairs generated in dispersion flattened 200m HNLF

pump is suppressed using a set of DWDM filters with FWHM bandwidth of 0.8 nm. The signal and idler are detected using a pair of SPDs gated at ninetieth of MLL repetition rate, i.e., 1.05 MHz. This is due to the circuit limitation of the SPD and not due to the setup itself. An AWG provides gating pulses to both SPDs with a tunable delay so as to measure the photon statistics. Fig. 2(a) shows the coincidence count measurements between signal and idler. The histograms are plotted by collecting  $5 \times 10^6$  samples for each delay. The 0 ns delay counts are mainly due to the SFWM interaction while the peaks at other delays, taken at pulse repetition rate, are due to SpRS and detector dark counts. Fig. 2(b) plots the coincidence counts at signal and idlers at 1552.52 and 1547.72 nm as a function of average pump power. We see that the coincidence count is a quadratic function indicating that the setup emits entangled photon pairs in this operational regime [2]. Fig. 3 shows JSI across 1500-1600 nm covering S,C, and L bands. The coincidence counts at ITU grid wavelengths in C-band are shown in Fig. 3(b).

## References

1. B. Fang, O. Cohen, M. Liscidini, *et al.*, *Optica* **1**, 281 (2014).
2. X. Li, J. Chen, P. Voss, *et al.*, *Opt. Express* **12**, 3737 (2004).

# Quantum Antibunching in Nonlinear Coupler Using Wigner Representation

Mohd Syafiq M. Hanapi<sup>1</sup>, Abel-Baset M. A. Ibrahim<sup>1</sup>, Pankaj K. Choudhury<sup>2\*</sup>

<sup>1</sup>Faculty of Applied Sciences, Universiti Teknologi MARA, 40450 Shah Alam, Selangor, Malaysia

<sup>2</sup>International Research Center for Advanced Photonics, Zhejiang University, Building 1A, 718 East Haizhou Rd., Haining, Zhejiang 314400, P. R. China

\*E-mail : pkchoudhury@ieee.org

## 1. Introduction

Antibunching, a key characteristic of single-photon sources, is crucial for quantum cryptography and quantum computing [1]. Nonlinear couplers have significant potential as generators of nonclassical light [2,3]. However, Limited research has been reported on antibunching in nonlinear couplers [4,5]. This study investigates antibunching in an innovative design of a nonlinear coupler (as fig. 1 shows) featuring three nonlinear waveguides, each comprising a material that exhibits the second-order nonlinearity.

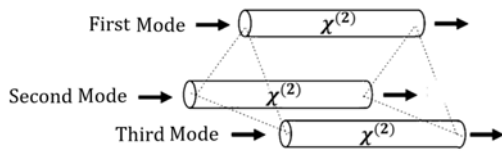


Fig. 1. Schematic of three-channel nonlinear coupler operating with SHG.

## 2. The model

With reference to fig. 1, we assume the interaction of light with the nonlinear waveguide material produces second-harmonic generation (SHG). The Hamiltonian for this three-mode system can be expressed in the form as [6]

$$\frac{\hat{H}}{\hbar} = \sum_j^3 \omega_j \hat{a}_j^\dagger \hat{a}_j + 2 \sum_j^3 \omega_j \hat{b}_j^\dagger \hat{b}_j + \frac{ig}{2} \sum_j^3 (\hat{a}_j^\dagger \hat{b}_j^\dagger - \text{h.c.}) + \kappa (\hat{a}_1^\dagger \hat{a}_2 + \hat{a}_2^\dagger \hat{a}_3 + \hat{a}_3^\dagger \hat{a}_1 + \text{h.c.}). \quad (1)$$

In the Hamiltonian equation,  $\hat{a}_j^\dagger \hat{a}_j$  is the ladder operator where  $j = 1, 2$ , and  $3$  that correspond to the first, second, and third modes, respectively.  $\hbar$  is the reduced Planck constant,  $\omega_j$  is the input frequency,  $g$  is the nonlinear coupling constant, and  $\kappa$  is the linear coupling parameter. Using this Hamiltonian in symmetrical order, the evolution of the current three-mode system is described using the von Neumann equation to obtain a quantum density master equation. The quantum density matrix equation is then converted to its corresponding classical Fokker-Planck (FP) equation using the Wigner representation. The FP equation is subsequently mapped to a system of stochastic differential equations following Ito calculus. This system is solved numerically, and the antibunching is evaluated using the correlation criteria

$$D_j = \langle (\Delta \hat{N}_j)^2 \rangle - \langle \hat{N}_j \rangle^2. \quad (2)$$

Herein,  $\hat{N}_j = \hat{a}_j^\dagger \hat{a}_j$  is a number operator,  $\langle \hat{N}_j \rangle$  signifies the average particle or photon count in the  $j^{\text{th}}$  mode, and the antibunching is indicated by  $D_j < 0$ .

## 3. Discussion

Figure 2 illustrates the antibunching behavior in the first channel waveguide for various values of the linear coupling

parameter  $\tilde{\kappa}$ . At  $\tilde{\kappa} = 0.1$  (fig. 2a), the antibunching oscillations are slow. As  $\tilde{\kappa}$  increases to  $0.3$  (fig. 2b) and  $0.7$  (fig. 2c), the oscillations become more rapid. This behavior is very likely due to narrower channel separation, which allows for more efficient energy exchange between the waveguides (in three-channel nonlinear coupler system), leading to a faster antibunching response.

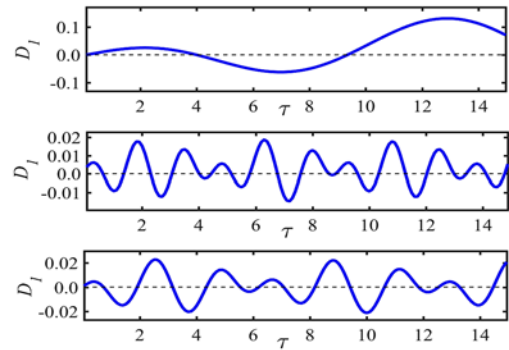


Fig. 2. Photon antibunching exhibited by the first mode. Evolution below the  $y = 0$  line indicates antibunching. (a)  $\tilde{\kappa} = 0.1$ , (b)  $\tilde{\kappa} = 0.3$ , and (c)  $\tilde{\kappa} = 0.7$ . The other input parameters are  $\alpha_1 = \alpha_2 = \alpha_3 = 1$ ,  $\tilde{\omega}_1 = \tilde{\omega}_2 = \tilde{\omega}_3 = 1$  and  $\tilde{g} = 0.01$ . The dimensionless parameters are related to their dimensionless counterparts by  $\tilde{\omega}_1 = \omega_1/\omega_1$ ,  $\tilde{\omega}_2 = \omega_2/\omega_1$ ,  $\tilde{\omega}_3 = \omega_3/\omega_1$ ,  $\tilde{g} = g/\omega_1$ ,  $\tilde{\kappa} = \kappa/\omega_1$ , and  $\tau = \omega_1 t$ .

## 4. Conclusion

We have investigated the potential for generating photon antibunching in a three-channel waveguide nonlinear coupler system that operates with second-order nonlinearity and produces SHG, using the Wigner representation in phase space. The results demonstrate the effectiveness of a three-channel SHG-based nonlinear coupler in generating quantum antibunching. This simple-structured device would serve as an efficient source of antibunching light.

## Acknowledgement

A-BMAI acknowledges the Ministry of Higher Education (MOHE, Malaysia) for the grant FRGS/1/2021/STG07/UITM/02/10 and PKC acknowledges the financial support by Zhejiang University (China) through the grant 11133000\*194232301/002.

## References

- [1] H. Zhu, X. Li, Z. Li, F. Wang, and X. Zhong, *Opt. Express* **31** (2023) 22030.
- [2] M. S. M. Hanapi, A.-B. M. A. Ibrahim, and P. K. Choudhury, *Optik* **243** (2021) 167420.
- [3] R. Julius, A.-B. M. A. Ibrahim, P. K. Choudhury, A. N. Alias, and M. S. Abd Halim, *Sci. Rep.* **12** (2022) 8245.
- [4] R. Julius, A.-B. M. A. Ibrahim, P. K. Choudhury, and H. Eleuch, *Chin Phys B* **27** (2018) 114206.
- [5] S. Mandal and J. Perina, *Phys. Lett. A* **328** (2004) 144.
- [6] R. Julius, A.-B. M. A. Ibrahim, H. Eleuch, and P. K. Choudhury, *J. Mod. Opt.* **66** (2019) 1129.

4 JSAP-Optica Joint Symposia 2024 | 一般セッション(口頭講演)：4.8 Optica Special Lecture

## [17p-A25-1~1] 4.8 Optica Special Lecture

[17p-A25-1]

Silicon photonics and its application to LiDAR

○Toshihiko Baba<sup>1</sup> (1.Yokohama National University)

---